A study of the transformation behaviour and mechanical properties of iron-manganese alloys.

BOLTON, J. D.

Available from the Sheffield Hallam University Research Archive (SHURA) at:

http://shura.shu.ac.uk/19367/

A Sheffield Hallam University thesis

This thesis is protected by copyright which belongs to the author.

The content must not be changed in any way or sold commercially in any format or medium without the formal permission of the author.

When referring to this work, full bibliographic details including the author, title, awarding institution and date of the thesis must be given.

Please visit http://shura.shu.ac.uk/19367/ and http://shura.shu.ac.uk/information.html for further details about copyright and re-use permissions.

Bar Code
101 381 284 0.

CENTRAL LIBRARY
SHEFFIELD POLYTECHNIC
LIBRARIES

THIS BOOK MAY BE BORROWED
return it promptly, or renew the loan by
te shown. Failure to do so will incur fines.
ary rule 6.)

CANCELLED

CANCELLED

2414-2055

ProQuest Number: 10694248

All rights reserved

INFORMATION TO ALL USERS
The quality of this reproduction is dependent upon the quality of the copy submitted.

In the unlikely event that the author did not send a complete manuscript
and there are missing pages, these will be noted. Also, if material had to be removed,
a note will indicate the deletion.

ProQuest 10694248

Published by ProQuest LLC (2017). Copyright of the Dissertation is held by the Author.

All rights reserved.
This work is protected against unauthorized copying under Title 17, United States Code
Microform Edition © ProQuest LLC.

ProQuest LLC.
789 East Eisenhower Parkway
P.O. Box 1346
Ann Arbor, MI 48106 – 1346

A STUDY OF THE TRANSFORMATION BEHAVIOUR AND MECHANICAL PROPERTIES OF IRON - MANGANESE ALLOYS

by

J. D. Bolton

Sheffield Polytechnic April 1970

SHEFFIELD POLYTECHNIC
LIBRARY
669.96141
BO
Q

This thesis is submitted to the Council for National Academic Awards for the degree of Doctor of Philosophy.

The work was carried out at Sheffield Polytechnic during the period January 1965 to March 1970, under the supervision of Dr. E. R. Petty and Mr. G. Allen. A number of post graduate courses were attended at Sheffield Polytechnic during the above period and included:

1. Crystallography of Martensite transformations.
2. Mathematics of diffusion.
3. Quantitative metallography.
4. Martensite Fundamentals and Technology Conference November 1966.

The results obtained by this programme of work, and their explanation, are to the best of my knowledge original except where reference is made to other authors. No part of this thesis has been submitted for degrees at any other college or university.

[redacted]

J. D. BOLTON.
April 1970.

CONTENTS

SYNOPSIS

1.0 INTRODUCTION

REVIEW OF LITERATURE Part I

2.0 TRANSFORMATION IN IRON ALLOYS

2.1 Modes of austenite decomposition in iron alloys
2.1.1 Equiaxed ferrite
2.1.2 Massive ferrite
2.1.3 Massive martensite
2.1.4 Acicular martensite
2.1.5 Epsilon martensite

2.2 General characteristics of massive ferrite and martensite in iron alloys
2.2.1 Massive ferrite
2.2.1.1 Morphology
2.2.1.2 Crystallography
2.2.1.3 Kinetics
2.2.1.4 Mechanisms
2.2.2 Martensite transformations
2.2.2.1 General characteristics
2.2.2.2 Phenomenological theories of martensitic transformations
2.2.2.3 Kinetic theories
2.2.2.4 Thermodynamics
2.2.2.4.1 Ideal solution
2.2.2.4.2 Regular solution
2.2.2.5 Characteristics of Lath martensite
2.2.2.5.1 Morphology
2.2.2.5.2 Crystallography
2.2.2.5.3 Phenomenological theory
2.2.2.5.4 Kinetics
2.2.2.5.5 Thermodynamics
2.2.2.5.6 Effects of alloying elements
2.2.2.6 Twinned martensite in ferrous alloys
2.2.2.7 Epsilon martensite

2.3 Transformation in iron manganese alloys

REVIEW OF LITERATURE Part II

3.0 PROPERTIES

3.1 Properties of maraging steels

3.2 Mechanical properties of iron manganese alloys

CONTENTS (cont'd.)

3.3 Criteria for brittle fracture

3.3.1 Significance of the σ_i parameter
3.3.1.1 Significance of the σ_0 parameter
3.3.1.2 Significance of the σ_* parameter
3.3.1.2.1 Peierls Nabarro friction stress mechanism
3.3.1.2.2 Thermal component of flow stress in martensitic steels
3.3.1.3 Summary of $\sigma_i = \sigma_0 + \sigma_*$
3.3.2 Significance of the k_y parameter
3.3.2.1 k_y for martensitic steels
3.3.3 Significance of grain size $d^{-\frac{1}{2}}$
3.3.4 Significance of γ the surface energy term
3.3.5 Significance of β and μ

3.4 Summary

4.0 EXPERIMENTAL PROCEDURE

4.1 Alloy preparation

4.2 Transformation studies
4.2.1 Specimen preparation
4.2.2 Dilatometric analysis
4.2.3 Isothermal recording dilatometer
4.2.4 Thermal analysis
4.2.5 Metallographic examination
4.2.5.1 Optical
4.2.5.2 Hot Stage
4.2.5.3 Electron metallography
4.2.6 X-Ray diffraction

4.3 Mechanical Properties
4.3.1 Impact properties
4.3.2 Tensile testing
4.3.3 Hardness tests

5.0 RESULTS

5.1 Transformation Studies
5.1.1 Determination of the A_s and A_f temperatures on heating
5.1.2 Determination of transformation temperatures on cooling
5.1.3 Metallographic examination
5.1.3.1 Optical metallography
5.1.3.2 Electron metallography
5.1.4 X-Ray examination

CONTENTS (Cont'd.)

5.1.5 Hardness measurements.
5.1.6 General comparison of the lath martensitic structures
5.1.7 Isothermal transformation studies
5.1.7.1 Hot stage microscopy
5.1.7.2 X Ray diffraction
5.1.8 Effects of austenitizing time and temperature
5.1.9 Crystallographic observations of the lath martensite structure

5.2 Mechanical properties
5.2.1 Impact results
5.2.1.1 Examination of fractures
5.2.1.2 Effects of tempering
5.2.1.2.1 Examination of fractures
5.2.1.2.2. Examination of structural changes on tempering
5.2.1.3. Impact properties of high purity iron manganese and iron manganese molybdenum alloys
5.2.2 Measurements of the parameters controlling brittle fracture
5.2.2.1 Petch analysis
5.2.2.1.1 Fracture stress
5.2.2.2 Determination of the thermal component of flow stress
5.2.3 Effects of tempering on tensile properties

6.0 DISCUSSION

6.1 Transformation behaviour
6.1.1 Driving force for transformation
6.1.1.1 Ideal solution
6.1.1.2 Regular solution
6.1.2 Transformation behaviour in iron manganese alloys
6.1.3 Effects of austenitizing time and temperature

6.2 Mechanical properties
6.2.1 Brittle fracture behaviour
6.2.2. Fundamental properties in relation to brittle fracture
6.2.2.1 Assessment of σ_i
6.2.2.1.1 σ_0 the athermal component of flow stress
6.2.2.1.2 σ^* the thermal component of flow stress
6.2.2.1.2.1 Analysis of flow stress data to determine H
6.2.2.1.2.2 Analysis of flow stress data to determine activation volume

CONTENTS (Cont'd.)

6.2.2.1.2.3 Determination of H and V_* by stress relaxation
6.2.2.1.2.4 Assessment of flow stress in terms of the Dorn Rajnak theory
6.2.2.1.3 Summary of σ_0 and σ_* and their importance to brittle fracture
6.2.2.2 Assessment of K_y
6.2.2.3 Assessment of grain size
6.2.2.4 Summary of the effects of the property parameters on brittle fracture in relation to the Cottrell equation

7.0 CONCLUSIONS

7.1 Transformation behaviour

7.2 Mechanical properties

8.0 RECOMMENDATIONS FOR FURTHER WORK

ACKNOWLEDGEMENTS.

I should like to thank the Polytechnic Authorities and Mr. D. Thacker, Head of the Metallurgy Department, for permission to carry out the programme of work and to submit this thesis.

My thanks are also due to Mr. G. Allen of British Steel Corporation (Special Steels Division) and to Dr. E. R. Petty of Sheffield Polytechnic for their continued help and encouragement during the course of the work.

The assistance of various staff at both the British Steel Corporation (Special Steels Division), and within the Metallurgy Department of Sheffield Polytechnic is also gratefully acknowledged. In particular I should like to thank those who were responsible for making the alloys, machining test pieces, and for aiding the building of equipment.

Finally, my special thanks are due to my wife for typing this thesis.

SYNOPSIS

A study has been made of both the transformation behaviour and mechanical properties of a series of very low carbon iron manganese alloys within the range 0 to 10% manganese.

Alloys containing between 4 and 10% manganese were found to undergo a martensitic transformation which was identical to the "lath" or "massive" martensite reaction found in other iron alloys. A possible bainitic reaction was also found in alloys containing between 4 and 6% manganese, and was referred to as recovery assisted martensite owing to the possible assistance to growth by recovery processes in either the austenite or martensite.

In the "lath" martensitic condition the iron manganese alloys were shown to possess good tensile strengths and ductilities but their impact properties were markedly inferior to equivalent iron nickel alloys. An explanation of this poor impact resistance was sought in terms of both structural peculiarities, i.e. twinned martensite formation and from any deviation between iron manganese and iron nickel alloys in their dependence of flow stress on temperature and strain rate. Neither of these two avenues of investigation revealed any source of explanation, and the most likely cause of brittleness was shown to be the possible segregation of impurities at prior austenite grain boundaries which created all of the effects usually encountered with temper brittleness

1.0 INTRODUCTION

Many of todays ultra high strength and cryogenic steels contain appreciable quantities of nickel, and thereby suffer from high costs. The underlying objective of this research has been therefore to test the validity of replacing nickel by a cheaper element. Manganese was chosen for this purpose because of its cheapness and also since it has similar effects to nickel upon austenite stability.

In the present work the aim has been to assess the basic transformation behaviour and mechanical properties of a series of iron manganese alloys within a composition range which produces an austenite - ferrite transformation, e.g. 0 to 10% manganese. The higher manganese alloys in which epsilon formation occurs were avoided since they would not have been comparable with iron nickel alloys.

It was hoped originally that by proving that iron manganese alloys could produce equivalent properties and heat treatment characteristics to iron nickel alloys; work could go on into the development of strengthening by precipitation hardening. However, poor impact properties were encountered in binary iron manganese alloys, and the emphasis shifted towards finding the cause of embrittlement. This was tackled by an attempt to discover any inherant feature of iron manganese alloys such as the response of their flow stress to low temperatures and to changes in strain rate, or to peculiarities in the austenite decomposition process. Neither of these two approaches managed to distinguish iron manganese alloys from iron nickel alloys, and it became evident that brittleness was due to grain boundary weakness. This grain boundary effect was given some attention, but the impurity responsible for embrittlement was not identified.

REVIEW OF LITERATURE Part I

2.0 TRANSFORMATION IN IRON ALLOYS

2.1 Modes of Austenite decomposition in iron alloys

Five basic modes of transformation from austenite to ferrite, which do not involve carbide separation, have been established for iron alloys, and may briefly be described as follows:

2.1.1 Equiaxed Ferrite

Austenite decomposes to ferrite during cooling by nucleation and growth, and involves equilibrium partitioning of alloying elements. The resulting structure consists of equiaxed ferrite grains of fairly low dislocation density, i.e. equivalent to annealed ferrite, and their growth is unaffected by prior austenite grain boundaries. No surface tilting is observed on prepolished surfaces which indicates that no shape change occurs during transformation.

2.1.2 Massive Ferrite

This differs from equiaxed ferrite in two major respects. Firstly, no equilibrium partitioning of alloying elements occurs during transformation, so that the structure maybe supersaturated, and secondly because it depends only upon short range diffusion its growth rate is much more rapid. Otherwise the massive ferrite transformation resembles equiaxed ferrite since it does not produce surface tilting on a prepolished surface, and its growth is also unaffected by orientation changes across prior austenite grain boundaries.

2.1.3 Massive Martensite

This has also been referred to as "self accommodating" [1] "lath" [2], or "slipped" [3] martensite, but shall herein be termed as lath martensite. At this stage it will suffice to say that lath martensite is the product of austenite decomposition to body centred cubic ferrite via a shear mode of transformation. The structure produced is often characteristically described was "Widmanstatten" ferrite, but it should not be confused with the Widmanstatten ferrite formed in carbon steels.

2.1.4 Acicular Martensite

This is also referred to as twinned martensite and occurs in high carbon steels [4], binary iron platinium alloys [5] and in binary iron nickel alloys containing more than 28% nickel [6]. Acicular martensite in iron nickel alloys is a body centred cubic structure, but is body centred tetragonal in carbon steels. It differs from lath martensite mainly by its morphology, which consists of lenticular plates, whose internal structure is cross hatched by transformation twins. Lath martensites do not exhibit any evidence of a twinned substructure.

2.1.5 Epsilon Martensite.

This occurs chiefly in steels whose austenite has a low stacking fault energy, e.g. 18 Cr 8 Ni stainless steels.[7] and is generally believed to represent an intermediate stage in the decomposition of austenite to ferrite. Its structure is hexagonal close packed and it forms in parallel sided bands bounded by the $\{111\}$. austenite planes. There are a variety of means, e.g. cold working, tempering, or sub-zero treatment by which epsilon can be made subsequently to transform to a body centred cubic ferrite whose structure closely resembles that of lath martensite.

Other products of austenite decomposition such as pearlite or bainite usually involve carbide separation, and so have not been included in the above list. However, the inclusion of a Bainite mode of transformation maybe justified, since there are reports [8,9] of an isothermal shear transformation in binary iron alloys containing virtually no carbon. From a structural aspect this isothermal transformation product resembles lath martensite.

In binary iron manganese alloys several of the above modes of transformation are likely to be encountered and will be given further attention in the following sections.

2.2 General characteristics of massive ferrite and martensite in iron alloys

2.2.1 Massive Ferrite.

Massive ferrite derives its name from its morphological resemblence to the structures observed in copper alloys [10] and which were termed massive" by Massalski [11]. In ferrous alloy systems massive ferrite structures have been observed in numerous alloys including iron nickel [8 12 13 14] iron chromium [15 16] iron silicon [12] iron copper [17] iron carbon [18-20] iron nitrogen [18-21] and iron manganese[22]

2.2.1.1 Morphology

A typical example of a massive ferrite structure, shown in Fig. 1, reveals a structure consisting of irregular ragged ferrite grains, which are often difficult to distinguish from equiaxed ferrite by optical metallography. By over-etching massive ferrite develops etch pitting due to a substructure, whereas equiaxed ferrite does not, and this substructural feature is even more clearly shown by either thin foil electron metallography or by the measurement of line broadening in X ray diffraction. Electron metallography reveals that massive ferrite consists of grains separated by high angle boundaries, which contain areas of a high density (10^{11} - 10^{12} lines/cm)[23] of uniformly distributed dislocations. These dislocations tend to adopt planar distributions[14]. Low angle boundary sub cells are sometimes formed particularly when either the cooling rate is increased or the transformation temperature decreased[16.20].

The high dislocation density of massive ferrite compared to equiaxed ferrite also produces X ray line broadening with the result that massive ferrite causes broad diffuse X ray lines in contrast to the sharp lines produced by equiaxed ferrite[13].

2.2.1.2 Crystallography

Transformation to massive ferrite as stated earlier does not produce surface tilting on a prepolished surface, and this implies that no lattice correspondence exists between the parent and product phase [24]. Furthermore, the growth of massive ferrite appears to pay little regard to changes in orientation across prior austenite grain boundaries which suggests that no orientation relationships exist between the ferrite and austenite phase. Aaronson[25] however has questioned this and has suggested that both a rational habit plane and orientation relationship might exist, because planar facets are occassionally observed in massive crystals[10]. A crystallographic orientation relationship can exist however only during the nucleation stage if massive ferrite growth is truly unaffected by prior austenite grain boundaries. In Fig. 2 a process of sympathetic nucleation either side of an austenite grain boundary is schematically illustrated which leads to a suggestion of apparant growth across the boundary and a situation where an orientation relationship could exist between the austenite and ferrite. The basis for this is essentially that described by Smith[26] for proeutectoid ferrite and consists of the formation of a coherent ferrite nucleus at a grain boundary which grows more rapidly into the grain in which it forms an incoherent boundary. No orientation relationship exists between the ferrite and the austenite grain in which growth has occurred but one does exist with the adjacent austenite grain. It is also possible that this effect could occur with massive ferrite transformations, and this would account for the failure to detect any orientation relationship between the ferrite and austenite.

2.2.1.3 Kinetics

Several authors[8,12,14] have confirmed that massive ferrite transformation occurs isothermally from evidence of the ability to suppress the transformation temperature with increased cooling rates. Also a characteristic C type transformation curve has been established for iron chromium[15,27] alloys which clearly indicates an isothermal nucleation and growth mode of transformation for massive ferrite. It has also been found that the transformation temperature is depressed by increasing the cooling rate, but a limiting temperature is eventually reached which is unaltered by any further increase in cooling rate [28,29]. This limiting transformation temperature probably corresponds to the temperature at which the nose of the C - curve occurs[15], since a cooling rate designed to supress transformation below the critical temperature would miss the C curve and completely supress massive ferrite transformation.

Alloying elements may also depress the massive ferrite transformation start temperature and displace the C curve further to the right due to their influence upon diffusion rates and the T_o temperature, where the T_o temperature is that for thermodynamic equilibrium between austenite and ferrite of the same composition. Transformation can occur only at temperatures below T_o and elements such as nickel or manganese which are austenite stabilizers tend to lower T_o and hence the massive ferrite transformation start temperature. Ferrite stabilizers, for example chromium and silicon, initially decrease T_o but raise it above a certain composition, and so tend to produce similar effects upon α_s the massive ferrite transformation start temperature[12]

In addition to the effects of alloying upon T_0, the α_s temperature is lowered by the reduced rates of diffusion, and it is thought that alloying elements could retard growth rates by creating a frictional drag upon boundary mobility [14]. This drag effect is due to the need for solute atmospheres to diffuse with the boundary, so that its mobility is controlled by solute diffusivity [30]. In iron carbon alloys for example the massive ferrite boundary migration rate is reduced from 0.8 mm/sec to less than 0.1 mm/sec by altering the carbon level from 0 to 0.1 Wt% [31].

Finally, the massive ferrite transformation is also affected by both the austenitizing temperature and time, because these both control the austenite grain size, and the number of nucleation sites for transformation. Any factor which encourages small austenite grain sizes will promote the formation of massive ferrite [14].

2.2.1.4 Transformation Mechanisms

Initially massive ferrite transformations were classed as diffusionless transformations [32] due to their apparently rapid growth rates and to the absence of compositional change. This possibility is now exluded however due to the absence of surface tilts on a prepolished surface, and the evidence concerning the isothermal kinetic behaviour. Massive ferrite transformation is, then, a diffusion controlled transformation which is thought to achieve rapid growth rates by a process of short range diffusion of atoms across the interface region only, i.e. one or two interatomic distances[33]. An alternative proposal to this, put forward by Aaronson[34], is a ledge mechanism which employs a ferrite/austenite boundary composed largely of coherent interfaces but also containing a series of disorderly (incoherent) ledges lying perpendicular to the main boundary, see Fig. 3. Rapid boundary migration is said to occur by the rapid diffusion controlled lateral movement of these disorderly ledges, so that the coherent boundary is moved forwards. This coherent component of the boundary does not exclude the possibility of an orientation relationship from existing between massive ferrite and austenite, and the idea of ledges might explain the jagged nature of massive ferrite boundaries which is frequently observed.

2.2.2 Martensitic Transformation

Prior to a detailed discussion of lath martensites it will be useful to review briefly some of the characteristics of martensite, and also the theories put forward in explanation of these characteristics.

2.2.2.1 Characteristics

Martensitic transformation is defined as a shear movement of atoms such that atoms move from a parent to a product lattice by a fully coordinated movement [35]. The term "Military" has been used to describe such transformations, in contrast to "Civilian" transformation, where atom movement is a random process, i.e. diffusion controlled. As well as the above definition, martensite has several characteristic features which collectively aid the definition of martensite. These characteristics are as follows:[36,37].

(i) Athermal Kinetics. In most martensitic transformations the amount of martensite formed is a function only of the temperature, and to induce complete transformation requires continuous cooling through the M_s - M_f temperature range. Cases of isothermal martensitic transformation almost certainly arise due to isothermal nucleation, and not isothermal growth. Athermal growth is probably a unique feature of martensitic transformations.

(ii) Crystallography The parent and product phases in a martensitic transformation exhibit certain characteristic crystallographic orientation relationships and habit planes, but this is not unique to martensite.

(iii) Surface Tilting Martensitic transformation produces surface tilting on a prepolished surface which indicates that the transformed region has undergone a shape change. Past workers have always regarded surface tilting as proof of a shear transformation, i.e. martensite, but later thinking has shown that this is not necessarily true [24]. Non-martensitic transformations, e.g. Widmanstatten ferrite[38] and bainite[39], and the early stages of precipitation may also produce surface tilts.

(iv) Diffusionless Growth Compositions remain unchanged by a martensitic transformation, and growth rates are extremely rapid, i.e. they approach the speed of sound within the metal, but as seen with the case of massive ferrite, neither of these two facts are unique to martensite.

2.2.2.2. Phenomenological theory of martensitic transformation.

Phenomenological theories of martensitic transformation are designed primarily to explain the observed orientation relationships, habit planes, and the shape change produced by transformation. The two original theories are essentially equivalent although arrived at independently and are due to Wechsler Liebermamm & Read (W.L.R),[40] and to Bowles and Mackenzie,[41] (B.M). Both these theories have been the subject of numerous reviews.[35,42,44]

The essential basis of these theories is that when martensitic transformation occurs, the transforming region undergoes a shape change, and must also remain in contact with the surrounding parent phase or the material will disintegrate. This means that a habit plane which is either coherent or semi-coherent must exist, and imposes the condition that the shape change must at least approximate to an "invariant plane strain", i.e. at least one plane must remain both unrotated and undistorted by the shape change. Two examples of invariant plane strains are simple shear or dilatation, see Fig. 4, but neither of these is capable of producing the necessary crystal structure change required for martensitic transformation. Only by combining the two is it possible to produce an invariant plane strain together with a change in crystal structure, and hence the shape change involved in a martensitic transformation consists essentially of shear parallel to the habit plane plus dilatation normal to the habit plane, and the angle ϕ defines the shape change, see Fig. 4.

In the W.L.R. and B.M. theories the total shape change is broken down into component parts such that both the necessary change in crystal structure and the invariant plane strain condition is fulfilled. First to be considered is the strain necessary to create the correct change in crystal structure, and this requires knowledge of the "lattice correspondence", which is simply the relationship between the two crystal lattices. In the face centred cubic austenite cell, an equivalent cell can be found which after homogeneous deformation converts to a body centred cubic cell, and there are several possible correspondences. The most suitable correspondence of the austenite - ferrite transformation is the "Bain correspondence", since this requires less strain to transform to a body centred cubic cell, see Fig. 5. From the "Bain correspondence" a body centred tetragonal cell maybe selected and its dimensions made equivalent to that of any martensitic cell by contraction along the $[010]_\gamma$ axis plus expansion along both the $[100]_\gamma$ and $[001]_\gamma$ axis. This homogeneous deformation is referred to as the "Bain strain" with principal strains equal to $+\eta_1$, $+\eta_2$, $-\eta_3$. In practice the principal strains depend upon the relative lattice parameters of the two phases, but for example in iron nickel alloys they are $\eta_1 = \eta_2 = 1.12$, $\eta_3 = 0.8$. Although the Bain strain produces the necessary change in crystal structure it does not satisfy the invariant plane strain condition, and contact could not be maintained between the transformed region and the surrounding parent material. This is shown more clearly if reference is made to Fig. 6 where the austenite lattice is represented by a unit sphere which deforms to an ellipsoid by a deformation equivalent to the Bain Strain. In this diagram no plane is left either unrotated or undistorted, but instead there are a series of vectors lying on cones at the intersection between the original unit sphere, the strain ellipsoid, and the reciprocal strain ellipsoid, which are undistorted but not unrotated. These two unextended cones refer to a series of vectors and plane normals left undistorted by the Bain Strain.

To fulfill the invariant plane strain condition requires that the deformation has principal strains where one is positive, one is negative, and the third is zero and this condition is clearly not met by the Bain Strain. It is possible however to achieve this by introducing an additional deformation. Simple shears such as mechanical twinning or slip on adjacent planes are termed "lattice invariant shears " since they do not alter the crystal structure, and furthermore they may result in certain vectors being shortened or increased in length, see Fig 7. Thus by the addition of a slip or twinning deformation to the Bain Strain one of the principal Bain strains can be restored to its original length, and this will apparently produce an overall invariant plane strain. This is however not quite correct since the Bain Strain also results in vectors being rotated, and an additional operation is required to return them back to their original positions; this is termed a "Rigid Body Rotation".

The total shape change involved in a martensitic transformation may therefore by summarised as the sum of Bain Strain plus Lattice Invariant Shear plus Rigid Body Rotation. Quantitative predictions of the habit plane, orientation relationship, and shape change accompanying martensitic transformation are obtainable from a stereographic analysis or by matrix algebra. The two basic matrix equations are represented by:

1. $E = RBS$ (W.L.R.)

2. $ES^{-1} = BR$ (B-M)

and where:

1. E is a matrix which determines the changes occurring to vectors following the total shape change.

2. B is a matrix determing the changes in vectors following the Bain Strain, and is fixed by the lattice parameters of the austenite and martensite. These therefore determine the values of the principal strains. An additional variable introduced by the B-M theory is one which allows for the habit plane to be slightly distorted, and is referred to as the dilatation parameter δ . The effect of including δ is to alter the dimensions of the original unit sphere by an amount equal to δ and this alters the Bain principal strains to become $\delta\eta_1 . \delta\eta_2 . \delta\eta_3$.

3. S is a matrix which determines the changes in vectors due to a lattice invariant shear with a fixed plane and direction, and with a definite angle of shear. By varying the choice of this shear system, different predictions of habit plane are produced.

4. S^{-1} is an inverse matrix of S and represents an invariant plane strain or lattice invariant shear in an opposite direction to S.

5. R is a matrix which represents a rigid body rotation such that all vectors which are rotated by the Bain Strain and lattice invariant shear are rotated back to their original positions.

The two equations for the W.L.R. and B.M. theories are equivalent to each other despite their apparent difference, and this can be shown by the following:

$$E = RBS \qquad (\text{W.L.R.})$$

$$ES^{-1} = RBSS^{-1}$$

but since $SS^{-1} = I$ a unit matrix

$$ES^{-1} = RB \qquad (\text{B.M.})$$

In order to predict the habit plane the B-M equation relies upon the condition that both E and S^{-1} are invariant plane strains and, as such, will create an invariant line along the intersection of the two shear planes. Furthermore, the plane containing the two shear directions of E and S^{-1} has an invariant normal which together with the invariant line of intersection defines the habit plane.

When the theory is applied to steels it successfully predicts the $\{259\}_\gamma$ habit plane found in high carbon steels and in iron-30% nickel alloys when the lattice invariant shear system is chosen to be twinning on the $(112)_M$ $[\bar{1}\bar{1}1]_M$ = $(110)_\gamma$ $[\bar{1}10]_\gamma$ system. However the frequently observed $\{225\}_\gamma$ habit plane requires the use of the additional dilatation parameter δ , and thus allows the habit plane to be distorted. Whether this is justified is doubtful and recent work has shown that there is no experimental justification for including δ as a variable.[46.47] Further shortcomings of the theory are its inability to account for the observed scatter in habit planes found for carbon steels, and also the complete failure to predict the habit plane found for lath martensites. The theory is nevertheless successful in predicting the $\{259\}_\gamma$ or $\{3,10,15\}_\gamma$ habit plane, and perhaps more importantly it predicts that martensite should contain an internal substructure such as mechanical twins which is fully in accord with metallographic observations.[4]

2.2.2.3 Kinetic Theories.

Kinetic theories are designed primarily to account for both athermal and isothermal transformation behaviour during martensitic reaction, and also have attempted to predict a nucleation model. There are numerous theories based upon both classical and non classical approaches which have been reviewed previously,[48,49] but to date they have not been successful. For example, the classical nucleation approach using either a homogeneous or heterogeneous nucleation model predict nucleation activation energies which are several order of magnitude too high, and non-classical models such as the strain embryo theories[50,51] predict critical nucleus sizes which are far too large and which do not explain the effects of pressure upon the M_s temperature.[45] The only clear indication given by the kinetic theories is that martensite formation must overcome some form of nucleation barrier, since it requires considerable undercooling below the T_o temperature to initiate transformation. Some of the factors which have been suggested as contributors to the nucleation barrier include:

1. Interfacial energy.
2. Elastic energy which is equivalent to the volume strain energy.
3. Non reversible plastic deformation of the surrounding austenite, e.g. accommodation slip.

and it is necessary for the total chemical free energy to overcome these before spontaneous transformation can occur or continue.

2.2.2.4 Thermodynamics.

Closely linked to the kinetic theories is the development of methods for deriving the driving force at the M_s temperature and this has received the attention of various workers.[12, 21, 52, 56]

The free energy for a martensitic transformation is a measure of the nucleation barrier and is therfore proportional to the degree of undercooling $\{T_o - M_s\}^o$. Its value follows from the relationships

$$G^{\gamma} = (1 - x_A)\, G^{\gamma}_{Fe} + x_A\, G^{\gamma}_{A} + G^{\gamma}_{M}$$

$$G^{\alpha} = (1 - x_A)\, G^{\alpha}_{Fe} + x_A\, G^{\alpha}_{A} + G^{\alpha}_{M}$$

$$\Delta G^{\alpha-\gamma} = (1 - x_A)\, \Delta G^{\alpha-\gamma}_{Fe} + x_A\, \Delta G^{\alpha-\gamma}_{A} + \Delta G^{\alpha-\gamma}_{M} \qquad (1)$$

where X_A = mole fraction of alloying element A

$\Delta G^{\alpha-\gamma}_{Fe}$ = the free energy change for the α-γ change in pure iron

$\Delta G^{\alpha-\gamma}_{A}$ = the free energy change for the α-γ change in pure metal A

$\Delta G^{\alpha-\gamma}_{M}$ = the difference in free energy of mixing between solutions of iron and the element A in the α and γ forms.

$\Delta G^{\alpha-\gamma}$ represents the free energy change for the martensitic transformation, and its evaluation requires that the terms in equation (1) should be known. In this respect the two most difficult terms to evaluate are $\Delta G_A^{\alpha-\gamma}$ and $\Delta G_M^{\alpha-\gamma}$ and can only be estimated by assuming that either an ideal or regular solution exists. Measured values for $\Delta G_{Fe}^{\alpha-\gamma}$ are already available.

2.2.2.4.1 Ideal Solution [52,53]

By definition $\Delta G_M^{\alpha-\gamma}$ for ideal solutions is zero and equation (1) hence becomes

$$\Delta G^{\alpha-\gamma} = (1 - x_A)\, \Delta G_{Fe}^{\alpha-\gamma} + x_A\, \Delta G_A^{\alpha-\gamma}$$

Also by definition

$$\bar{G}_A - G_A = RT\ln A_A = RT\ln X_A$$

where $\bar{G}_A$ = the partial molar free energy of element A dissolved in iron.

A_A = the activity of element A

X_A = the mole fraction of element A

Therefore the following can be writted

$$\bar{G}_A^{\gamma} - G_A^{\gamma} = RT\ln X_A^{\gamma}$$

$$\bar{G}_A^{\alpha} - G_A^{\alpha} = RT\ln X_A^{\alpha}$$

where X_A^{γ} and X_A^{α} are the equilibrium solubilities of metal A in γ and α iron respectively.

Since $\bar{G}_A^{\gamma} = \bar{G}_A^{\alpha}$ at equilibrium

$$\Delta G_A^{\alpha-\gamma} = RT\ln \frac{X_A^{\alpha}}{X_A^{\gamma}} = \Delta H_A^{\alpha-\gamma} - T\Delta S$$

The free energy for martensitic transformation is therefore given by

$$\Delta G^{\alpha-\gamma} = (1 - x_A)\, \Delta G_{Fe}^{\alpha-\gamma} + x_A\, RT\ln \frac{X_A^{\alpha}}{X_A^{\gamma}} \tag{2}$$

Equation (2) is of limited use owing to the assumption of ideality and rarely applies in practice except perhaps to dilute solutions. The alternative analysis is based upon assuming that a regular solution exists.

2.2.2.4.2 Regular Solution.[54,55]

To determine $\Delta G_m^{\alpha-\gamma}$ By definition of a regular solution the excess entropy of mixing is zero; the entropy of solution is ideal, and there is a small excess enthalpy of solution. It is also assumed that for a given composition the free energies of martensite and equilibrium ferrite are equal.

Therefore:

$$G_m^{\gamma} = H_m^{\gamma} - TS_m$$
$$G_m^{\alpha} = H_m^{\alpha} - TS_m$$

where H_m and S_m are the enthalpy and entropies of mixing in either the γ or α phase.

Both vary with temperature according to the relationships

$$H_m = H_o + \int_o^T Cp_m \, dT$$
$$S_m = S_o + \int_o^T \frac{Cp_m}{T} \, dT$$

where Cp_m is the specific heat of mixing.

Further, by definition in regular solutions, Cp_m, H_m, and S_m vary with composition such that

$$Cp_m = e \, x_A \, (1-x_A)$$
$$H_{mo} = d \, x_A \, (1-x_A)$$

and $$S_m = -R \left\{ x_A \ln x_A + (1-x_A) \ln (1-x_A) \right\}$$

which enables the equations for G_m and G_m to be written

$$G_m^{\gamma} = d^{\gamma} x_A(1-x_A) - T \left\{ R(x_A \ln x_A + (1-x_A)\ln(1-x_A)) + \int_0^T e^{\gamma} x_A(1-x_A) \, dT \right\}$$
$$G_m^{\alpha} = d^{\alpha} x_A(1-x_A) - T \left\{ R(x_A \ln x_A + (1-x_A)\ln(1-x_A)) + \int_0^T e^{\alpha} x_A \frac{(1-x_A)\, dT}{T} \right\}$$

and $\Delta G_m^{\alpha-\gamma}$ which is the difference between these two is given by

$$\Delta G_m^{\alpha-\gamma} = x_A\ (1-x_A)(B-A) \tag{3}$$

where $B = d^{\gamma} - e^{\gamma}\ T(1-\ln T)$ and $A = d^{\alpha} - e^{\alpha} T\ (1-\ln T)$

To determine $\Delta G_A^{\alpha-\gamma}$

At equilibrium the partial molar free energies of each component are equal in the α and γ phase.

i.e.

$$\bar{G}_{Fe}^{\gamma} = \bar{G}_{Fe}^{\alpha}$$

$$\bar{G}_A^{\gamma} = \bar{G}_A^{\alpha}$$

furthermore from Fig. 8 it can be shown that

$$\bar{G}_A = G + (1-x_A)\ \frac{dG}{dx}$$

$$\bar{G}_{Fe} = G - x_A\ \frac{dG}{dx}$$

Therefore

$$\bar{G}_A = G_{xA_\alpha}^{\alpha} + (1-x_{A_\alpha})\ \frac{dG}{dx} = G_{xA_\gamma}^{\gamma} + (1-x_{A_\gamma})\ \frac{dG}{dx} \tag{4}$$

where G_{xA_α} and G_{xA_γ} are the free energies of the α and γ phases at the equilibrium concentrations of x_{A_α} and x_{A_γ} respectively, and may also be written in accordance with equation (1) as

$$G_{xA}^{\alpha} = (1-x_A)\ G_{Fe}^{\alpha} + x_A\ \ G_A^{\alpha}\ + G_m^{\alpha}$$

$$G_{xA}^{\gamma} = (1-x_A)\ G_{Fe}^{\gamma} + x_A\ \ G_A^{\gamma}\ + G_m^{\gamma}$$

when these are substituted in equation (4)

$$\left\{(1-x_{A_\alpha})G_{Fe}^{\alpha} + x_{A_\alpha} G_A^{\alpha} + G_m^{\alpha}\right\} + (1-x_{A_\alpha})\ \frac{dG}{dx} = \left\{(1-x_{A_\gamma})G_{Fe}^{\gamma} + x_{A_\gamma} G_A^{\gamma} + G_m^{\gamma}\right\} + (1-x_{A_\gamma})\ \frac{dG}{dx} \tag{5}$$

and the difference between the two sides of the equation leads to an expression for $\Delta G_A^{\alpha-\gamma}$ in terms of x_{A_α} x_{A_γ} $\Delta G_{Fe}^{\alpha-\gamma}$ and $\Delta G_m^{\alpha-\gamma}$, all of which are known, e.g. x_{A_α}, x_{A_γ} are known from the equilibrium diagram and $\Delta G_m^{\alpha-\gamma}$ follows from equation (3).

Thus the following expressions are obtained from equation (5)

$$\Delta G_A^{\alpha-\gamma} = (1-x_{A_\alpha})^2 A - (1-x_{A_\gamma})^2 B - RT\ln \frac{x_{A_\gamma}}{x_{A_\alpha}} \qquad (6)$$

$$\Delta G_{Fe}^{\alpha-\gamma} = x_{A_\alpha}^2 A - x_{A_\gamma}^2 B - RT\ln \frac{(1-x_{A_\alpha})}{(1-x_{A_\gamma})} \qquad (7)$$

and by assuming that the $x_{A_\alpha}^2$ term in equation (7) is small a solution for B can be obtained, but not for A. If however A is also assumed to be small an approximate solution for $\Delta G_A^{\alpha-\gamma}$ can be obtained from equation (6) which enables $\Delta G^{\alpha-\gamma}$ for the martensite transformation to be determined.

Finally, $\Delta G^{\alpha-\gamma}$ maybe calculated using measured values of M_s temperature and A_s temperature by the assumption that

$$\Delta G^{\alpha-\gamma} = (1-x_A)\Delta G_{Fe}^{\alpha-\gamma} + x_A(A+BT^2+CT^3)+x_A(1-x_A)d^{\alpha-\gamma}+e^{\alpha-\gamma}T(1-\ln T) \qquad (8)$$

where $\Delta G_A^{\alpha-\gamma}$ is represented by the series $(A+BT^2+CT^3)$ and $\Delta G_m^{\alpha-\gamma}$ equals $x_A\ (1-x_A)d^{\alpha-\gamma} + e^{\alpha-\gamma}\ T\ (1-\ln T)$

A series of simultaneous equations can be formed to enable the coefficients $A,B,C,d^{\alpha-\gamma},e^{\alpha-\gamma}$, to be solved, using the criterion that at T_0, $\Delta G^{\alpha-\gamma} = 0$ and $T_0 = \frac{1}{2}\ (A_s + M_s)^0$ where A_s is the start temperature for reverse martensite to austenite transformation and M_s is the austenite to martensite start temperature.

2.2.2.5 Characteristics of Lath martensites in ferrous alloys

When the massive ferrite transformation is totally supressed either by the addition of alloying elements or by rapid cooling, transformations in many iron alloys occurs martensitically and produces lath martensite.

2.2.2.5.1 Morphology.

A typical example of the structure of lath martensite for an iron nickel alloy is shown in Fig. 9, and similar structures are observed in pure iron,[19.28] iron chromium,[13 16] iron copper,[17] iron carbon,[4.18.19] and iron nitrogen[18.21] alloys. This structure is best described as a series of straight-sided slabs which do not cross the prior austenite grain boundaries and do not occur in more than four orientations within any single austenite grain. Within the slabs a substructure exists which can be more clearly revealed by the use of a suitable etchant, and consists of fine striations parallel to the slab boundaries,[57] see Fig. 10, and are described as bundles of laths. The use of two surface trace analysis reveals that the slabs approximate to parallellopipeds[58] with one side rather longer than the other two.

A more detailed picture of the lath martensite structure is obtained by examination with thin foil electron microscopy, and reveals that the fine substructure consists of elongated cells or laths in a series of parallel bundles.[58.59] The cell boundaries are composed of regions of high dislocation density and there is also a fairly high uniform distribution of random dislocations within each cell. Cell dimensions vary with alloy content and quenching speed but typical ones are 0.2 - 1.0μ wide and $10\text{-}50\mu$ long. For example, several authors[16.20] have noted a tendency for the cells to become larger and more equiaxed if the transformation temperature is high, and have suggested that recovery might be taking place during transformation. Alloying elements have also been shown to reduce the cell dimensions,[20.60] one possible explanation being the reduction of austenite stacking fault energy caused by alloying,[60] although the lowering of transformation temperature could be equally important. A further frequent observation is that the lath or cell boundaries are often wavy[13] and are curved towards their ends where cells of different orientation dovetail together.[14]

Examination of a prepolished surface reveals that surface tilting occurs to produce parallel bundles of laths, and these bundles correspond to the slabs observed after etching.[58.62.61] Individual surface tilts probably correspond to the single cells or laths found in thin foils, but this is not absolutely certain.[58] There is nevertheless no doubt that they are related to the underlying structure and do not represent surface martensite.[63]

Finally, interferometric observations of the surface tilts have revealed that adjacent pairs are sheared in opposite directions, and for this reason a process of "self accommodation" is thought to exist. Furthermore the tilts have rounded tops, and this has led to the suggestion that slip has taken place in the surrounding austenite,[64] which could also produce a sympathetic nucleation effect for each adjacent lath. This accommodation slip is shown in Fig. 11.

2.2.2.5.2 Crystallography

In common with other martensitic transformations, lath martensites exhibit both a characteristic orientation relationship and habit plane, and these have been determined both by direct measurement and by inference from indirect observation. Evidence that the habit plane is the $\{111\}_\gamma$

plane stems initially from the observation of a characteristic Widmanstatten arrangement of slabs,[4.58.65.66] and the existence of slabs lying parallel to annealing twins in the prior austenite grains.[67] Both of these observations suggest that the habit plane lies parallel to the $\{111\}_\gamma$ planes, but do not establish the fact beyond doubt. More recently direct measurements in iron nickel alloys containing retained austenite[68] have confirmed that the habit plane is the $\{111\}_\gamma$ plane, and the analysis of Bryans[58] confirms these findings. In fact, it is now generally accepted that the habit plane for lath martensites is the $\{111\}_\gamma$ plane, but there are alloys in which a martensitic ferrite forms with a completely different habit plane. The particular alloys are those with low stacking fault energy austenites such as 18%Cr. 8%Ni stainless steels, and the martensitic transformation produces a structure which, although metallographically indistinguishable from other lath martensites, has a habit plane of either $\{225\}_\gamma$,[69] $\{259\}_\gamma$[70] or $(\overline{1}\overline{1}2)_\gamma$[71]. Two further differences also exist, namely that (1) the transformation seems to have occurred via the $\gamma \rightarrow \varepsilon \rightarrow \alpha$ sequence and (2) adjacent pairs of laths are in twin orientations of each other. This latter observation is not normally the case for the $\{111\}_\gamma$ type lath martensite, although occassional examples of twin related lath pairs have been reported.[4.23.72]

The orientation relationship for lath martensite is consistant with a Kurdjumov Sachs relationship, i.e. $\{111\}_\gamma // \{110\}_\alpha : \langle 110\rangle_\gamma // \langle 111\rangle_\alpha$ and this has been found to apply both for martensites with the $\{111\}_\gamma$[4.58.65.68] habit plane and the low stacking fault energy $\{225\}_\gamma$[71] type alloys.

The relative orientation between adjacent laths is such that as each lath forms in an adjacent position it must continue to observe the Kurdjumov Sachs orientation relationship with the surrounding austenite, and to do this restricts the number of possible adjacent lath pair orientation relationships to three:

(1) Adjacent laths are of the same orientation, but in fact must be rotated by 180° about the interface normal to produce a separating boundary.

(ii) Adjacent laths are alternate twin orientations.

(iii) Adjacent laths are rotated by 10° about their interface normal, i.e. the $\langle 110\rangle_\alpha$ direction.

In most lath martensitic structures with the $\{111\}_\gamma$ habit plane it seems that the relative lath orientation relationship is of the type (iii),[8.13.16] although type (ii) have been observed, especially in iron carbon[4] and iron nitrogen[72] alloys.

The final crystallographic feature of lath martensites is their growth direction, and it has been found that the major cell axis is usually along the $\langle 111\rangle_\alpha$ direction,[4.8.45.72] although laths lying parallel to the $\langle 110\rangle_\alpha$ direction have also been reported.[16] The direction normal to the major lath boundary is usually the 110 direction[72] and this is consistent with a $\{110\}_\alpha$ habit plane, or a $\{111\}_\gamma$ habit plane due to the Kurdjumov Sachs relationship.

2.2.2.5.3 Phenomenological theory applied to lath martensites.

In the earlier review of phenomenological theories it was shown that the habit plane prediction could be varied by altering the mode of lattice invariant shear and the magnitude of the dilatation parameter. Frequently the lattice invariant shear system adopted is either:

System I $(110)_\gamma\ [1\bar{1}0]_\gamma = (112)_\alpha\ [11\bar{1}]_\alpha$
System II $(111)_\gamma\ [1\bar{2}1]_\gamma = (101)_\alpha\ [\bar{1}01]_\alpha$

It has further already been shown that the system I shear may account for both the $\{259\}_\gamma$ and $\{225\}_\gamma$ habit planes, but no matter what value of dilatation parameter or shear angle is applied, the $\{111\}_\gamma$ habit plane cannot be predicted, especially if the correct orientation relationship is also to be observed. Shear on system II is most likely to occur in low stacking fault energy austenites since it describes essentially the movement of a Shockley partial dislocation, and as such it predicts satisfactorily the $(\overline{11}2)_\gamma$ [71.73] habit plane observed in 18/8 stainless steels. It also accounts for the observation that adjacent lath pairs are twin related because this is the only way of achieving four variants of the $(\overline{11}2)_\gamma$ habit plane in any one austenite grain. When applied to $\{111\}_\gamma$ type lath martensites however it is again unable to predict both the habit plane and orientation relationship.

Later attempts at using the phenomenological theory have adopted different shear systems, i.e. $\{110\}_\alpha \langle 111\rangle_\alpha = \{111\}_\gamma \langle 110\rangle_\gamma$ [74] and even multiple shear on several systems,[47.75] but they still do not satisfactorily predict the $\{111\}_\gamma$ habit plane. In applying the phenomenological theory to the specific case of lath martensites Bryans[58] was able to show that the total shape change is approximately a $6\frac{1}{2}^\circ$ shear along the $\langle 110 \rangle_\alpha$ direction, and leads to the $\{111\}_\gamma$ planes being unrotated but not undistorted. He then argues that this distortion is accommodated by forming an adjacent lath sheared in the opposite direction, so that an undistorted α/γ interface is produced between the laths. Despite this, however, it still remains difficult to imagine how the actual austenite/martensite interface, which still remains distorted, can grow.

In conclusion, the phenomenological theories do not as yet provide a satisfactory explanation for the crystallographic features of lath martensites, but it at least seems probable that a lattice invariant shear system involving slip occurs, and this is one reason why lath martensite is frequently termed slipped martensite. The reasons for the failure of the phenomenological theories are not clear, but one possible reason could be that the laths do not contain a planar interface. It has been suggested, for instance, that lath martensite is composed of needles[4.43] and this would mean that the shape change is an invariant line strain instead of an invariant plane strain. The metallographic evidence however seems to dispute this suggestion.

2.2.2.5.4 Kinetics

Transformation to lath martensite has been reported to occur by athermal means,[13] on the evidence that changes in cooling rate do not alter the slope of the percentage of transformation versus temperature curve. Evidence to the contrary does however exist and there are a number of factors which could indicate that transformation may occur isothermally. Firstly, in some reports[22.28.29] the so-called M_s temperature shows a slight depression when the cooling rate is raised, and this is certainly not the expected behaviour of athermal transformation. Furthermore, there is evidence that structures closely resembling those of lath martensites are produced isothermally in certain iron alloys,[8.9] particularly it seems if the interstitial content is very low. The term Bainite has been used to describe these transformation products[8] and it is perhaps worthwhile to remember the close similarity in structure between upper bainite and lath martensite in carbon steels. Another factor which may point to the existence of either isothermal martensite or bainite is the discrepancy between the M_s temperature for pure iron obtained by the extrapolation of M_s temperature versus composition data. The normal straight line extrapolation for the M_s temperature in iron carbon alloys gives a value for the M_s temperature of pure iron of 560°C,[18.76] but from binary substitutional alloys data the extrapolated M_s temperature in pure iron equals 750°C,[16] and this raises the question as to whether transformation in these alloys was truly martensitic. The mere observation of surface tilts or microstructure is not a sufficient means of establishing that a martensitic reaction has occurred, and thus it is possible that the higher M_s temperature, i.e. 750°C [16.22.29] for pure iron corresponds to a bainitic type reaction. In support of this it is interesting to note that if the transformation temperatures in more dilute alloys are ignored the transformation temperature versus composition curve shown in Fig. 12 can be extrapolated back to around 560°C. Finally, careful measurements of the M_s temperature at very low carbon contents have attempted to justify the higher M_s temperature for pure iron,[28] by showing that the M_s temperature versus carbon content does not extrapolate in a straight line but via a curve to 750°C. This also could be due to a bainitic transformation occurring in the lower carbon alloys and it is interesting to note that a marked increase in cell size occurs [20] in the region of the curve corresponding to this slope change. The above suggests that it is possible for the isothermal transformation to lath martensite to occur, and that it may arise more easily if the interstitial contents are low.

Final evidence for isothermal transformation behaviour is provided by Yeo[67.77] who claims to have observed the slow growth of surface tilts on a prepolished surface in iron nickel alloys, and has also measured a C curve for the time temperature dependence of transformation. There are some however who dispute this evidence on the basis that (i) the holding temperature may not have been stable and (ii) that the surface tilts correspond to surface martensite and not to lath martensite. The first of these two criticisms maybe valid since it only requires a 30° drop in temperature to produce 80% of transformation in lath martensites.[14]

2.2.2.5 Thermodynamics of lath martensites.

Several authors have determined the driving force for martensitic transformation as a function of alloy composition, using either ideal or regular solution models.[12.13.16.21.33.34] Their results vary mainly in respect to what value of M_s temperature is taken for pure iron. Using the value of 560°C for pure iron the driving force for lath martensite is approximately 270 cals/mole (1120J/mol) and this is only slightly increased by alloying additions, e.g. nickel increases it to 315 cals/mole (1350J/mol) at approximately 28% nickel. The overall magnitude of the driving force seems to be little affected by what alloying element is involved, see Fig. 13, but the rate of change with composition varies in accordance with the effect of alloying elements upon the T_0 temperature.

If the M_s temperature for pure iron is assumed to be 750°C instead of 560°C the driving force for transformation varies considerably with composition, from approximately 104 cals/mole (450J/mol) for pure iron to something in the region of 300 cals/mole (1250J/mol) as the alloying concentration is increased. In view however of what was said previously this value for driving force may not in fact correspond to a martensitic transformation.

2.2.2.5.6. Effect of alloying elements upon the lath martensite transformation.

The effect of alloying elements is to retard the massive ferrite transformation and encourage transformation to lath martensite, see Fig. 14. They also affect the M_s temperature in a manner which is largely determined by their influence upon the T_0 temperature. For example, elements which are austenite stabilizers, e.g. nickel or manganese, continuously lower the M_s temperature, whereas the ferrite stabilizers such as chromium may reduce the M_s temperature less effectively.[16] An additional effect of alloying elements is that they produce strengthening in the austenite phase, which increases the level of constraint opposing the shear transformation, and thereby lowers the M_s temperature.

2.2.2.6 Twinned Martensite in ferrous alloys.

Since the existence of twinned martensite structures can have profound effects upon the mechanical properties of iron alloys, the following section which deals with a review of twinned martensite formation is included in the literature survey. This is justified since it may be necessary to explain certain aspects of the behaviour of iron manganese alloys in terms of twinned martensite.

Twinned martensites arise in iron carbon and iron nitrogen alloys due to the formation of transformation twins as a means of relieving the habit plane misfit. This type of behaviour has already been predicted in the previous section dealing with the phenomenological theories, and results in a martensite which differs from lath martensites in a number of respects. These differences include difference in habit plane, internal structure and, in the case of iron carbon or iron nitrogen alloys, a change in crystal structure from body centred cubic to body centred tetragonal. The crystal structure change occurs at interstitial concentrations of about 2.85a/o[14] but is a gradual rather than sudden change, and results in the habit plane being altered from the $\{111\}_\gamma$ plane to the $\{225\}_\gamma$ plane.[4] Above approximately 1.4% carbon a further change in habit plane from the $\{225\}_\gamma$ to the $\{3,10,15\}_\gamma$ plane occurs, and this also accompanies a change in morphology. The martensite now adopts a lenticular appearance and is often referred to as acicular martensite.

In iron nickel alloys there is also a change from lath to acicular martensite above approximately 28% nickel, but in contrast to the iron carbon alloys the crystal structure remains body centred cubic instead of changing to body centred tetragonal.[78]

Several ideas have been put forward to explain the transition in martensitic structure and these include:

i. At a critical M_s temperature twinning which is favoured by low temperatures becomes an easier mode of deformation than slip. Hence as the M_s temperature is lowered by the addition of alloying elements, an eventual change in morphology from slipped to twinned martensite occurs. The critical M_s temperature has been suggested to be about 200°C[79] But it does not seem to apply universally to all alloy systems, e.g. slipped martensite is formed in 18/8 stainless steels at well below room temperature.

ii Mechanical twinning in face centred cubic austenite is easier with low stacking fault energies due to the presence of partial dislocations. Thus it has been suggested that alloying elements which lower the austenite stacking fault energy encourage the formation of twinned martensites.[80] This may be true in the case of iron nickel alloys, since nickel does lower the austenite stacking fault energy,[81] but it does not seem to apply to other iron alloys in which stacking fault energy is lowered, e.g. Fe 18 Cr 8 Ni and furthermore the effects of carbon on the austenite stacking fault energy are uncertain. An additional criticism is that strictly speaking the mechanical twins are observed within the martensitic phase, and there is no reason to suppose that the austenite stacking fault energy can be related to that of the martensite.

iii Transition from lath to twinned martensite occurs at a critical level of driving force $\Delta G^{\alpha-\gamma}$ = approximately 315 cals/mole (1350J/mol)[21] which means that relief of the habit plane misfit occurs by twinning instead of slip once the level of constraint opposing transformation reaches a critical level. In many ways this is an identical suggestion to (i) but it also takes into account the varying affects of alloying elements on the T_0 temperature.

iv During the Bain strain carbon atoms may be trapped in their face centred cubic interstitial positions, e.g. $[\frac{1}{2}.\frac{1}{2}.\frac{1}{2}]_\gamma$ and this partially prevents the full contraction of the $[010]_\gamma$ axis. The resulting structure is a body centred tetragonal martensite and is considered to be an "ordered" lattice, but if short range diffusion can occur the interstitial atoms may move from their $[00\frac{1}{2}]_\gamma$ sites into both the $[\frac{1}{2}00]_\gamma$ and $[0\frac{1}{2}0]_\gamma$ sites. When this occurs the lattice is expanded equally along all three cube directions and produces a body centred cubic cell which is referred to as a "disordered" structure. As with all order - disorder reactions the ordered lattice only becomes stable below a critical temperature T_c, which has been established for iron carbon alloys by Zener.[82] When T_c is plotted with the M_s temperature against carbon content a curve like that shown in Fig. 15 is produced which shows that transformation to martensite for carbon levels below approximately 2.85 a/o occurs at temperatures above the T_c temperature and this permits the disordered austenite to produce a body centred cubic martensite. At higher carbon concentrations the M_s temperature is lower than the T_c temperature which allows the ordering reaction and produces martensite which is body centred tetragonal. There is good agreement between the theoretical and observed interstitial content at which the crystal structure change takes place,[18] but the theory does not strictly account for the morphological change which also occurs. One possible suggestion is that since $E = RBC$, B must alter to account for the change from a body centred cubic to a body centred tetragonal crystal structure, and this requires that S must also change. The main difficulty with this theory however is that no change in crystal structure accompanies the morphological change in binary iron nickel alloys, and thus there is no reason for S to change.

2.2.2.7 Epsilon martensite.

Epsilon martensite which is a hexagonal close packed structure appears in iron alloys either as a result of a pressure induced shear transformation[83] or by cooling from the austenite region with alloys of low austenite stacking fault energy. The structure consists of parallel straight sided bands lying along the $\{111\}_\gamma$ planes and with an orientation relationship where both the close packed planes and directions of the two phases are parallel, i.e.

$$\{111\}_\gamma \parallel \{00.1\}_\varepsilon \qquad \langle 111\rangle_\gamma \parallel \langle 1\bar{2}10\rangle_\varepsilon$$ [69.71]

The formation of epsilon is of limited interest to the present investigation and it will suffice to deal briefly with its probable mode of formation. The most likely mechanism is that epsilon results from the growth of a stacking fault within the austenite by the formation of Shockley partial extended dislocations on every alternate plane, and this could be achieved by a pole mechanism consisting of a single Shockley partial dislocation rotated about a screw dislocation.[84]

Of more immediate interest than the mechanism of epsilon formation is the role that epsilon plays in the eventual formation of body centred cubic α martensite, since it is almost certain that epsilon is only a transition structure in the transformation sequence $\gamma \rightarrow \varepsilon \rightarrow \alpha$ [70.71]. In this role it has been shown that epsilon forms sheets lying parallel to the $\{111\}_\gamma$ planes and α is nucleated at the intersections of these sheets, i.e. along the $\langle 110 \rangle_\gamma$ direction. The α martensite so nucleated appears as laths lying along the $\langle 110 \rangle_\gamma$ directions [70.71] and obey the Kurdjumov Sachs orientation relationship with the austenite. Structurally these laths resemble normal lath martensite, but as stated previously their habit plane is different, and is either the $\{225\}_\gamma$ or $(\bar{1}\bar{1}2)_\gamma$ plane. The transformation of epsilon to alpha occurs on cooling, but frequently does not go to completion and ε is retained as a metastable structure which can be made to transform to alpha by either cold work,[85,87] sub zero treatment,[86] or by low temperature annealing.[86.88] If retained austenite is present these treatments may also lead to an increase in the percentage of epsilon [88] from the breakdown of retained austenite.

2.3 Transformations in iron manganese alloys.

The transformation of iron manganese alloys has been shown to occur by two basic modes, namely the $\gamma \rightarrow \alpha$ transformation and the $\gamma \rightarrow \varepsilon$ transformation. Troiano & McGuire[89] have determined both the equilibrium and non equilibrium transformation behaviour shown in Fig. 16 and found that under non equilibrium conditions alloys containing up to ten percent manganese transform from austenite direct to alpha, but above 13% manganese the transformation is via the formation of epsilon and there is an increasing tendency for austenite to be retained at room temperature. At intermediate compositions between 10% and 13% manganese mixed $\alpha+\varepsilon$ structures were formed, and the epsilon was transformed to alpha by low temperature annealing. Later work[85.88] has verified these findings and has established more precisely the composition ranges at which the different transformation products exist, see Fig. 17.

The present work was inspired partly by the prospect of using iron manganese alloys as a substitute for the cryogenic nickel steels and the maraging steels, and so the main interest centres on the $\gamma \rightarrow \alpha$ transformation. The results of previous work in measuring the $\gamma \rightarrow \alpha$ transformation are shown in Fig. 18.[22.88.90] Most of these measurements of the $\gamma \rightarrow \alpha$ transformation temperature were done at slow cooling rates, and can be seen to extrapolate to a transformation temperature of 906°C in pure iron. This means that transformation in the more dilute alloys is not martensitic but occurs by either a massive ferrite or an equiaxed ferrite reaction. In the range of 5-10% manganese there is less scatter between the $\gamma \rightarrow \alpha$ transformation temperatures measured by the various workers, and it is interesting to note that they can be extrapolated back to a temperature near to 560°C for pure iron. On this evidence there is the possibility that transformation for the 5-10% manganese range is martensitic even at slow cooling rates, and there is also some metallographic evidence for this.[88] Gommersall & Parr[22] however were unable to establish the existence of surface tilts on a prepolished surface and found that the underlying structure appeared to cross thermally etched prior austenite grain boundaries which suggests a non martensitic transformation. Their results are probably misleading however due to the phenomenon of surface volatilization of manganese[91] during vacuum heating and it is almost certain that their alloys, which contained more than 5% manganese, transformed martensitically. A question remaining however concerns the type of martensite produced, i.e. whether it is true, lath martensite, epsilon nucleated martensite or twinned martensite and there is no definite evidence to answer this. Typical photomicrographs [88] tend to indicate that it is probably of the true lath type.

3.0 REVIEW OF LITERATURE Part II

Properties.

In the preceeding sections the transformation characteristics of iron and its alloys have been described, and the most probable transformation modes established for iron manganese alloys. The remaining part of the review of literature relates to the mechanical properties of iron manganese alloys, and especially to the problem of brittle fracture. This is necessary to determine whether the substitution of manganese for nickel in cryogenic and maraging steels is a feasible proposition.

3.1 Properties of maraging steels.

The 18% nickel base maraging steels are capable of achieving mechanical properties which include a high tensile strength combined with good ductility, and extremely good low temperature impact resistance.[92] They owe these properties to some extent to precipitation hardening, but it seems likely that their high toughness also stems from the lath martensitic structure. If this is the case it would seem reasonable to expect that other, perhaps cheaper, iron base alloys might be used to create an equivalent steel to the nickel base steels.

3.2 Mechanical properties of iron manganese alloys.

Manganese is approximately twice as effective as nickel in producing solid solution strengthening in iron[93.94] and thus similar strength levels could be achieved to the maraging steels in the solution treated condition, by the use of much smaller quantities of manganese than nickel.

Some indication of the level of mechanical properties it is possible to achieve in iron manganese alloys is shown in Fig. 19 and these are the results of Walter et al.[95] These show that strengthening occurs by the addition of manganese up to approximately 12%, but beyond this the strength declines. Almost certainly these results reflect the changing microstructures caused by the addition of manganese, and it is certain that the appearance of epsilon martensite in manganese concentrations greater than 12% is responsible for the decline in strength. The structure of alloys in the alpha range is uncertain, but it is possible that they are martensitic except in the very dilute alloys. Others who have studied the mechanical properties of iron manganese alloys confirm that it is possible to achieve the same levels of strength as with iron nickel alloys,[97] but there is one distinctive difference, namely that the iron manganese alloys are often brittle. This brittleness was first reported by Hadfield,[96] but since his alloys were rather impure, the brittleness may not have reflected the true behaviour of iron manganese alloys.

The more recent evidence tends to corroborate the suspicion that iron manganese alloys are more brittle than their iron nickel counterparts, but has been unable to establish any reasons for this. For example, Rees et al[93] found that the transition temperature for iron was raised by the addition of manganese, and that particularly poor impact properties were obtained in an iron 5% manganese alloy which possessed a martensitic structure. It is nevertheless important to note that similar behaviour was noted for iron nickel alloys,[97] and that the fractures which caused poor impact behaviour were intergranular. This suggests that some grain boundary impurity is responsible for the poor properties. Also when the iron manganese alloy was tempered to produce recovery of the martensitic structure a considerable improvement in impact properties took place which indicates that brittleness was not a function of the solution of manganese in iron. Brittleness was also experienced by Nicochenko[98] when attempting to cold roll an iron 8% manganese alloy, and this was attributed to the transformation of retained epsilon to alpha during cold work. Earlier evidence has shown however epsilon martensite should not be present in alloys containing less than 10% manganese. Boniszewski[57.99] has shown that iron 7% manganese alloys are considerably more brittle than the equivalent 9% nickel cryogenic steels and are much more susceptible to hydrogen embrittlement.[99] The reason for this was stated to be the formation of twinned martensite in the iron manganese steel in contrast to the lath martensite formed by the nickel steels, but there is no real evidence for this. The possible existence of twinned martensites in iron manganese alloys was also used by Wilson[91] to explain the brittleness that he found when evaluating the complete substitution of manganese for nickel in maraging steels, but again no real evidence was produced.

Finally evidence exists that when nickel is supplemented by manganese in maraging steels, a loss of impact resistance occurs,[100.102] but it is significant that the fractures were intergranular, and Patterson[101] has shown that providing the Mn:Si or Mn:Ti ratios are high then manganese becomes less deleterious to impact properties.

The evidence above seems therefore to suggest that iron manganese alloys are brittle but this may be due to several possible explanations:

(i). It is due to an inherent effect on the flow and fracture properties of iron, caused by manganese in solid solution.

(ii) It is possible that the transformation behaviour of iron manganese alloys is different from that of iron nickel alloys, namely that twinned martensites occur. Also of course the epsilon martensite transformation exists in iron manganese alloys but not in iron nickel alloys.

(iii) Manganese may enhance the effects of impurities in causing intergranular weakness.

The problem of brittleness seems to be vital if manganese is to be successfully substituted for nickel in a maraging steel, and it is therefore necessary to assess the criteria for brittle fracture in the hope that some explanation and cure can be affected.

3.3 Criteria for brittle fracture.

It is well known that brittle fracture results when micro cracks formed by dislocation interaction reach a size which in relation to the Griffiths Orowan[103] equation exceed the critical size for fracture to occur. The critical stage in the process is crack propagation and not nucleation since hydrostatic stresses do not affect the brittle fracture behaviour, i.e. crack nucleation depends upon dislocation glide which is controlled by the level of shear stress, whereas crack propagation depends upon the level of normal stress. Only the normal component of stress is unaffected by hydrostatic stresses.

A criterion often used to describe the factors influencing brittle behaviour is that due to Cottrell[104]

$$\left\{\sigma_i d^{\frac{1}{2}} + k_y\right\} k_y = \beta \mu \gamma \qquad (9)$$

which gives the condition that brittle fracture occurs when the left hand side of equation (9) exceeds that on the right. The terms in the above equation have the following significance:

σ_i = The lattice friction stress which resists dislocation movement and is the same as in the Petch[105] equation, i.e. σ_i = extrapolated value of yield stress at $d^{-\frac{1}{2}}=0$

K_y = The slope of the yield stress versus grain size curve of the Petch relationship

$d^{\frac{1}{2}}$ = A grain size parameter where the grain size equals D and $d = \frac{D}{2}$

β = A constant which varies from 1.0 to 0.3 and represents the level of stress concentration related to the geometry of the test piece.

μ = Shear modulus

γ = The surface energy term, which in the case of metals is the combined interfacial energy plus the plastic work done by the propagation of a crack.

It should be possible to assess the differences in brittle fracture behaviour between different metals, e.g. iron manganese and iron nickel alloys by measuring possible differences in the parameters of equation (9) and this is the intention of the following sections.

3.3.1 Significance of the σ_i parameter.

σ_i may be expressed as the sum of two components

$$\sigma_i = \sigma_o + \sigma_*$$

where σ_i = tensile flow stress

σ_o = the athermal component of flow stress

σ_* = the thermal component of flow stress

and it is necessary to know the physical meaning of both these terms in order to assess the affect of σ_i upon the brittle fracture process. First of all however there is a critical temperature T_o at which the thermal component σ_* becomes zero, and this has been found to be at about 350°K[106] for most ferrous alloys. On this basis it can be assumed that any changes occurring in the room temperature flow stress of iron alloys are essentially due to changes in σ_o. This assumption will be used to allow an assessment of σ_o to be made.

3.3.1.1 Significance of σ_o, the athermal component of flow stress

σ_o represents the contribution to overall flow stress made by the factors which cause long range stress fields and produce resistance to dislocation movement. These are essentially due to:

(i) Solute atom misfit strains.

(ii) Stress fields surrounding neighbouring dislocations

(iii) Coherency or volume strain fields associated with precipitate and inclusions.

The first of these two factors are likely to be of importance in determining the σ_0 parameter for iron manganese alloys, namely the role of manganese as a solid solution hardening element and secondly the influence of the dislocation substructure inherited from the martensitic transformation.

In dealing with iron nickel alloys Speich and Swann[23] attempted to separate the effects of solid solution strengthening from other effects, and concluded that the solid solution strengthening, and not the dislocation substructure produced by lath martensite, was of major importance in determining the overall room temperature strength. It is doubtful that their structures were properly controlled, and it is almost certain that the more dilute alloys did not achieve the lath martensitic structure intended. Later work[107] has shown that in iron nickel lath martensites the contribution due to solid solution strengthening is less important, e.g. 34% of the total strength, and the greater source of strengthening is due to the dislocation substructure. Significantly it has also been shown that the strength of iron nickel martensites does not vary when the nickel content exceeds approximately 8%, and also does not change after the transition from lath to twinned martensite occurs beyond 28% nickel. Reasonable agreement exists between the observed solid solution strengthening and the strengthening predicted by the Mott& Nabarro [108] theory, which attributes strengthening to misfit and relates it to a lattice parameter change, i.e.

$$\tau_0 \propto \frac{\sigma_0}{2} = \mu \varepsilon_a^{4/3} \times \left[\frac{X^{2/3}}{2\pi} \left(\ln \frac{1}{X} \right)^4 \right]^{1/3}$$

where τ_0 = room temperature flow stress

μ = shear modulus

ε_a = misfit parameter = $\frac{1}{a} \frac{da}{dX}$ where a = lattice parameter

X = atomic fraction of solute.

It is difficult to establish whether iron manganese lath martensitic structures will behave in a similar way to iron nickel alloys but at least it seems certain that manganese will be a more effective solid solution strengthener than nickel.[93.97]

The other major contributor to the strength of martensitic iron alloys in terms of solid solution strengthening is that due to interstitial solute atoms. Within the present investigation however, the interstitial concentration should be sufficiently low so as not to cause any major change in strength. The most widely accepted prediction is that solid solution strengthening in ferrous martensites should vary with the square root of the interstitial content, i.e. $\sigma_0 = f \sqrt{X_c}$ where X_c is the atomic fraction of interstitial.[109.110] The slope of the relationship varies slightly between lath and twinned martensites, and is slightly less for lath martensites, i.e. Slope = $\mu/17$ for lath and $\mu/13$ for twinned martensite.[110] If then, as suggested earlier, iron manganese alloys produced a twinned martensite structure, the small amount of interstitial elements which are inevitably present, could create a difference in behaviour between iron nickel and iron manganese alloys.

After the martensitic transformation in iron nickel alloys the inherited dislocation substructure has been estimated to contribute approximately 40% of the overall strength, and there is no difference whether the substructure consists of dislocations as in lath martensites or as transformation twins. The precise level of contribution however must vary with differences in heat treatment, and alloying elements, since it has been shown previously that the substructure size can vary with these factors. Again it may be possible to detect differences in behaviour between iron manganese and iron nickel alloys in this respect.

The remaining factor liable to influence the magnitude of σ_o is the contribution due to precipitates. In the present work there is no deliberate intention to create precipitation hardening, and the only possible factors likely to have influence in the iron manganese alloys are (1) the presence of inclusions and (2) the effects of carbide clustering due to autotempering.[111]

In conclusion the σ_o parameter for a low carbon iron manganese alloy in the martensitic condition will be a function of

$$\sigma_o = \Delta\sigma_\alpha + \Delta\sigma_s + \Delta\sigma_d$$

where σ_o = athermal component of flow stress

$\Delta\sigma_\alpha$ = athermal contribution due to the flow stress of pure annealed iron

$\Delta\sigma_s$ = contribution due to solid solution hardening

$\Delta\sigma_d$ = contribution due to dislocation substructure.

In iron nickel alloys these have been shown to contribute the following to overall strength

$$\Delta\sigma_\alpha \; 25\% , \; \Delta\sigma_s \quad 34\% , \; \Delta\sigma_d \quad 41\%$$

3.3.1.2 Significance of σ_* the thermal component of flow stress.

σ_* arises from the ability of dislocations to escape from barriers, by a thermally activated process, and under such conditions the flow stress becomes both temperature and strain rate sensitive.[106] This dependence upon strain rate and temperature is given by:

$$\dot{\gamma} = \rho_m b v = \rho_m b A \nu_o l e^{-H/KT} = \nu e^{-H/KT} \qquad (10)$$

where $\dot{\gamma}$ = shear strain rate

ρ_m = density of mobile dislocations

V = dislocation velocity

b = burger's vector

A = area of glide plane swept by a thermally activated dislocation movement.

ν_o = Debye frequency factor

K = Boltzmans constant

T = Temperature ^oK

H = Activation energy for dislocation movement

l = length of dislocation involved in thermal activation

ν = Frequency factor which equals $\rho_m b A \nu_o l$

The activation energy for the thermally activated dislocation movement, H, follows from equation (10) such that

$$- H = KT \left[\ln\dot{\gamma} - \ln\nu\right]$$

and this can be determined experimentally via the relationship

$$- H = KT^2 \left(\frac{\partial \ln\dot{\gamma}}{\partial \tau_*}\right)_T \left(\frac{\partial \tau_*}{\partial T}\right)_{\dot{\gamma}} \qquad (11)$$

where τ_* is the thermal component of flow stress expressed in terms of shear stress. For the purpose of determining H, τ_* is measured as a function of strain rate $\dot{\gamma}$ and temperature T.

In addition to the activation energy H, a further quantity can be determined experimentally which is a measure of the work done as the dislocation escapes from its barrier. This quantity is known as the activation volume V_* and is effectively the product of three length terms, i.e.

$$V_* = KT \left(\frac{\partial \ln \dot{\gamma}}{\partial \tau_*} \right)_T = - \frac{H}{\partial \tau_*} \qquad (12)$$

This parameter V_* together with the activation energy H and the frequency factor ν are extremely important, since they are all dependent upon the type of dislocation barrier operative, and their measurement assists the choice of the dislocation barrier which will account for the thermal component of flow stress. Various suggestions have been made for the type of dislocation reaction involved and these include:

(i) Lomer-Cottrell locking:[112] thermal activation is required to enable dislocations to escape from Lomer-Cottrell barriers by a process of cross slip.

(ii) Forest theory:[113] thermally activated dislocation movement is controlled by the ease with which dislocations on the glide plane can cut through the Forest dislocations threading through the glide plane.

(iii) Jog theory:[114] extended jogs can move non-conservatively if the diffusion controlled flow of vacancies or interstitials is sufficiently rapid.

(iv) Cluster theory:[115] dislocation movement is arrested by the strain fields associated with clusters of interstitial atoms, and thermal energy is required to assist the dislocation in overcoming such strain fields.

(v) Peierls-Nabarro friction stress:[116-118] dislocation movement is restricted by the Peierls-Nabarro friction stress, but dislocations overcome this restriction by a thermally activated double kink formation process.[117,118]

(vi) Cross slip: dislocation movement is controlled by the rate at which thermally activated cross slip can occur.[119]

The above is a brief description of the major proposals, and strictly speaking all do not apply to body centred cubic metals. The theory which accounts most satisfactorily for the behaviour of body centred cubic metals is the Peierls-Nabarro mechanism.[117,118]

3.3.1.2.1 Peierls-Nabarro Mechanism.

A brief description of the double kink mechanism, by which dislocations are able to overcome the Peierls barrier is as follows. In Fig. 20 it is shown that the dislocation initially adopts a position of minimum strain energy by lying parallel to the minimum stress valleys of the Peierls-Nabarro force field, and in order to surmount the stress maximum of the Peierls barrier a double kink is formed. This kink consists of a pair of screw dislocations of opposite sign which are connected together by a segment of edge dislocation on the opposite side of the Peierls hill.

With such an arrangement it is possible for the dislocation to surmount the Peierls barrier by the lateral movement of the two kinks in opposite directions to each other.

The critical stage of the above process is the nucleation of the double kink with a sufficient spacing to be stable, and this critical kink configuration is the stage requiring thermally activated dislocation movement.

Two fundamentally different approaches to the determination of the energy required for the nucleation of a double kink, exist one of which due to Seeger[116] considers only the part played by thermal energy in nucleating the kink pair. The other approach due to Dorn and Rajnak[117] or Arsenault[118] also includes the contribution due to the effective stress τ_* and it is this approach which is more applicable to the analysis of flow stress in body centred cubic metals.

Briefly, the activation energy is the energy required to nucleate a double kink with a critical spacing, and this is controlled by the following energy considerations. Activation Energy H is proportional to A + B + C - D where

A = the increase in dislocation line energy produced by the creation of two kinks.

B = the energy to move a small segment of edge dislocation over the Peierls barrier.

C = the energy to overcome the mutual attraction between the two kinks and which tends to cause collapse of the double kink.

D = the work done by the effective stress τ_* which aids double kink formation.

According to the above it will be seen that H the activation energy should vary with the effective stress and must therefore be a function of the temperature or strain rate. Furthermore H should vary significantly with the Peierls-Nabarro stress due to the C term of the above equation. The above model also permits further predictions to be made, namely that from sensibly predicted dimensions of a double kink it follows that

the frequency factor $\nu = \rho_m a b \nu_0 \frac{L}{W}$ (13)

where ρ_m = mobile dislocation density

a = distance between adjacent Peierls valleys

b = burgers vector

ν_0 = Debye frequency factor

L = length of dislocation involved in thermal activation

W = critical spacing of double kink

and the activation volume V_* is approximately Wb.

When the theoretical and observed functions are compared it is found that H does vary with τ_* in a manner more or less predicted by the theory, but the activation volume V_* is only found to be in agreement with theory at temperatures below approximately 160°K. For higher temperatures which essentially means low values of τ_*, the measured values of V_* are very much too high. Furthermore, since the critical kink spacing W should not vary with dislocation density then V_* should not vary with strain, but there are several examples where V_* has been shown to vary with strain.[120.121] A final criticism is that it has also been shown that in many iron alloys the micro-yield stress does not vary with temperature,[122.124] which suggests the unlikely behaviour that dislocation movement in the micro-yield region does not require any energy to surmount the Peierls-Nabarro barrier.

Despite the criticisms levelled at the double kink theory however, it still remains the only theory to give reasonable agreement between the calculated and observed behaviour of flow stress in body centred cubic metals. Furthermore it may account for the effects that alloying elements have upon the temperature dependent flow stress . These effects are chiefly that alloying additions alter the level of temperature dependent flow stress, and it is found in many cases that τ_* is lowered by alloying elements. Such solid solution softening has been noted in iron alloys containing chromium,[93.97] molybdenum, and vanadium,[122] and is possibly due to the reduction of τ_* by alloying. In these cases, however, it has also been suggested that the effect is due to the scavenging influence of these elements, which reduces the degree of interstitial solid solution hardening. Similar observations with nickel[125] and cobalt[122] however cannot be attributed to this since they do not form carbides. It is possible therefore that the alloying elements create changes in the level of τ_* due to their influence upon the Peierls-Nabarro friction stress, and this may be determined from the following relationship.

$$\tau_{p_s} \doteq \frac{\alpha\mu b}{2C} \exp - \frac{2\pi\gamma}{C} \qquad 126$$

where τ_{ps} = Peierls stress which equals τ_* at 0^oK

α = a constant equal to 0.5 to 1.0

μ = shear modulus

b = burgers vector

γ = dislocation width along the slip plan

$c \simeq b$ the burgers vector.

There are two main parameters within the above equation which may be altered by alloying elements, namely μ and γ and it has been shown for example that nickel lowers the shear modulus μ of iron,[107] and so may lower the Peierls-Nabarro stress. The alternative is that alloying elements alter γ by their effect upon the stacking fault energy, and it is possible that alloying elements which raise the stacking fault energy could reduce the dislocation width and lower the Peierls-Nabarro stress.

An additional way in which alloying elements might influence the Peierls stress is due to their influence upon the degree of directional bonding within a body centred cubic structure, and it is reasonable to assume that elements with an excess of 3 d electrons will help complete the filling of the 3 d shell of iron, thus reducing the level of directional bonding. Nickel and manganese will on this basis have opposing effects in iron and it is possible that nickel lowers the Peierls stress whereas manganese increases it.

3.3.1.2.2 The thermal component of flow stress τ_* for martensitic steels.

The Dorn-Rajnak theory predicts that the thermally dependent component of flow stress is independent of dislocation density, and as a result of this, martensitic transformation should have no effect upon τ_*. There is reasonable proof of this since it is found that the thermal component of flow stress in pure iron does not vary after severe deformations, and the substructures produced are very similar to those of lath martensites.[127] Additional evidence is that pure iron exhibits the same behaviour both after annealing and after inducing a dislocation substructure of a lath martensitic nature by shock loading.[128] These same authors also showed that in a nickel base maraging steel the level of temperature dependent flow stress was unaffected by precipitation hardening, and was also significantly smaller than for pure iron. This latter observation possibly indicates the lowering of the Peierls-Nabarro stress by alloying elements.

Other workers have measured the temperature and strain rate sensitivity of flow stress both in iron nickel[109.129] and iron nickel chromium alloys [130] with structures that were lath martensitic. Their results tend to agree with the findings for other iron alloys, and give the same measure of agreement between the observed behaviour and that predicted by the Dorn-Rajnak theory. One significant feature however is that no difference in flow stress behaviour was claimed to have been found between alloys of different nickel plus chromium contents and this was inspite of a considerable difference in their brittle fracture properties, i.e. the higher chromium alloys gave much poorer impact properties.[130] It may nevertheless be significant that the activation energies H for the iron nickel chromium alloys with poor impact properties were considerably higher than found for iron nickel alloys which produced good impact properties.

3.3.1.3 Summary of the σ_o and σ_* parameters.

It has been shown that two factors σ_o and σ_* contribute to the σ_i parameter of equation (9) and brittle fracture behaviour can hinge on a complex relationship between these two. In iron manganese alloys the expected behaviour is that σ_o will be increased by solid solution strengthening and by the martensitic transformation, but it is by no means certain what changes in σ_* will occur,

3.3.2 Significance of the K_y parameter.

Iron alloys with lath martensitic structures do not exhibit true yield points,[129.130] and it is necessary to measure a proof stress to represent the yield stress. Strictly therefore it is improper to refer to the slope of yield stress versus the $d^{-\frac{1}{2}}$ grain size relationship by the term K_y and instead the parameter K_f which refers to flow stress should be used. To avoid confusion however the parameter K_y will be used in all future discussion.

The K_y parameter is considered by many authorities on brittle fracture behaviour in steels to be an important parameter. In carbon steels for example there is a direct link between an increase in transition temperature and an increase in K_y as the carbon concentration is increased,[131] and it is important therefore to know the precise physical meaning of the K_y parameter. Unfortunately none is universally accepted at the present time, although several ideas exist. Almost certainly K_y is not a measure of the unpinning stress as originally proposed by Cottrell[134] in his model for yield propogation, since if this were so K_y should vary both with temperature and strain rate due to thermally assisted unpinning of dislocations from solute atmospheres. This does not occur[132] except in special circumstances, i.e. the early stages of strain ageing.[133]

More recently K_y has been interpreted as simply a measure of the ease with which yielding can be propogated from one grain to another, and this has been expressed in a number of ways including:

1. The Gilman & Hahn theory[135] for yielding which interpretes K_y as a measure of the ease of dislocation multiplication.
2. That K_y depends upon the work hardening rate, since in order to propagate yielding the applied stress must overcome the strain hardened layer which is formed in the region of grain boundaries by accommodation stresses.[136]
3. Yield propagation is dependent upon the relative orientations between adjacent grains and hence K_y is an orientation factor.[137]
4. Yield propagation is dependent upon the number of available slip systems, which is dependent upon the ease of cross slip.[122]

The most obvious conclusion to be drawn from the above interpretations is that K_y is simply a measure of the ease of yield propagation which depends on no single factor, but upon all of the above.

3.3.2.1 K_y for martensitic iron alloys.

Martensitic steels obey the Petch relationship when the yield stress is plotted versus either prior austenite or martensite plate size.[129.130] In low carbon lath martensitic steels values for K_y have been determined for both iron nickel and iron nickel chromium alloys, and are close to values determined for pure iron.[132] They are in fact very low, which indicates that the yield stress varies with grain size by only a slight amount. In the case of iron nickel alloys, K_y was also shown to vary with testing temperature, the value at -196°C being much higher than at room temperature, and was probably due to mechanical twinning at low temperatures.[129] No values of K_y are available for iron manganese alloys but manganese has been shown to decrease K_y in carbon steels.[131]

3.3.3 Significance of $d^{\frac{1}{2}}$

Equation (9) implies that metals become more susceptible to brittle fracture as the grain size increases, and this is generally found to be true. The impact transition temperature can in fact be related to grain size, and one relationship suggested is that due to Stroh,[138]

i.e. $$\frac{1}{T_c} = \frac{-7}{2}\frac{K}{Q}\ln d + C \qquad (14)$$

where T_c = impact transition temperature

K = Boltzmanns constant

Q = Activation energy for the transition

d = grain size

C = a constant.

3.3.4 Significant of γ the surface energy term.

As stated earlier the surface energy term is determined by the amount of plastic work necessary to propagate the crack. If plastic flow can occur easily crack propagation is blunted and this is reflected in high surface energy values. Any factor which reduces the ability of plastic deformation to occur encourages crack propagation, and several such factors exist which are essentially the same as those listed previously to define the K_y parameter, e.g. difficult cross slip or low mobile dislocation densities inhibit the ease of plastic flow around the crack tip and lead to catastrophic propagation. The formation of intergranular weakness by precipitates or solute atom segregation promotes an easy path for crack propagation and premature intergranular fracture, e.g. temper brittleness is usually attributed to a lowering of the surface energy term.

3.3.5 Significance of β and μ

No special significance should be attached to either of these two terms, since their effects upon brittleness should be similar for all ferrous alloys. Nevertheless they are important, and it is well known that any factor which creates stress concentration causes easier brittle failure. The changes in shear modulus μ produced by alloying elements are usually small, and thus the shear modulus is unlikely to produce significant changes in brittle fracture properties.

3.4 Summary.

During the review of literature it has been reasonably well established that martensitic iron manganese alloys are brittle. The major property parameters likely to be responsible for this behaviour have also been assessed, but information regarding their specific values in iron manganese alloys is lacking.

4.0 EXPERIMENTAL PROCEDURE.

4.1 Alloy Preparation.

A series of iron manganese alloys were prepared from ferrovac iron and electrolytic manganese to give nominal manganese composition of 2, 4, 6, 8, and 10%. The alloys were air melted in a high frequency furnace and cast into twenty five pound ingots, which were homogenized at 1200°C for seven days whilst packed in sand to prevent excessive oxidation. This treatment was followed by swaging to half inch diameter bar and these were subsequently annealed at 1000°C for one hour. At this stage a preliminary microexamination revealed that the alloys were homogeneous since they exhibited a uniform structure with no visible segregation.

In addition to the above series of alloys which were air melted to simulate industrial conditions, two additional alloys were vacuum melted using very high purity base materials. Both of these were aimed at a nominal composition of 9% manganese, and an approximately half percent addition of molybdenum was made to one in an attempt to overcome intergranular brittleness.

The analysis figures obtained from each of the above alloys are shown in Table 1. The manganese contents are reasonably close to the nominal compositions, and with the exception of the silicon contents, all of the other impurities are at a low and reasonably constant level.

4.2 Transformation Studies.

The transformation behaviour for the series of iron manganese alloys was studied using a dilatometric technique backed by optical and electron metallography, but occasional use was made of thermal arrest measurements for high rates of cooling. The identification of microstructure was also assisted by the use of x-ray diffraction.

4.2.1 Specimen preparation.

Dilatometer specimens were prepared by machining the original bar material after first swaging down further to 5 mms diameter. This additional swaging treatment served both to conserve material and to improve homogeneouity.

The specimen size was chosen as the most convenient to fit inside the dilatometer tube, whilst its length was sufficient to detect transformation and minimize the possibility of temperature gradients. This size was 10 mms long by 3.8 mms diameter and a 1.3 mm diameter hole was drilled along the specimen centre line to accommodate a thermocouple. Finally, the machined specimens were annealed at 1000°C for one hour in argon, and water quenched, prior to use for the measurement of transformation temperature.

4.2.2 Dilatometric Analysis

A schematic illustration of the type of dilatometer used is shown in Fig. 21. The dilatometer consists of a 4 mm inside diameter silica tube into which the specimen is fed through a window ground into the bottom. The specimen length change is transmitted via a silica push rod to a Philips type PR9310/01 transducer mounted at the top of the silica tube, and its output is then fed into a Philips type PR9300 phase bridge to record a millivolt output on the X axis of a Philips type PR2220/00 X-Y recorder

A spring loaded mounting for the transducer is moved up and down through a controlled distance by a micrometer head and this allows calibration of the specimen length change. The specimen temperature is simultaneously recorded on the Y axis of the X-Y recorder from a chromel alumel 0.1 mm diameter thermocouple which is fed from the underside into a small hole drilled along the centre line of the cylindrical specimen. Surrounding the dilatometer tube is an outer sealed silica tube which allows an argon atmosphere to be maintained around the specimen, and the argon is fed in from the top of the dilatometer tube to pass down over the specimen. Finally, the whole assembly is mounted vertically in a frame carrying a counterbalanced furnace which is able to move up and down when either heating or cooling is required. A range of cooling rates is possible both by adjusting the position of the furnace and by altering the rate of argon flow through the dilatometer.

To measure temperature requires that the millivolt scale chart of the X-Y recorder is calibrated, and this is done using a potentiometer and standard thermocouple. Cold junction temperature is automatically compensated for, and it is possible to distinguish a temperature difference of equivalent to 1.0 MV which is approximately ± 2°C.

4.2.3 Isothermal Recording Dilatometer.

This dilatometer used an identical measuring system to that described previously, namely a Philips transducer head, but did not incorporate the outer silica tube, and used instead a millivolt-time pen recorder to measure dilatation. The specimen temperature was also recorded simultaneously on a separate millivolt-time recorder from a chromel/alumel thermocouple made from 0.1 mm diameter wire and threaded down the push rod into the hole at the top of the specimen. The complete assembly was mounted on a vertical frame and could be slid into either a high temperature tube furnace or a controlled temperature bath situated adjacent to one another. The controlled temperature bath used a molten lead tin alloy mixture whose temperature was controlled to within ± 2°C via a proportional controller and was also monitored during an experiment with a potentiometer. Two window openings were ground on either side of the bottom of the silica tube in order to facilitate cooling of the specimen to the required temperature, since it was found that the time taken for the specimen to reach an equilibrium temperature in the controlled temperature bath was excessively long, if the specimen was completely enclosed by the outer silica sheath. The specimen size and shape was the same as that previously described.

4.2.4 Thermal Analysis

A few experiments were done to measure the transformation temperature by thermal arrests. Firstly, the hot junction of a chromel/alumel thermocouple made from 0.1 mm diameter wire was spot welded into a specially prepared hole in the specimen, by discharging a bank of condensers through thermocouple and specimen. The specimen was heated to a required austenitizing temperature in air and quenched into a brine solution. A plot of the time temperature curve during cooling was measured on a one second response millivolt/time pen recorder which had been calibrated to record temperature, and by this means it was found possible to detect thermal arrests for transformation at cooling rates in the order of 4000°C/minute.

4.2.5 Metallographic Examination.

4.2.5.1 Optical Metallography

Every specimen used in the measurement of transformation temperature was afterwards examined metallographically, and it was found that mechanical polishing proved to be the simplest technique. The best etching technique was found to be a double etch, using 2% nital to lightly etch the polished structure, followed by immersion in an aqueous solution of sodium thiosulphate plus sodium bisulphite to develop a blue-brown staining of the surface. This latter solution was developed by Schummann[88] and worked well independent of the solution concentration. In practice solutions of approximately 30% concentration were used.

4.2.5.2 Hot Stage Microscopy.

Hot stage microscopy was conducted with a Reichert hot stage assembly to study transformations during the heating and cooling of iron manganese alloys. The method was not particularly successful however due to problems which arose concerning the type of inert atmosphere. It was found that under high vacuum conditions excessive manganese volatilization occurred which made it impossible to distinguish surface topography. Other atmospheres which were tried included high purity argon and a reducing atmosphere containing 98% argon and 2% hydrogen. These were also further purified with a purification train containing alkaline pyrogallol and a molecular sieve, but proved to be ineffective in maintaining the type of surface on which transformation could be observed. The main cause for this was the masking of the true structure by thermal etching of any pre-existing structure.

Thin foils were prepared after first cold rolling the original bar material into strip 0.2 mm thick. This cold rolling treatment required no interstage annealing, and was unhindered by cracking, which seems to indicate a high ductility for the iron manganese alloys. Various heat treatments were then carried out using the cold rolled strip in order to simulate the behaviour of specimens used to measure transformation temperature, and these were subsequently prepared for thin foil electron metallography.

Initial thinning was by chemical means and various solutions were tried with varying success. Least successful was a mixed acid solution of HNO_3, H_2SO_4, HF,[139] which tended to produce severe pitting, while a solution of 20 Vol H_2O_2 (100 Vol), 20 Vol H_2O, 10 Vol HCl [140] proved to be only moderately successful, since it did not produce a clean polished surface. By far the best solution was one containing 50 Vol H_2O_2 (100 Vol), 42 Vol H_2O, 8 Vol HF[141] and this gave rapid thinning together with a clean polished surface and also enabled thinning to perforation to be carried out.

Final thinning was carried out by electropolishing using what is essentially a "window" technique,[142] with the polishing potential being controlled though a potentiostat. Various polishing solutions were tried including 5% Perchloric acid in acetic acid at room temperature, 1% Perchloric acid in methanol at -70°C, and chromic acid - acetic acid at 0°C. The first of these tended to give rapid polishing which was difficult to control and the two latter solutions proved to give the best results, although problems with oxide contamination of the foil could arise if the chromic acid solution was not freshly made.

After thinning, the foils were cut and examined using J.E.M. 6A microscope at 100 KV.

4.2.6 X-ray Diffraction Techniques.

X-ray examination was carried out upon the bulk dilatometer specimens after mounting, polishing and etching, using a Philips diffractometer and a Cobalt radiation source. Cobalt radiation was chosen in order to separate the lines at small differences in Bragg angle, and so distinguish between ferrites of slightly different composition.

4.3 Determination of mechanical properties.

4.3.1 Impact properties.

Measurements of the impact strength and transition temperature were made using a Hounsfield Balanced Impact testing machine with notched specimens 44.5 mm long by 7.92 mm diameter machined from the original $\frac{1}{2}$" diameter bar material. Notching was carried out using the standard Hounsfield notching device, and was done prior to heat treatment to avoid machining stresses at the root of the notch. Various testing temperatures were obtained by the immersion of test pieces in controlled temperature baths consisting of either cardice and acetone mixtures or a thermostatically controlled electrically heated oil bath. The time delay in transferring the test piece from its temperature enviroment to the test machine was extremely small, and the temperature change was negligible.

4.3.2 Tensile testing.

Normal room temperature tensile tests were carried out on a 5000 kg capacity Instron tensile testing machine, using standard Hounsfield No. 12 tensile test pieces, see Fig. 22. This machine was adapted for gripping Hounsfield tensile test pieces by using a Polanyi bridging arrangement shown in Fig. 23.

Testing was also carried out at temperatures below room temperature using the Polanyi bridge and immersing the whole specimen and gripping arrangement in a temperature controlled enviroment contained in a Dewar flask. Two techniques of achieving controlled low temperatures were used, (i) by immersion of the test piece in a liquid media such as boiling liquid nitrogen at -196°C or cardice + acetone at -78°C and (ii) by a Wessel[143] spray device, which sprayed liquid nitrogen around the specimen from a pressurised liquid nitrogen container. The flow of liquid nitrogen was controlled through a magnetic valve, which was coupled to an on-off temperature controller and allowed a preset specimen temperature to be achieved. A schematic illustration of the low temperature testing device is shown in Fig. 24.

The various property parameters which were measured from the tensile tests included, limit of proportionality, flow stress, maximum tensile stress and the reduction in area. It was not possible to measure yield stress since no distinct yield points occurred, but instead use was made of the calibration between the specimen elongation versus chart movement to measure the flow stress at some fixed level of strain. This calibration was done using a travelling microscope to determine specimen elongation. Elongation values were not generally measured since the specimens had rather short gauge lengths, and necking was very severe.

The effects of temperature and strain rate upon the flow stress of lath martensitic alloys were also determined on the Instron tensile machine using two techniques, namely load cycling, and stress relaxation. With the load cycling technique the flow stress was firstly measured at room temperature after loading to a fixed level of strain, i.e. 2% or 5%, at a crosshead speed of 0.005 cms/min, i.e. a shear strain rate $\dot{\gamma}$ of 0.604×10^{-4}/s. After unloading, the specimen temperature was altered using either the Wessel spray device or a constant temperature liquid bath, and its new flow stress determined by reloading until its limit of proportionality was just reached. This was done at three crosshead speeds, i.e. 0.005, 0.05, and 0.5 cms/min which were equivalent to shear strain rates of equal to 0.604×10^{-4}, 0.604×10^{-3}, and 0.604×10^{-2} s^{-1} respectively. The specimen cross sectional area was remeasured after each loading cycle in order to make corrections for the extra deformation produced by each cycle, and at each test temperature the specimen was given a final reloading cycle at the slowest strain rate to determine the extent of strain hardening that had occurred. The final flow stresses calculated for the different strain rates and temperatures were then corrected for this strain hardening. As a means of checking the above results, individual test pieces were also tested for each temperature and strain rate, and the flow stress at a given strain determined from the complete load elongation curves which were obtained.

The alternative method used to determine the dependence of flow stress upon temperature and strain rate which was adopted, consisted of stress relaxation measurements.[164] This method is considered to be more accurate [167] than the previous, load cycling, technique since changes in dislocation substructure might be produced by loading the specimen at a series of testing temperatures. The dislocation substructure inherited from each previous temperature, i.e. whether cellular or planar, could possibly influence the level of athermal flow stress, and affect the value of determined by $\tau_* = \tau_A - \tau_{RT}$. The stress relaxation was done by loading at 0.02 cm/min into the plastic range, where the load was magnified by using a zero suppression device and switching to a smaller load scale. At some predetermined level of strain the crosshead motion was stopped and load readings taken at fifteen second intervals up to a maximum period of five minutes. This process was repeated at successive levels of strain in the plastic range and at different testing temperatures for the series of alloys within 4 to 10% manganese.

4.3.3. Hardness tests.

Every specimen including those used to study transformation and those used to assess mechanical properties was subjected to a hardness test by averaging the results of at least three Vickers hardness impressions.

Some microhardness tests were also made by the Reichert microhardness tester.

5.0 RESULTS.

5.1 Transformation Studies.

5.1.1 Determination of A_s and A_f on heating.

In many carbon free iron alloys the martensitic structure reverts to austenite, when heated, by a mechanism that is essentially a reverse martensite transformation.[45] The critical A_s temperature at which this reversion takes place was determined for the series of iron manganese alloys using verious heating rates within the dilatometer. Before heating to record the A_s temperature, the dilatometer specimens were heated to 1000°C for one hour and then water quenched. The various heating rates were obtained by presetting the furnace to a different temperature before it was slid into position over the dilatometer tube containing the specimen, and the heating rate was determined from the time lapse between room temperature and the temperature for the start of austenite reversion. Shown in Fig. 25 are the results of this experiment and the major effects were as follows:

(i) The A_s-A_f temperature range is depressed by increasing the percentage of manganese.

(ii) Transformation is completed within a narrow range of temperature, i.e. the A_s to A_f interval is only approximately 30°C (see Fig. 26).

(iii) Increased heating rates produce a significant increase in the A_s and A_f temperatures.

5.1.2 Determination of transformation temperatures on cooling.

Dilatometer specimens which had previously been heat treated by water quenching from 1000°C after one hour in an argon atmosphere, were reaustenitised in the dilatometer at 1000°C and held for fifteen minutes prior to cooling. Cooling at various rates was then achieved by blasting argon through the dilatometer or by altering the furnace position, and the average cooling rate was determined by measuring the time taken for the specimen to cool from its austenitizing temperature to that for the start of transformation. It was found that by using this technique of gas quenching a range of cooling rates between 100°C and approximately 2000°C/min could be obtained, and only by allowing the specimen to cool within the furnace was it possible to obtain slower rates of cooling than 100°C/min. When furnace cooled a cooling rate of approximately 5°C per minute was obtained and this was reduced to $\frac{1}{2}$°/min by using a motorized drive to slowly turn down the furnace variac. Attempts were made to obtain cooling rates faster than 2000°C per minute by liquid nitrogen and water spray devices but were not very successful. The main reason for this failure was the high sensitivity of the measuring system towards vibrations, and liquid media quenching tended to create erratic traces of the length change. It was necessary therefore to use the thermal analysis technique described earlier to obtain results for high cooling rates.

With all of the alloys examined only a single transformation kink in the dilatation versus temperature curves was obtained during cooling. The results for the transformation start temperature versus cooling rates are plotted in Fig. 27 for the various alloys. The main features of these results were as follows:

(1) 2% Manganese alloy The temperature for the start of the $\gamma \rightarrow \alpha$ transformation was continuously depressed by increased cooling rates, and it was also shown that the temperature interval between the start and finish of transformation was increased by increased cooling rates.

(2) 4% Manganese alloy The temperature for the start of the $\gamma \rightarrow \alpha$ transformation was initially depressed from 560°C but reached a plateau temperature of approximately 500°C at rapid cooling rates.

(3) 6% Manganese alloy A slight depression of the transformation temperature occurred on increasing the cooling rate, i.e. from 420°C - 390°C, but a plateau temperature was quickly developed. There was a significant increase in the transformation temperature range as the cooling rate increased for this alloy, see Fig. 28, but there was no evidence of more than one transformation arrest on the dilatation curve.

(4) 8 and 10% Manganese alloy In neither of these alloys was the transformation temperature or transformation temperature range altered by cooling rate. The dilatation curves of the 10% manganese alloy were also examined for possible epsilon transformation, by the detection of a

slight expansion on cooling (prior to the M_s), but no evidence of this was found.

5.1.3 Metallographic examination of transformation structure.

5.1.3.1 Optical Metallographic Examination.

Each of the dilatometer specimens from the above was subjected to optical metallographic examination in an attempt to determine the transformation mode.

In Fig. 29 a structure typical of those found in the 2% manganese alloy at cooling rates between 5°C to 2000°C/min is shown, and can be seen to consist of irregular ferrite grains with no evidence of either the prior austenite grain boundaries or any substructure. A structure such as this may be regarded as either equiaxed ferrite, or massive ferrite since both are similar, and there was no evidence available from which a distinction could be made. The structure is certainly not martensitic which means that the transformation temperatures shown in Fig 27 for the 2% manganese alloy were non-martensitic. Some specimens were also quenched into iced brine to determine whether it was possible to produce a martensitic structure. The resulting structure is shown in Fig. 30 and consists of mixed massive ferrite plus lath martensite.

Since it was not possible to produce a completely martensitic structure in the 2% manganese alloy it was excluded from any further investigation.

4% Manganese alloy.

In the 4% manganese alloy a pronounced change in microstructure occurred with increased cooling rate. and corresponded with the range where the transformation temperature was depressed. At slow cooling rates the structure produced was like that shown in Fig. 31A and can be seen to consist of an extremely ragged ferrite of a feathery nature. As the cooling rate was increased the depression of the transformation temperature was accompanied by a corresponding change in microstructure, in which the ragged appearance of Fig. 31A was lost and a series of straight sided slabs began to appear, see Figs. 31B and 31C, although the slabs were often rather ill defined and possessed wavy boundaries. This progressive change in microstructure eventually ceased in very rapidly cooled specimens and a well defined Widmanstatten ferrite typical of lath martensites was formed, see Fig. 31D.

6% Manganese alloy.

Considerable microstructure differences could be seen in this alloy between the slowly cooled and rapidly cooled condition. The rapidly cooled specimens all exhibited structures typical of lath martensite, see Fig.32A, but the slowly cooled specimens also contained an additional phase. These areas of second phase were distinguishable from the lath martensite by several features, including (i) their reaction to stain etching by sodium bisulphite which turned them light blue instead of the blue-brown colour of the lath martensite, and (ii) their ragged boundaries and irregular shape which was in contrast to the straight sided slab appearance of the martensite. The substructure produced by etching within these areas of second phase was also reminiscent of small equiaxed sub cells rather than of laths. All of the distinguishing features described above are shown by the micrograph in Fig. 32C and it is further significant that all of these areas appeared to grow from the prior austenite grain boundaries, and often on only one side of the boundary, see Fig. 32B. Where growth had appeared on both sides of the prior austenite grain boundary there was an impression of growth across the boundary, but in the majority of cases the original prior austenite grain boundary had not disappeared. see Fig. 32C.

8-10% Manganese alloys.

Both of these alloys gave consistently the same microstructures for the complete range of cooling rates, and they were typical of lath martensite, see Fig. 33.

5.1.3.2 Electron metallographic examination of transformation structures.

Thin foils were prepared by the technique previously described from 0.20 mm thick cold rolled strip material which had been austenitized for one hour at 1000°C in an argon atmosphere and then cooled at different rates by furnace cooling, argon blasting or water quenching. Prior to further thinning each specimen was polished and examined by optical metallography to confirm that their structures reproduced those found in the dilatometer specimens.

No specimens of the 2% manganese alloy were examined since they did not produce the martensitic structutes aimed at.

4% Manganese alloy

Shown in Fig. 34A is a thin foil electron micrograph for a furnace cooled specimen whose structure was equivalent to that shown optically by Fig. 31A. The structure can be seen to consist of irregularly shaped sub cells which contain a high density of planar dislocations, see Fig.34B. These sub cells varied in shape from elongated to equiaxed cells, see Fig. 34C, and it was shown by selected area diffraction that the boundaries between cells were low angle boundaries, see Fig. 35A and B. With the more rapidly cooled specimens the structure became less irregular and the cells appeared more lath like, see Fig. 36, until it finally became a complete series of parallel elongated cells with nearly straight boundaries.

The structure shown in Fig. 37 is typical of lath martensites and consists of laths separated by boundaries of high dislocation density with other dislocations randomly distributed in the lath interiors.

6% Manganese alloy.

After giving similar heat treatments to the cold rolled strip, to simulate the effects of cooling rate upon transformation in the dilatometer specimens, the types of structure observed optically were the same as those shown in Figs. 32B and C,. When the duplex structure was electropolished however to produce thinning it was found that preferential polishing took place and no good areas of the second phase were preserved in the final foil. The structure generally observed was typical of lath martensite, see Fig. 38A, although near to prior austenite grain boundaries there was occassional evidence of a less lath like appearance, see Fig. 38B. In the rapidly quenched specimens which were optically defined as lath martensite, the thin foils revealed typical lath martensitic structures, and there was absolutely no evidence of twinned martensite.

8-10% Manganese alloys.

Thin foils revealed typically lath martensitic structures for both of these alloys after both extremely slow and rapid cooling, see Fig. 39. No examples of twinned martensite were seen and also there was no evidence that epsilon martensite existed in either of these alloys.

5.1.4 X-ray diffraction

With the exception of the non martensitic 2% manganese alloy, the dilatometer specimens from which cooling transformations had been determined were studied by x-ray diffraction on the Philips diffractometer.

4% Manganese alloy.

Only one set of diffraction lines, namely the body centred cubic lines, were produced by specimens of this alloy and they all tended to be broad and diffuse. A distinctive difference between the broadening of the high angle diffraction lines for the slow and rapidly cooled specimens was that the slowly cooled specimens produced assymmetrical broadening. Shown in Fig. 40 are the traces for the $\{220\}_{\alpha}$ line for both slowly and rapidly cooled specimens in which this difference can be seen, and it is almost certainly due to the partial resolution of the $K\alpha_1$ and $K\alpha_2$ doublet which has led to the assymetrical broadening in the slowly cooled specimen.

6% Manganese alloy.

As with the 4% manganese alloy only a single set of diffraction lines occurred with these specimens. Furthermore no difference could be detected between the slowly cooled duplex structure alloy and one containing all martensite, i.e. the lines were all broadened considerably. Since no double reflections occurred from the duplex structure of the slowly cooled specimens it would seem that the two "phases" are both ferritic, and are probably of the same composition.

8 and 10% Manganese alloys.

Broad diffuse, body centred cubic diffraction lines were also observed for both of these specimens, but in the 10% manganese alloy an additional faint line was observed. This was shown to correspond to a $\{10\cdot1\}_\varepsilon$ hexagonal close packed reflection which suggests that epsilon martensite was present. The fact, however, that epsilon was not detected dilatometrically or metallographically and also because the $\{10\ 1\}_\varepsilon$ line could only just be detected tends to indicate that the amount of epsilon present was extremely small, i.e. 5%.

5.1.5 Hardness measurements.

The dilatometer specimens were hardness tested after they had been used to determine transformation temperature at various cooling rates, and the results are plotted in

Fig. 40. In both the 4% and 6% manganese alloys there is a considerable increase in hardness with cooling rate which corresponds to the changes in structure and transformation temperature previously described, but no such changes occur for the 8% and 10% manganese alloys.

In addition to the macro hardness tests some micro hardness tests were carried out on those alloys which appeared to have a duplex structure. These results are listed below:

2% manganese alloy brine quenched, see Fig. 30.

micro hardness massive ferrite 175 ± 10 20 gm load

lath martensite 225 ± 10 20 gm load

4% manganese alloy

(i) cooled at 5°/min, see Fig. 31A

microhardness, overall 200 ± 10 20 gm load

(ii) cooled at 1800°/min, see Fig.31C

overall 270 ± 10 20 gm load

6% manganese alloy

(i) cooled at 5°/min, see Fig. 32B

microhardness of grain boundary ferrite 200 ± 10 20 gm load

microhardness of lath martensite 270 ± 10 20 gm load

5.1.6 General comparison of the lath martensitic structure for varying manganese contents.

The structures formed by alloys containing between 4% and 10% manganese were typical of lath martensites, in that they consisted of parallel bundles of laths, but minor differences between them were apparent. For example, it has already been shown that the laths in the 4% manganese alloy tended to be irregular in shape compared to the higher manganese alloys, and it was also found that the lath width decreased with increasing manganese content. Shown in Fig. 42 are the average lath widths plotted against the percentage of manganese, where a linear intercept method was used to measure the lath width. These results indicate that there is a decrease in the lath width from between 4% and 6% manganese, but beyond this the lath width becomes more or less constant.

5.1.7 Isothermal transformation study.

The depression of transformation temperature by increased cooling rate inthe 4% and 6% manganese alloys suggested the possibility of isothermal transformation, and it was decided to study this in further detail.

The apparatus used was the isothermal dilatometer previously described, and specimens were quenched to a constant temperature after austenitizing at 1000°C for five minutes.

With the 4% manganese alloy various holding temperatures between 450 and 650°C were used, and it was found that no transformation occurred by holding at temperatures above 560°C for periods of up to nine hours. As soon as specimens were held at temperatures below 560°C transformation began immediately, and even began during the stage when the specimen was still cooling to the constant temperature bath temperature. In the early experiments no simultaneous specimen temperature and length change recordings were kept and it appeared that transformation was continuing with time at constant temperature, for a short while before stopping, i.e. it was assumed that the specimen quickly cooled to the equilibrium temperature of the constant temperature bath. This assumption was proved later to be incorrect, and it was found by measuring simultaneously both the specimen temperature and dilatation that the specimen in fact continued to cool for at least thirty seconds after the initial quench. In Fig. 43 typical time, temperature, and dilatation curves are shown for the 4% manganese alloy and these show quite clearly that transformation begins at 560°C and only continues whilst the specimen is still cooling. Transformation stops when a constant temperature is reached and does not continue despite further prolonged holding at this temperature. When subsequently cooled to room temperature, transformation recommences, but not immediately, and slight cooling was necessary before transformation restarted which suggests that austenite stabilization had occurred.

The above results suggest that transformation is athermal, i.e. the percentage transformation is a function of the holding temperature and does not alter with time, but this may only be true in respect to nucleation. In the experimental technique used the cooling rates to the equilibrium holding temperature were in fact rather slow and it would have been quite possible for growth of the transformation product to have occurred isothermally. Shown in Fig. 44 is the relationship between percentage transformation and temperature which was derived from the above isothermal studies and also by the estimation of percentage transformation from the dilatation temperature curve after rapid continuous cooling. It is significant that the slopes of these three continuous cooling curves in Fig.44 are the same despite the shift in temperature range for the start and finish of transformation, due to a difference in cooling rate.

Finally, the isothermally held specimens were examined by optical metallography and shown to produce microstructures identical to those shown in Fig. 31A, e.g. see Fig. 45.

6% Manganese alloy

The experiments described in the previous section were repeated for the 6% manganese alloys for a temperature range of 350-600°C. At temperatures above 420°C no transformation was detected after prolonged holding, e.g. nine hours, but transformation began immediately the temperature dropped below 420°C. In contrast to the 4% manganese alloy, transformation did continue for a short time even when the specimen temperature had reached a constant level, but soon stopped. By maintaining the specimen at its fixed temperature for prolonged periods no further transformation occurred and it required further cooling to restart the transformation. Before transformation restarted however there was again a slight delay and a slight temperature drop was required.

Typical time, temperature, dilatation curves which illustrate the above behaviour are shown in Fig. 46 and point conclusively to the existence of some isothermal transformation which only occurs below 420°C. This isothermal transformation however does not continue until complete transformation of residual austenite has been achieved.

Metallographic examination of the isothermally treated 6% manganese alloys revealed that their microstructures were identical to those produced by slow continuous cooling, i.e. see Fig. 32B. This structure was previously described as a duplex one consisting of lath martensite and an irregular grain boundary ferrite, and it was probably this latter phase which gave rise to isothermal transformation. To test this prediction a series of specimens were quenched to a constant temperature and held for varying times before brine quenching. The results of hardness measurements on these specimens are given in Fig. 47 and they show that the hardness decreases with holding time. By a point counting method the percentage of second phase (grain boundary ferrite) was established, and it was possible to correlate this with the specimen hardness, see Fig. 48. It seems certain therefore that this second phase is increasing with time and is responsible for the isothermal transformation observed.

8% and 10% Manganese alloys.

No evidence of any isothermal transformation was found in either of these alloys at any temperature between 200 and 600°C.

5.1.7.1 Hot Stage Microscopy.

Specimens of both the 4% and 6% manganese alloys were examined in a Reichart hot stage microscope, but little worthwhile information was obtained. The major problem encountered with these alloys was in preserving a polished surface at high temperature which would allow structural transformations to be observed. Prolonged soaking periods at high temperatures were necessary in order to develop coarse austenite grain sizes, and it was found that this led to surface deterioration. This deterioration occurred after heating under high vacuum conditions due to excessive surface volatilization of manganese which produced a grain boundary penetration effect not related to the underlying structure. A positive pressure of high purity argon reduced volatilization but produced a pitted surface which entirely hid any signs of transformation, and even the use of a reducing atmosphere containing argon + 2% hydrogen did not produce a thermally etched surface suitable for observation. Perhaps the only useful evidence gained by hot stage microscopy was that surface tilts occurred during transformation on cooling, but even this evidence was rather poor, see Fig. 49.

5.1.7.2 X-ray diffraction.

Specimens of 6% manganese alloy which had been isothermally treated were examined by x-ray diffraction and were shown to be identical in structure to the previously described continuously cooled specimens.

5.1.8 Effects of austenitizing time and temperature.

Several effects in terms of structure, hardness and transformation temperatures were noted by varying the austenitizing time and temperature and these are detailed below.

10% Manganese alloy.

When a single dilatometer specimen was cycled by heating and cooling through the $\alpha \rightarrow \gamma \rightarrow \alpha$ transformation, and the specimen was austenitized for one minute at successively higher austenitizing temperatures for each cycle, changes were produced in the M_s temperature, hardness and structure.

In Fig. 50A and B, the M_s temperature and hardness measured after each cycle are plotted against the austenitizing temperature. Each of these curves was determined with specimens which had initially been water quenched from 850°C and 1100°C respectively. The cycling treatment can be seen to produce an initial decrease in the M_s temperature which is accompanied by an increase in hardness, and after further cycling, the M_s temperature increases whilst the hardness decreases. In specimens which had previously been heat treated to produce a fine prior austenite grain size, fewer cycles were required to produce the M_s temperature minima, and hardness maxima.

The changes in hardness and M_s temperature described above were also accompanied by microstructural changes which are shown in Figs. 51A,B,C,D, and these show that the structure is a relatively coarse distorted lath martensite after the first cycle, see Fig. 51A, which becomes progressively more refined as the M_s temperature decreases to its minimum, see Fig. 51B. When cycled to successively higher temperatures the microstructure becomes coarser once more and eventually becomes a coarse clearly defined lath martensitic structure, see Fig. 51D. This coarsening of the microstructure occurred simultaneously with the decrease in hardness and increase in M_s temperature which occurred beyond their respective maximum and minimum values.

By repeating the above cycling treatment with a separate specimen for each austenitizing temperature identical changes in the M_s temperature and hardness were found, see Fig. 52, which were accompanied by microstructural changes similar to those described above. The same effects were also created by heating to a fixed austenitizing temperature and by varying the holding times, as is shown in Fig. 53A-C, and it was significant that with higher austenitizing temperatures shorter times were required to produce the changes observed.

Finally, single dilatometer specimens were cycled to a fixed austenitizing temperature for a constant time of one minute and the effects on the M_s temperature and hardness are shown in Fig. 54. This shows that the cycling treatment caused a reduction in the M_s temperature and an increase in the hardness, and both of these changes coincided with a refinement of the microstructure similar to that shown in Fig. 51B.

The metallographic examination of thin foils made to reproduce the changes in M_s temperature and hardness described in the preceding sections did not reveal any structural distinctions and neither did x-ray diffraction.

Both of these techniques however are probably restricted in their ability to detect changes in a structure which was already highly distorted by a martensitic transformation.

5.1.9. Crystallographic observation of the lath martensite structure.

The lath martensitic structure which was observed in alloys containing between 4% and 10% manganese was examined to ascertain whether it resembled ordinary lath martensite or the type observed in low stacking fault energy austenite steels.

Firstly, the relative orientations between adjacent laths was determined using selected area diffraction on thin foils, and particular attention was paid to the detection of twin related lath pairs. Many of the foils which were examined gave rise to $\langle 111\rangle_{\alpha}$ zone diffraction patterns which showed very little misorientation between adjacent laths, see Fig. 55, but this particular zone does not distinguish a twin orientation if the twin is produced by a 180° rotation about a $\{112\}_{\alpha}$ plane. Diffraction from other zones, e.g. $\langle 100\rangle_{\alpha}$ or $\langle 110\rangle_{\alpha}$ also indicated however that the misorientation between adjacent laths was slight, see Figs. 56A-B, and the $\langle 110\rangle_{\alpha}$ zone is particularly favourable for the detection of twin orientations. Of the many foils which were examined with all of the different alloy compositions, not one example of a twin oriented lath pair was found.

The martensite habit plane was also determined using selected area electron diffraction in thin foils. As there was no retained austenite, the technique consisted of the measurement of the direction lying parallel to a lath boundary for a variety of zones. This direction occurs at the intersection between the habit plane and the foil surface and so can define the habit plane if two or more such directions are known. It was necessary first of all to determine the relative rotations produced when the instrument was switched from normal viewing to diffraction and this was done by using a cubic molybdenum trioxide crystal whose major growth axis was along the $\langle 100 \rangle$ direction. The relative rotation between this easily identified direction and its equivalent ina diffraction pattern was then determined and shown to be 18° in an anticlockwise direction. Diffraction patterns were then taken from areas of iron manganese alloy foils in which the laths could be clearly seen, and whose boundaries produced a sharp image. After indexing the pattern, the direction parallel to the lath boundary was plotted on a standard cubic projection. These lath axis poles are plotted in this way in Fig. 57 and a typical lath martensite structure with its accompanying selected area diffration pattern is shown in Fig. 58. Fig. 57 shows that the lath axis directions are all within ± 5° of the $\{110\}$ great circles, which suggests that the martensite or lath habit plane is close to a $\{110\}_\alpha$ plane. If it is also assumed that the orientation relationship between the austenite and these laths is of the Kurdjumov Sachs type, then the habit plane may also be described as the $\{111\}_\gamma$ plane. Some additional evidence of the habit plane also arose from optical metallographic observations in which slab boundaries could be seen lying parallel to annealing twin boundaries in the prior austenite grains, see Fig. 59. This at least means that the martensite habit plane lies in a plane which has a common direction with the $\{111\}_\gamma$ planes. Slabs were also found with their major axis lying at an angle to the annealing twin boundary, and their angular relationship to this boundary was the same on both sides of the twin boundary, see Fig. 59. This suggests that the slabs are parallel to the K_2 plane of the annealing twin which is also a $\{111\}_\gamma$ plane, and provides further evidence that the habit plane is the $\{111\}_\gamma$ plane. The above observations also suggest that the assumed Kurdjumov Sachs orientation relationship was correct.

5.2. Mechanical Properties.

5.2.1 Impact Results.

Specimens were machined from the 4, 6, 8, and 10% manganese alloys, and then austenitized at a range of temperatures between 750 and 1100°C in an argon atmosphere. They were then brine quenched to produce a lath martensitic structure with a range of different prior austenite grain sizes, which was confirmed by optical metallographic examination after the specimens had been impact tested. Impact tests were then carried out at a range of testing temperatures between -70°C and 180°C to determine the ductile/brittle transition temperature and the results of these tests on the various alloys can be seen in Figs 60A-D. A metallographic examination of the broken specimens was then carried out to determine both their structure and prior austenite grain size; the latter being measured by a linear intercept method using three specimens for each heat treatment condition, and by averaging the results for several fields of examination. In Fig. 61 the reciprocal impact transition temperature, which is defined as the temperature to give 50% of the maximum ductility, is shown plotted as a function of log d, where d is half the grain size, and this gave a straight line relationship which was in accordance with the predictions of Stroh [138], see equation 14. This means that the impact transition temperature for these iron manganese alloys increases with increasing grain size, and it was interesting to note the varying sensitivity of the different alloys. The 10% manganese alloy showed that grain size had little effect upon the transition temperature whereas in the 6% manganese alloy the impact transition is very sensitive to grain size. It is difficult to state a precise relationship between the impact transition temperature and the manganese content since it varies with different grain sizes, and there is no consistent relationship. At coarse grain sizes there appears to be little difference between the impact transition temperatures of the 4%, 8% and 10% manganese alloys, but the 6% manganese alloy produced a very much higher transition temperature. In fine grain sized material this trend is somewhat reversed and the 4%, 6% and 8%

manganese alloys become better than the 10% manganese alloy.

As a final overall comment upon the results shown in Fig. 61, it is obvious that the ductile/brittle transition temperatures are either near to or considerably above room temperature, and this confirms the suspicion expressed earlier that iron manganese alloys are brittle in most heat treated condition.

5.2.1.1. Examination of Fractures.

Specimens which had fractured in a completely brittle manner were sectioned and mounted to enable metallographic examination of a transverse section through the fracture surface. This examination showed that the fractures for the 6%, 8% and 10% manganese alloys were intergranular and evidence of this is shown in Fig. 62. An examination of the fracture surface was also carried out on an scanning electron microscope, and this confirmed that the fractures were mainly intergranular, see Fig. 63A, although some areas of transgranular cleavage could also be seen, see Fig. 63B. The 4% manganese alloy fractures were considerably different from those of the other alloys and were an intergranular and transgranular mixture, see Fig. 64.

The intergranular fractures were subjected to further examination in order to determine whether they were caused by some intergranular precipitation. With optical metallography however no evidence was revealed of any intergranular precipitation, although it was found that preferential attack seemed to occur at the prior austenite grain boundaries when the specimens were etched in sodium bisulphite. Microhardness measurements at the grain boundary also detected no significant hardness differences from within the grain itself. Carbon extraction replicas also failed to produce evidence of any grain boundary film although a series of pits could be seen running along the grain boundaries, see Fig. 65, which were most probably produced by preferential etching attack. Thin foils also failed to reveal any grain boundary precipitation. Finally, the electron scanning microscope also revealed little to suggest the presence of any grain boundary films or precipitates. Only the occassional grain boundary inclusions lying on the fracture surface was shown.

5.2.1.2 The effects of tempering on impact properties.

Impact specimens for the various manganese alloy contents were brine quenched from 1000°C after one hour in an argon atmosphere, and this was followed by tempering for one hour at temperatures varying between 300°C and 600°C followed by water quenching. The effects of this tempering treatment upon the room temperature impact strength are shown in Fig. 66, and this shows that the impact strength increased sharply when tempering above approximately 500°C was carried out. Little change in impact strength occurred in the 4% manganese alloy when tempered at temperatures up to 400°C but both the 6% and 10% manganese alloys suffered a slight decrease in impact strength which suggested temper embrittlement. In addition to the room temperature impact measurements tests were conducted on tempered specimens for a range of testing temperatures. Tempering at 600°C followed by water quenching for instance was shown to lower considerably the transition temperature from its as quenched value, and these results are plotted in Figs. 67A, B, and C. In the 6% manganese alloy this reduction in transition temperature was from approximately 170°C to -65°C and in the 10% manganese alloy from approximately 35°C to -140°C. Specimens of the 6% manganese alloy were also tempered at 600°C but allowed to furnace cool to 300°C before removal into the air. After this treatment there was still a considerable improvement in impact properties over the untempered as quenched condition, but the impact transition temperature was now only approximately -10°C instead of -65°C, see Fig. 67B. An additional treatment tried with the 6% manganese alloy was to temper at 350°C for one hour followed by water quenching, and this produced an extremely marked embrittlement, the transition temperature being raised to 180°C+, see Fig. 67B. A similar treatment with the 4% manganese alloy also raised the transition temperature but by a much smaller amount, see Fig. 67A.

Finally, tests were made upon the 4% and 6% manganese alloys which had been allowed to air cool instead of being brine quenched from the austenitizing temperatures. The effect of this was to produce microstructures for the two alloys which were essentially similar to those described in the previous section, and shown in Figs. 31A and 32B. The effect of this treatment was to produce a considerable increase in transition temperature, i.e. 4% manganese air cooled from 1000°C, T_c = 140°C, see Fig. 67A, 6% manganese air cooled from 1000°C T_c = 180°C+, see Fig. 67B.

5.2.1.2.1 Examination of the fractures from tempered specimens.

After the 600°C tempering treatment the impact fractures became transgranular and tended to reveal evidence of the martensite sub-boundaries on the fracture surface, see Fig. 68A. Tempering at 350-450°C produced intergranular fractures and even tempering at 600°C produced some intergranular fracture within specimens which were allowed to slow cool from the tempering temperature, see Fig. 68B. Furthermore even the 4% manganese alloy revealed more evidence of intergranular fractures after tempering at 350°C whereas previously there had been less evidence of intergranular fractures.

Finally, the 4% and 6% manganese alloys which had slowly cooled from their austenitizing treatments also both gave rise to intergranular fractures, see Fig. 69.

5.2.1.2.2 Examination of structural changes due to tempering

Metallographic examination revealed that after tempering at temperatures up to 450°C little change in structure occurred. There was, however, a slight tendency for the lath martensitic structure to react more quickly to etching and to show signs that the lath boundaries were becoming broken up. A very definite change in microstructure took place after tempering at 600°C where the lath martensitic structure showed obvious signs of breaking up, see Fig. 70, but there was no evidence that the prior austenite grain size had changed from its original form and there was no evidence of austenite reversion. Examination by thin foil electron metallography revealed that specimens tempered at temperatures below 500°C did not differ structurally from the as quenched condition although there was some slight evidence to suggest that the misorientation between adjacent laths had increased slightly. In specimens tempered at 600°C areas similar to those shown in Fig. 34B could be seen where laths had become irregular in shape, but there was no evidence of reverted austenite or of precipitation.

As a further test to check whether tempering had produced any austenite reversion, dilatometer specimens of both the 6% and 10% manganese alloys were held in the isothermal recording dilatometer by heating from room temperature and holding at 600°C for one hour. During this period no contraction took place which indicates that there was no austenite formation, and furthermore there was no evidence of transformation taking place during the period when the specimen cooled to room temperature. Such transformation could have occured if austenite formed during holding had transformed back to martensite on cooling.

Finally, the tempered specimens were examined by x-ray diffraction and this also produced no evidence of residual austenite. What did occur however was that the lines became sharper and it was possible to resolve the

$K\alpha_1$ $K\alpha_2$ doublet for the high angle lines of specimens tempered at 600°C, see Fig. 71.

5.2.1.3. Impact properties of high purity iron manganese and iron manganese molybdenum alloys.

The behaviour exhibited by the iron manganese alloys after tempering resembles very closely the temper brittleness phenomenon observed in low alloy carbon steels, and for this reason some further alloys were produced as was previously described in the experimental procedure, see section.4·1

These two high purity vacuum melted alloys contained approximately 8½ - 9% of manganese and one of them also contained 0.5% of molybdenum. After holding for one hour at 1000°C in argon, brine quenching produced a lath martensite structure, and the impact tests results for this are shown in Fig. 72. This shows that despite their high purity the impact transition temperature was very high and rather surprisingly the molybdenum containing alloy was the slightly more brittle of the two. The molybdenum containing alloy was also tempered at 350°C for one hour, and this produced a marked increase in impact transition temperature, see Fig. 72. This shows that 0.5% molybdenum does not alleviate the temper brittleness in iron manganese alloys. The fractures of these high purity alloys were largely along the prior austenite grain boundaries.

5.2.2. Measurement of the parameters controlling brittle fracture.

5.2.2.1 Petch Analysis

Hounsfield test pieces of the type previously described were heat treated to produce lath martensitic structures with different prior austenite grain sizes. This was achieved by austenitizing for one hour in argon at temperatures between 750-1200°C followed by brine quenching. Tensile testing was then carried out on the Instron machine at a crosshead speed of 0.02 cms/min, i.e. strain rate approximately 1.14×10^{-2} per minute and the following data determined from the load versus elongation curves.

(i) Flow stress at 1% strain.

(ii) Stress at maximum load

(iii) Limit of proportionality.

(iv) Fracture stress

A typical series of these load elongation curves for the different alloys are shown in Fig. 73 and all were characteristic of the type usually observed for lath martensitic iron alloys. This characteristic shape shows a very small elongation to the onset of necking, i.e. approximately 5% followed by an extremely high reduction in area until final fracture, e.g. 60-70%, and this tends to indicate that there was a high initial rate of work hardening, since the onset of necking occurs when the strain hardening index $\frac{d\sigma}{d\epsilon} = \sigma_T$ the true stress. In Table II some typical room temperature tensile properties are given for the series of alloys tested.

After tensile testing the grip portions of the broken test pieces were examined metallographically in order to (a) check whether their structures were martensitic and (b) determine the prior austenite grain size.

Figures 74A-D show the Petch plots made for the room temperature tensile data of the series of martensitic alloys, and they show first of all that the Petch equation was obeyed. The most reliable data were obtained with the 1% flow stress values and the stress at maximum load, i.e. approximately 5% flow stress, but there was a considerable amount of scatter for the limit of proportionality values. There was virtually no difference in slope, K_y, between the 1% flow stress and maximum load stress values, but the slope of the limit of proportionality curve tended to be slightly greater. K_y varied between approximately $\begin{array}{l} 1\ \text{kg/mm}^{3/2} \\ 0.03\ \text{MN/m}^{3/2} \end{array}$ to $\begin{array}{l} 0.4\ \text{Kg/mm}^{3/2} \\ 0.012\ \text{MN/m}^{3/2} \end{array}$ and is shown in Fig.75 to decrease linearly with an increase in manganese content. These values of K_y are rather low and indicate that flow in lath martensitic iron manganese alloys was largely unaffected by the grain size, particularly in the case of the 10% manganese alloy. Similar tensile tests to those described above were also carried out at -196°C in liquid nitrogen, and it was found that many specimens broke prematurely in a completely brittle manner. A sufficient number survived however to demonstrate that there was no significant difference in slope of the Petch curve between -196°C and room temperature. In Fig. 76 the room temperature values of σ_i taken from the Petch curves are plotted against the percentage manganese and it can be seen that between 4% and 10% manganese there was virtually no dependence of σ_i upon composition

The values of σ_i used in Fig. 76 for pure iron and the 2% manganese alloy were obtained by using a conversion factor between the known microhardness of lath martensite and the flow stress. This was determined from the measured 1% flow stress and microhardness values of the 4% to 10% manganese alloys, and was found to be Hv x 0.225 = σ_i Kg mm^{-2}. For pure iron an approximate value of σ_i for lath martensite was obtained by conversion of hardness given in previous reports[28] but the value for the 2% manganese alloy was obtained using the microhardness given in section 5.1.5. It can be seen that the flow stress for iron manganese lath martensites increased sharply to a maximum when the manganese content was increased to 4% but was then hardly altered by further addition. Also shown in Fig. 76 are the values of flow stress for iron manganese alloys in the annealed ferritic condition, as determined by previous authors, and this enables the comparison between the strength of ferrite and lath martensite to be made.

When the mean hardness values were also plotted versus manganese content a similar type of curve to that shown in Fig. 76 is obtained, see Fig. 77, and this again indicated that the strength of the lath martensite increased sharply with additions of manganese up to 4% but is hardly affected by further additions.

The room temperature measurements of hardness and flow stress were thought to demonstrate essentially the solution hardening effects of manganese in terms of the athermal component σ_o and it was decided that the correletion between this solution hardening and the lattice parameter should be checked.

Bulk specimens were used to determine the lattice parameters using the diffractometer and also by calibrating the angles of reflection with a silicon standard. The specimens were austenitized at 1000°C for one hour in argon and then brine quenched to produce a martensitic structure which was subsequently tempered at 600°C for one hour. This tempering treatment enabled the $K\alpha_1$ $K\alpha_2$ doublet for the high angle lines to be resolved and permitted more precise lattice parameter measurements to be made. Fig. 78 shows the effect of manganese on the lattice parameter, which was calculated from the $\{112\}_\alpha$ and $\{220\}_\alpha$ $K\alpha_1$ $K\alpha_2$ reflections using at least three specimens, and by carrying out a calibration check for each one. Although these values may not be the precise lattice parameters because of the method used for their determination they are sufficiently accurate, e.g. ± 0.001 Å, to illustrate the changes which take place, and it can be seen that the lattice parameter increases with manganese in a manner equivalent to the changes in hardness and flow stress.

5.2.2.1.1 Fracture stress.

The fracture stresses were determined with the Petch analysis specimens by measuring the reduction in area for necked region and by noting load at fracture. Difficulty was experienced in measuring the precise fracture area and considrable scatter in results occurred, but despite this a reasonable correlation between fracture stress and $d^{-\frac{1}{2}}$

was obtained, see Fig. 79. Owing to the scatter in results it was not possible to distinguish whether differences in fracture stress existed between the different manganese contents, but there did not seem to be very much. Very little difference was also found between the fracture stress at -196°C and at room temperature for the 6% manganese alloy

5.2.2.2. Determination of the thermal component of flow stress.

Hounsfield tensile specimens for the 4%, 6% and 10% manganese alloys were heat treated by brine quenching after one hour at 1000°C in argon, to produce a lath martensitic structure. They were then tested on the Instron tensile machine to determine the influence of temperature and strain rate upon flow stress, using the load cycling technique previously described in section 4.3.2. A number of specimens were used for each alloy composition to give complete coverage of the temperature range 293 to 77°K and of the strain rate changes. Additional tests using individual specimens for each strain rate and temperature were also carried out with three specimens for each alloy, test temperature, and strain rate. The results found by both load cycling and individual tests agreed well, and showed that no difference existed for the flow stresses of the different manganese contents, e.g. no solution softening such as described in 3.3.1.2.1 was found. By assuming that room temperature equalled T_0 the temperature at which τ_* the thermal component of flow stress, becomes zero, values of τ_* were found for the different alloys, as a function of temperature and strain rate, i.e.

i.e. $$\tau_* = \frac{\sigma_A}{2} - \frac{\sigma_{293^\circ K}}{2}$$

where σ_A = actual flow stress

$\sigma_{293^\circ K}$ = flow stress at room temperature.

These are shown in Figs. 80A-C and indicate that τ_* increased both with increased strain rate and decreased testing temperature, but there was no difference between alloys for 4% to 10% manganese. Comparison between the τ_* flow stress values at different strain levels also shows that it was independent of prior strain.

The results of the alternative method, i.e. stress relaxation, will be discussed later.

5.2.3 Effects of tempering on mechanical properties.

Both the tensile and hardness properties were determined for the lath martensitic iron manganese alloys after they had been tempered at different temperatures. The as quenched state consisted of austenitizing for one hour at 1000°C and followed by brine quenching, and tempering was carried out for the range 300 to 600°C for a time of one hour. Figs. 81A,B show these results and it will be seen that only after tempering at above 400°C was there any significant drop in either tensile strength or in hardness. At tempering temperatures below 400°C there were slight increases in the flow stress from the as quenched condition, a peak being reached at temperatures around 350°C.

6.0 DISCUSSIONS

6.1 Transformation Behaviour.

6.1.1 Driving force for transformation.

The relationship between the transformation start temperatures and the manganese concentration, for both the $\gamma \rightarrow \alpha$ and $\alpha \rightarrow \gamma$ transformations are shown in Fig. 82. The temperatures shown for the $\gamma \rightarrow \alpha$ transformation refer to those which led to martensite either by its structure or athermal kinetics and thus it has been labelled M_s. Two temperatures are plotted for the 4% and 6% manganese alloy, namely an upper temperature which corresponds to the maximum temperature above which no transformation took place after holding for prolonged periods, and also the minimum plateau temperature produced by rapid quenching. These two temperatures represent the two different criteria used to define martensite, i.e. athermal kinetics or metallographic structure. Two values for the A_s temperature are also shown and represent the maximum and minimum range recorded by altering the heating rate. Finally, a range of temperatures are shown for the position of T_o which was deduced from $T_o = \frac{1}{2}(A_s + M_s)$ for the different M_s and A_s values.

When the present results are compared with those of previous authors there was reasonable agreement with the M_s temperature between 4% and 10% manganese. Comparing the results with those of Schummann[88] for example shows that there was excellent agreement above approximately 6% manganese and there was also good agreement for alloys of less than 6% manganese providing the upper temperature of the present results are taken. This is quite reasonable since Schummanns'[88] results were obtained by slow cooling. On comparing the results, with previous determinations of the M_s temperature at rapid cooling rates, e.g. Gommersall and Parr[22] the present results within the range 4% to 6% manganese agreed well if the lower plateau M_s temperature was used.

The transformation temperatures given in Fig. 82 were used to determine the transformation driving force using two basic approaches.

6.1.1.1 Ideal solution

Referring to section 2.2.2.4.1 the driving force of the $\gamma \rightarrow \alpha$ transformation is given by:

$$\Delta G^{\alpha-\gamma} = (1-x_A)\,\Delta G_{Fe}^{\alpha-\gamma} + x_A\,RT\ln \frac{x_{A_\gamma}}{x_{A_\alpha}} \qquad (2)$$

and shown in Table III are the values for the various coefficients necessary for the solution of this equation.

In the first four columns different values for $\Delta G_{Fe}^{\alpha-\gamma}$ are shown, and have been determined by different authors. Columns two to four provide values which are in good agreement with each other and which are also more comparable with the values of $\Delta G_{Fe}^{\alpha-\gamma}$ used by most previous workers in derivations of the driving force for martensitic transformation. Shown in columns five and six are the equilibrium solubility limits x_{A_α} and x_{A_γ} for manganese in iron taken from the published equilibrium diagram.[147]

The values for the driving force at the M_s temperature derived from equation (2) are shown plotted as a function of manganese content in Fig. 83A and can be seen to vary from between 250-600 cals/mole (1100-2300 J/mol) at the minimum plateau M_s temperature or from between 150-600 cals/mole (600-2300 J/mol) at the maximum M_s temperature. Also shown in Fig. 83A are the driving forces derived by previous authors[53,148] for iron manganese alloys using an ideal solution model.

The present set of results are considerably higher than those of the previous workers and are also somewhat higher than the normally expected values for lath martensite transformation in other ferrous systems. However, it was also true that the previous results were rather lower than expected, especially with the more dilute alloys. With regard to the discrepancy between the previous and present results it cannot have been due to any major difference between the measured transformation temperatures but was most likely to have been caused by using different values for $\Delta G_{Fe}^{\alpha-\gamma}$. Previously $\Delta G_{Fe}^{\alpha-\gamma}$ was calculated from the iron manganese equilibrium diagram via the ideal solution approximation that:

$$\Delta G_{Fe}^{\alpha-\gamma} = RT\ln \frac{(1 - x_{A\gamma})}{(1 - x_{A\alpha})}$$

and this gave very much lower values for $\Delta G_{Fe}^{\alpha-\gamma}$ than those used in the present determination. This seems to be an indication that it was incorrect to assume that iron and manganese form an ideal solid solution, and further evidence of this was that the equation for $\Delta G_{Mn}^{\alpha-\gamma}$, i.e. $\Delta G_{Mn}^{\alpha-\gamma} = RT\ln \frac{x_{A\gamma}}{x_{A\alpha}}$

produced solutions for $\Delta G_{Mn}^{\alpha-\gamma}$ which were independent of temperature, which must be incorrect. It would seem therefore that the values of driving force derived in the present investigation by assuming ideal solution conditions are in error. They are in fact too high, and this must be due to the free energy of mixing term being ignored.

6.1.1.2 Regular Solution.

In the section 2.2.2.4.2 it was shown that:

$$\Delta G_{Mn}^{\alpha-\gamma} = (1 - x_{A_\alpha})^2 A - (1 - x_{A_\gamma})^2 B - RT\ln \frac{x_{A_\gamma}}{x_{A_\alpha}} \qquad (6)$$

and that $\Delta G_M^{\alpha-\gamma} = x_A (1 - x_A)(B-A)$

By substituting these into equation (1) an expression for the driving force is obtained.

$$\Delta G^{\alpha-\gamma} = (1 - x_A)\Delta G_{Fe}^{\alpha-\gamma} + x_A\left((1 - x_{A_\alpha})^2 A - (1 - x_{A_\gamma})^2 B - RT\ln \frac{x_{A_\gamma}}{x_{A_\alpha}}\right) + x_A (1 - x_A)(B-A)$$

and this simplifies to

$$\Delta G^{\alpha-\gamma} = (1 - x_A)\Delta G_{Fe}^{\alpha-\gamma} - x_A\left(RT\ln \frac{x_{A_\gamma}}{x_{A_\alpha}} + B(x_A - 2x_{A_\gamma} + x_{A_\gamma}^2)\right) + A x_A (x_A - 2x_{A_\alpha} + x_{A_\alpha}^2) \qquad (15)$$

All of the terms in equation (15) can be determined with the exception of that containing A, but it can be assumed that this term is sufficiently small to be ignored in dilute solutions. Shown in Table IV are the values for the coefficients needed to solve equation (15), where B was determined from the relationship:

$$-Bx_{A_\gamma}^2 \simeq \Delta G_{Fe}^{\alpha-\gamma} + RT\ln \frac{(1 - x_{A_\gamma})}{(1 - x_{A_\alpha})} \qquad (7)$$

This equation gave a linear relationship for B and T(1-lnT) below 800°K but large discrepancies arose above this temperature. The most probable cause of this was the extreme sensitivity of B to slight changes in the values of $\Delta G_{Fe}^{\alpha-\gamma}$, x_{A_α} and x_{A_γ} and it was decided therefore to assume that they were in error. For temperatures above 800°K the values of B used in calculation were taken from the linear relationship between B and T(1 -lnT).

Plotted in Fig. 83B are the driving force values derived from equation (15) and these were shown to vary from between 285 and 450 cals/mole at manganese contents within the range 4% to 10% when the minimum M_s temperature was used. The driving force for alloys of between 4% and 6% manganese was reduced to 165-250 cals/mole at the maximum M_s temperature.

In addition to the method described above use was also made of information provided by Hillert[149] which gave theoretical values of $\Delta G_{Mn}^{\alpha-\gamma}$ for the $\alpha \rightarrow \gamma$ transformation in pure manganese. These values were derived from the iron manganese equilibrium diagram by using essentially the same regular solution approximations that were made by Kaufman & Cohen [54] in iron nickel and are shown in Table V

For the $\alpha \rightarrow \gamma$ transformation the driving force $\Delta G^{\alpha-\gamma}$ may be written as

$$\Delta G^{\alpha-\gamma} = (1 - x_A)\Delta G_{Fe}^{\alpha-\gamma} + x_A \Delta G_{Mn}^{\alpha-\gamma} + x_A(1 - x_A)(B-A) \qquad (16)$$

where (B-A) is obtainable from equations (6) and (7), i.e.

$$(B-A) = \left\{ x_{A_\alpha}^2 (1 - 2x_{A_\gamma}) - x_{A_\gamma}^2 (1 - 2x_{A_\alpha}) \right\}^{-1} \left\{ (x_{A_\gamma}^2 - x_{A_\alpha}^2)\left(\Delta G_{Mn}^{\alpha-\gamma} + RT\ln \frac{x_{A_\gamma}}{x_{A_\alpha}}\right) + \right.$$

$$\left. (1 - x_{A_\alpha})^2 - (1 - x_{A_\gamma})^2 \left(\Delta G_{Fe}^{\alpha-\gamma} + RT\ln \frac{(1 - x_{A_\alpha})}{(1 - x_{A_\gamma})}\right) \right\}$$

and the solutions of which are shown in Table VI

Values for the driving force at the M_s temperature which were derived from equations (15) and (16) are in good agreement with each other, the only difference being that those derived via equation (16) are slightly lower.

Shown in Fig. 82 are the theoretical T_0 temperatures which were determined from equations (15) and (16), and these can be seen to agree well with the maximum of the observed T_0 temperatures for the dilute alloys but are rather higher than the observed values in the richer alloys, e.g. 10% manganese. Obviously this discrepancy is due to the approximate nature of the regular solution model, but it may also indicate that the measured A_s temperatures are not the true reverse $\alpha \rightarrow \gamma$ martensitic transformation temperatures. It has been shown that the A_s temperature increased with heating rate and it was possible that a plateau temperature might have been reached if higher rates of heating could have been obtained. This higher A_s temperature would no doubt have reduced the discrepancy between the observed and calculated T_0 temperatures.

For alloys containing between 4% and 6% manganese the driving forces at the minimum M_s temperature agree well with previously published values for other iron alloys, e.g. 285-300 cals/mole, (1200-1260 J/mol), but at higher manganese concentrations they are very much higher. If the value for the 10% manganese alloy, i.e. 430 cals/mole (1806 J/mol) was correct then twinned martensite should have formed according to the suggestion by Bell[21], since the driving force is well above the critical level of 315 cals/mole (1323 J/mol) for the lath to twinned transition. Since this did not occur, and also due to the discrepancy between the observed and calculated T_0 temperatures, it suggests therefore that the result was incorrect, and indicates that the assumptions made by the regular solution model are invalid for the more concentrated alloys. If in fact the driving force for the 10% manganese alloy is corrected to the observed T_0 temperature then a figure of approximately 300 cals/mole (1260 J/mol) is obtained and this agrees with previously published values for other iron alloys.

Finally, in Fig. 82 it will be seen that by extrapolation, two figures for the M_s temperature of pure iron can be obtained. The lower M_s temperature values extrapolates to within the region of 550-600°C and the higher M_s to 750-800°C. Both of these are close to the temperatures normally quoted for pure iron and indicates that the propositions of section 2.2.2.5.4 concerning bainite and martensite may be correct.

6.1.2 Transformation behaviour of iron manganese alloys

In alloys containing between 6% and 10% manganese the results have clearly established that the $\gamma \rightarrow \alpha$ transformation is martensitic over a wide range of cooling rates. It was in fact impossible to produce massive ferrite in either the 8% or 10% manganese alloys. The martensite formed has been shown metallographically to be lath martensite and not twinned martensite as suggested by some previous authors[57.99] and it was also shown to be crystallographically indistinguishable from the lath martensites formed in other iron base alloys, e.g. iron nickel alloys. No examples were found of lath martensites with a $(\bar{1}\bar{1}2)_\gamma$ habit plane which is the type found in low stacking fault energy austenite steels, and is probably nucleated by epsilon.

In both the 4% and 6% manganese alloys certain features of transformation existed which do not allow the immediate conclusion that they were martensitic.

These features for the 4% manganese alloy included:

(i) depression of the transformation temperature by increased rates of cooling.

(ii) changes in the microstructure, where after slow cooling a non lath like appearance existed which was more reminiscent of pro-bainitic ferrite than lath martensite.

(iii) changes in the mechanical properties which led to considerably lower hardness and tensile strength values after slow cooling.

The most probable explanation of the above behaviour is that in the 4% manganese alloy the M_s temperature is sufficiently high to allow recovery to take place during transformation, since these effects are not produced in alloys whose M_s was below the normal recovery temperature of iron, e.g. 400°C. Certainly the microstructural observations are consistent with this argument and it is most likely that the slow cooled structures were formed as a result of recovery in the lath martensitic structure. Additional evidence of this comes from the x-ray diffraction results. The recovery processes also seem to assist transformation since, if slow cooling is used, the M_s temperature is raised, and the driving force for transformation is reduced from 285 cals/mole (1200 J/mol) to 150 cals/mole (630 J/mol). There are several possible ways in which this could arise, but all are due essentially to thermally activated dislocation movement.

(i) By the thermally assisted movement of the austenite/martensite interface dislocations (transformation dislocations).

(ii) The lattice invariant shear, i.e. slip could be assisted by easier dislocationmovement due to thermal activation. This would mean that existing nuclei or embryos could produce transformation at a higher M_s temperature, or smaller driving force.

(iii) If recovery can take place in the surrounding austenite or in the martensite, then the degree of strain hardening produced by the constraint between the austenite and martensite will be reduced. This would enable the martensite embryos to start growth at a smaller driving force.

Whichever of these three suggestions is correct, depends on whether they fulfill the condition that the thermally activated process is one which assists only in the growth of existing nuclei and not in the formation of new nuclei. This must be true since the results showed that it was not possible to achieve continued isothermal transformation. What really happened was that it became possible to allow growth of the martensite nuclei at a higher temperature by slower cooling. The last of the above three suggestions is the most likely mechanism involved, and thus transformation in the 4% manganese alloy at slow cooling rates could be referred to as a "recovery assisted" martensite. During cooling therefore, martensite embryos or nuclei form which could be regions of high dislocation density, e.g. "strain embryos", but their growth is restricted by the constraint of the surrounding austenite, and a sufficient driving force must be created by supercooling before transformation can occur. At high rates of cooling no recovery can occur to reduce constraint and a normal martensitic transformation arises when the driving force reaches the critical level, e.g. 285 cals/mole. With slower cooling rates an incubation period is provided during which the constraints are reduced and martensitic transformation can occur at a slightly higher temperature with a lower driving force. Since, however, thermally activated process does not assist in producing further embryos, i.e. nucleation is athermal, further undercooling is still required to produce further transformation.

An interesting point which emerges from these results is that shown by the extrapolation of the transformation temperatures to pure iron in Fig. 82. Extrapolation of the recovery assisted M_s temperatures gives an M_s temperature for pure iron of approximately 750°C whereas the minimum plateau M_s temperatures extrapolate to approximately 560°C. It may be therefore that the controversy described in section 2.2.2.5.4 is due to different martensitic reactions. An M_s temperature of 560°C in pure iron refers to martensite formation without thermal assistance whereas transformation at 750°C is by a recovery assisted mechanism. If this is true then it is also possible to speculate concerning the role of interstitial atoms whereby the pinning of dislocations by solute atmospheres could reduce recovery and inhibit martensite formation above 560°C. This may account for the changes in M_s temperature in pure iron at very low carbon levels such as described by Swanson & Parr[28]. Finally, there is the question of bainite transformation such as described in section 2.2.2.5.4 for iron nickel alloys, iron nickel molybdenum alloys, and iron manganese chromium alloys. The apparent isothermal transformation produced in these alloys could quite conceivably be due to recovery in the austenite which leads to an incubation period prior to martensitic transformation, and this explains the ability to suppress transformation by rapid cooling or to display a time, temperature, transformation curve. It would in fact be interesting to measure the activation energies for transformation in these alloys and compare them with that for recovery in austenite. Upper bainite transformation in low carbon steels could also be explained on the above basis, namely, that the transformation is martensitic but its rate is controlled by the rate of recovery in the austenite. This in turn could be controlled by the rate of carbon diffusion.

The other puzzling transformation effects occurred in the 6% manganese alloy and it was shown that a second phase, additional to the lath martensite, was produced by either slow cooling or holding at a fixed temperature between the M_s and M_f. This second phase was produced at the prior austenite grain boundaries and was undoubtedly genuine as evidenced by the changes in metallographic structure and mechanical properties which it produced. It also seems reasonably certain that it formed isothermally and produced a supersaturated ferrite of ragged appearance, and possibly it was massive ferrite. However, there are several questions and observations which contradict this.

(i) Why should massive ferrite form in a 6% manganese alloy and not in alloys containing less manganese ? e.g. the 4% manganese alloy.

(ii) Why does it form only after cooling to below 420°C when the driving force has reached 300 cals/mole (1260 J/mol)? Normally the driving force for massive ferrite is only approximately 60 cals/mole (252 J/mol)

(iii) Why does the formation of massive ferrite, which occurs isothermally, stop during holding at a fixed temperature before all of the remaining austenite has decomposed?

Question (i) and (iii) could perhaps be resolved by suggesting that localized segregation existed within the 6% manganese alloy which enabled massive ferrite to form. However, there was absolutely no evidence of this, e.g. x-ray diffraction analysis and furthermore no separate transformation kink for massive ferrite was detected during cooling with the dilatometer. If a difference in composition, i.e. segregation, had occurred then a separate transformation temperature should have been produced.

The alternative to massive ferrite being responsible for the duplex structure was that recovery assisted martensite formed during slow cooling. Certainly this would explain the transformation driving forces and the ability to slightly depress the M_s temperature in the 6% manganese alloy. Compared with the 4% manganese alloy the M_s temperature for the 6% manganese alloy is much lower, and the opportunities for recovery to take place much less, so that only slight assistance is given to transformation and the M_s temperature is only raised slightly by slow cooling. It may also be possible that only in regions where impurity segregation occurs, e.g. prior austenite grain boundaries, is it possible for the recovery assistance to occur. This would explain why normal lath martensite structures occurred except at the prior austenite grain boundaries. Furthermore due to the lower M_s temperature and the slower recovery rates the growth rate of recovery assisted martensite will be slower, and this would explain why isothermal transformation was observed inthe 6% manganese but not the 4% manganese alloy. This is because the time taken for the 4% manganese alloy specimens to cool to the holding temperature in the dilatometer was perhaps too slow for isothermal growth to be detected, i.e. it had probably been completed before a constant temperature had been reached. In the 6% manganese alloy the slower growth rates allowed isothermal growth to be detected despite the delay in reaching a constant temperature.

The most favourable explanation of the observed behaviour seems therefore to be that the duplex structures formed in the 6% manganese alloys after slow cooling were due to the formation of recovery assisted martensite, and not massive ferrite, and if this is so it implies that lath martensite may exhibit isothermal growth. The nucleation however remains athermal and does not produce transformation until cooling below a critical temperature has been achieved. Further cooling is then required once these nuclei have been exhausted in order to continue transformation, and behaviour such as this closely resembles upper bainite formation. It may be proper therefore to describe the transformation as bainitic.

Summarising therefore, transformation in alloys containing between 4% and 10% manganese has been shown to occur by a lath martensitic mechanism and produces a structure which is metallographically and crystallographically identical to the lath martensites produced in iron nickel alloys. Increasing the manganese content lower the M_s temperature due mainly to the lowering of the T_o temperature, but there is also a small increase in driving force, e.g.

from 285 to 300 cals/mole (1200-1260 J/mol), which suggests that greater constraint is resisting transformation at higher manganese concentrations. This could be due to the solution hardening of austenite caused by increased manganese additions. With manganese concentrations of less than 6% manganese the M_s temperature is sufficiently high to allow recovery to take place in the martensite during its formation, and this produces some thermal assistance to the martensite reaction by allowing isothermal growth to occur if sufficient time is allowed. Massive ferrite structures could not be produced except in the 2% manganese alloy.

6.1.3. Effects of austenitizing time and temperature.

In section 5.1.8 the results are given for the effects of austenitizing time and temperature on subsequent martensite transformation in a 10% manganese alloy. The purpose of this work initially was to establish the possibility of forming massive ferrite by producing fine austenite grain sizes, and also to determine whether it was possible to alter prior austenite grain sizes by variation in heat treatment. Massive ferrite could not in fact be produced but it was possible to alter the prior austenite grain size by varying austenitizing temperatures and/or time, and also in the pursuit of this result several interesting effects were noted. These effects have been fully described elsewhere[150] but may be briefly summarized as follows. In the event of increasing either the austenitizing temperature or time the M_s temperature, hardness, and microstructure underwent the changes described in section 5.1.8, and the interpretation of these is that they are due to the accumulation of dislocations in the austenite following the $\alpha \rightarrow \gamma$ reverse transformation. Immediately on reheating through the $\alpha \rightarrow \gamma$ transformation a high dislocation density is inherited by the austenite due to the reverse martensitic reaction and it is proposed that due to the austenite's low stacking fault energy these dislocations initially adopt planar distributions with elastic stresses due to pile ups. With austenite in this condition subsequent transformation to martensite is stimulated by the presence of elastic stresses, and a high M_s temperature results. The structure formed also retains the original austenite grain size but is distorted due to the dislocations of the austenite being transposed back to the martensite. The hardness at this stage is also relatively low due to the inheritance by the martensite of the original coarse austenite grain size. With subsequent reheating either to a higher austenitizing temperature or for a longer austenitizing time the dislocations produced by the reverse $\alpha \rightarrow \gamma$ transformation in the austenite are able to undergo recovery processes such as the formation of sub-cells by thermally activated cross slip, and this then removes the elastic stresses due to pile ups. On cooling, transformation back to martensite becomes more difficult, and this is reflected by a decrease in M_s temperature, see Figs. 50A-B, which may be caused by the action of sub-cell boundaries in the austenite, preventing the propagation of martensite. Alternatively the sub cells may be said to increase the austenite flow stress and restrict martensite formation by imposing greater constraint. During this stage of the changes in M_s temperature the martensitic structure is refined by the austenite sub cells and its hardness is increased. The final stage occurs when either the austenitizing time or temperature have been sufficient to promote recrystallization within the highly dislocated austenite formed by the $\alpha \rightarrow \gamma$ transformation. Upon the removal of the dislocations from the austenite by recrystallization, the barrier to martensitic transformation is reduced and the M_s temperature increases, but with the completion of recrystallization however a limiting constant M_s temperature is reached, i.e. the M_s temperature is unaffected by prior austenite grain size and does not alter during the grain growth stage. The microstructure gradually becomes coarser and its hardness is reduced during this period.

Summarizing the changes shown in Figs. 50-54, they are probably due to varying degrees of recovery and/or recrystallization in the austenite caused by variations in austenitizing time or temperature. If no recovery is allowed to occur the dislocations inherited by the austenite from the reverse $\alpha \rightarrow \gamma$ transformation produce stimulation of a subsequent martensite reaction, but if recovery does occur the martensite reaction is retarded and its hardness increased. Eventually recrystallization in the austenite leads to an increase in M_s temperature and a reduction in hardness.

The effects of cycling through the $\alpha \rightarrow \gamma \rightarrow \alpha$ transformation sequence to a fixed austenitizing temperature causes a build up of dislocations within the austenite which enhances recovery. Thus the effect of cycling is to depress the M_s temperature, refine microstructure, and increase its hardness.

The results also demonstrate that refinement of the austenitic grain size is possible by reaustenitization. This occurs inspite of the reversible $\alpha \rightarrow \gamma$ martensitic reaction which should cause the original grain size to be retained, and is due to the recrystallization produced by the high dislocation density inherited within the austenite.

6.2 Mechanical Properties.

6.2.1. Brittle Fracture Behaviour

The impact test results show that iron manganese alloys are relatively brittle when in a lath martensitic condition, but when tempered above 600°C and quenched, good impact properties are obtained. The brittle fracture behaviour also exhibited many of the characteristics of the temper brittleness phenomenon for low alloy steels. These were namely:

(i) Fracture tended to follow paths along the prior austenite grain boundaries.

(ii) Either by tempering in, or slow cooling through, the temperature range 350-450°C, severe embrittlement at prior austenite grain boundaries was produced.

(iii) Tempering above 600°C removed embrittlement, but brittleness returned if specimens were allowed to slow cool from 600°C or were retempered in the range 250°C - 450°C, see Fig. 67C

(iv) Although no evidence of grain boundary precipitates was found, grooving along the prior austenite grain boundaries occurred after etching an embrittled alloy in sodium bisulphite reagent.

In low alloy steels two types of embrittlement can occur during tempering. These are:

(i) "350°C embrittlement". This is produced by the tempering of an as quenched martensitic steel within the range 250-400°C, and is revealed by a reduction in the room temperature impact strength. The brittle fracture which occurs usually does so by intergranular failure at prior austenite grain boundaries.

(ii) "Temper brittleness". This occurs when a hardened steel after tempering at above 600°C is either allowed to slow cool through, or is reheated within, the temperature range 350-580°C. Again the brittle fracture produced usually occurs by failure at prior austenite grain boundaries, but the embrittlement is revealed by an increase in transition temperature, and there may not be any reduction in room temperature impact strength. A further feature of temper brittleness is one of **reversibility whereby** an embrittled steel can be restored to a tough condition by retempering at above 600°C.

The 350°C embrittlement is thought by some authors[151 154] to originate due to structural changes which occur during tempering, such as (i) the replacement of $Fe_{2.4}C$ epsilon carbide by cementite during tempering. (ii) the formation of coarse platelike carbides at prior austenite grain boundaries. (iii) the formation of a weak ferrite film at prior austenite grain boundaries due to depletion in carbon via carbide precipitation. (iv) the pinning of dislocations by solute atmospheres involving carbon and/or nitrogen. However, it has been shown by Capus[155] that embrittlement does not occur unless either chromium or manganese is present as a major alloying element together with certain impurities. These impurities in decreasing order of importance were phosphorus, arsenic, tin, silicon, and possibly manganese. Nitrogen also could give rise to considerable embrittlement.

With regard to temper brittleness the most acceptable explanation also involves the presence of either chromium or manganese as a major alloying element, and also the presence of impurities. The impurities required are essentially those which are associated with the 350°C embrittlement and include antimony, phosphorus, tin, arsenic, silicon, and possibly manganese,[156] again in order of decreasing importance. Unless these impurities are present, steels containing nickel and chromium do not suffer temper brittleness,[156] and conversely steels containing the impurities but not either chromium or manganese also will not produce temper brittleness.[157] The most widely accepted explanation of temper brittleness is that impurity atoms segregate to austenite grain boundaries during austenitization by a process of equilibrium segregation. This arises since with the exception of manganese all of the embrittling impurities are ferrite stabilizers which show little tendency towards forming solid solutions with austenite. By segregating to the austenite grain boundaries therefore the impurities produce less misfit strain, but lead to a severe weakening of prior austenite boundaries when the steels is subsequently quenched to form martensite. Tempering at above 600°C however causes the segregated impurities to boil off from their grain boundary sites and toughness is restored. Subsequent retempering or slow cooling within the range 350-580°C enables the impurities to rediffuse to prior austenite grain boundaries with the result that brittleness returns, and the time temperature relationship for this return of embrittlement exhibits a C shaped curve. The basis for this C curve is that for low temperatures, e.g. 350°C, diffusion of the impurity is slow and prolonged times are required for embrittlement to return. At high temperatures, e.g. 580°C, the impurities are tending to boil off from grain boundaries and this again increases the time necessary for embrittlement to return. The maximum degree of embrittlement, requiring the shortest time occurs at some intermediate temperature between these two extremes. Perhaps the greatest difficulty which arises with the above interpretation of temper brittleness however is the role played by the major alloying element in making the embrittlement occur. The explanations put forward for the need of their presence include:

(i) The enhancement of the impurity diffusivity rates by the major alloying element. Manganese has been shown in fact to enhance the rates of phosphorus diffusion.[158]

(ii) The tendency of the alloying element itself to segregate to prior austenite grain boundaries, which helps to attract impurities to grain boundaries by the affinity between the impurity and alloying element.[159] Capus[159] has suggested that carbide forming elements, e.g. Mn and Cr, may segregate more readily than ferrite forming elements, e.g. Ni owing to the formation of grain boundary alloy carbides which help to concentrate the alloying element at grain boundaries.

From the evidence presented above it would seem reasonable to suppose that the two types of embrittlement, namely 350°C embrittlement and temper brittleness, stem from essentially the same causes. Both require the presence of chromium and/or manganese together with similar impurities. Furthermore both types of embrittlement occur by intergranular fracture at prior austenite grain boundaries, and the addition of molybdenum often reduces the embrittlement susceptibility In view therefore of these similarities, both forms of embrittlement should be capable of being explained by a single theory, and this is achieved by the following proposals. Firstly, it may be suggested that susceptible steels suffer from equilibrium segregation of impurities during austenitization which leads to a potential weakening of grain boundaries. Tempering of the as quenched steel within the range 250 - 400°C then creates an even more embrittled steel by secondary processes which aggravate the effects of equilibrium segregation. These secondary processes could possibly include carbide precipitation, carbide coarsening, or strain ageing affects due to both carbon and nitrogen, and this might explain the damaging effects of nitrogen found by Capus[155]. When the steel is tempered at above 600°C the segregated impurities are dispersed from grain boundary sites, as outlined previously, and the steel then behaves by responding to temper brittleness by either slow cooling or ageing within the temperature range 350-580°C, i.e. as outlined previously.

With regard to the present results, the iron manganese alloys tested have been shown to register symptoms of both of the two types of embrittlement discussed above, and since manganese steels have been shown to be highly susceptible to embrittlement there seems to be little doubt that the brittleness encountered by the present tests are due to temper embrittlement.

In the preceeding discussion, manganese itself was quoted as a potential embrittling element, but it does not fit within the pattern of the other impurities since it is not a ferrite stabilizer. For this reason, it is conceivable that the impression that manganese causes embrittlement is mistaken, and the effects noted by previous authors may have been due to the presence of another impurity, e.g. phosphorus or silicon. In support of this, are observations that as little as 0.001%P can produce embrittlement in the presence of only 2% Mn.[157] Thus because of the very high concentrations of manganese in the alloys at present under discussion extremely small impurity concentrations would be required to create brittleness. Which impurities however are not easily decided, but it may be significant that the alloy which proved to be the most susceptible to brittleness, namely that containing 6% manganese, also contained the most silicon. Conversely the least susceptible alloy, i. e. the 4% manganese alloy, contained the least silicon. A further argument favouring silicon is a well established dependence of embrittlement on an interaction between manganese and silicon,[156] although this is also true for phosphorus. There was however no significant variation in the phosphorus content between the various alloys tested. A further contender for the embrittling impurity especially in regard to the 350°C type embrittlement is undoubtedly nitrogen, since manganese not only increases nitrogen solubility in austenite, but may also produce manganese nitride precipitation in ferrite. In view of the previous arguments however it seems to be more proper to regard any effects due to nitrogen as being secondary to those created by the segregation of either silicon or phosphorus. No doubt when the alloys were tempered at 350°C, nitrogen or even carbon for that matter could be responsible for the loss in impact strength by causing an aggravation of the equilibrium segregation effects. Since no evidence of either carbide or nitride precipitation was found after tempering, dislocation pinning by solute atmosphere formation seems to be the most likely cause of this aggravation.

Summarizing with respect to the present results, the most plausible explanation for the brittleness observed is that some form of equilibrium segregation of impurities occurs during austenitization. This leads to poor impact properties after quenching, and failure by intergranular fracture. When the alloy is then tempered or allowed to slow cool within the range 250-400°C an aggravation of the grain boundary weakness occurs and this has been tentively linked with the effects of carbon and nitrogen in forming solute atmospheres or precipitates. No precipitates were detected. Finally, when the alloy is tempered at 600°C the brittleness disappears due to the removal of grain boundary segregation. Its reappearance depends then on allowing the impurities to rediffuse to grain boundaries, as in the normal manner encountered within temper brittleness.

Perhaps the greatest difficulty with the above interpretation is that the $\frac{1}{2}$% molybdenum addition failed to produce any improvement in impact properties, whereas in low alloy steels such additions are usually effective in causing an improvement. It is possible of course that the molybdenum addition made was insufficient to counteract the high manganese concentration present, but Wilson[91] also found that alloys containing 5% Mn and up to 8% Mo were brittle, especially after ageing in the range 400-500°C. This ageing treatment unfortunately produces grain boundary precipitation[160] and it may have been this which was responsible for embrittlement instead of the failure of molybdenum to counteract temper brittleness. Finally, Capus[155] and also Gould[161] have shown that molybdenum did not reduce temper brittleness in a low alloy steel embrittled by silicon, and since the present alloys are also suspected to be embrittled by silicon it becomes understandable that molybdenum additions failed to create any improvement.

6.2.2 Fundamental Properties in relation to brittle fracture.

The criterion for brittle fracture was given in section 3.3, as

$$\left[\sigma_i d^{\frac{1}{2}} + k_y\right] k_y = \beta \mu \gamma \qquad (9)$$

and the various parameters of this equation have been measured for iron manganese alloys.

6.2.2.1 Assessment of σ_i

6.2.2.1.1 σ_o the athermal component of flow stress

In section 3.3.1 σ_i was shown to consist of two components $\sigma_i = \sigma_o + \sigma_*$. σ_o, the athermal component was mainly dependent upon strengthening due to substructure and solid solution hardening and may be assessed from the data shown in Figs. 58-59. These show that the strength of lath martensite in iron manganese alloys rises sharply with additions of up to 4% manganese, but further additions produce little further strength increases. By using data for the hardness of pure iron lath martensite together with data published for the solution hardening of annealed iron by manganese, an assessment of the relative contributions made by each strengthening factor is possible and was found to be:

$$\sigma_o = \Delta\sigma_\alpha + \Delta\sigma_s + \Delta\sigma_D$$

$$= 25\% + 30\% + 45\%, \text{ see Fig. 76.}$$

These values compare very closely with data published for iron nickel alloys.[107] which also produced a sharp initial increase in flow stress with nickel additions. However, manganese is more effective than nickel in initially raising the strength of iron, although the final strength level is about the same for both alloy systems.

The solution hardening produced by nickel and manganese during the initial part of the strength versus % solute curves were:

Iron - nickel $\sigma_o = 37 + 220 \times Ni$ Kg/mm^2

Iron - manganese $\sigma_o = 40 + 750 \times Mn$ Kg/mm^2

These equations show that manganese is a much more effective solution strengthener than nickel, but there is some exaggeration of the real difference due to comparisons being made between the 0.2% Flow stress for iron nickel and a 1% Flow stress for iron manganese. If the limit of proportionality measurements are used instead of a 1% Flow stress a closer comparison can be made with the iron nickel 0.2% Flow stress results and the iron manganese solution strengthening equation becomes:

$$\sigma_o = 37 + 450\ \%\ Mn\ kg/mm^2$$

which means that manganese is approximately twice as effective as nickel in producing solution hardening, and this agrees with previous predictions.[93.97] Within the range 4% to 10% manganese the slope of the strength versus manganese content curve is virtually zero and this also occurs for iron nickel alloys between 10% and 30% nickel. The levels of flow stress produced at this stage by solution strengthening were; 4%-10% manganese, 1% Flow stress $\sigma_i = \begin{array}{l} 70\ kg/mm^2 \\ 687\ MN/m^2 \end{array}$; Limit of Proportionality, $\sigma_i = \begin{array}{l} 55\ kg/mm^2 \\ 540\ MN/m^2 \end{array}$; iron 10%-30% nickel, 0.2% Flow stress $\sigma_i = \begin{array}{l} 55\ kg/mm^2 \\ 540\ MN/m^2 \end{array}$; and this shows that the flow stresses for iron nickel and iron manganese lath martensites are virtually identical.

A theoretical interpretation of the solid solution strengthening produced by manganese follows from Fig. 78 which shows that the lattice parameter increases with manganese in exactly the same manner as flow stress. Between 0% and 4% manganese the lattice parameter increases sharply and almost linearly, but above 4% manganese there is a very much more gradual increase in lattice parameter This suggests that solution hardening occurs due to the interaction of the stress field produced by solute atoms misfit with the stress field of dislocations, and since substitutional atoms produce no shear displacement the interaction occurs only with the edge components of dislocations. Solid solution hardening for iron by manganese is therefore similar to that caused by nickel, and appears to follow the predictions made by Mott and Nabarrds[108] theory. When the measured lattice parameter changes were used in accordance with their equation, the theoretical flow stress for an iron 4% manganese alloy was found to be $\begin{matrix} 55\ \mathrm{kg/mm^2} \\ 540\ \mathrm{MN/m^2} \end{matrix}$ and this is the same as the measured limit of proportionality which also included a substructure strengthening factor. Obviously therefore the theoretically predicted solution strengthening is greater than the actual value, but this may be due to inaccuracies in the lattice parameter change measurements plus the inevitably approximate nature of this type of equation.

6.2.2.1.2 the thermal component of flow stress.

The data in Fig. 80A-C showed that σ_* did not vary with manganese concentration for alloys between 4% - 10% manganese as was also found for σ_0. This implies that the Peierls-Nabarro stress is unaffected by manganese additions, assuming that Peierls mechanism is responsible for the changes in σ_* or τ_*. In section 3.3.1.2.1 a prediction was made that manganese might increase the

Peierls-Nabarro stress due to an increase in directional bonding caused by depletion of the 3 d electron shell, but this apparently does not occur. When the present results are compared with previous measurement on iron manganese alloys, e.g. Rees et al [93] and Wynblatt [162.163] there was good agreement; Wynblatt for example determined that τ_* was equal to $\begin{matrix}17.5\ \text{kg/mm}^2\\ 171.7\ \text{MN/m}^2\end{matrix}$ at 77°K in an annealed 2% manganese alloy which is identical to the results of the present tests for alloys between 4% to 10% manganese. With the present 2% manganese alloy after heat treating to produce an equiaxed ferrite structure, τ_* at 77°K was $\begin{matrix}21\ \text{kg/mm}^2\\ 206\ \text{MN/m}^2\end{matrix}$ which is slightly higher than the values obtained for the 4%-10% manganese alloy and indicates that manganese may initially lower τ_*, but the effect is slight. Finally, the values of τ_* given by previous authors[105] for pure iron are also very similar to those determined by the present experiments.

The evidence above suggests that manganese does not alter the level of τ_* in iron and also confirms previous experiments[118.120] that τ_* does not alter with dislocation substructure, i.e. virtually no difference exists between lath martensites and annealed ferrites. It also appears that the level of τ_* is the same for both iron manganese and iron nickel lath martensites.[109.129]

6.2.2.1.2.1 Analysis of Flow stress data.

Values of H the activation energy were determined from the flow stress versus temperature and strain rate data, using the equations developed in section 3.3.1.2,

i.e. $$H = -KT^2 \left\{\frac{\partial \ln \gamma}{\partial \tau_*}\right\}_T \left\{\frac{\partial \tau_*}{\partial T}\right\}_\gamma \qquad (11)$$

$$H = -KT \ln \frac{\nu}{\gamma} \quad \text{where } \nu = \rho_m bAl\nu_0 \qquad (12)$$

Solutions of equation (11) were obtained by measuring the slope $\left(\frac{\partial \tau_*}{\partial T}\right)_\gamma$ of the curves in Fig. 80A-C at some fixed level of τ_* together with $\left(\frac{\partial \ln \gamma}{\partial \tau_*}\right)_T$ at the temperatures for the fixed τ_* levels in each of the three curves. The solution of equation (12) was obtained by equating equations (11) and (12) in order to obtain

$$KT^2 \left\{\frac{\partial \ln \gamma}{\partial \tau_*}\right\}_T \left\{\frac{\partial \tau_*}{\partial T}\right\}_\gamma = KT \ln \frac{\nu}{\gamma}$$

$$\left\{\frac{\partial \tau_*}{\partial T}\right\}_\gamma = \frac{1}{T} \left\{\frac{\partial \tau_*}{\partial \gamma}\right\}_T \ln \frac{\nu}{\gamma}$$

and the slope of this relationship, i.e. $\left\{\frac{\partial \tau_*}{\partial T}\right\}_\gamma$ versus $\frac{1}{T}\left\{\frac{\partial \tau_*}{\partial \gamma}\right\}_T$ gives a solution for ν from the value of $\ln \frac{\nu}{\gamma}$ obtained. ν the frequency factor was found to equal $3.17 \times 10^9/s$ which agrees well with those obtained for other iron alloys, i.e. $= 10^8 - 10^{11}/s$ [106]

The values of H determined by equations (11) and (12) are plotted in Fig. 84. They agreed with each other and were also shown to be independent of prior strain. Also shown in this figure are the values of H determined for lath martensite in iron nickel alloys [109.129] and it will be seen that the two are almost identical. Values for iron nickel chromium alloys are included in Fig. 84 and are seen to be considerably higher, which may be the result of a higher Peierls-Nabarro stress.

6.2.2.1.2.2 Activation Volume.

The two methods used to determine V_*, i.e (i) $V_* = -\frac{\partial H}{\partial \tau_*}$, (ii) $V_* \doteq KT\left\{\frac{\partial \ln \gamma}{\partial \tau_*}\right\}_T$. gave results which are plotted in Fig.85. Both were in good agreement and V_* varied between 15-20 b^3 at τ_* equals 20 kg/mm^2 to 50+ b^3 at τ_* equals 2 kg/mm^2
196.2 MN/m^2 19.6 MN/m^2

6.2.2.1.2.3 Determination of H and V_* by Stress Relaxation Measurements.

During straining the level of stress depends upon the temperature and strain rate, but if straining is stopped stress relaxation occurs due to the thermally assisted escape of dislocations from obstacles. This relaxation occurs at a rate given by the following equation[164]

$$\Delta\sigma_{\phi} = S \ln\left\{1 + Ct\right\} \triangleq S\ln t$$

$\Delta\sigma_{*}$ = stress change at time t

C = constant

S = a function which depends upon the activation energy for the thermally activated escape of dislocations, and according to Feltham[164]

$$S = 2.303\,\sigma_{*}\,\frac{KT}{H} \tag{21}$$

S is given by the slope of the $\Delta\sigma_{*}$ versus log t relationship and enables H to be calculated.

A more detailed appraisal of the stress relaxation process due to Sargeant[121] also takes into consideration other factors likely to affect the rate of relaxation, e.g. test machine relaxation, and strain hardening due to dislocation movement during relaxation. The relationship given by this approach is

$$\Delta\sigma_{*} = \frac{1}{B}\ln\left\{1 + CB\exp\,(B\sigma_0)\,t\right\} \tag{22}$$

where $C = \frac{E\cdot ls}{a}\nu\exp - \frac{1}{KT}\left\{H^{*} + V_{*}\,\frac{\theta_a\sigma_0}{E\,l_s} + V_{*}\sigma_u^{o}\right\}$

$B = \frac{V_{*}}{KT}\left\{1 + \frac{\theta_a}{E\cdot l_s}\right\}$

E = modulus of load cell 50.7 kg mm^{-1}

l_s = specimen gauge length

ν = frequency factor

H^* = Activation energy at $0^\circ K$

V_* = Activation volume

θ = $d\sigma/de$ strain hardening rate

a = Specimen cross sectional area

σ_o = Stress at zero time

σ = Stress at time t o

σ_u^o = a constant

Equations (21) and (22) are basically similar and it follows that

$$S = \frac{1}{B} = \frac{1}{\frac{V_*}{KT}} \left\{ 1 + \frac{\theta a}{E \cdot l_s} \right\}$$

by using typical values of θ, a, E, l_s for the present iron manganese alloys it was found however that the $\frac{\theta a}{E\, l_s}$ term was sufficiently small to be ignored, and thus $S \doteq \frac{KT}{V_*}$ (23)

By using the stress relaxation data given by section 4.3.2, values of the activation volume V_+ were determined from equation (23). Typical curves of the $\Delta\sigma_*$ versus log t relationship are shown in Fig. 86 and the values of V_* are plotted in Fig. 85. There was excellent agreement between these results and those determined previously via equation (12)

Since it may be unrealistic to compare the results of the present iron manganese alloys with those determined for iron nickel alloys by previous authors, stress relaxation tests were conducted simultaneously on sheet tensile specimens of iron 15% nickel and iron 9% manganese after brine quenching from 1000^{o}C. The values of V_* measured by this experiment for tests at 293^{o}K and 77^{o}K were

Alloy	$T^{o}K$	$\tau_* = \tau_A - \tau_{293^{o}K}$	V_*
Iron 15% Ni	293	0	44-55 b^3
Iron 9% Mn	293	0	43-50 b^3
Iron 15% Ni	77	16 kg/mm^2 157 MN/m^2	9-10 b^3
Iron 9% Mn	77	16 kg/mm^2 157 MN/m^2	8.3-9 b^3

Since there was no significant difference between these results, the earlier statement that iron nickal and iron manganese alloys behave identically seems justified.

6.2.2.1.2.4. Assessment of flow stress in terms of the Dorn Rajnak theory.

The present measurements of activation energy and activation volume for flow in iron 4% to 10% manganese alloys not only agree with previous determinations for iron nickel alloys,[109.129] but also with those for other iron alloys, e.g. pure iron,[118.120] iron 2% manganese[162 163] both H and V_* were independent both of prior strain, i.e. dislocation substructure, and of transformation substructure which is compatible with the prediction of the Peierls-Nabarro barrier mechanism. Furthermore the range of values for V_*, i.e. 10-70b^3 is reasonable for a double kink model, i.e. assuming that $V_* = b^2 l$ where l is the double kink separation, then l varies from 0.25×10^{-6} to 1.25×10^{-6} cms, which are sensible values for the dimensions of a double kink. The agreement between theory and practice for the present results may however be tested further by the Dorn, Rajnak theory on the following basis. At $0^{o}K$ double kink formation receives no thermal assistance and nucleation depends entirely upon the effective stress.

Therefore at $0^{o}K$

$$\tau_p = f\left\{2H_k\right\}$$

where τ_p = Peierls stress

H_k = Energy of a single kink

Above $0^{o}K$ thermal assistance can occur which reduces the stress to nucleate kinks

Therefore $\tau_* = f\left\{H\right\} = f\left\{T\right\}$

where H = Activation energy to form a double kink

It now follows that

$$\frac{\tau_*}{\tau_p} = f\left\{\frac{H}{2H_k}\right\} = f\left\{\frac{T}{T_o}\right\}$$

where T_o is the temperature at which double kinks are formed entirely by thermal energy, i.e. $\tau_* = 0$

The theoretical curves of the relationship between $\frac{\tau_*}{\tau_p}$ versus both $\frac{T}{T_o}$ and $\frac{H}{2H_k}$ are shown in Figs. 87A,B and are such that when either $T = T_o$ or $H = 2H_k$ $\frac{\tau_*}{\tau_p} = 0$; and when $\tau_* = \tau_p$ $\frac{T}{T_o} = 0$; or $\frac{H}{2H_k} = 0$. Also shown in these two figures are the calculated relationships from the experimental data for the iron manganese alloys. In the case of Fig. 87A the calculated curve was determined by extrapolating the flow stress versus temperature curves, i.e. Fig. 80A-C to $0^{o}K$, and this gave a value for τ_p equal to 37 kg/mm^2. Fitting this to the theoretical curves, Fig. 87A,B, at $77^{o}K$ gave the following for γ

the strain rate = $0.604 \times 10^{-4}/s$

$$\text{at } 77^{\circ}K \quad \frac{\tau_*}{\tau_p} = 0.4$$

therefore $\frac{T}{T_o}$ from the theoretical curve equals 0.40 and

$T_o = 193^{\circ}K$

for the strain rate = $0.604 \times 10^{-3}/s$

$$\text{at } 77^{\circ}K \quad \frac{\tau_*}{\tau_p} = 0.48 \text{ and } \frac{T}{T_o} = 0.33;$$

therefore $T_o = 236^{\circ}K$

By using these values for T_o the relationship between $\frac{\tau_*}{\tau_p}$ and $\frac{T}{T_o}$ was then determined from all of the flow stress data. The calculated curve of Fig. 87B was determined using the calculated values of H and a value for $2H_k$ equal to 0.55 ev which is given by Dorn & Rajnak from a theoretical analysis of the double kink.

Comparison between the theoretical and calculated relationships of Figs. 87A,B, show good agreement except at either $\frac{T}{T_o}$ values greater than 0.8, i.e. Fig. 87A or when τ_* approaches zero in Fig. 87B. Thus the present results for H, V_*, and the $\frac{\tau_*}{\tau_p}$ versus $\frac{T}{T_o}$ or $\frac{H}{2H_k}$ relationships are compatible with overcoming the Peierls-Nabarro stress as the rate controlling mechanism at low temperatures, except at temperature above approximately $190^{\circ}K$ or at low values of effective stress τ_*. This is therefore one failing of the theory. A further criticism is that τ_* does not vary with manganese concentration, which does not agree with the suggestion that manganese should alter the Peierls-Nabarro stress. Furthermore by fitting the

$\frac{\tau_*}{\tau_p}$ value to the theoretical curve of $\frac{\tau_*}{\tau_p}$ versus $\frac{T}{T_o}$ it was shown previously that T_o varied between 193 and 236°K for the two particular strain rates chosen. These temperature are very much lower than the normally quoted T_o temperature for iron, e.g. 380°K, and which according to Conrad[106] is given when $\frac{d\tau_*}{dT} = 5 \times 10^{-3}$ kg/mm^2/°K. By extrapolating plots of log $\frac{d\tau_*}{dT}$ versus temperature for the present results T_o was shown to be 420°K for iron manganese alloys, which is considerably higher than those predicted by a Peierls-Nabarro barrier mechanism. The failure of calculated $\frac{T}{T_o}$ or $\frac{H}{2H_k}$ values to fit the theoretical curves at temperatures above 190°K or at low effective stresses is almost certainly due to this discrepancy in the T_o temperatures, and this suggests that a different deformation mode to the Peierls-Nabarro mechanism is operative in this region. Other iron alloys,[106, 109, 118, 129, 130, 162, 163,] and also other body centred cubic metals[106, 121] also exhibit this deviation from theoretical behaviour, and as yet there is no satisfactory explanation. Several authors[162, 163] have proposed that the new thermally activated deformation mechanism may be cross slip, i.e. τ_* is controlled by the ease of cross slip, and it is perhaps significant that changes in slip morphology do occur in some iron alloys with change in temperature. In iron silicon alloys for example[165] wavy slip predominates at higher temperatures, but becomes straight at low temperatures and this suggests that restricted cross slip occurs at low temperatures. Thus without cross slip the factor governing thermally activated flow is the Peierls-Nabarro stress, but when cross slip occurs other factors take control, e.g. the ease of constriction of extended dislocations.

6.2.2.1.3 Summary of σ_o and σ_* and their relationship to brittle fracture.

The results for alloys containing between 4% and 10% manganese have shown that both σ_o and σ_* do not vary with manganese concentration, and are also identical to those found for iron nickel alloys. Differences in σ_i, i.e. $\sigma_i = \sigma_o + \sigma_*$ for iron manganese alloys cannot therefore explain either the variation of impact properties with manganese content, or their relatively poor impact properties compared to iron nickel alloys.

6.2.2.2 Significance of the K_y parameter.

The K_y parameter for iron manganese alloys within the range 4% to 10% manganese has been shown to decrease with increased manganese concentration, and to be independent of temperature. The values for the K_y parameter, i.e. 0.45 - 1.0 $kg/mm^{3/2}$ (0.014 - 0.031 $MN/m^{3/2}$) were very similar to those measured for pure iron, i.e. 0.97 $kg/mm^{3/2}$ (0.030 $MN/m^{3/2}$)[132] and an iron 18% nickel alloy, i.e. 0.7 $kg/mm^{3/2}$ (0.022 $MN/m^{3/2}$) [129]

In section 3.3.2 K_y was defined as a measure of the ease of slip propagation from grain to grain, and possibly depends upon a number of factors including, mobile dislocation density, ease of cross slip, number of available slip systems, and work hardening rate. Rates of work hardening were measured from logarithmic plots of stress strain data for the various iron manganese alloys in the lath martensitic condition, but no differences were found, and thus the decrease in K_y with manganese concentration cannot be due to changes in the rate of work hardening. A further possibility however is that manganese increases the ability for cross slip to occur which increases the number of available slip systems, and there is evidence that the formation of deformation cell structures is enhanced by the addition of manganese to iron.[166] In face centred cubic metals cell structure formation occurs more readily in high stacking fault energy materials, where cross slip can occur, and this may also be true for body centred cubic metals. In the previous section however it was suggested that cross slip may be the cause of thermally activated flow above 190°K, and no difference was found between the various manganese alloy concentrations. This would tend to suggest therefore that increasing the manganese content does not alter cross slip ability and cannot account for the changes in K_y.

Finally, manganese may decrease the resistance to moving dislocations by removing interstitials from solid solution, i.e. carbide and/or nitride formation, so that solute atmosphere formation is reduced. This seems to be the only reasonable explanation.

The importance of K_y to brittle fracture is that high K_y values produce poor impact properties. With the present iron manganese alloys however very low values of K_y were found, and the impact properties should have been at least as good as those of iron nickel alloys. Furthermore an increase in manganese content should have improved the impact properties by way of the reduction in K_y. In fact, however, the alloy which gave the best impact properties was that containing the least manganese, i.e. 4%, and there was no simple relationship between impact properties and manganese content.

6.2.2.3 Significance of Grain Size.

Fig. 61 illustrates that the transition temperature increases with increase in prior austenite grain size, but the alloys show differing grain size sensitivity and the most sensitive alloy to grain size variation was that containing 6% manganese.

By using the Stroh[138] relationship, i.e. $\frac{1}{T_c} = \frac{-7}{2}\frac{K}{Q} \ln d + C$ an activation energy for brittle fracture was determined and this gives a quantitative guide to the grain size susceptibility. These activation energies were as follows:

4% Mn. Q. 17.9 K cal/mole = 0.78 ev = 75.2 K J/mol
6% Mn. Q. 7.9 K cal/mole = 0.34 ev = 33.2 K J/mol
8% Mn. Q. 25.4 K cal/mole = 1.1 ev = 106.7 K J/mol
10% Mn. Q. 33 K cal/mole = 1.34 ev = 138.6 K J/mol

and show that in general brittle fracture becomes more difficult with increasing manganese content.

Variation in the transition temperature with grain size depends primarily upon the slopes of the yield stress, and fracture stress curves, with grain size, and their dependence upon temperature. In the present alloys the variation in yield stress with both grain size and temperature did not alter significantly with manganese concentration, and thus the difference in brittle fracture versus grain size relationship must arise from differences in fracture stress. The fracture stress versus grain size relationship for the different alloys was shown however to be reasonably similar and only the variations in fracture stress with temperature between the series of alloys can account for the changes in activation energy shown previously. It is perhaps significant that there is a direct correlation between the activation energy Q and the Mn: Si ratio of the different alloys, i.e. a high silicon content produces a low activation energy, e.g.

Alloy	Q	Mn/Si ratio
4% Mn.	17.9 K cal/mole (75.2 K J/mol)	59.2
6% Mn.	7.9 K cal/mole (33.2 K J/mol)	50.5
8% Mn.	25.4 K cal/mole (106.7 K J/mol)	85
10% Mn.	33 K cal/mole (138.6 K J/mol)	91

This indicates that silicon could be responsible for reducing the fracture stress, and adds some support to the arguments stated in section 6.2.1 regarding the part played by silicon in encouraging temper embrittlement.

A final comment on the grain size effects concerns the actual meaning of the activation energy values measured. This is not absolutely clear, but since in theory brittle fractures should occur when the flow stress exceeds the fracture stress. the activation energies at fracture should be inversely proportional to the activation energies for flow; i.e. the higher the activation energy for flow so the more likely it is that fracture will occur. With the present results no difference existed between the different alloys in respect to the activation energies for flow, and this again suggests that the differences in fracture behaviour are responsible for the different grain size effects observed.

6.2.2.4 Summary of the parameters in the Cottrell brittle fracture equation $(\sigma_i d^{\frac{1}{2}} + K_y) K_y = \beta\mu\gamma$

The results have shown that no factor in the left hand side of the Cottrell equation, (equation 9) i.e. those which determine the ease of plastic flow, can be held responsible for the poor impact properties of iron manganese alloys. Admittedly the σ_i parameter is increased in these alloys due to solution hardening by manganese and due to the dislocation substructure produced by lath martensite transformation, but this is also true for iron nickel alloys, and these do not suffer with poor impact properties. On the right hand side of the above equation only the γ surface energy term might possibly create profound differences between iron manganese and other iron alloys, and there is considerable evidence that the surface energy for fracture is being lowered in these alloys by segregation at prior austenite grain boundaries. There is no clear indication as to the impurity responsible, but either phosphorus or silicon appear to be likely candidates, and there is also the possibility that interstitials, e.g. carbon and nitrogen, aggravate their effects.

7.0 CONCLUSIONS.

7.1 Transformation Behaviour.

1. Alloys of iron plus manganese within the range 3.75-10% manganese undergo a $\gamma \rightarrow \alpha$ martensitic transformation over a wide range of cooling rates, i.e. $\frac{1}{2}$°C/min to 4000°C+/min

2. The α martensite formed is identical to the lath martensite found in other iron alloys, i.e. shear plates of body centred cubic ferrite are formed in parallel bundles of laths in a characteristic Widmanstatten arrangement. The individual laths are composed of elongated sub cells separated by a boundary of high dislocations density and contain a high density of dislocations within each cell. Their most probable habit plane is the $\{111\}_\gamma$ plane, and their orientation relationship to austenite is probably that given by Kurdjumov Sachs.

3. In alloys containing less than 6% manganese a maximum M_s temperature exists, above which no transformation occurs, but this temperature may be depressed to a minimum plateau temperature by increased cooling rates. No depression of the M_s temperature by increased cooling rate occurs in alloys containing more than 6% manganese. The explanation put forward for the depression of M_s temperature is that thermal assistance to the martensite transformation can occur with slow cooling when the M_s temperature is above 400°C. This assistance may be due to recovery, and there was metallographic evidence of recovery in the martensite structure.

4. No examples of twinned martensite were found in the iron manganese alloys studied, nor was there any indication that lath martensites formed in twin related adjacent pairs with a $(\bar{1}\bar{1}2)_\gamma$ habit plane. This suggests that no nucleation of alpha martensite via epsilon occurred in these alloys.

5. The driving forces for martensite transformation at the minimum M_s temperature ranged between 285-300 cals/mole (1200-1260 J/mol) providing that the values calculated by a regular solution model were corrected to the observed T_0 temperature, and were not based upon the calculated T_0 temperature. If the calculated T_0 temperature was used, the calculated driving force for the higher manganese alloys, e.g. 10% manganese, was rather higher than the figure normally quoted for lath martensite transformation in other iron alloys.

6. The results suggested that two M_s temperatures can exist for pure iron which can give rise to both bainitic and martensitic modes of transformation. One at 750°C arises when thermal assistance during the martensite transformation occurs, and the other occurs at 560°C when thermal assistance is prevented.

7. Massive ferrite transformation occurs only in iron manganese alloys containing less than 2% manganese.

7.2 Properties.

1. Iron manganese alloys in the lath martensitic condition have poor impact properties compared to alloys of iron nickel

containing less than 28% nickel. This is not due however to either a difference in the crystallography and morphology of the martensite, or to an inherant difference in the deformation and flow properties of iron manganese alloys. The flow stress at low temperatures in iron manganese alloys was independent of both composition and structure, it was also most probably controlled by the Peierls-Nabarro friction stress below 190°K. Above this temperature a different and undetermined mechanism for the control of flow stress existed.

2. Alloys containing between 4% and 10% manganese were brittle in the as quenched condition due to a weakness at prior austenite grain boundaries which became even more marked when the alloys were tempered at between 250°C and 400°C. This together with other evidence leads to the conclusion that α phase iron manganese alloys are brittle due to their susceptibility to temper brittleness.

3. Silicon was considered to be the element responsible for causing brittleness by segregating to austenite grain boundaries, although its effects may have been aggravated by the presence of carbon and/or nitrogen.

4. A $\frac{1}{2}$% molybdenum addition failed to prevent temper brittleness but one solution to the problem was to temper at 600°C. This also led unfortunately to a severe loss in the normal tensile properties which could exclude the use of these alloys as commercial high strength steels. In the medium strength field however there may be some future, especially as steels for which weldability is required.

8.0 RECOMMENDATION FOR FURTHER WORK.

Transformations.

One particular aspect requiring further work concerns what has been termed recovery assisted martensite and which was found to occur in the 4% and 6% manganese alloys. An understanding of the transformation mechanism would be aided by a more detailed study of the time, temperature, transformation behaviour, so that the kinetics of its transformation could be used to gain a better idea of the rate controlling step. Other important aspects are such features as the presence or absence of surface tilts, the relationship between growth and prior austenite grain boundaries, and crystallographic orientation relationships. The iron manganese system however does not seem to lend itself very well to this type of observations, owing to the problems of surface volatilization. An iron nickel alloy within the range 5% to 10% nickel may therefore prove to be more useful if the recovery assisted martensite reaction can be made to occur.

Properties.

Undoubtedly the major problem to be solved in the iron manganese system is that of brittleness. The present work has shown that this is likely to be due to a temper brittleness effect, but the impurity responsible has not been isolated. Further work is therefore needed not only to identify the impurity but also to determine the conditions under which its effects may be neutralized. For this purpose a further series of alloys are being prepared and consist essentially of an 8% manganese alloy with the following additions or modifications.

(i) Very low carbon high purity alloy in which special precautions have been taken to minimize both the silicon and phosphorus levels.

(ii) As above, but with an addition of 0.1% Ti to tie up interstitial elements.

(iii) Split melts of 8% manganese containing variable

(a) nitrogen
(b) carbon
(c) silicon.

By studying the effects of these impurities on the temper brittleness susceptibility of the iron manganese system, it is hoped that the source of embrittlement may be identified and an antidote found.

In addition to the above, work is already underway within the department to study the effects of molybdenum additions on the brittleness problem.

REFERENCES.

1.	J. W. Christian	Physical Properties of Martensite and Bainite ISI Spec Rep 93 1965 p1
2.	P.M.Kelly, J. Nutting.	JISI 1961 197. p199
3.	T. Homna.	J.Japan Inst.,Metals 1957 21 p126
4.	P.M.Kelly, J.Nutting	Proc.Royal Soc 1960 259A p45.
5.	C.M.Wayman, E.J.Efsic	Tran A.I.M.E. 1967, 239, p873
6.	R.L.Patterson, C.M.Wayman.	Acta Met 1966 14 p347
7.	J.A.Venables.	Phil Mag. 1962 7, p35
8.	R.H.Goodenow, R.F.Heheman.	Tran Met Soc AIME,233,p1777
9.	A.J.McEvily, R.G.Davies, C.L.Magee, T.L.Johnston,	Symposium Transformation and Hardenability in steels. University of Michigan, 1967, p179.
10.	D.Hull, R.D.Garwood.	Inst.of Metals Monograph No.18,1955 p219
11.	T.B.Massalski.	Acta Met.1958, 6, p243
12.	A.Gilbert, W.S.Owen.	Acta Met. 1962 10 p45 JISI 1960, 196, p142
13.	E.A. Wilson	Ph.D.Thesis, University of Liverpool, 1965
14.	W.S.Owen, E.A.Wilson, T.Bell.	"High Strength Materials" ed V.F. Zackay, J. Wiley & Son Inc N.Y. 1965, p167
15.	R. I. Entin.	Symposium on decomposition of austenite by diffusional processes.1962. New York Interscience, p 295
16.	J.S. Paseover. S.V.Radcliffe	Tran. Met. Soc. AIME 1968 242, p673.
17.	E.A. Wilson.	J.I.S.I. 1968. 206,164.
18.	T. BEll. W.S.Owen.	J.I.S.I. 1967, 205, p428

19.	G. Krauss.G. Marder	[illegible] Tran. AIME Quart; 1967. 60. p651
20.	G.R. Speich, H.Warlimont,	J.I.S.I. April 1968 p385
21.	T. Bell, W.S.Owen	Tran AIME 1967, 239 p1940
22	D.W.Gomersall, J.G.Parr,	J.I.S.I. March 1965, p275
23	G.R.Speich, P.Swann.	J.I.S.I. 1965, 203, p480
24.	J.W.Christian.	"The Decomposition of Austenite by Diffusional processes" 1962. New York and London (Interscience Publishers) p371
25.	H.J. Aaronson.	"The Decomposition of Austenite by Diffusional Processes" 1962 New York and London (Interscience Publishers) p387
26.	C.S. Smith	Tran. ASM 1953. 45. p533
27.	R.I. Entin.	Metalloved i Obrabotka Metall. 1956. 9. p10.
28.	C. Swanson. J.G.Parr	J.I.S.I 1964. 202.
29.	M.J.Bibby, J.G.Parr	J.I.S.I. 1964. 202. p45
30.	R.W.Cahn.	"Impurities and Imperfections" A.S.M.Cleveland, 1955, p41
31.	Erkh Rasana	PH D. thesis, University of Helsinki, 1969
32.	M. Cohen et al	"Perspectives in Materials Research" Office of Naval Research, U.S. Navy, 1961 p315
33.	G.Kurdjumov	Prob.Metall i Fiziki 1952 4
34.	H.J.Aaronson, C.Laird, K.R.Kinsman.	Scripta Met; 1968,2, p259
35.	J.W.Christian	"The Theory of Transformation in Metals and Alloys" 1965 Oxford & C (Pergamon Press)

36. A.B. Greninger. A.R.Troiano J. Metals. 1940, 1, p590

37. J.W. Christian "Martensite Fundamentals & Technology" Conf. Sheffield Polytechnic, Nov.1966, to be published.

38. A. P. Miodownik Inst. of Metals Monograph No.18 1955, p319

39. T.Ko. S.A.Cottrell J.I.S.I. 1952. 172. p307

40. M.S.Wechsler. D.S.Lieberman T.A.Read J.Appl.Phys.1955, 26, p473.

41. J.S.Bowles,J.K.Mackenzie Acta Met:1954, 2, p129.

42. B.A.Bilby,J.W.Christian. Inst.Metals Monograph, No.18, 1955, p121.

43. C. M. Wayman. "Introduction to the Crystallography of Martensitic Transformation" 1964, New York, Macmillan.

44. J.K.Mackenzie. J.Aust.Inst.Metals, 1960 5(2)p90

45. J.W.Christian "The mechanisms of Phase Transformations in Crystalline Solids" Institute of Metals Monograph, No.33, 1969, p129.

46. P.Krauklis,J.S.Bowles. Acta.Met. 1969, 17, p997.

47. R.M. Wood. Sheffield Polytechnic, private communication.

48. L. Kaufman,M.Cohen. "Progress in Metal Physics" London Pergamon, 1958, VII,p165.

49. D.G.Walker,D.W.Borland. J.Aust.Inst.Metals,1960,5,p75.

50. H.Knapp,U.Dehlinger. Acta Met. 1956, 4, p289

51 M. Cohen. Tran. AIME 1958, 212, p171

52. J.C. Fisher. Tran. AIME 1953, 197, p918.

53. F.W. Jones, W.I.Pumphrey. J.I.S.I. 163, p121.

54. L. Kaufman, M.Cohen. Tran. AIME, 1956, 206, p1393

55. L. Kaufman. "Physical properties of Martensite & Bainite" ISI Spec.Rep. 93, 1965, p48.

56. L. Kaufman — Acta.Met. 1959, 7, p575.

57. T. Boniszewski. — "Physical properties of Martensite & Bainite" ISI Spec. Rep. 93, 1965, p69.

58. R.G. Bryans, T. Bell, V.M. Thomas. — "The mechanisms of Phase Transformations in Crystalline Solids" Inst of Metals Monograph, No.33, 1969, p181.

59. T. Homna. — J.Japan. Inst. Metals, 1957, p122

60. B.R. Bannerjee, J.J.Hauser J.M. Capenos. — Met. Sci.Journ. 1968, 2, p76

61. C. M. Wayman, G.J.Altstetter — Acta.Met. 1962, 10, p992,

62. W.S. Owen, E.A. Wilson. — "Physical properties of Martensite and Bainite" ISI Spec.Rep. 93, 1965, p53.

63. J. A. Klostermann — Acta Met. 1964, 12, p355.

64. R. D. Garwood, — "Martensite Fundamentals and Technology" Conf. Sheffield Polytechnic, Nov.1966, to be published.

65. R. F. Mehl, G.Derge. — Tran. ASM, 1937, p482.

66. R. F. Mehl, D.W.Smith — Tran. ASM, 1934, p203.

67. R. B. Yeo — Tran AIME, 1962, 224, p1222.

68. P. McDougall — "Physical properties of Martensite and Bainite" ISI Spec. Rep. 93, 1965, p164.

69. J. Dash, H.M.Otte. — Acta Met. 1963, 11, p1169

70. R. Lagneborg. — Acta Met. 1964, 12, p823.

✓71. P.M. Kelly. — "High Alloy Steels" ISI Spec. Rep.86, 1964, p146.

72. M.G.A. Biswas, I.Codd. — J.I.S.I. 1968, 206(5) p494.

73. P.M. Kelly. — Acta Met. 1965, 13, p239.

74. H.M. Otte. — Acta Met. 1967, 15, p1082.

75. A.G.Crocker. — Acta Met. 1962, 10, p113.

76. A.B. Greninger. Tran. A.S.M. 1942, 30, p1.

77. R. B. Yeo. Tran. A.S.M. 1964, 57, p48.

78. Z. Nishiyama. Sci.Rep., Tohuku Imp.Univ. 1935, 23, p637.

79. C.M.Wayman "Physical properties of Martensite and Bainite" ISI Spec.Rep. 93, 1965, p153.

80. P.M. Kelly. "High Strength Steels" ISI. Spec. Rep. 86, 1964, p151.

81. W. Charnock, J.Nutting. Met. Sci. Journ. 1967, 1, p123

82. C.M. Zener Tran. AIME 1946, 167, p550.

83. H.G. Bowden, P.M.Kelly. Acta Met. 1967, 15, p1489.

84. A.H.Cottrell, B.A.Bilby. Phil Mag. 1951, 42, p573.

85. J. G. Parr. J.I.S.I. 1952, 171(2), p137.

86. B. Cina Acta Met. 1958, 6, p748.

87. C. H. White, R.W.K. Honeycombe. J.I.S.I. 1962, 200(6) p457.

88. H. Schumann Arch Eisen, 1967, 38, p647.

89. A. R. Troiano, F.T.McGuire Tran A.S.M. 1943, 31, p340.

90. F.M. Walters, C. Wells. Tran. A.S.M. 1935, 23, p727.

91. F.G. wilson. United Steels (Swinden Labs) Report No PM 5055/12/66, 1966.

92. W. Steven "High Alloy Steels" ISI Spec. Rep. 86, 1964, p115.

93. W.P. Rees, B.E.Hopkins, H. R. Tipler J.I.S.I. 1951, 169, p157.

94. E.C. Bain. "Function of Alloying Elements in Steel" Cleveland ASM, 1939. p65.

95. F. M. Walters, J.R.Kramer, R.M. Loring. Tran. AIME, 1942, 150, p401.

96. R. Hadfield. J.I.S.I. 1927, 115, p297.

97. W. P. Rees, B.E.Hopkins, H.R. Tipler. J.I.S.I. 1954, 177, p93.

98. A.S.Nicochenko. Phy. Met. Metallog; 1963, 16, No.5, p122.

99. T. Boniszewski. Brt. Weld. Journ: 1965, 12, p349

100. S. Floreen, G.R.Speich. Tran. A.S.M. 1964, 57, p714.

101 W. Patterson. Tran. A.S.M. 1966, 59, p71.

102. J. Nutting. "High Strength Steels" ISI Spec.Rep.86, 1964, p161.

103. E. Orowan. Repts.Prog.Phys., 1948, 12, p185

104. A.H.Cottrell. Tran. Met. Soc. AIME, 1958, 212, p192.

105. N. J. Petch. J.I.S.I. 1953, 174, p25.

106. H. Conrad. "High Strength Materials" ed. V.F. Zackay, J.Wiley & Son Inc. N.Y. 1965, p436.

107. M.J.Roberts, W.S.Owen. Tran.AIME Quart; 1967, 60, p687.

108. N.F. Mott, F.R.N. Nabarro. "Strength of Solids" Phy.Soc. London, 1948.

109. M.J.Roberts, W.S.Owen. J.I.S.I. 1968, 206, p375.

110. J.M. Chilton, P.M.Kelly, Acta Met. 1968, 16, p637.

111. P.M. Kelly, J. Nutting. "Physical properties of Martensite and Bainite" ISI Spec. Rep.93, 1965, p166.

112. A.H. Cottrell "Dislocations and Plastic Flow in Crystals" Oxford Univ.Press 1953.

113. M. J. Whelan. J.I.M. 1958, 87, p409.

114. P.B. Hirsh. Phil.Mag; 1962, 7, p67.

115. B.L. Mordike, P.Haasen. Phil.Mag; 1962, 7, p459.

116. A. Seeger. Phil. Mag; 1956, 1, p651.

117. J. E. Dorn, S.Rajnak. Tran. Met. Soc. AIME, 1964, 230, p1052.

118. R.J. Arsenault Acta Met. 1967, 15, p501.

119. A. Sleeswyk Acta Met. 1963, 11, p187.

120. R.J. Arsenault — Acta Met, 1964, 12, p547.

121. G. Sargeant. — Acta Met. 1965, 13, p663.

122. N.S. Stoloff, R.G. Davies. R. C. Ku. — Tran. Met. Soc. AIME, 1965, 233, p1500.

123. R. G. Davies, R.C.Ku. — Tran. Met. Soc. AIME, 1966, 236, p1691.

124. A. J. McEvily, R.C.Ku, T.L. Johnston. — Tran. Met. Soc. AIME, 1966, 236, p108.

125. H.H. Kranzlein, M.C.Burton. — Tran. Met. Soc. AIME, 1965, 233, p64.

126. J. Weertmen, J.R.Weertmen. — "Elementary Dislocation Theory" Macmillan New York, 1964, p159.

127. J.D. Embury, A.S.Keh, R.M. Fisher. — Tran Met. Soc. AIME, 1966, 236, p1252.

128. W.C. Leslie, R.J. Sober. — Tran. Quart. ASM, 1967, 60, p459

129. S. Floreen. — Tran. Met. Soc. AIME, 1964, 230, p842.

130. S. Floreen. — Tran. Met. Soc. AIME, 1966, 236, p1429.

131. N. J. Petch. — Phil. Mag. 1957, 2, p649.

132. J. Harding. — Acta Met. 1969, 117, p949.

133. D.V. Wilson, B.Russell. — Acta Met. 1959, 7, p628.

134. A.H. Cottrell — "Dislocations and Plastic Flow in Crystals" Oxford Univ;Press, 1953.

135. G. T. Hahn. — Acta. Met. 1962, 10, p727.

136. A. A. Johnson. — Phil. Mag. 1961, p177.

137. R. Armstrong, I. Codd, R.M. Douthwaite, N.J. Petch. — Phil. Mag. 1962, p45.

138. A.N. Stroh. — Adv in Phys; 1957, 6, p418.

139. A. Wirth. — Sheffield Polytechnic, private communication.

140. G. Davy. — J.I.S.I. 1966, 204, p1144.

141. S. R. Keown, F.B. Pickering J.I.S.I. 1962, 200, p757.

142. D.G. Brandon, J. Nutting. Brt. J. Appl. Phys; 1959, 10, p275.

143. E.T. Wessel, R.D. Olleman. Sci. Paper 1664, Westinghouse.

144. A. Gilbert. Ph.D Thesis, University of Liverpool, 1960.

145. L.S. Darken, R.W. Gurry. "Physical Chemistry of Metals" McGraw Hill, 1953, p397.

146. D. Orr, S. Chipman. Tran. AIME, 1967, 237, p201.

147. A. Hellawell. Inst of Metals. Annotated Equilibrium Diagram No.26, 1956.

148. J. Gordon Parr. Met. Trtmnt. Drop Forging, March 1953, p139.

149. M. Hillert, T. Wada, H. Wada. J.I.S.I. 1967, 205, p539.

150. J. D. Bolton, E. R. Petty, G. Allen. J.I.S.I. 1969, 207, p1314.

151. B. R. Bannerjee. J.I.S.I. 1965, 203, p166.

152. C. J. MacMahon, M. Cohen. Acta Met. 1965, 13, p591.

153. C. J. MacMahon. ASTM. STP 407, 1968, p127.

154. B.S. Lement, B.L. Averbach, M. Cohen. Tran. ASM 1954, 46, p851.

155. J. M. Capus, G. Mayer. Metallurgia, 1960, 62, p133.

156. W. Steven, K. Balajiva. J.I.S.I. 1959, 193, p141.

157. A. Preece, R. D. Carter. J.I.S.I. 1953, 173, p387.

158. P.L. Gruzin. V.V. Minal. Fizika Metallov i Metallovedenie 1964, 17, p62.

159. J. M. Capus. "Temper Embrittlement in Steel" ASTM.STP 407, 1968, p3.

160. D. Squires. Sheffield Polytechnic, to be published.

161. G. C. Gould. "Temper Embrittlement in Steels" ASTM.STP 407, p90.

162.	P. Wynblatt, J.E. Dorn.	Tran Met. Soc. AIME, 1966, 236, p1451.
163.	P. Wynblatt, A. Rosen, J. E. Dorn.	Tran Met. Soc. AIME, 1965, 233, p651.
164.	P. Feltham.	Phil Mag. 1961, 6, p847.
165.	D. Hull.	Acta Met. 1960, 8, p11.
166.	W. C. Leslie.	"Iron and its Dilute Solutions" New York, 1963, p119,
167.	P. M. Kelly	

TABLE I

Analysis Results.

Alloy	C	N	Si	P	S	Mn	Ni Cr	Mo
Air Melt 1	0.02		0.03	0.002	0.008	1.85		
" " 2	0.012	0.0104	0.06	0.004	0.009	3.78	0.02	0.01
" " 3	0.015	0.011	0.105	0.004	0.007	5.8	0.02	0.01
" " 4	0.011	0.014	0.09	0.003	0.010	7.55	0.02	0.01
" " 5	0.010	0.009	0.09	0.005	0.009	9.9	0.02	0.01
Vac Melt 1	0.004	-	0.021	0.002	-	9.2	-	-
" " 2	0.004	-	0.017	0.004	-	8.35	0	0.48

TABLE II

Typical room temperature tensile data for iron manganese alloys

Manganese %	Heat Treatment	Limit of Proportionality		1% Flow Stress		U.T.S.		Reduction in area %	Elongation %
		kg/mm^2	MN/m^2	kg/mm^2	MN/m^2	kg/mm^2	MN/m^2		
2%	Air cooled 1000°C 1 hr	18.5	181.5	-	-	33	323.7	-	35
	Brine quenched 1000°C 1 hr	45	441.5	50	490.5	53	520	65	22
4%	Air cooled 1000°C 1 hr	49.6	486.6	59.7	585.6	65.2	639.6	65	26
	Brine quenched 1000°C 1 hr	71	696.5	80	784.8	81	794.6	68	22
6%	Air cooled 1000°C 1 hr	55	539.5	71	696.5	74.5	730.8	66	25
	Brine quenched 1000°C 1 hr	66	647.5	76	745.5	78	765	69	22
8%	Brine quenched 1000°C 1 hr	73	717.2	87	853.5	91	892.7	63	22
10%	Brine quenched 1000°C 1 hr	62	608.2	83	814.2	89.5	878	65	22

TABLE III

Data for the free energy $\Delta G_{Fe}^{\alpha-\gamma}$ for the $\alpha \rightarrow \gamma$ transformation in iron, and the equilibrium solubilities of manganese in iron.

T °K	$\Delta G_{Fe}^{\alpha-\gamma}$ 53 cal/mole	$\Delta G_{Fe}^{\alpha-\gamma}$ 143 cal/mole	$\Delta G_{Fe}^{\alpha-\gamma}$ 144 cal/mole	$\Delta G_{Fe}^{\alpha-\gamma}$ 145 cal/mole	$\Delta G_{Fe}^{\alpha-\gamma}$ 52 cal/mole	$x_{M\alpha}$ a/o Mn	$x_{M\gamma}$ a/o Mn
1400			-82.2				
1200			10				
1000	112	75	76	81	154	0.023	0.094
900	194	180	188	191	220	0.030	0.143
800	309	320	327	333	293	0.034	0.205
700	441		504	497	385	0.035	0.280
600	590		690	677	456	0.035	0.360
500	738		885	870	504	0.035	0.440
400	879		1080				

TABLE IV.

Data for the solution of $\Delta G^{\alpha-\gamma}$
by a regular solution model

T^oK	$T(1-\ln T)$	$RT\ln\frac{1-x_{A\gamma}}{1-x_{A\alpha}}$	B Calculated	B Graphical Solution
1000	-5908	-151	7927	-500
900	-5230	-221.5	1491	-750
800	-4590	-510	-548	-1000
700	-3890	-407	-1302	-1302
600	-3240	-490	-1444	-1444
500	-2610	-541	-1698	-1698

TABLE V.

Data for the free energy $\Delta G^{\alpha-\gamma}$ for the transformation in manganese

$\Delta G^{\alpha-\gamma}_{Mn}$ cals/mole	-900	-2000	-2700	-3200	-3600	-3850	-4000
T^oK	1200	1000	900	800	700	600	500

TABLE VI.

Data for B-A, used in determining $\Delta G^{\alpha-\gamma}$ via a regular solution model.

$T^{\circ}K$	T(1-lnT)	B - A	Graph: Soln: B-A
1000	-5908	-10,180	-2850
900	-5230	-3888	-2550
800	-4590	-2242	-2240
700	-3890	-1967	-1967
600	-3240	-1724	-1724
500	-2610	-1417	-1417
400	-1995	-1100	-1100

FIG. 1: Massive ferrite in a quenched Fe - 4.0% Cu alloy.[17]

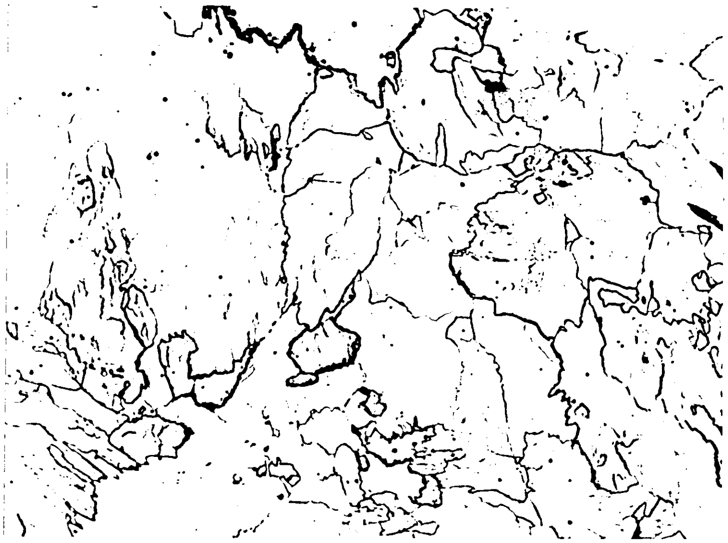

FIG.2: Schematic illustration of sympathetic nucleation of massive ferrite at prior austenite grain boundaries which creates an illusion of growth across the grain boundary.

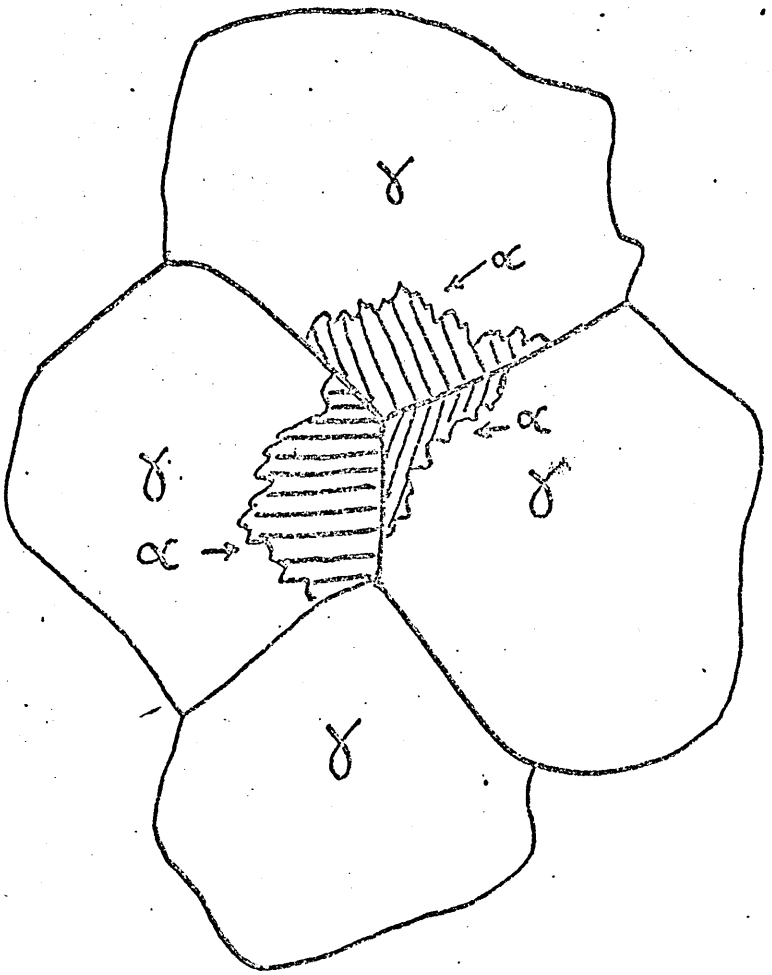
γ
← α
γ
← α
γ
α →
γ

FIG. 3: Ledge boundary showing the advance of a coherent interface via the movement of an incoherent ledge in a direction perpendicular to the main direction of advance

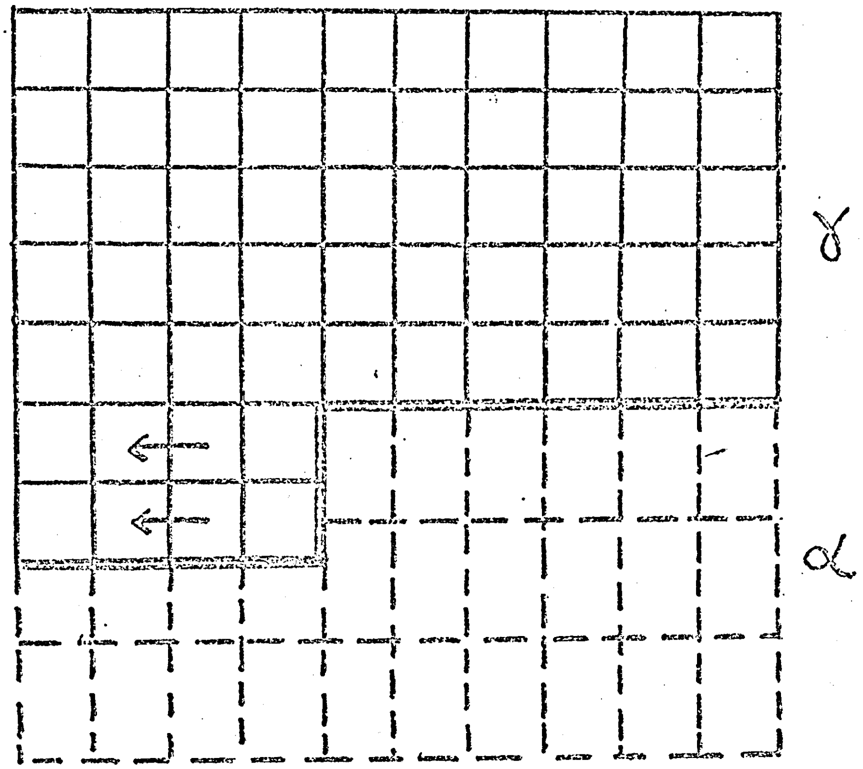
γ
α

FIG.4: Various forms of an invariant plane strain, only the last, i.e. shear + dilatation, is capable of producing a martensitic transformation

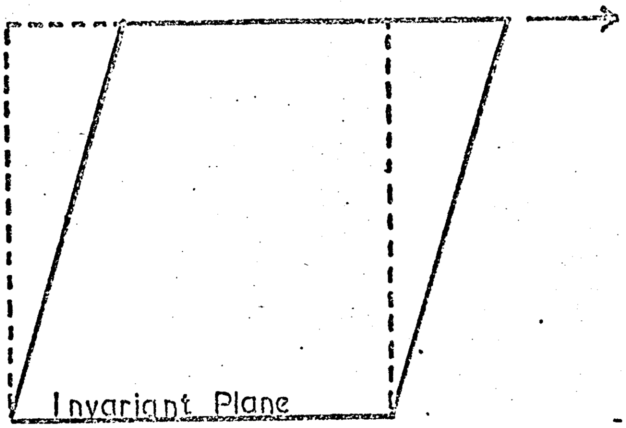
Invariant Plane

SIMPLE SHEAR

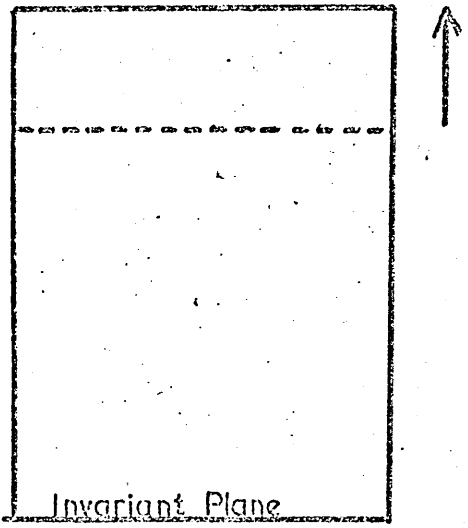
Invariant Plane

PURE DILATATION

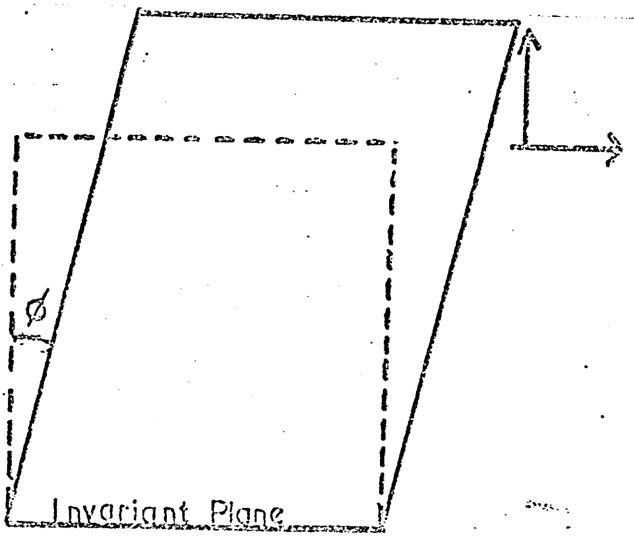
ø
Invariant Plane

SHEAR + DILATATION

FIG. 5: The Bain correspondence for the austenite-martensite transformation in ferrous alloys.

FIG. 6: Strain representation of the Bain strain in which the unit sphere is distorted to the strain ellipsoid by the three principal Bain strains. The cones of vectors OA' OB' OC' OD' are undistorted by the Bain strain but are rotated from their initial positions OA OB OC OD

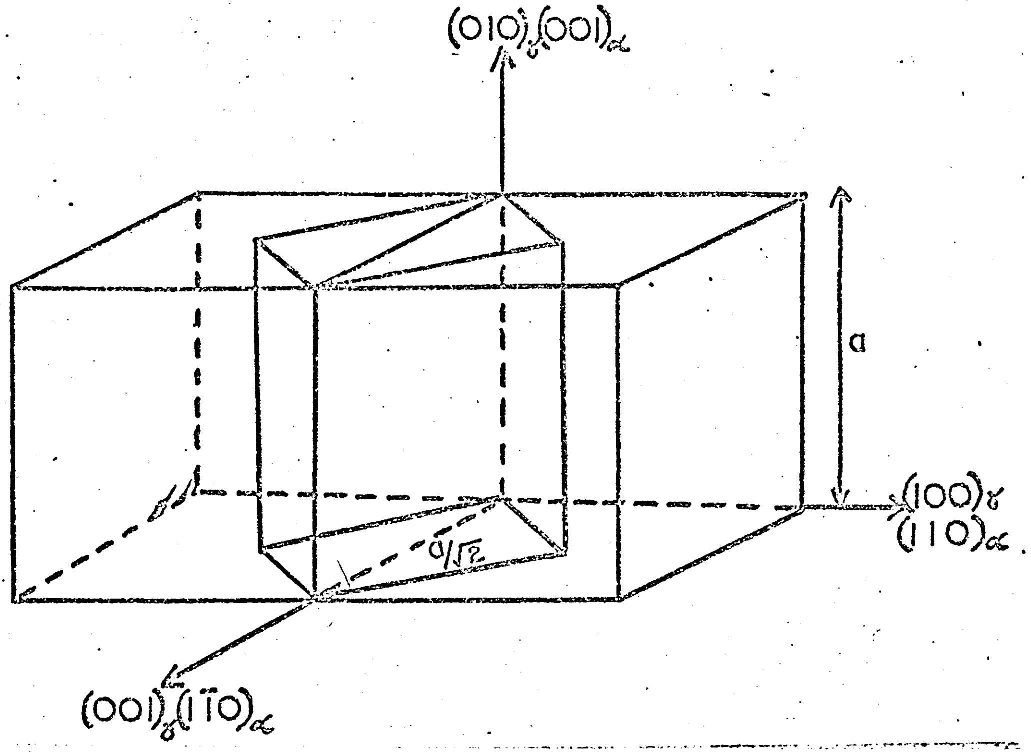
$(010)_\gamma (001)_\alpha$
a
$(100)_\gamma$
$(110)_\alpha$
$a/\sqrt{2}$
$(001)_\gamma (1\bar{1}0)_\alpha$

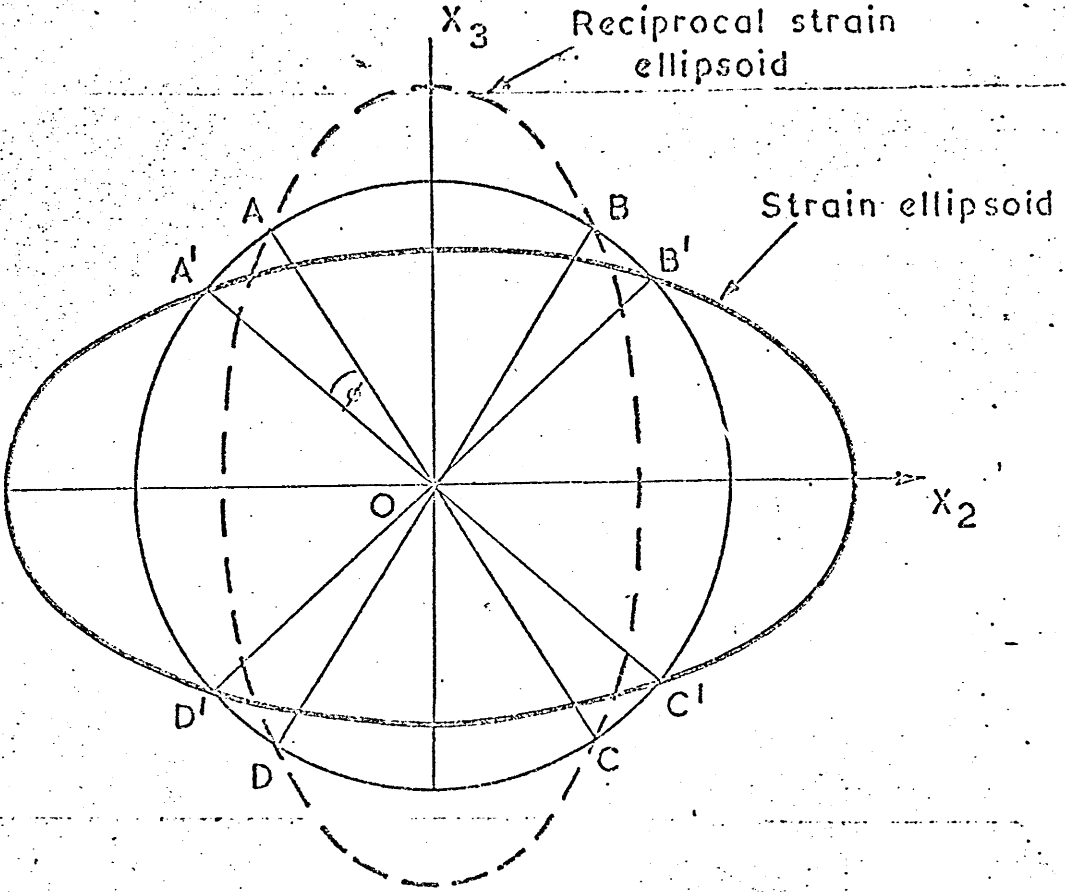
X_3
Reciprocal strain ellipsoid
A
B
Strain ellipsoid
A'
B'
ϕ
O
X_2
D'
C'
D
C

FIG. 7: Strain representation of a twinning shear showing the two undistorted planes, K_1 and K_2, and also showing the shortening or lengthening of other vectors which do not lie in either of these two planes.

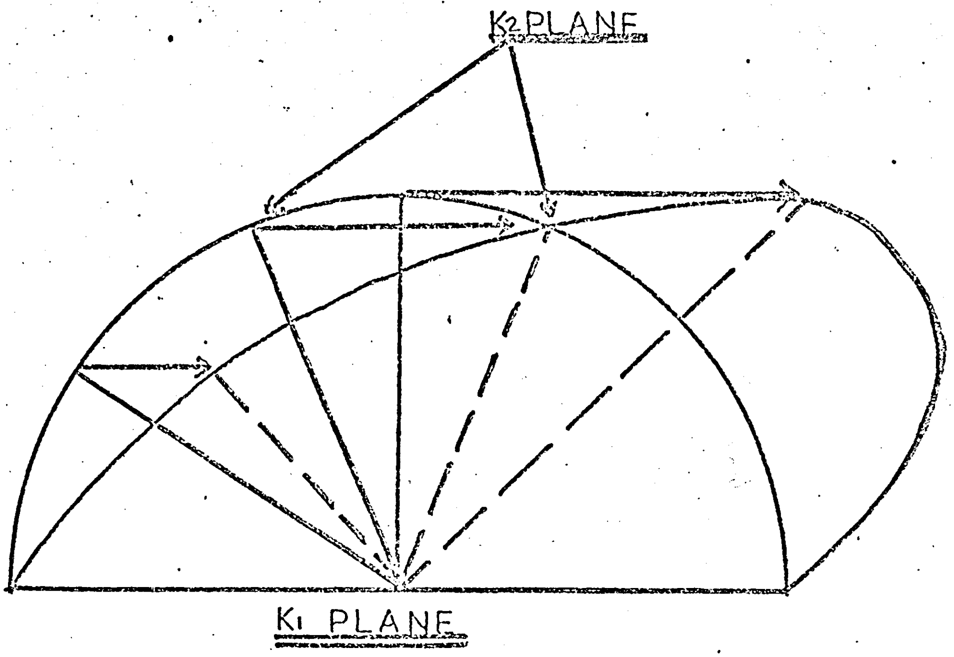
K2 PLANE
K1 PLANE

FIG. 8: Free energy versus composition curves for austenite and ferrite showing the equilibrium condition by which the partial molar free energies $\bar{G}$ are equal in both phases.

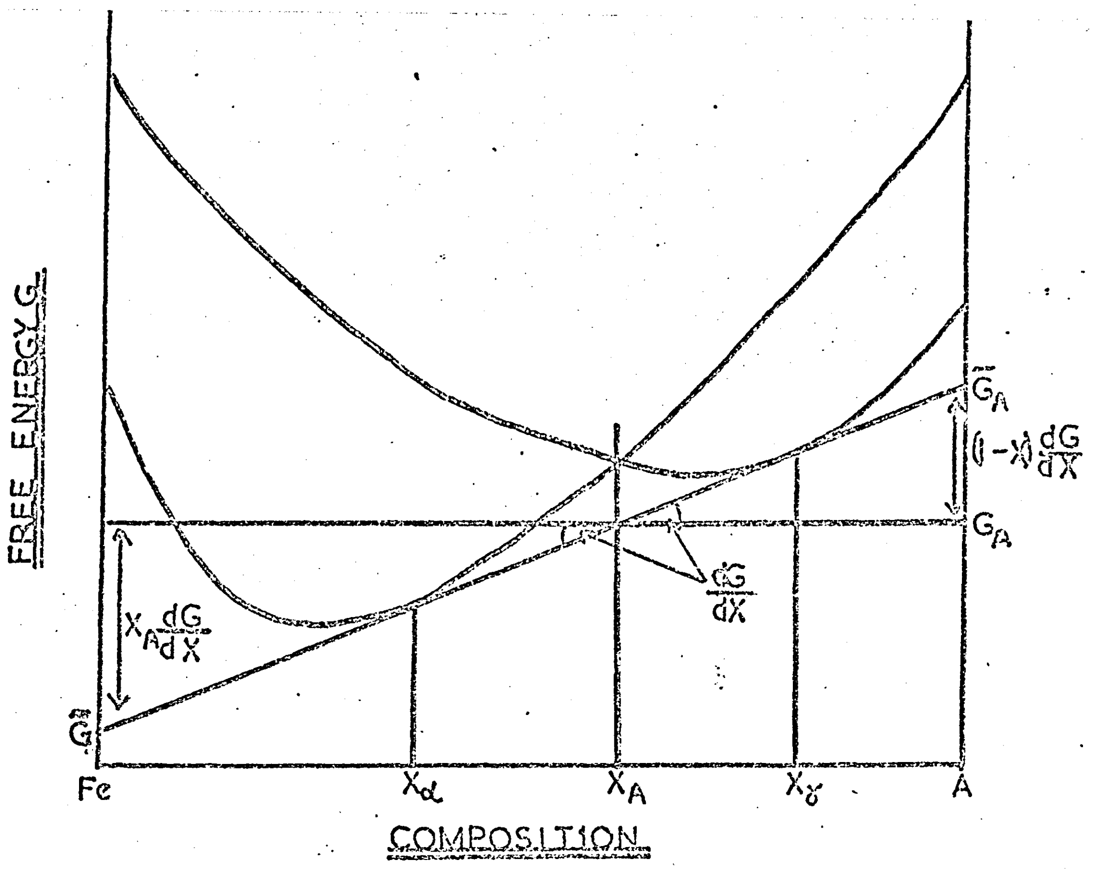
FREE ENERGY G
$\bar{G}_A$
$(1-X_A)\frac{dG}{dX}$
G_A
$\frac{dG}{dX}$
$X_A\frac{dG}{dX}$
$\bar{G}$
Fe
X_α
X_A
X_γ
A
COMPOSITION

FIG.9: Lath martensite in a drastically quenched Fe - 4% Cu alloy.[17]

FIG. 10: Lath substructure within slabs, revealed by etching in sodium bisulphite plus sodium thiosulphate.[88] Fe - 6% Mn alloy

x 500

FIG.11: Slip relief at a martensite/austenite interface.

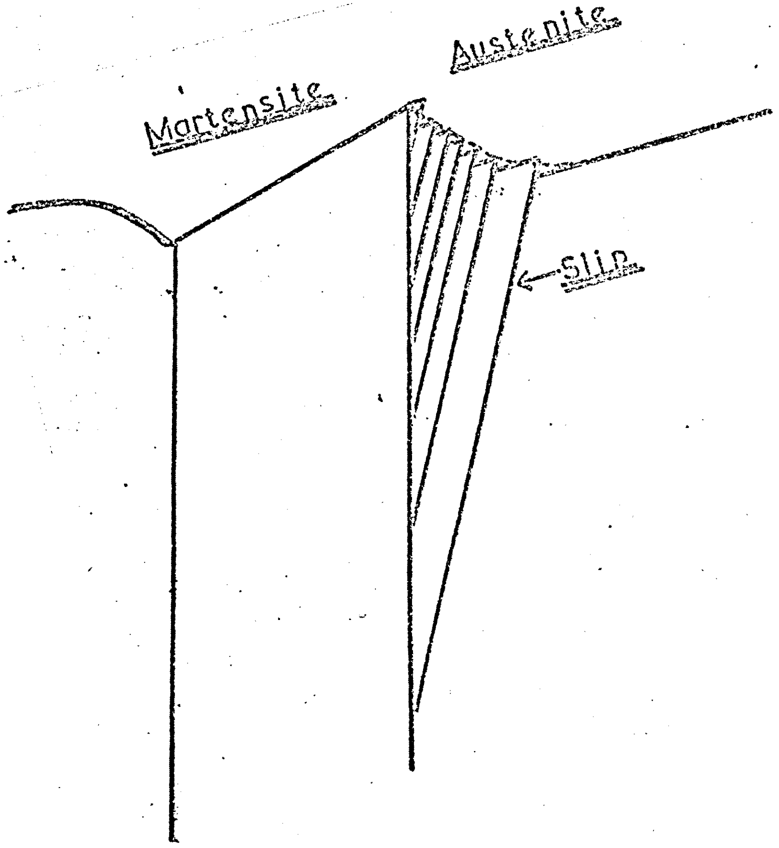
Martensite
Austenite
Slip

FIG. 12: M_S temperature data for iron nickel alloys showing the extrapolation of M_S to either 560°C or 750°C in pure iron.

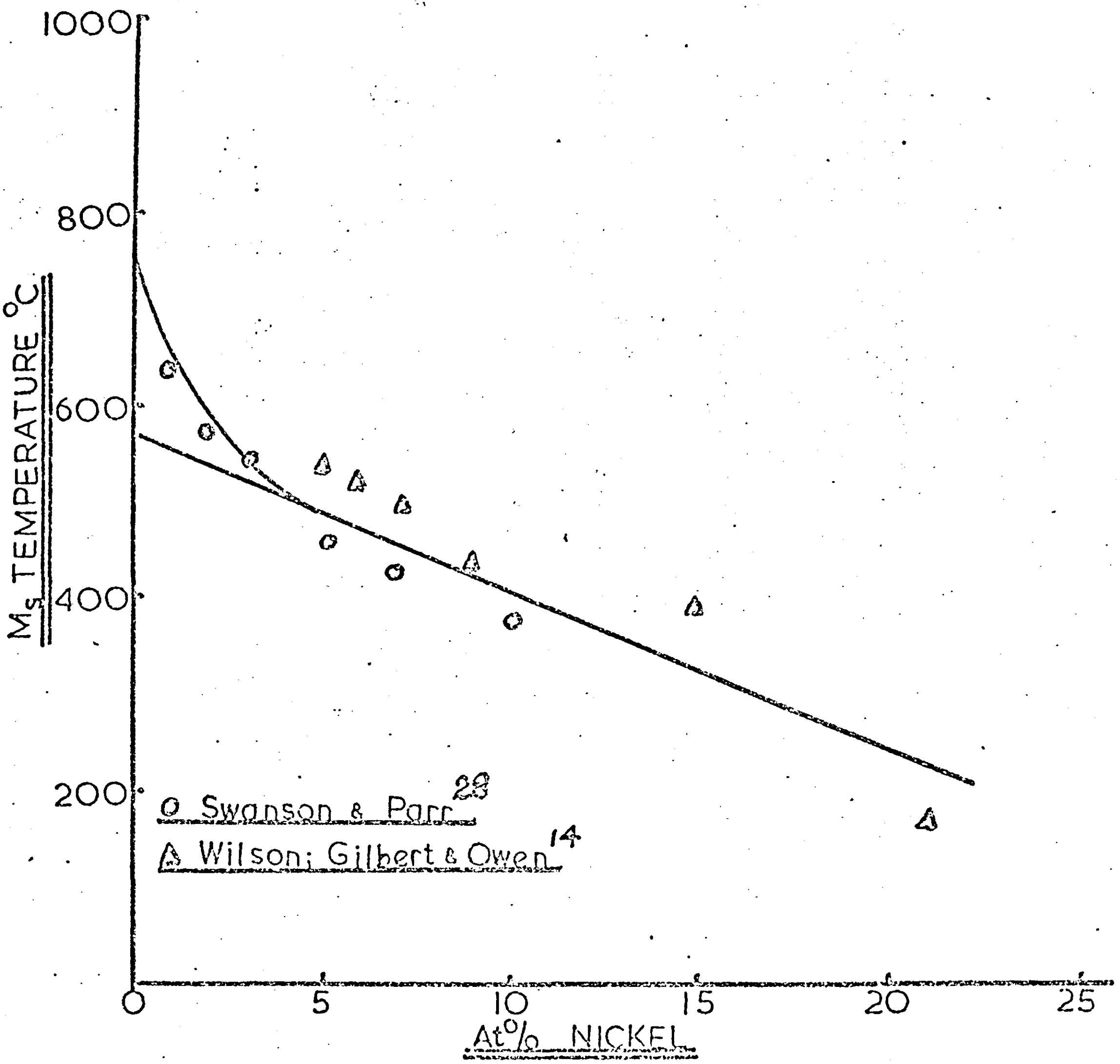
1000
800
600
400
200
0
5
10
15
20
25
M_s TEMPERATURE °C
At% NICKEL
o Swanson & Parr[28]
△ Wilson; Gilbert & Owen[14]

FIG. 13: Driving force for the $\gamma \rightarrow \alpha$ transformation in various iron alloys.[14.21.]

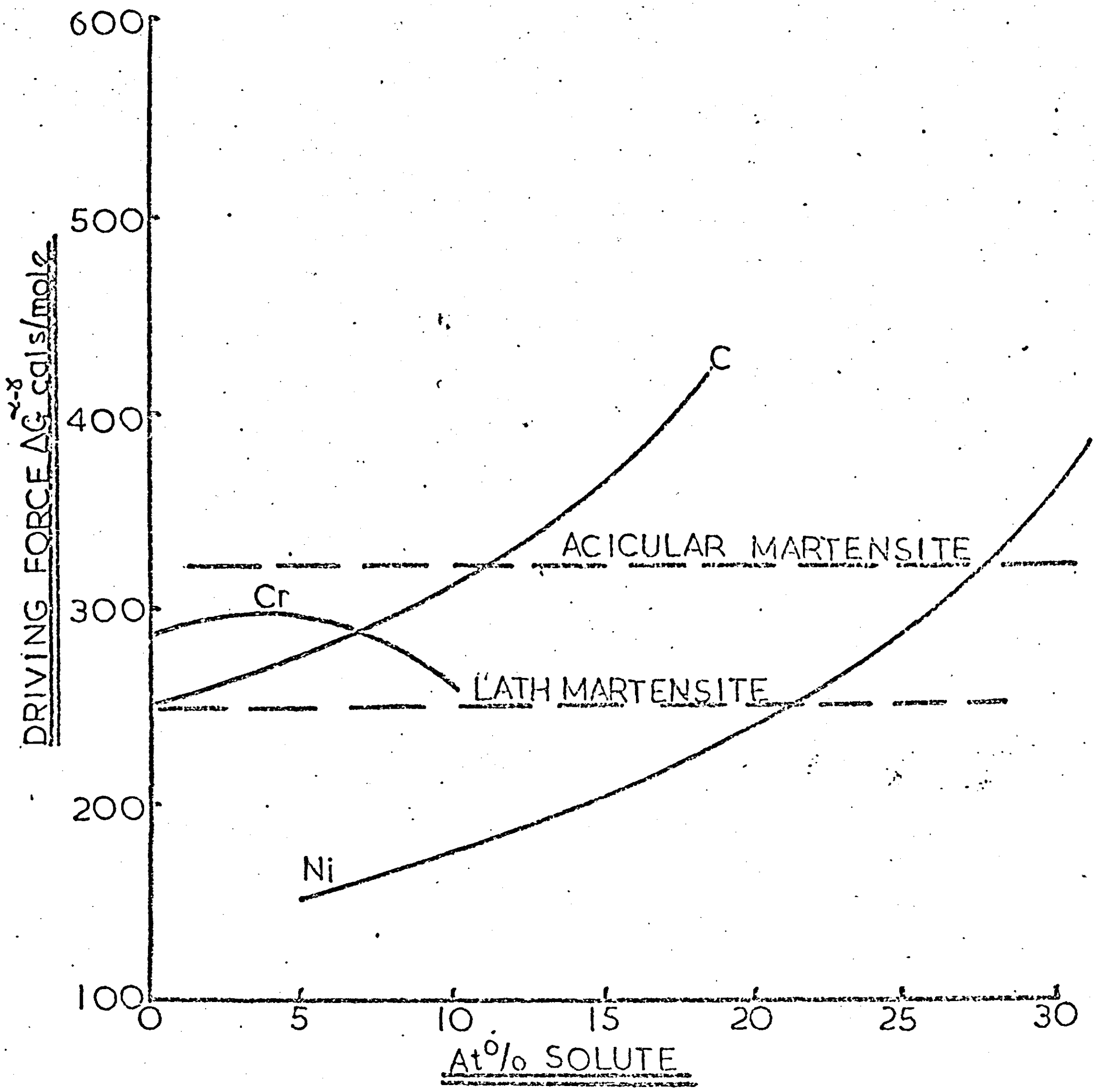

600
500
400
300
200
100
DRIVING FORCE $\Delta G^{\alpha-\gamma}$ cals/mole
C
Cr
Ni
ACICULAR MARTENSITE
LATH MARTENSITE
0
5
10
15
20
25
30
At% SOLUTE

FIG. 14: The effect of cooling rate and alloy composition on the massive ferrite to lath martensite transition in iron nickel alloys.[28]

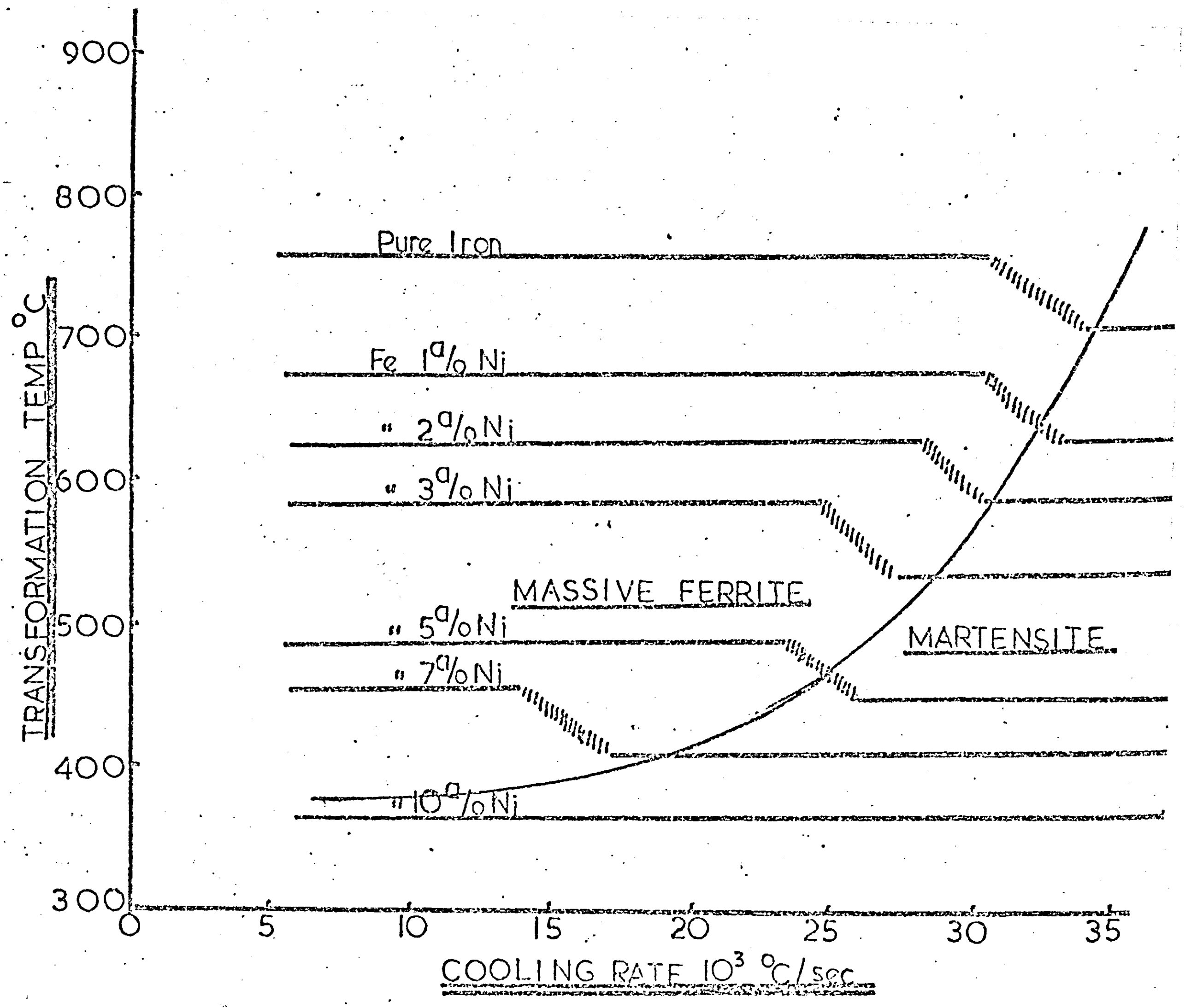

TRANSFORMATION TEMP °C
900
800
700
600
500
400
300
Pure Iron
Fe 1% Ni
" 2% Ni
" 3% Ni
MASSIVE FERRITE
" 5% Ni
" 7% Ni
MARTENSITE
" 10% Ni
0
5
10
15
20
25
30
35
COOLING RATE 10³ °C/sec

FIG.15: The transition from body centred cubic to body centred tetragonal martensite due to the influence of carbon upon the M_s temperature and the Zener order disorder temperature.[21]

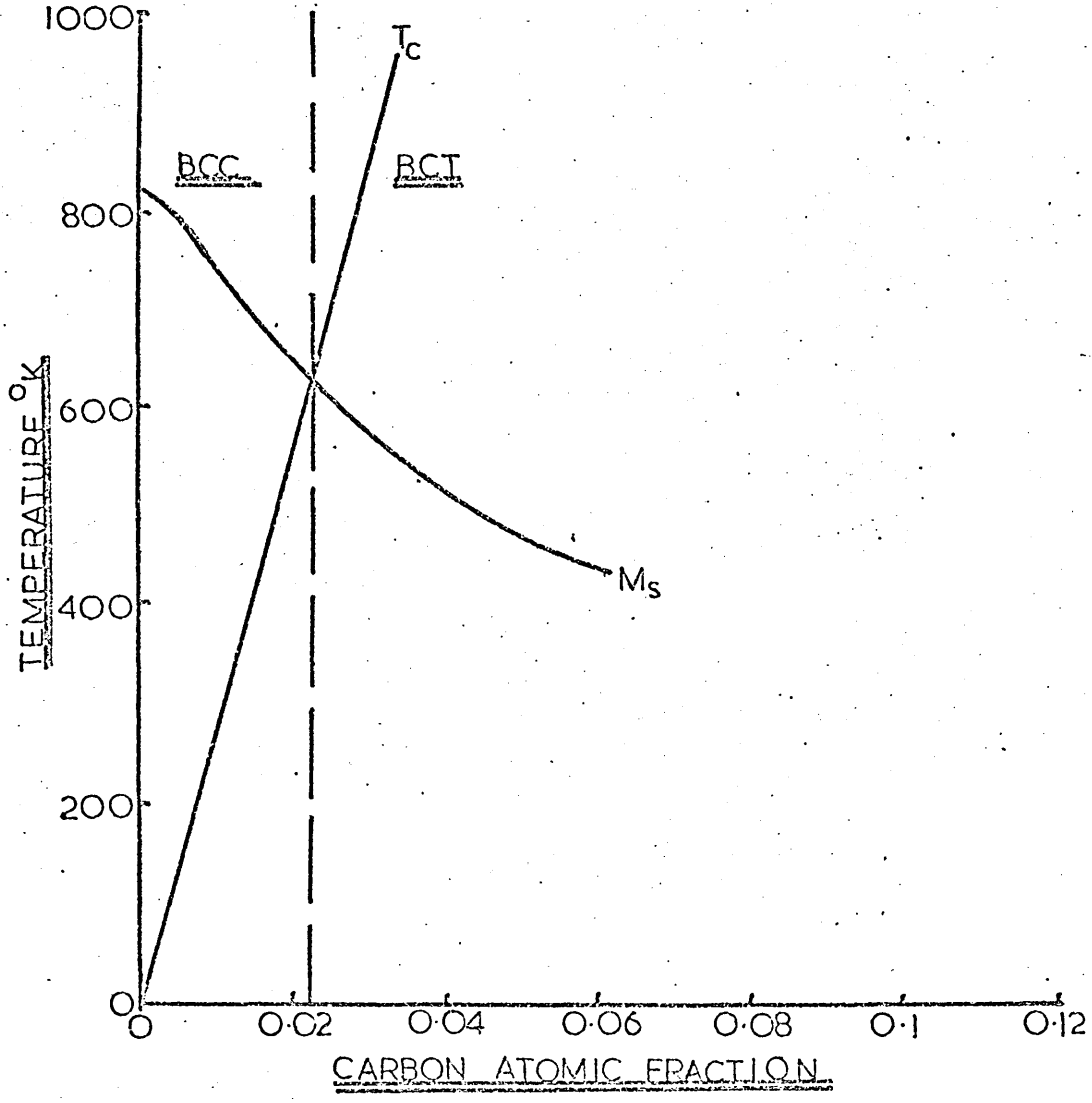
1000
800
600
400
200
0
TEMPERATURE °K
BCC
BCT
T_c
M_s
0
0·02
0·04
0·06
0·08
0·1
0·12
CARBON ATOMIC FRACTION

FIG. 16: Iron manganese equilibrium diagram; also showing the non equilibrium α and ε martensitic transformation temperatures.[89]

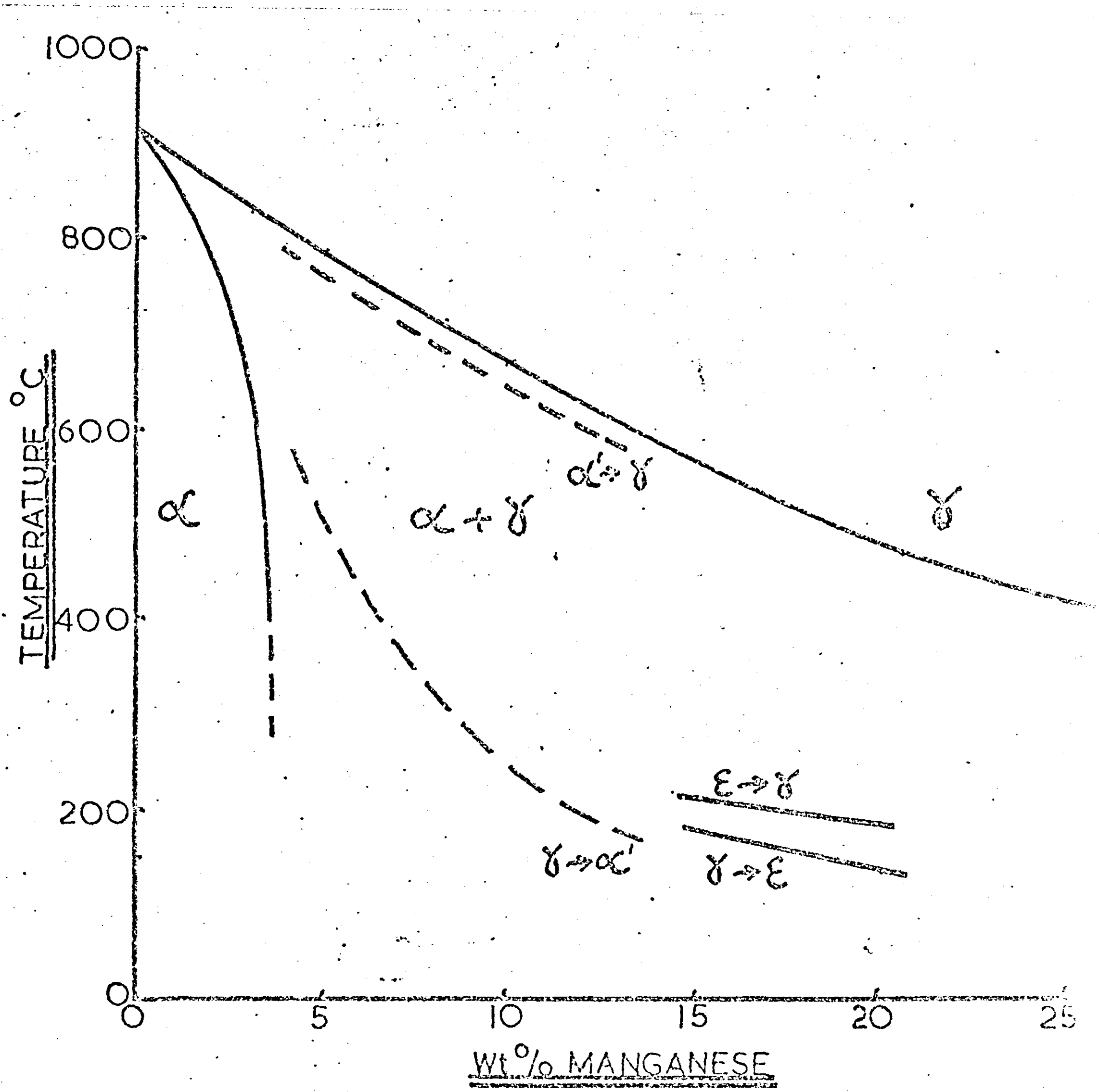

1000
800
600
400
200
0
TEMPERATURE °C
α
α + γ
α' → γ
γ
ε → γ
γ → ε
γ → α'
0
5
10
15
20
25
Wt % MANGANESE

FIG. 17: Effects of composition on the proportions of α, ε, and γ at room temperature in iron manganese alloys.[38]

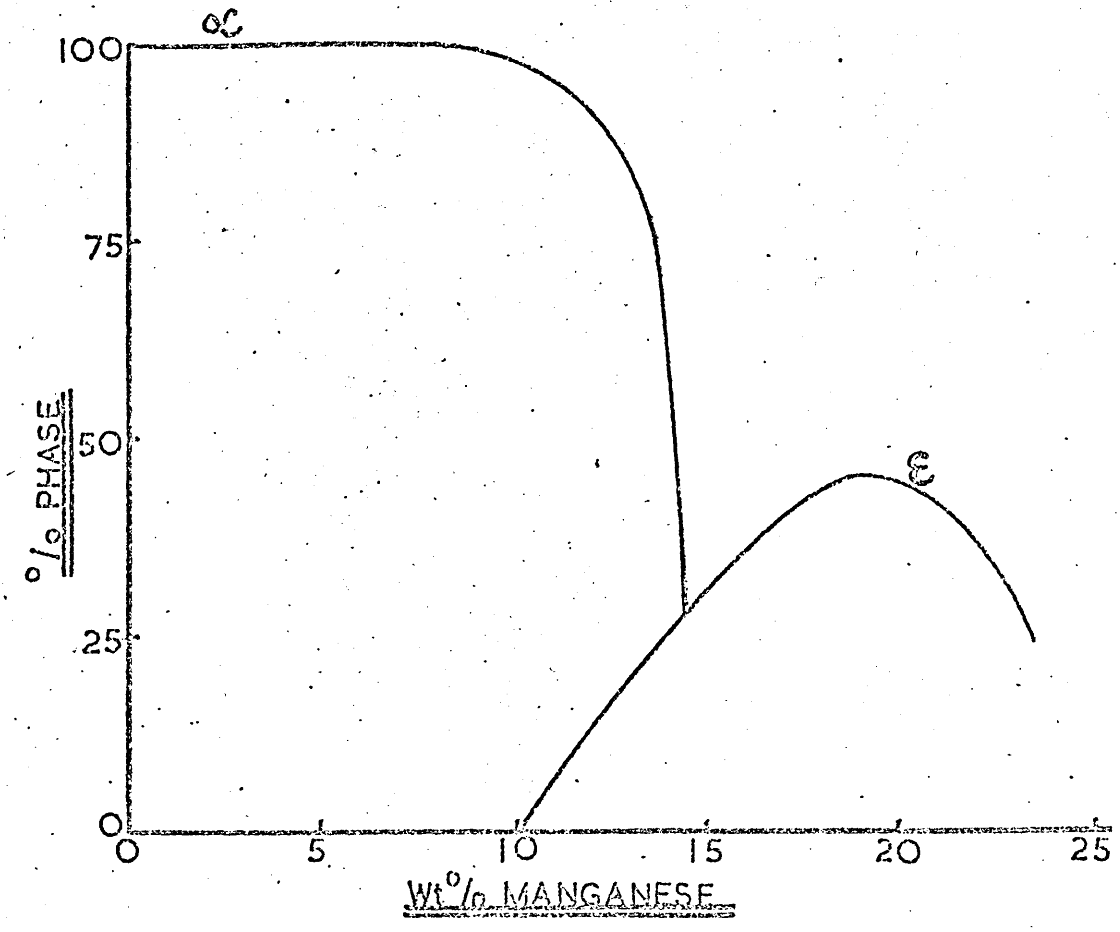

α
ε
100
75
50
25
0
% PHASE
0
5
10
15
20
25
Wt% MANGANESE

FIG. 18: Effects of manganese concentration on the $\gamma \rightarrow \alpha$ transformation temperatures in iron manganese alloys.

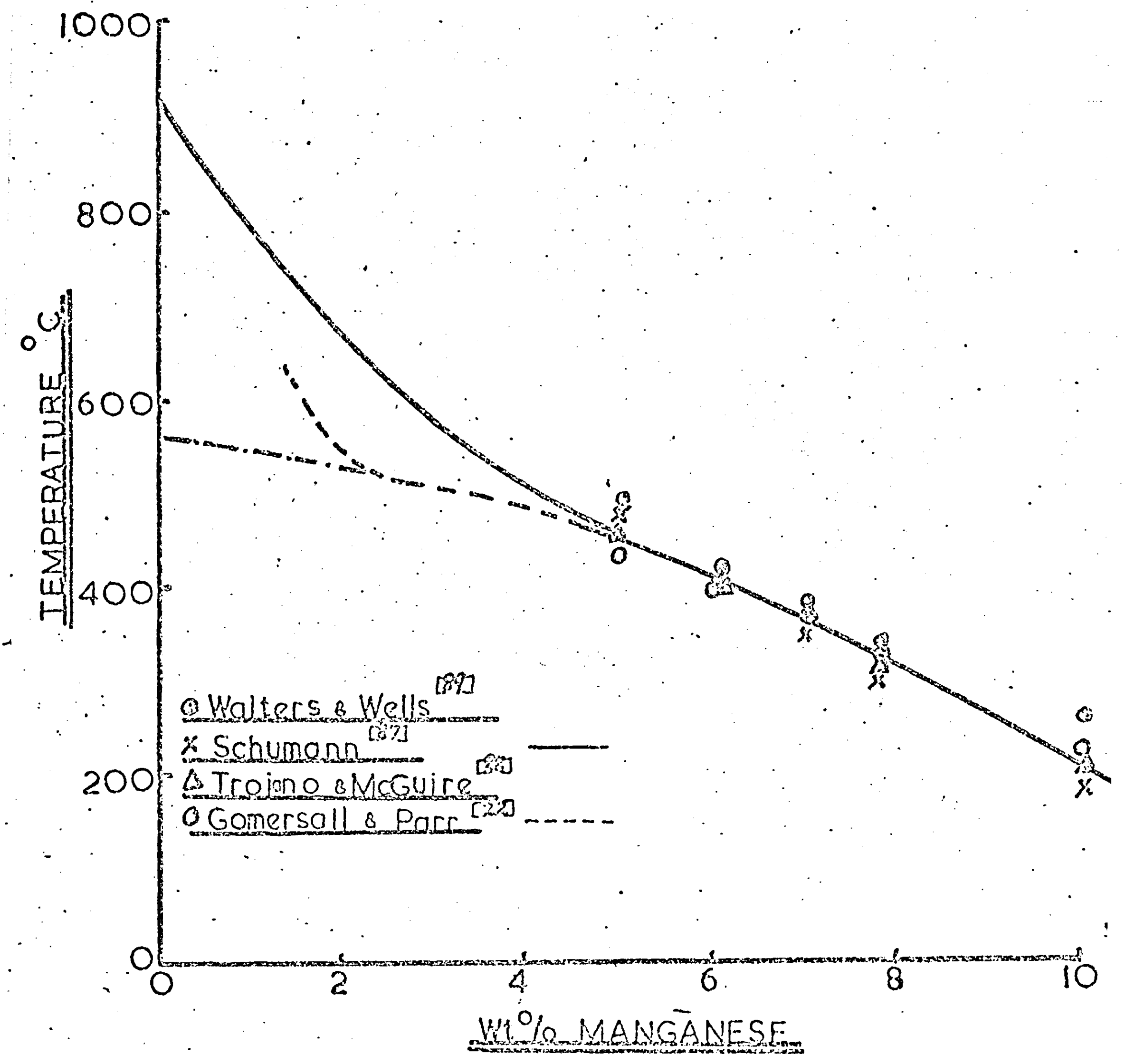

1000
800
600
400
200
0
TEMPERATURE °C
0
2
4
6
8
10
Wt% MANGANESE
⊙ Walters & Wells [89]
× Schumann [87]
△ Troiano & McGuire [88]
O Gomersall & Parr [22]

FIG. 19: The variation in yield stress with manganese concentration and heat treatment for iron manganese alloys. 95

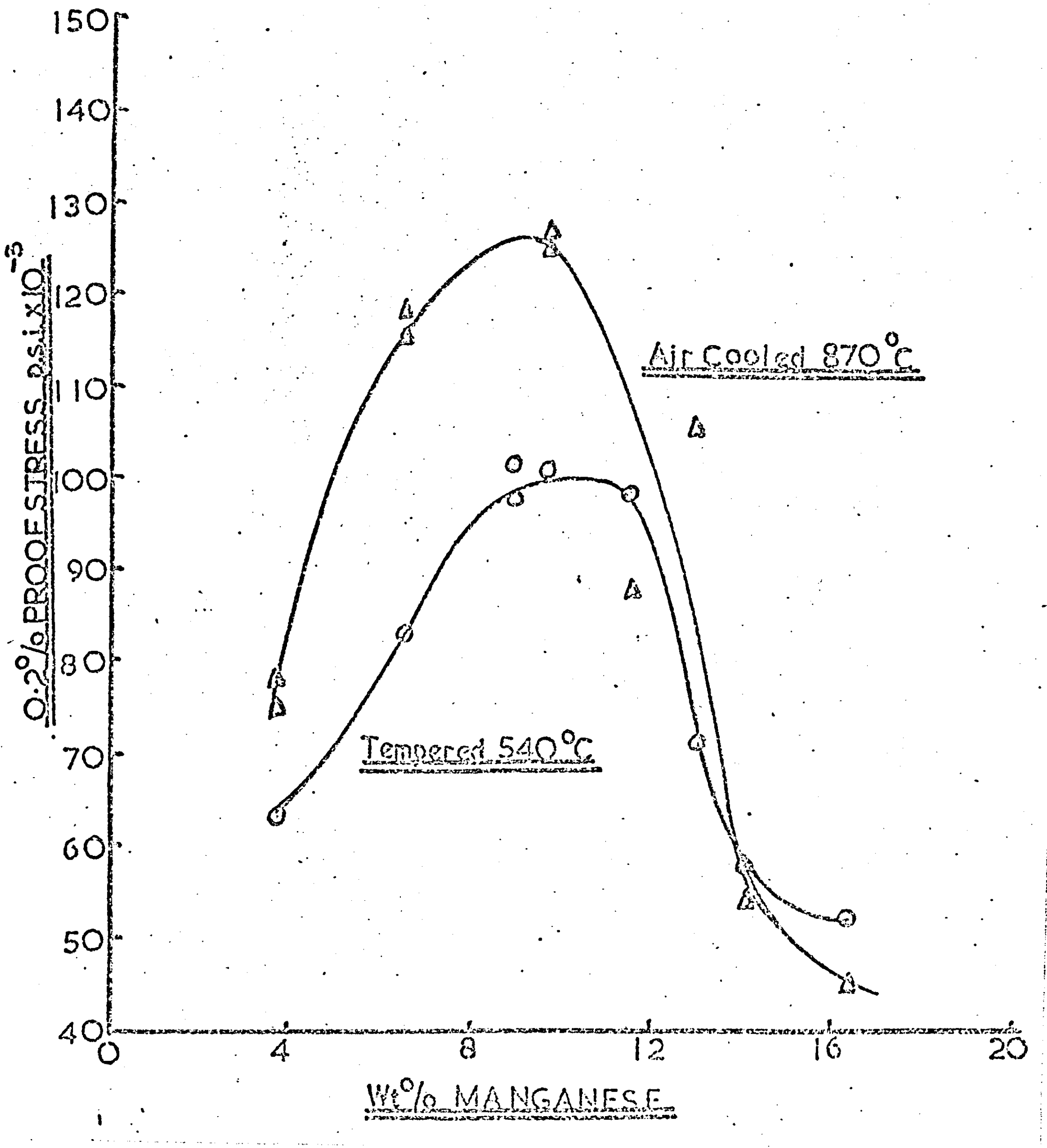

0·2% PROOF STRESS psi x10^{-3}
150
140
130
120
110
100
90
80
70
60
50
40
0
4
8
12
16
20
Wt% MANGANESE
Air Cooled 870°C
Tempered 540°C

FIG.20: Schematic illustration of the formation a double kink which assists dislocations in overcoming the Peierls-Nabarro friction stress.[117.118]

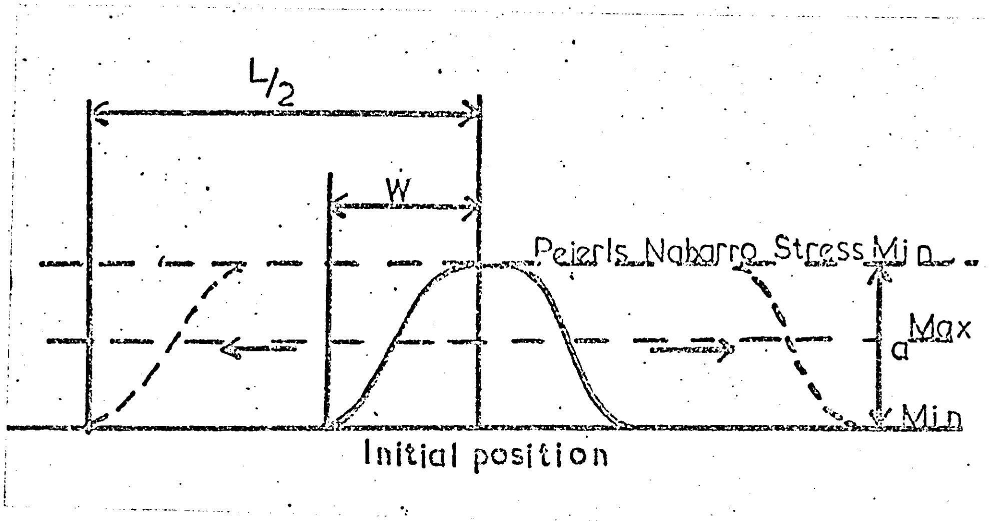

L/2
W
Peierls Nabarro Stress Min
Max
a
Min
Initial position

FIG.21: Schematic illustration of the continuous cooling dilatometer used to determine transformation temperatures.

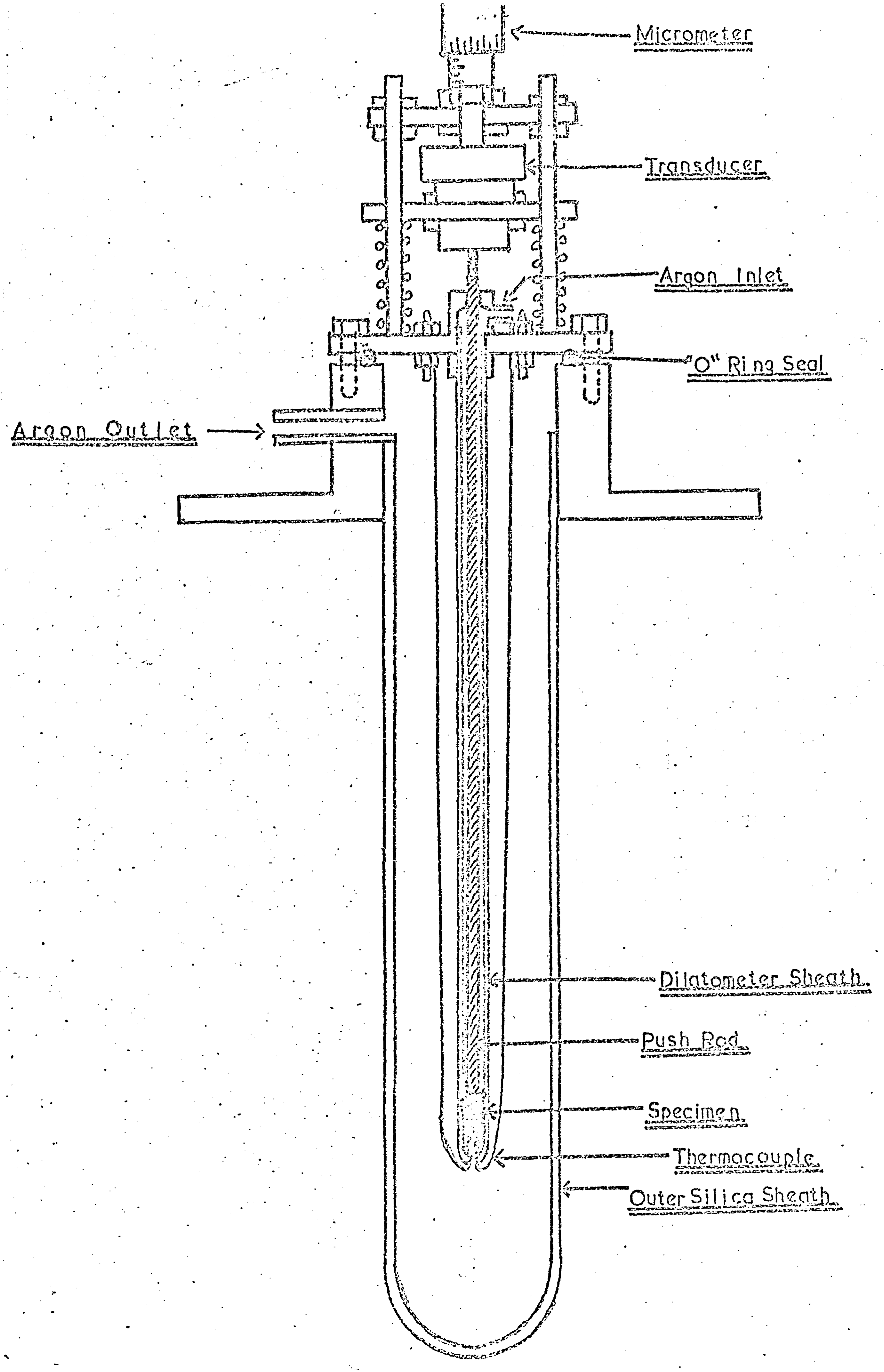
Micrometer
Transducer
Argon Inlet
"O" Ring Seal
Argon Outlet
Dilatometer Sheath.
Push Rod
Specimen.
Thermocouple.
Outer Silica Sheath.

FIG.22: No. 12 Standard Hounsfield tensile test specimen.

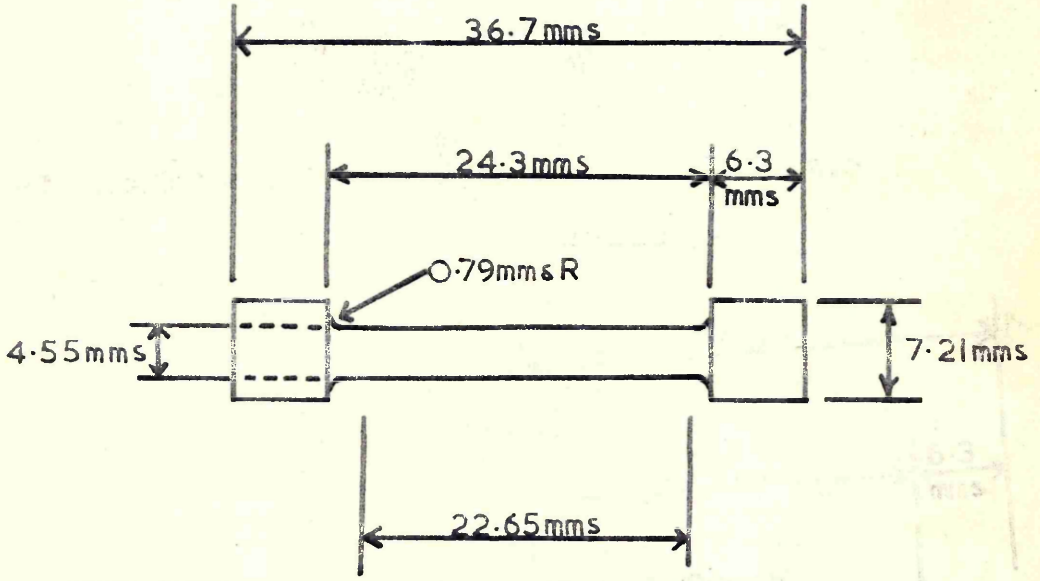
36·7mms
24·3mms
6·3 mms
0·79mms R
4·55mms
7·21mms
22·65mms

FIG.23: Polanyi gripping arrangement for tensile testing on the Instron test machine

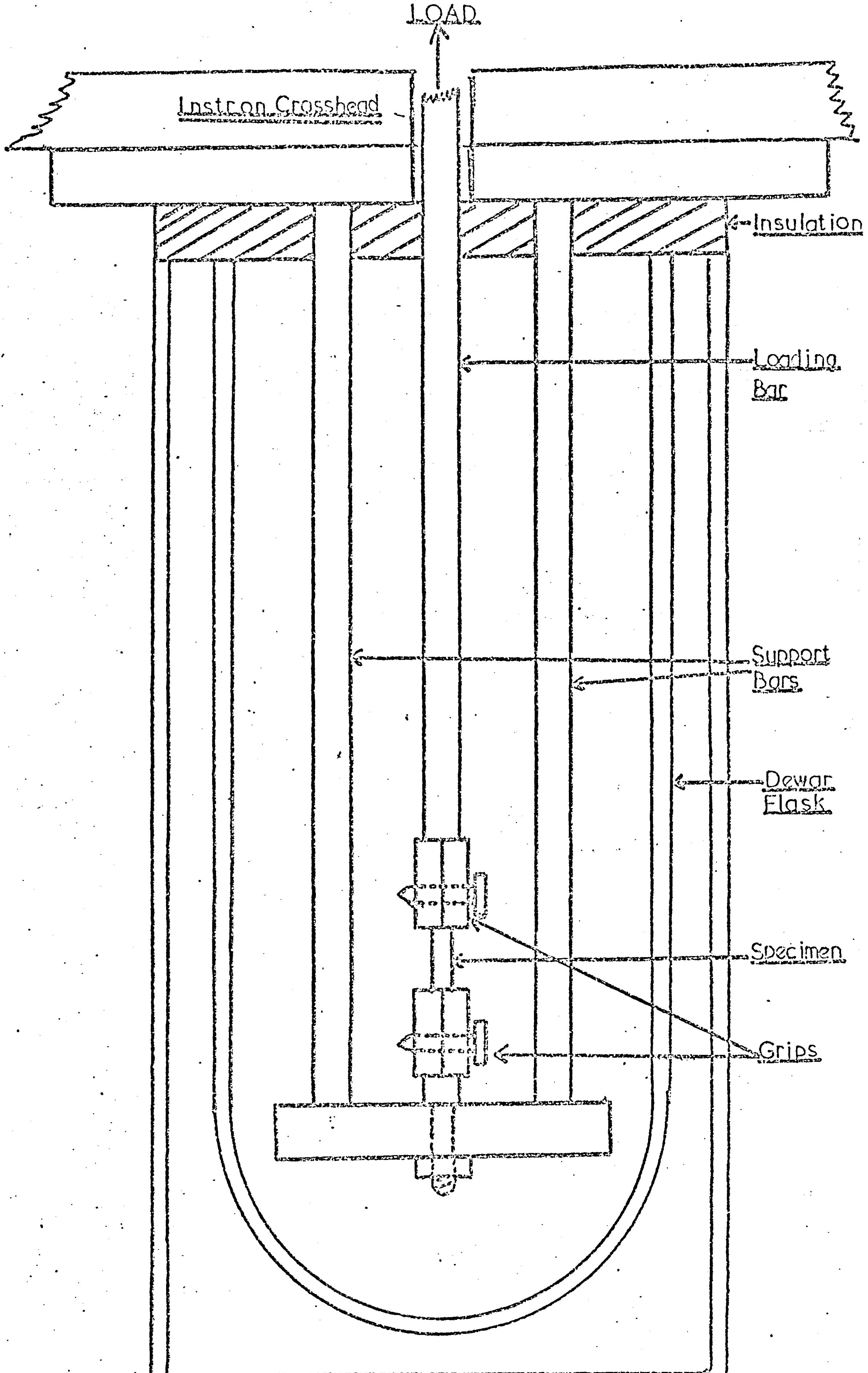
LOAD
Instron Crosshead
Insulation
Loading Bar
Support Bars
Dewar Flask
Specimen
Grips

FIG.24: Wessel[143] spray apparatus for obtaining controlled sub zero testing temperatures during tensile testing.

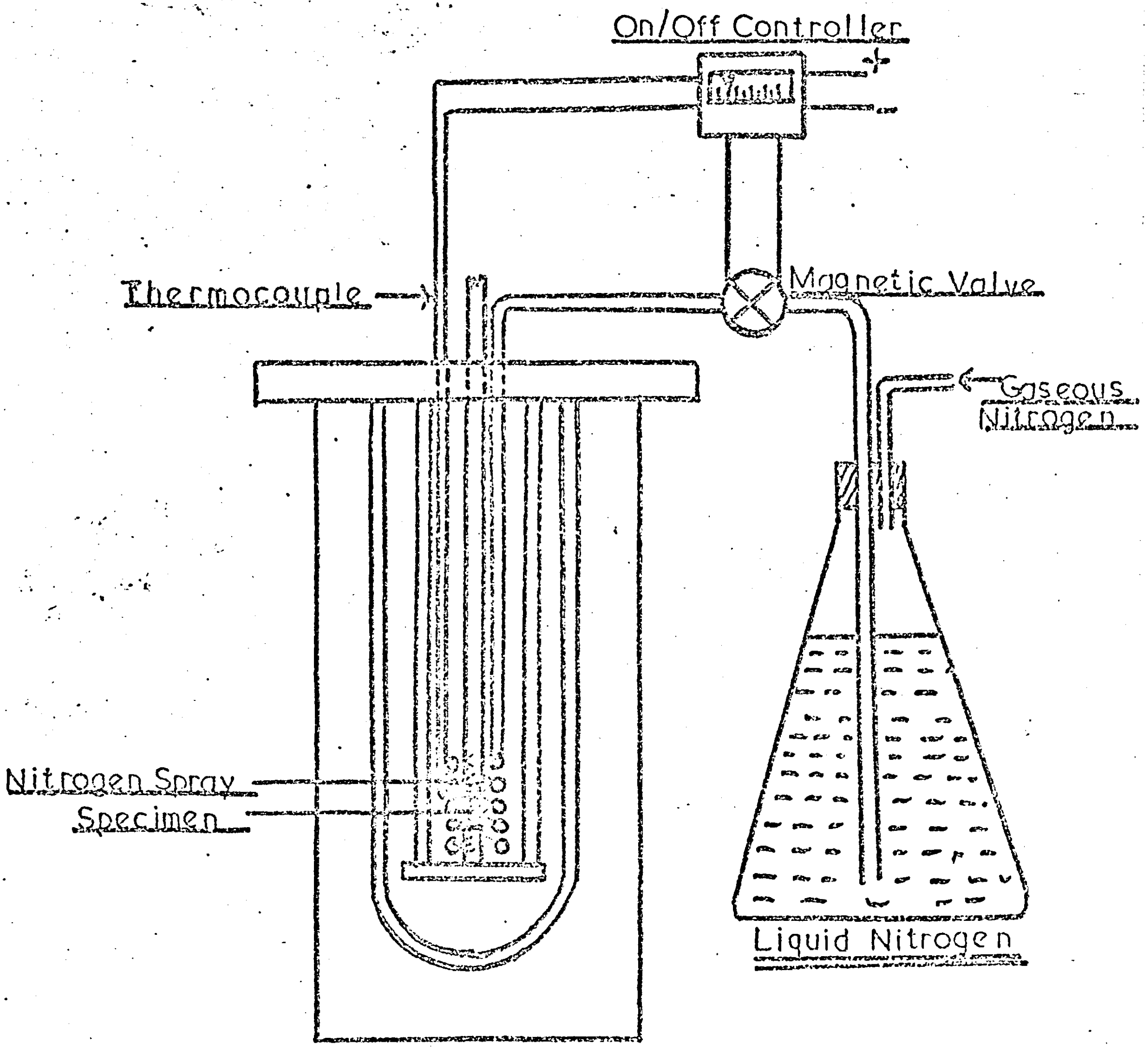
On/Off Controller
Thermocouple
Magnetic Valve
Gaseous Nitrogen
Nitrogen Spray
Specimen
Liquid Nitrogen

FIG.25: The variation in A_S temperature with heating rate for a series of iron manganese alloys.

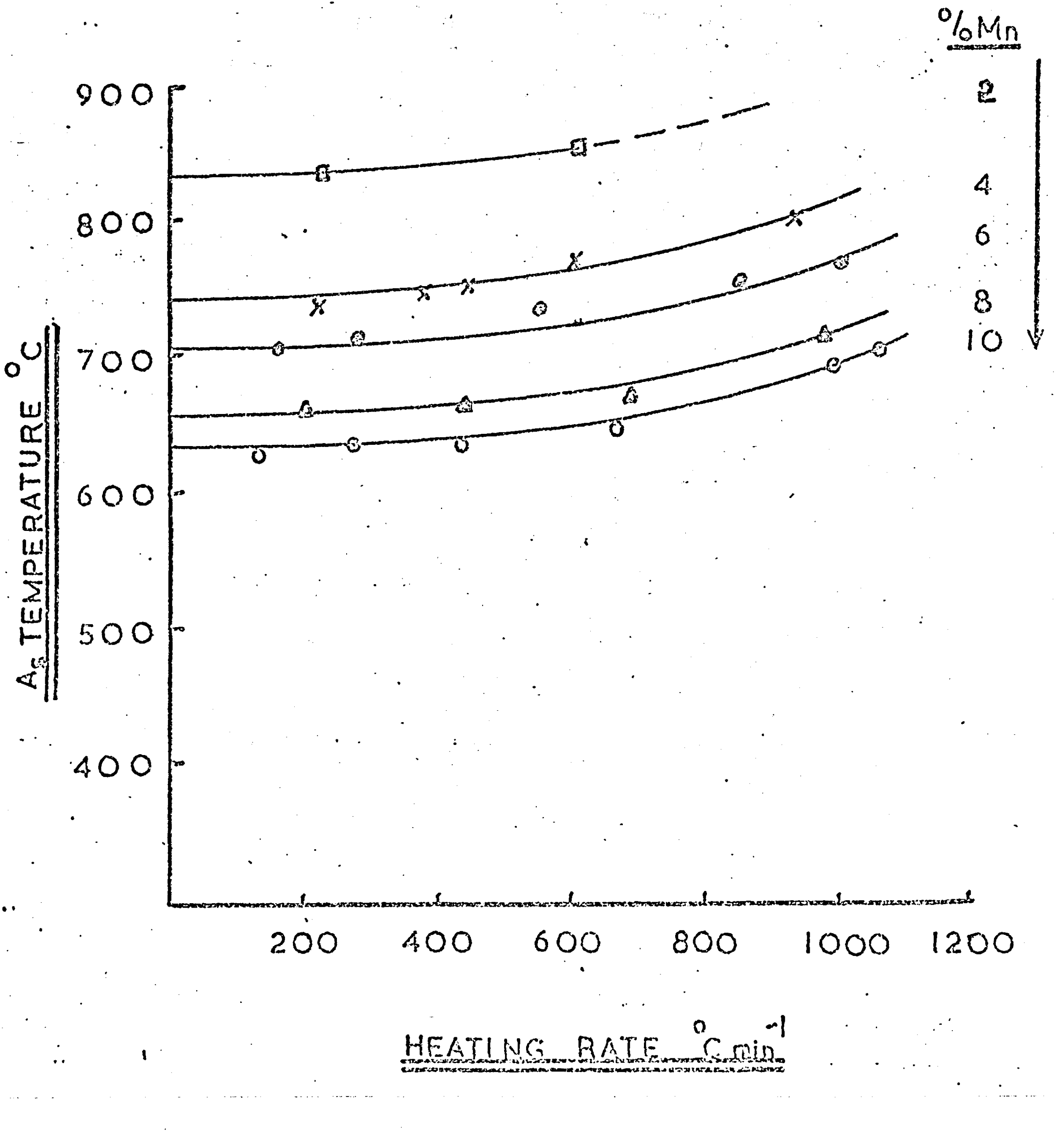
%Mn
2
4
6
8
10
900
800
700
600
500
400
A_s TEMPERATURE °C
200
400
600
800
1000
1200
HEATING RATE °C min^{-1}

FIG.26: Typical dilatometer heating curve showing the A_s - A_f transformation temperature on heating a 10% manganese alloy,

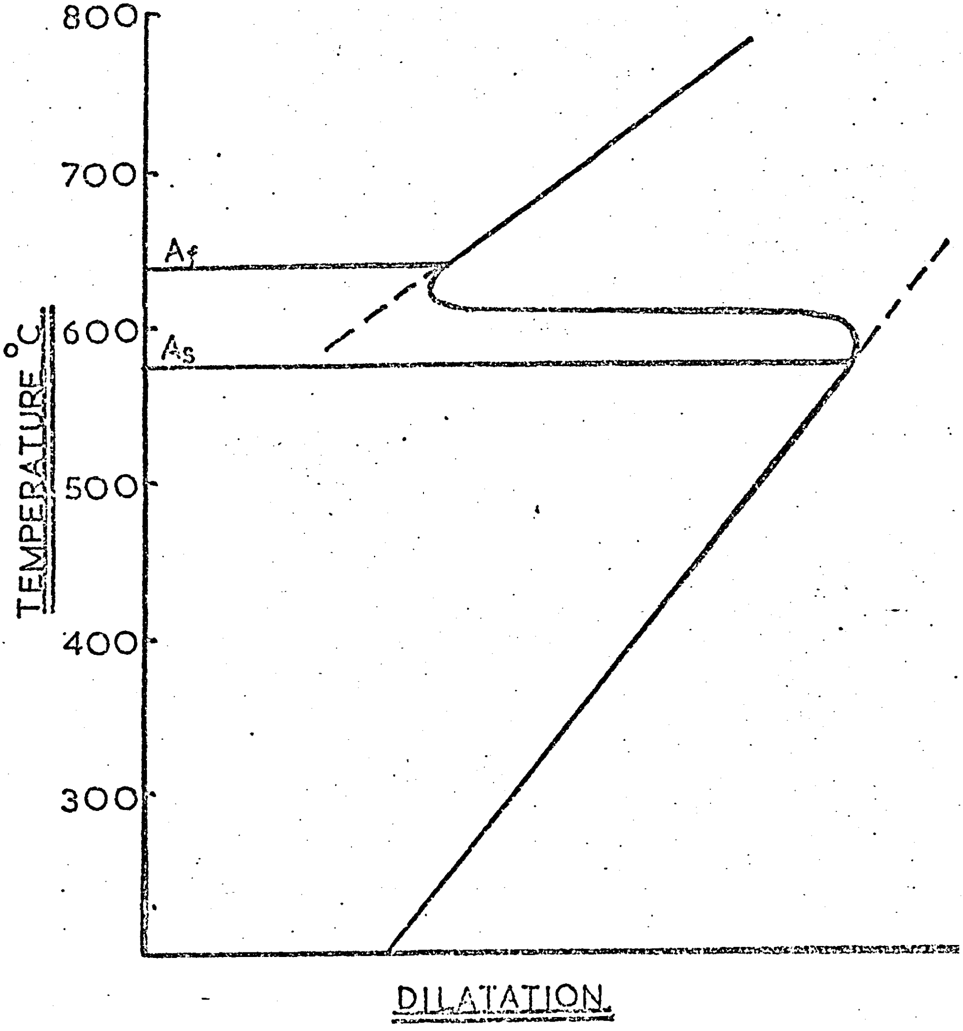
800
700
600
500
400
300
Af
As
TEMPERATURE °C
DILATATION

FIG.27: The effects of cooling rate on the $\gamma \rightarrow \alpha$ transformation start temperature in a series of iron manganese alloys.

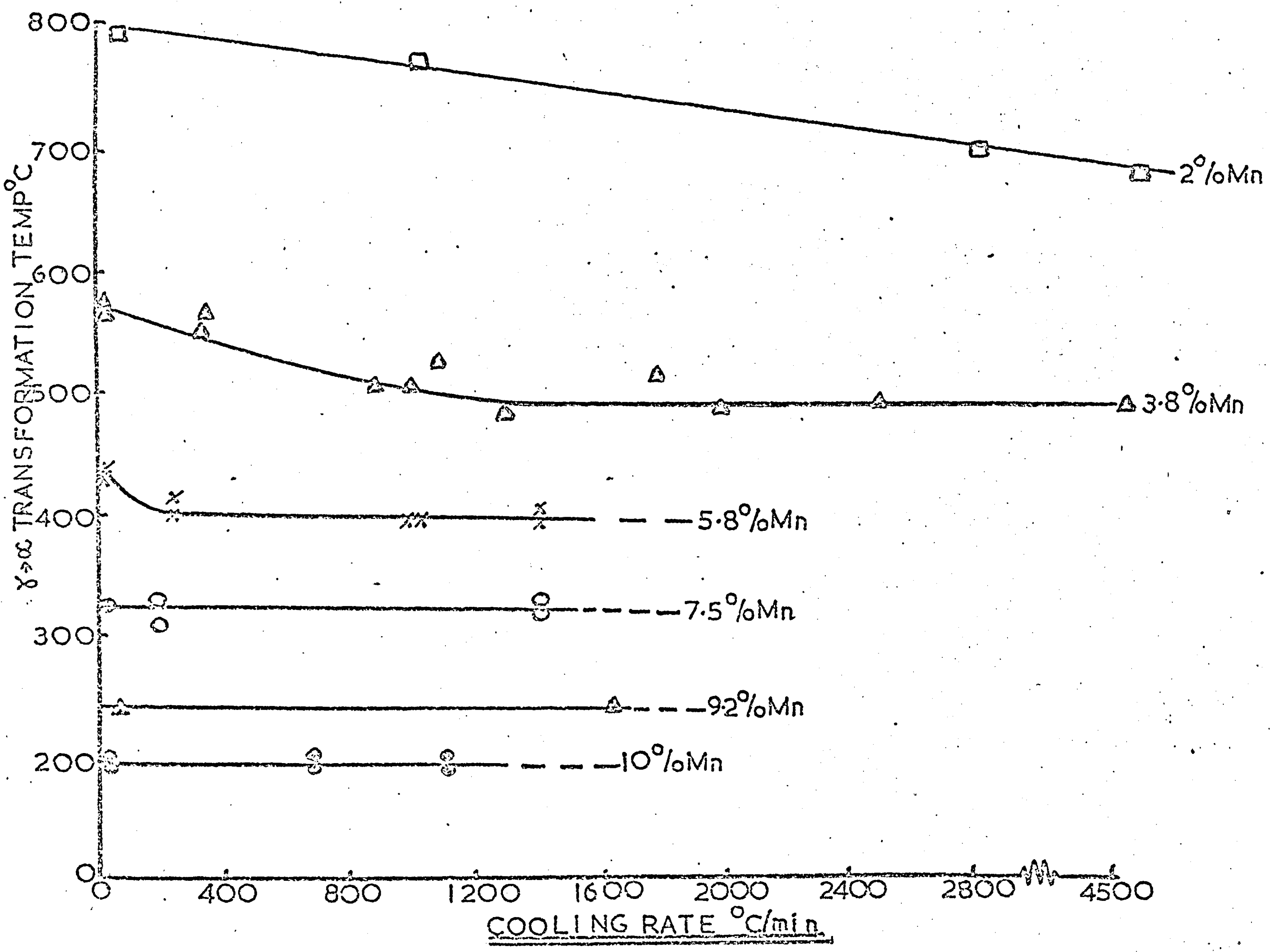

800
700
600
500
400
300
200
0
γ→α TRANSFORMATION TEMP°C
0
400
800
1200
1600
2000
2400
2800
4500
COOLING RATE °C/min.
2°/oMn
3·8°/oMn
5·8°/oMn
7·5°/oMn
9·2°/oMn
10°/oMn

FIG.28: Typical dilatometer cooling curves for a 6% manganese alloy when cooled at A. 1200°C/min B 150°C/min

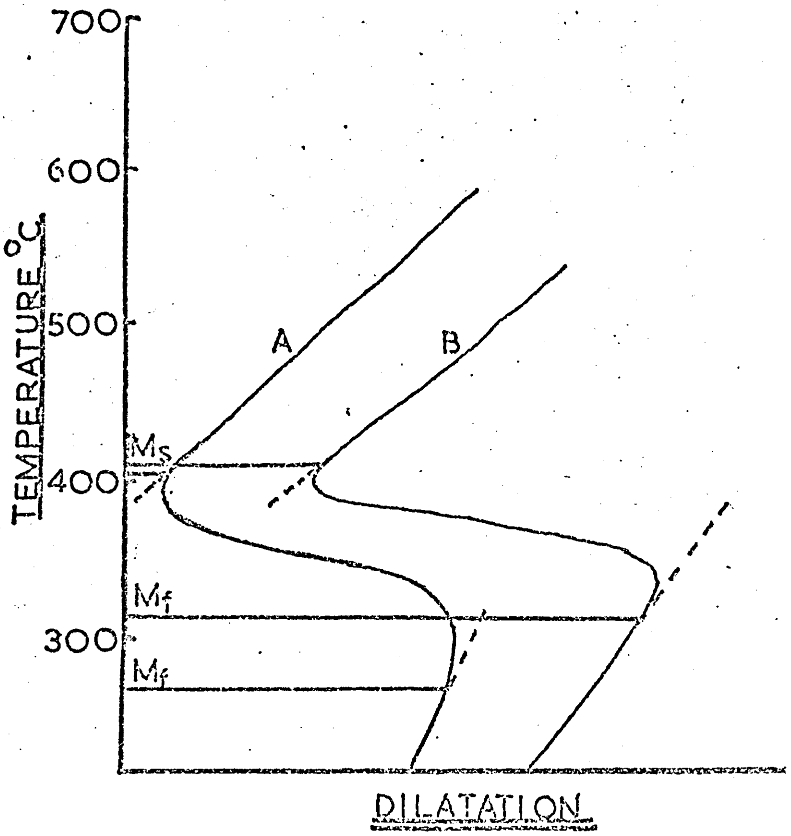
700
600
500
400
300
TEMPERATURE °C
A
B
Ms
Mf
Mf
DILATATION

FIG.29: Massive or equiaxed ferrite in an iron - 2% manganese alloy cooled at 2,800°C/min

Etched 2% nital x 200

FIG.30: Mixed massive ferrite plus lath martensite in an iron - 2% manganese alloy quenched in iced brine.

Etched 2% Nital followed by Aqueous sodium bisulphite, sodium thiosulphate staining etch

x 400

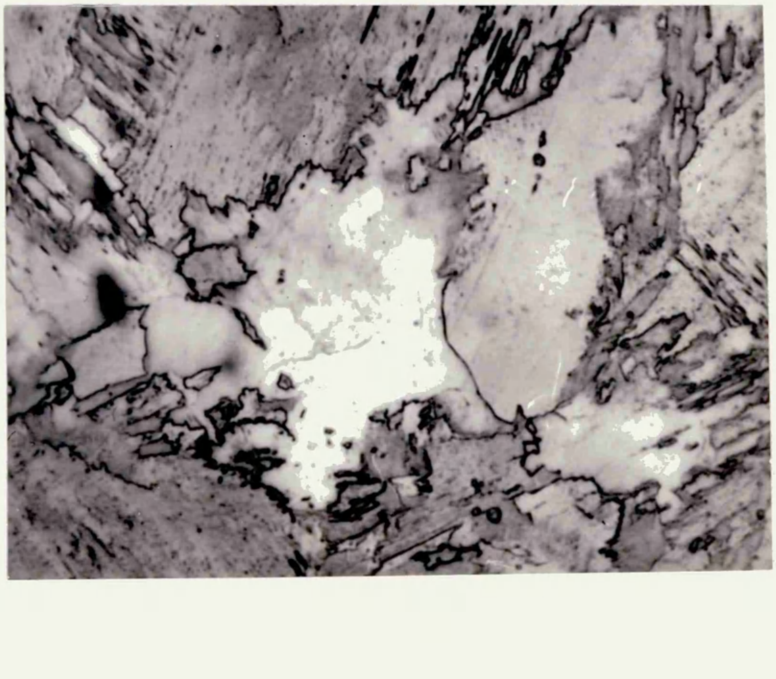

FIG. 31 Microstructures which show the increasingly lath like appearance of the structure of an iron - 4% manganese alloy as the cooling rate was increased.

Etched 2% Nital plus Schummann's reagent.

FIG.31A Cooled at 8°C/min

x 400

FIG.31B Cooled at 900°C/min

x 400

FIG.31C Cooled at 1800°C/min

x 400

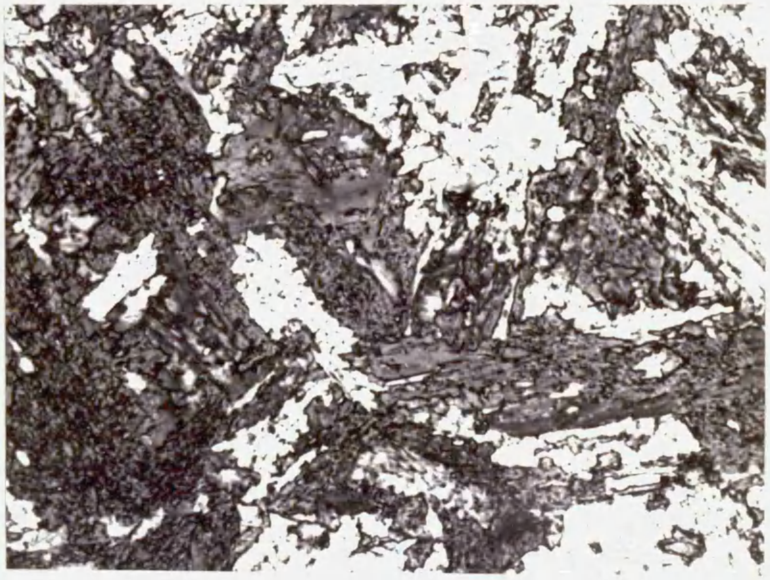

FIG.31D: Quenched into iced brine.

x 400

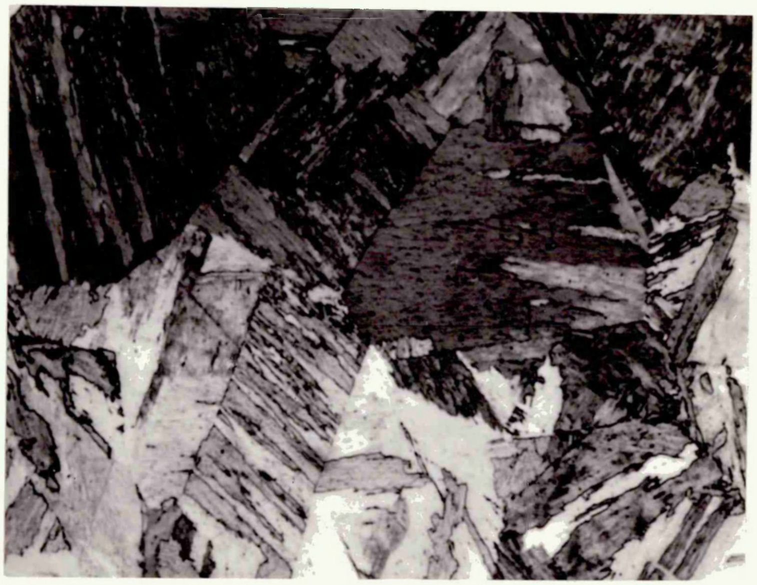

FIG.32: The variation in microstructure of an iron - 6% manganese alloy with cooling rate

Etched 2% Nital followed by Schummann's reagent.

FIG.32A: Lath martensite in an alloy cooled at 1000°C/min

x 400

FIG.32B: Lath martensite plus grain boundary ferrite in an alloy cooled at 5°C/min

x 400

FIG.32C: Ditto 32B. showing apparent growth of grain boundary ferrite across prior austenite grain boundaries.

x 1000

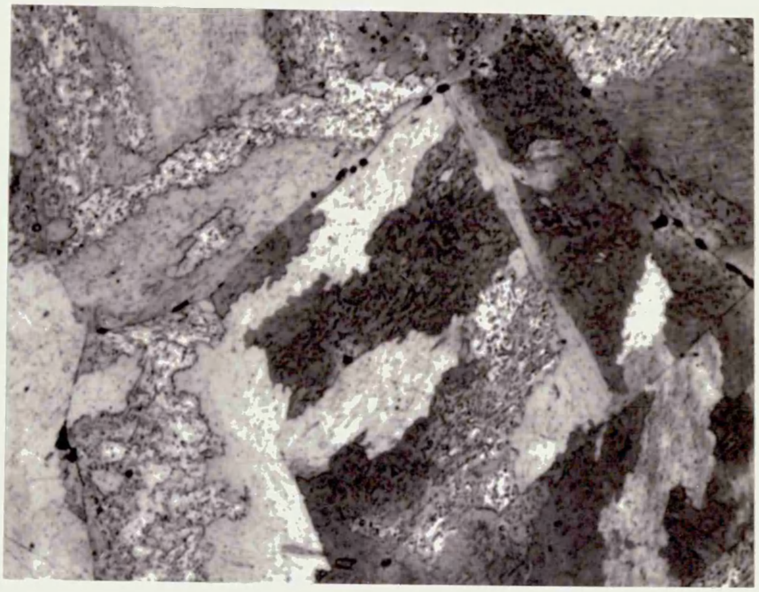

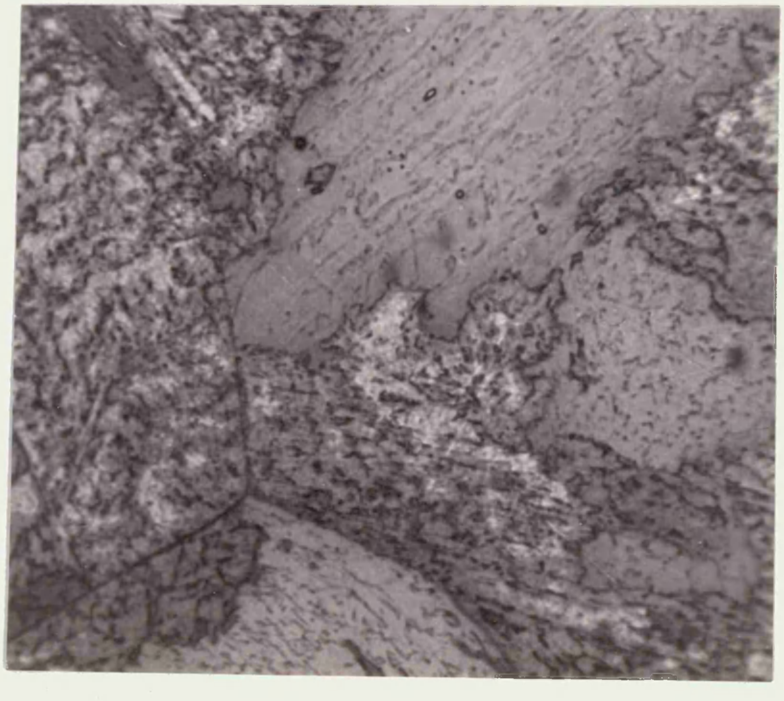

FIG.33: Typical lath martensite structure found in both iron - 8% manganese and iron - 10% manganese alloys even after very slow cooling

Etched 2% Nital followed by Schummann's reagent.

x 200

FIG.34: Thin foil electron micrographs of the structures produced by slow cooling in an iron - 4% manganese alloy.

FIG.34A: Furnace cooled at approximately 5°C/min showing equiaxed sub cells

x 45,000

FIG.34B: Dislocations within the sub cells of the structure shown in Fig. 34A.

x 100,000

FIG.34C: Air cooled at approximately 150°C/min showing mixture of equiaxed and finger like sub cells.

x 45,000

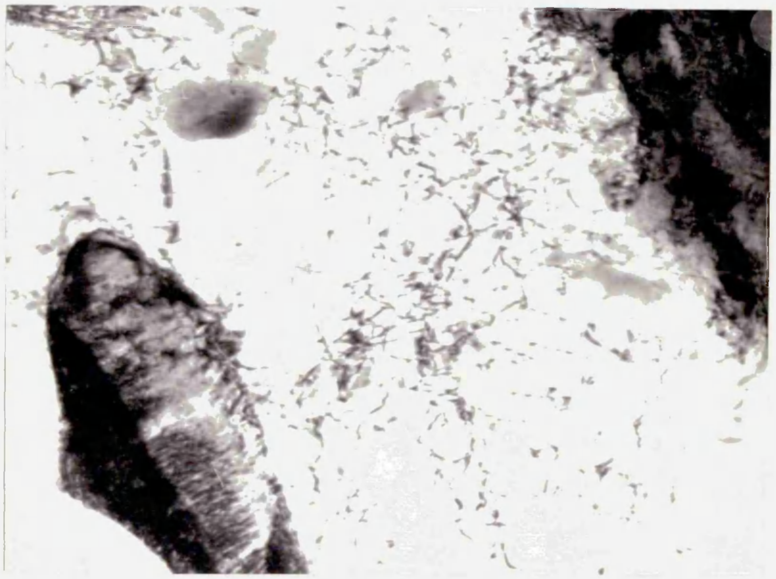

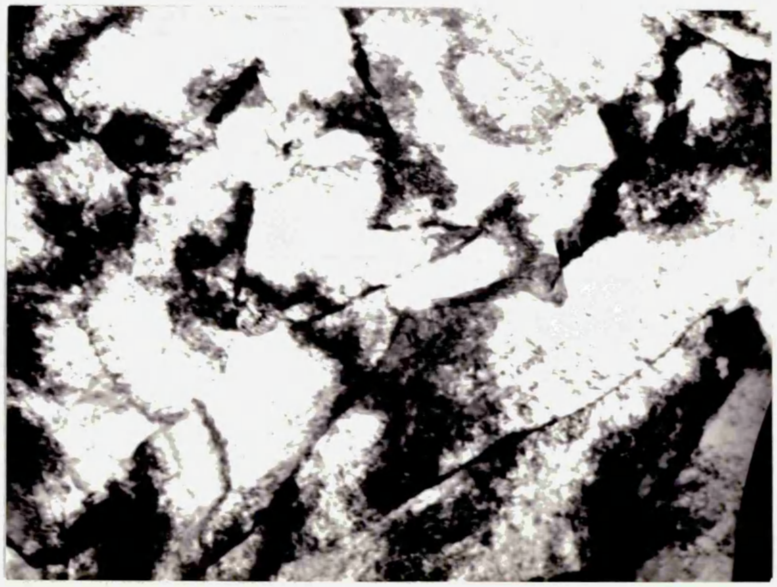

FIG.35A Cell boundary with uniformly distributed dislocations within each cell for an iron - 4% manganese alloy after slow cooling.

x 180,000

FIG.35B Selected area diffraction patterns taken from either side of the sub cell boundary shown in Fig. 35A. Both of the adjacent cells produce a $\langle 100 \rangle_{\alpha}$ zone diffraction pattern of almost identical orientation, which indicates little misorientation across the cell boundary.

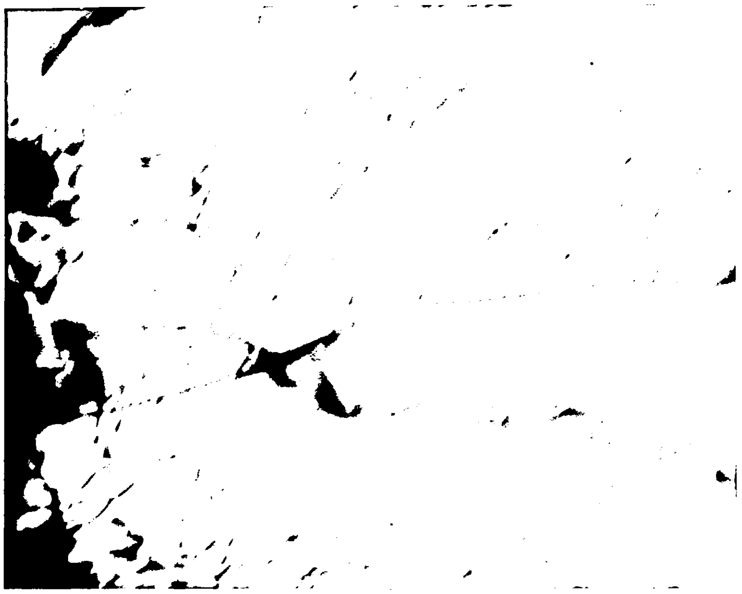

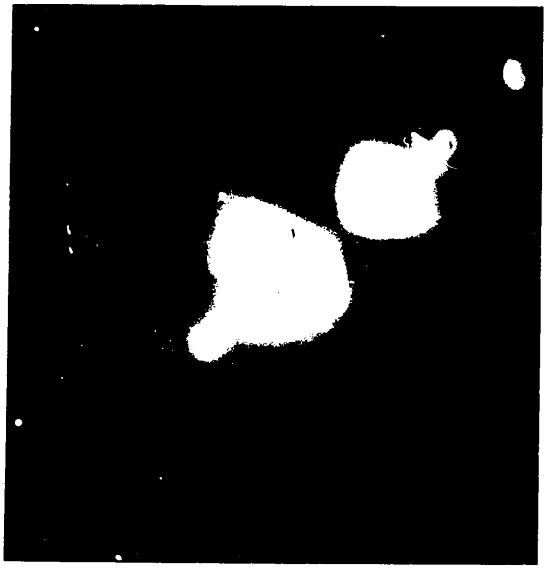

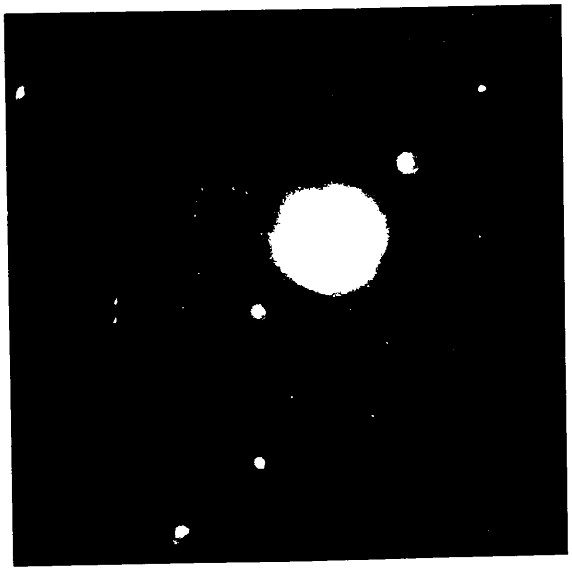

FIG.36: Thin foil electron micrograph showing semi lath like structure in an iron - 4% manganese alloy in the water quenched condition.

x 35,000

FIG.37: Thin foil electron micrograph showing lath martensite in an iron - 4% manganese alloy drastically quenched into iced brine.

x 45,000

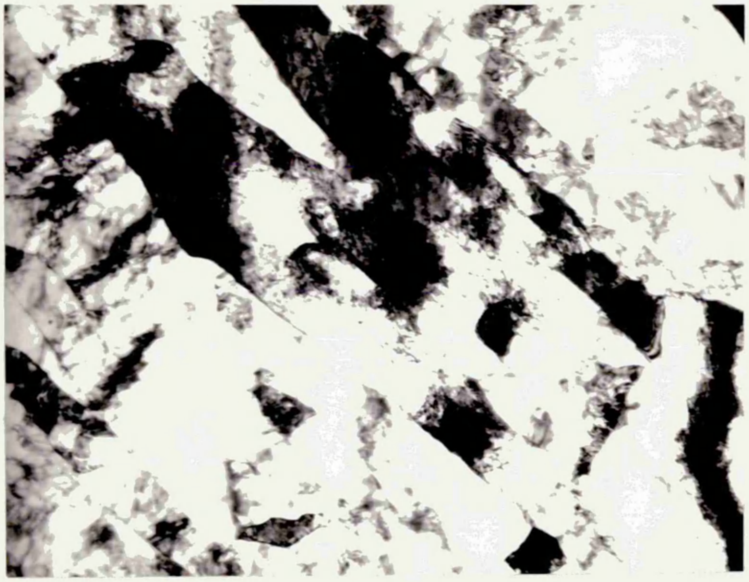

FIG.38A: Thin foil electron micrograph showing a typical lath martensite structure found in iron - 6% manganese alloys.

x 130,000

FIG.38B: Thin foil electron micrograph of prior austenite grain boundary area showing a non lath like area which may correspond to the grain boundary ferrite shown in Fig. 32C.

x 130,000

FIG.39: Thin foil electron micrograph typical of the lath martensite structure found in the iron - 10% manganese alloy.

x 100,000

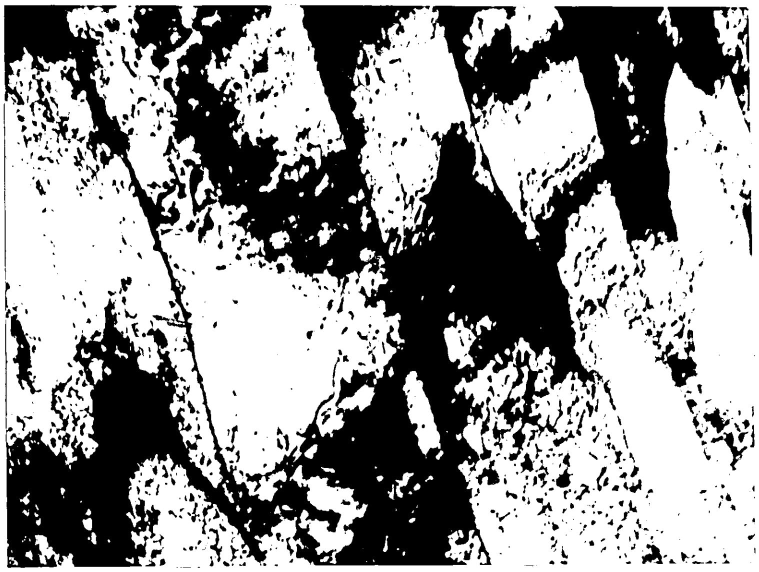

FIG.40: Tracing of the $\{220\}_{\alpha}$ diffraction line for an iron - 4% manganese alloy, taken from a diffractometer trace. Note the assymetry and sharpening of this line in the slowly cooled specimen.

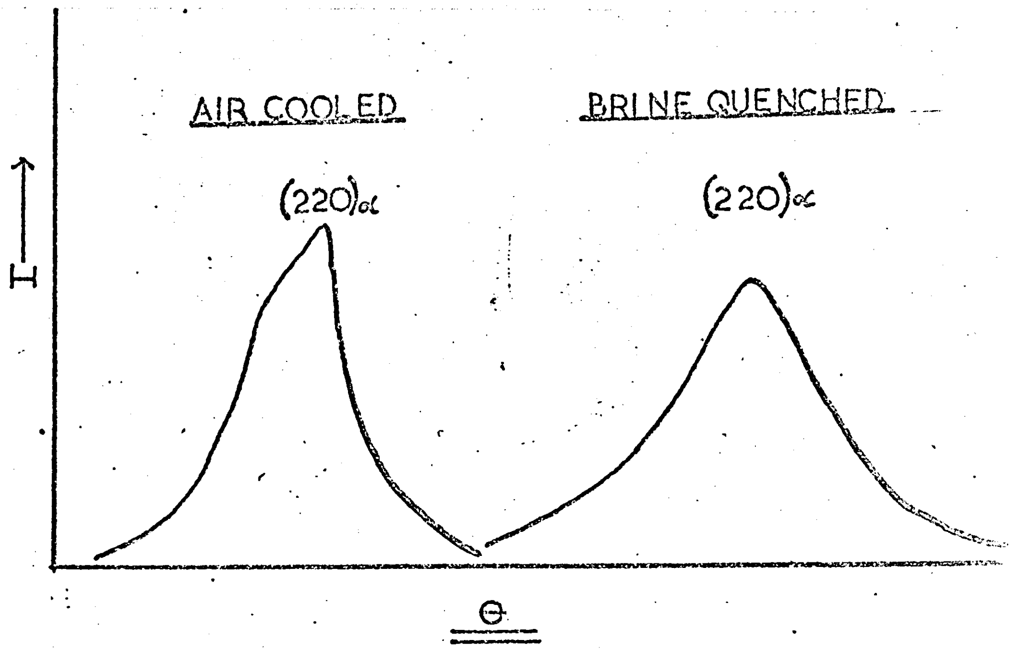
AIR COOLED
BRINE QUENCHED
(220)α
(220)α
I
θ

FIG.41: The variation in hardness with cooling rate for various iron manganese alloys.

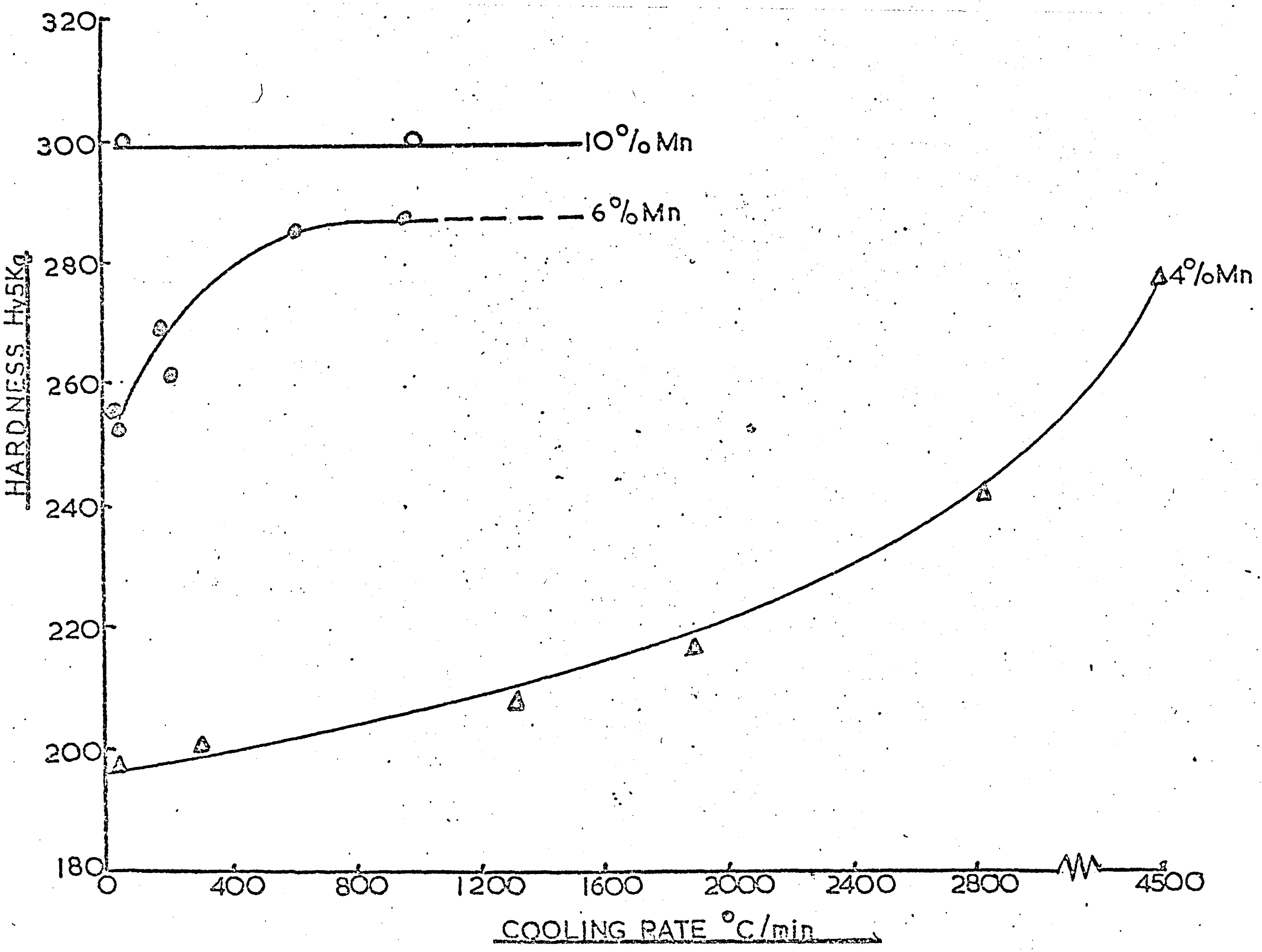

320
300
280
260
240
220
200
180
HARDNESS Hv5Kg
0
400
800
1200
1600
2000
2400
2800
4500
COOLING RATE °C/min
10%Mn
6%Mn
4%Mn

FIG.42: Plot of the weighted mean of lath width versus manganese concentration for lath martensites.

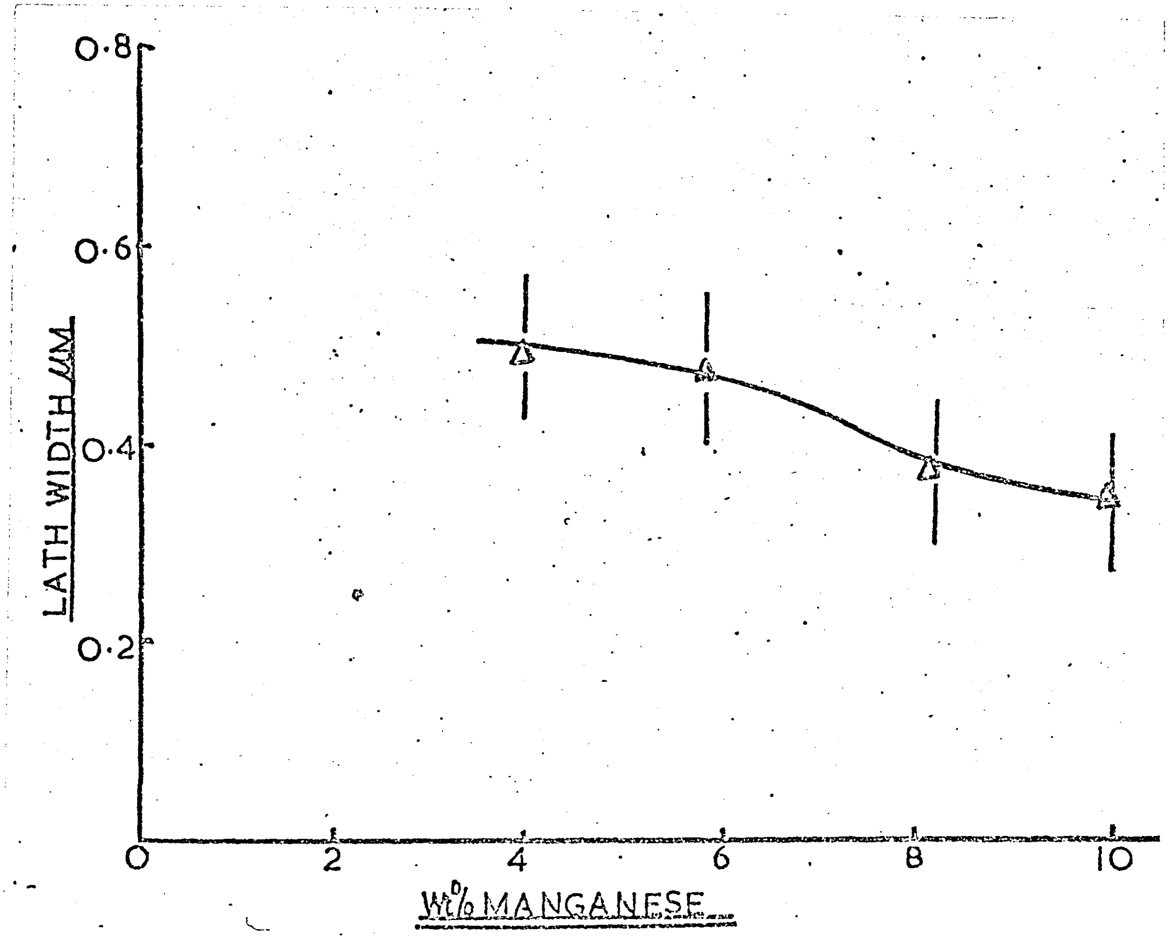
0·8
0·6
0·4
0·2
LATH WIDTH μm
0
2
4
6
8
10
Wt% MANGANESE

FIG.43: Simultaneous recordings of temperature and dilatation for an iron - 4% manganese alloy quenched to different isothermal holding temperatures, i.e. 523°C, 505°C, and 495°C

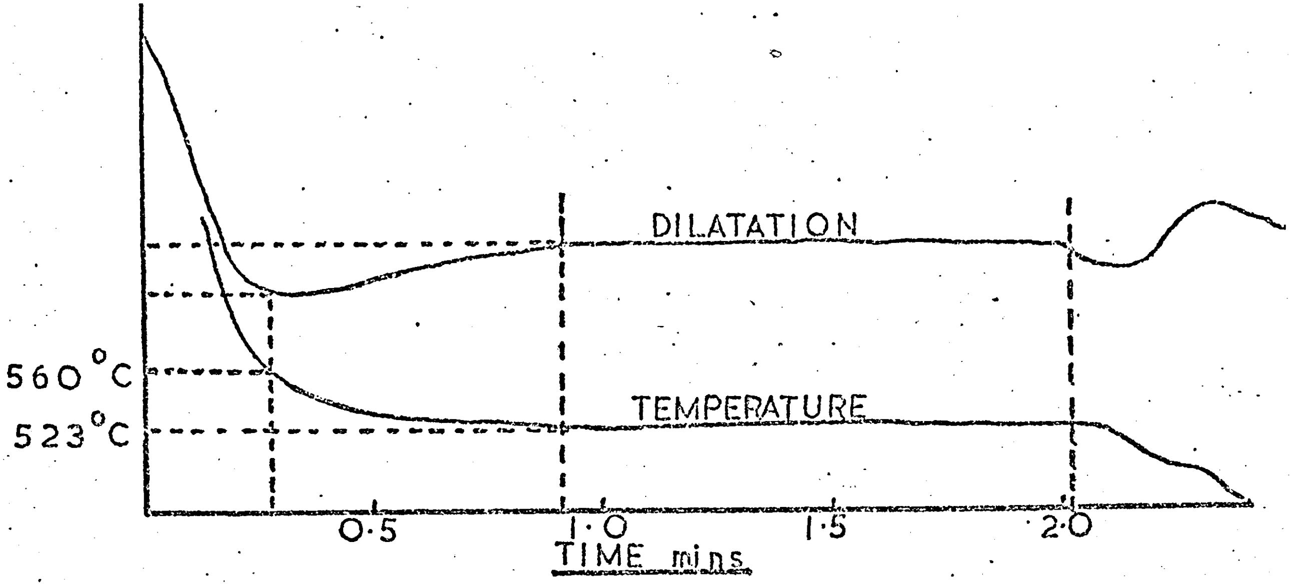
DILATATION
TEMPERATURE
560 °C
523 °C
0·5
1·0
1·5
2·0
TIME mins

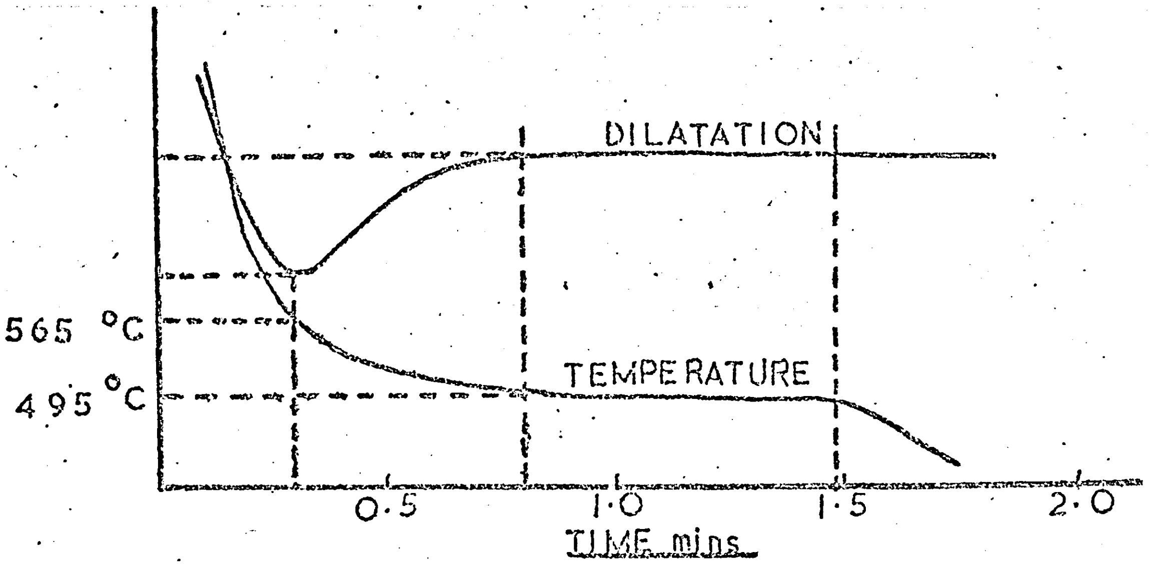
DILATATION
TEMPERATURE
565 °C
495 °C
0·5
1·0
1·5
2·0
TIME mins

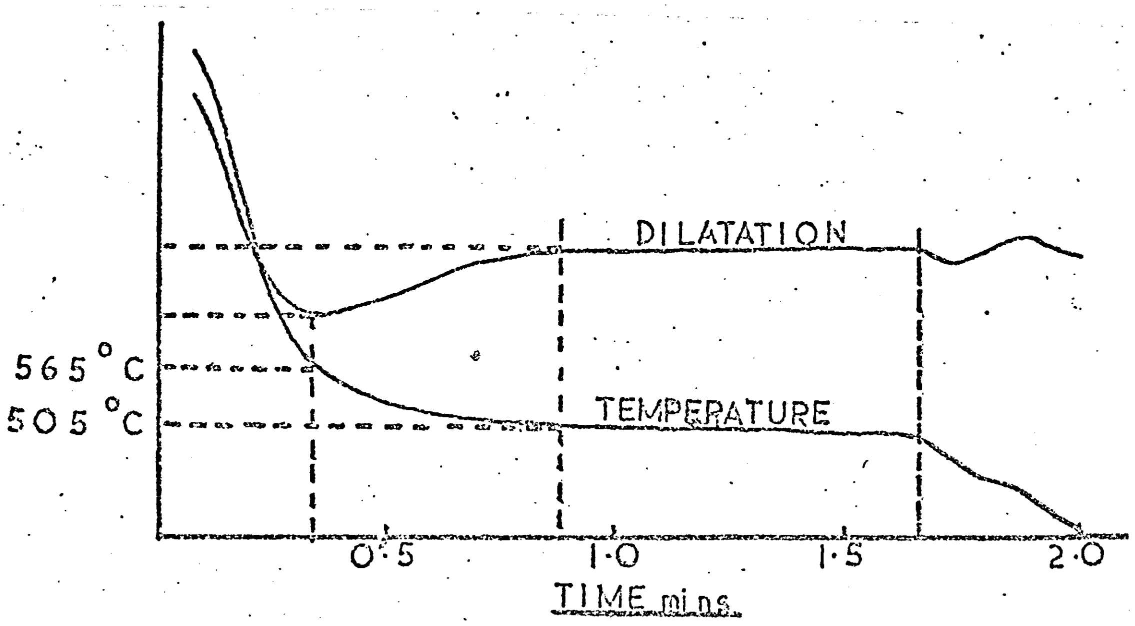
DILATATION
TEMPERATURE
565 °C
505 °C
0·5
1·0
1·5
2·0
TIME mins

FIG.44: The relationship between percentage transformation and temperature for an iron - 4% Manganese alloy. This shows that the temperature range for transformation is shifted by variation of the cooling rate, but their slopes remain constant.

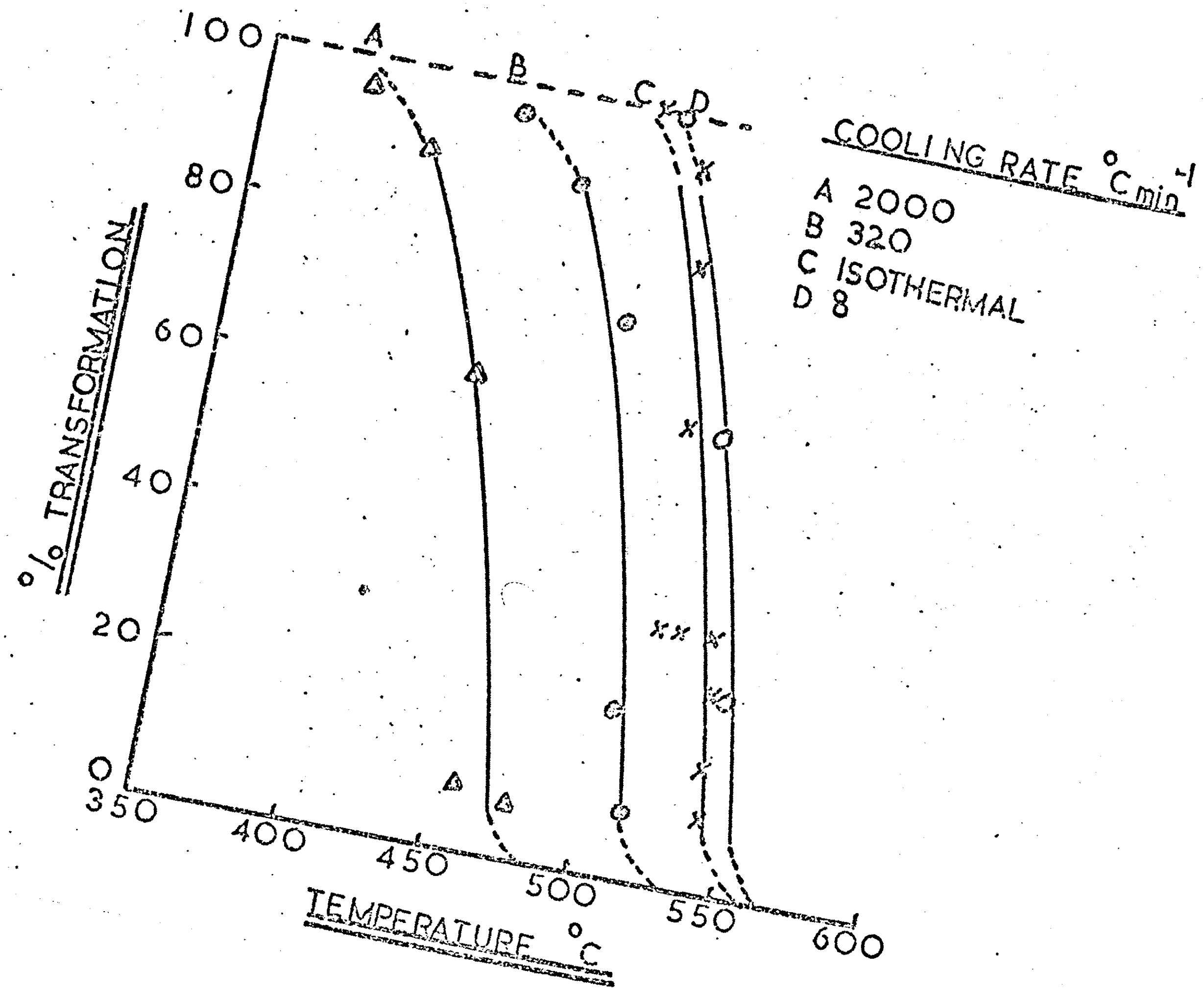
100
80
60
40
20
0
% TRANSFORMATION
350
400
450
500
550
600
TEMPERATURE °C
A
B
C
D
COOLING RATE °C min-1
A 2000
B 320
C ISOTHERMAL
D 8

FIG.45: Microstructure of an iron - 4% manganese alloy isothermally treated at 505°C for two minutes, and showing the ragged ferrite structure which was also produced by slow continuous cooling, see Fig. 31A

Etched 2% Nital followed by Schummann's reagent.

x 600

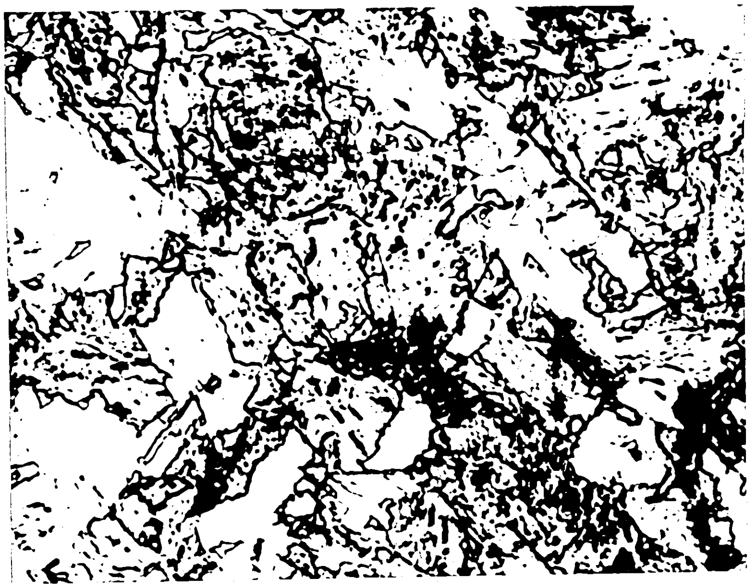

FIG.46: Simultaneous records of temperature and dilatation for an iron - 6%manganese alloy quenched to different isothermal holding temperatures, i.e. 420°C and 395°C. Note the isothermal transformation produced at 395°C

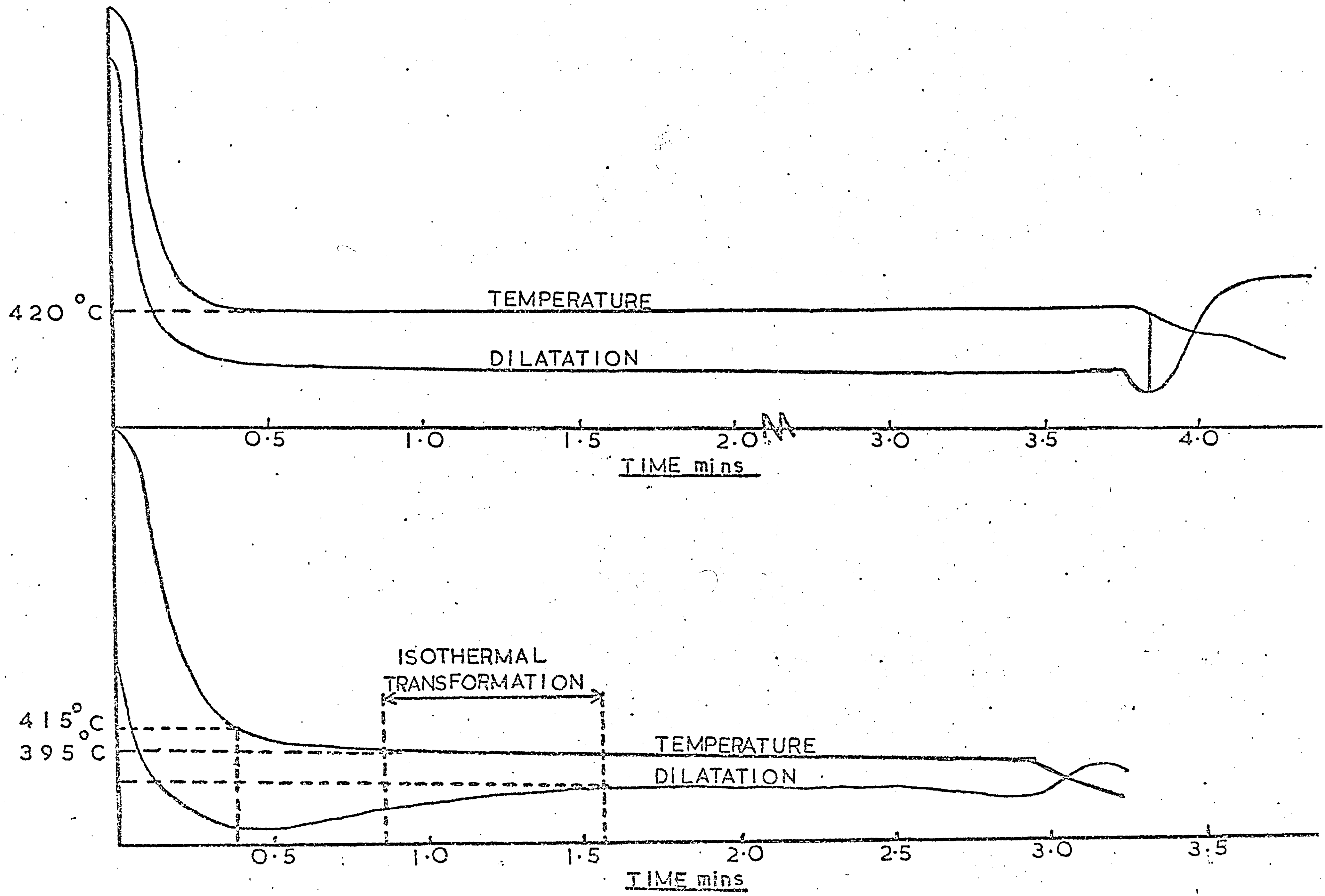
420 °C
TEMPERATURE
DILATATION
0·5
1·0
1·5
2·0
3·0
3·5
4·0
TIME mins
ISOTHERMAL
TRANSFORMATION
415 °C
395 °C
TEMPERATURE
DILATATION
0·5
1·0
1·5
2·0
2·5
3·0
3·5
TIME mins

FIG.47: The variation in room temperature hardness of an iron - 6% manganese alloy, quenched to a constant temperature of 400°C and held for varying times.

FIG.48: Correlation between the hardness and the amount of grain boundary ferrite, e.g. see Fig. 32C, produced in iron - 6% manganese alloys when either slowly cooled or isothermally treated within the range 350°C - 420°C

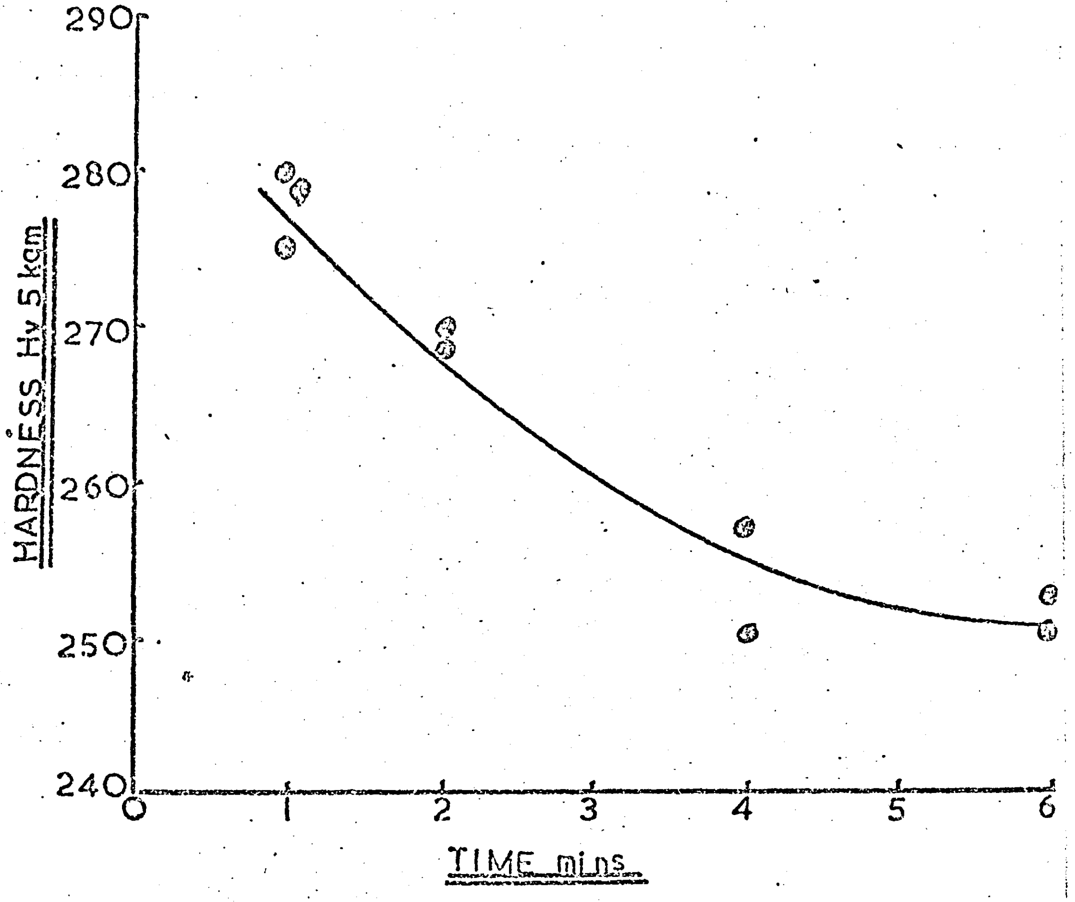

290
280
270
260
250
240
HARDNESS Hv 5 kgm
0
1
2
3
4
5
6
TIME mins

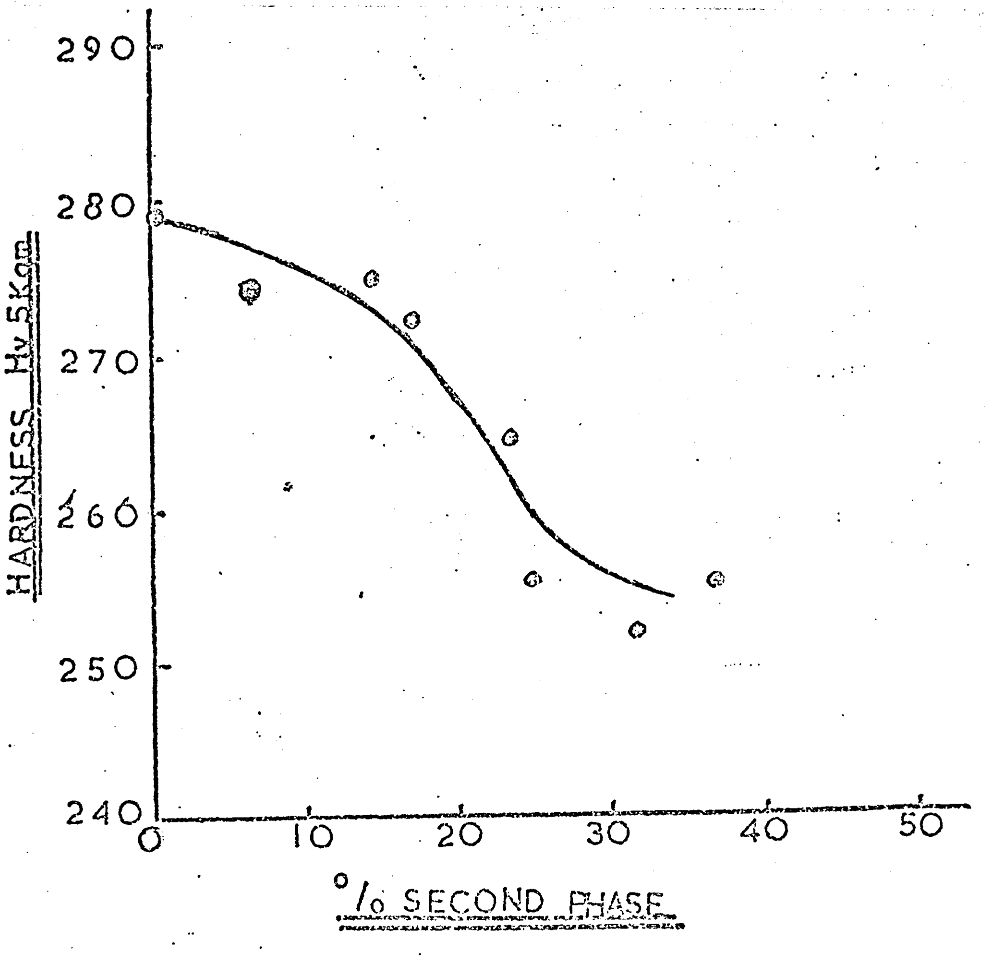

290
280
270
260
250
240
HARDNESS Hv 5Kgm
0
10
20
30
40
50
% SECOND PHASE

FIG.49: Showing the prepolished surface of an iron - 4% manganese alloy after heating to 1000°C in a high purity argon atmosphere and transforming to martensite by rapid cooling. Despite surface deterioration there is still some evidence of surface tilts.

x 200

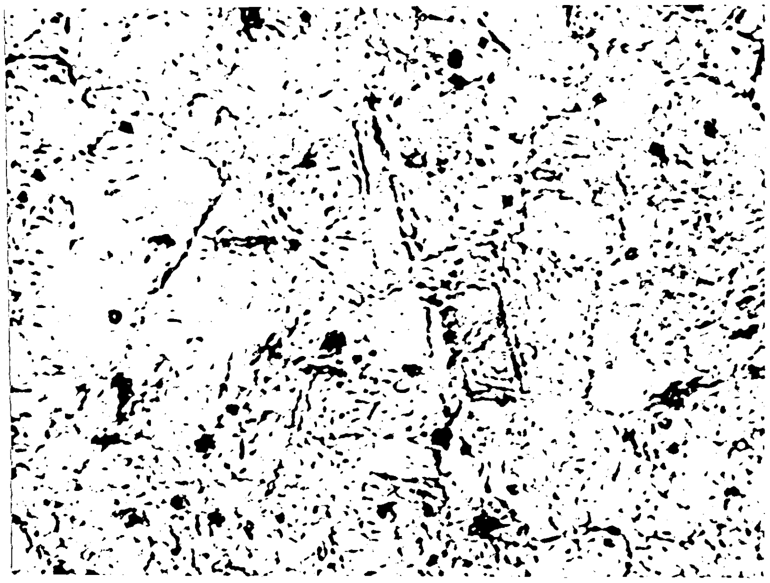

FIG.50: Showing the variation in hardness and M_s temperature produced by cycling a single specimen of iron - 10% manganese through the $\alpha \rightarrow \gamma \rightarrow \alpha$ transformation to a successively higher austenitizing temperature.

FIG.50A Specimen prior heat treated by austenitizing at 850°C for one hour and water quenched.

FIG.50B: Specimen prior heat treated by austenitizing at 1000°C for one hour and water quenched.

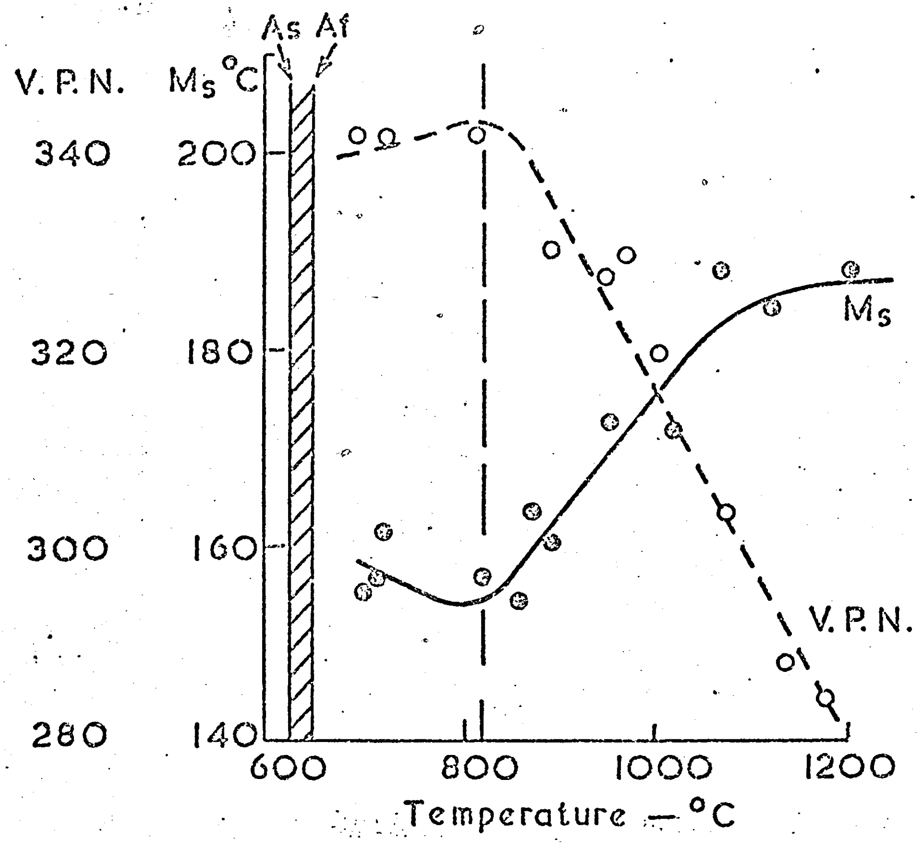
As
Af
V. P. N.
Ms °C
340
320
300
280
200
180
160
140
600
800
1000
1200
Temperature — °C
Ms
V. P. N.

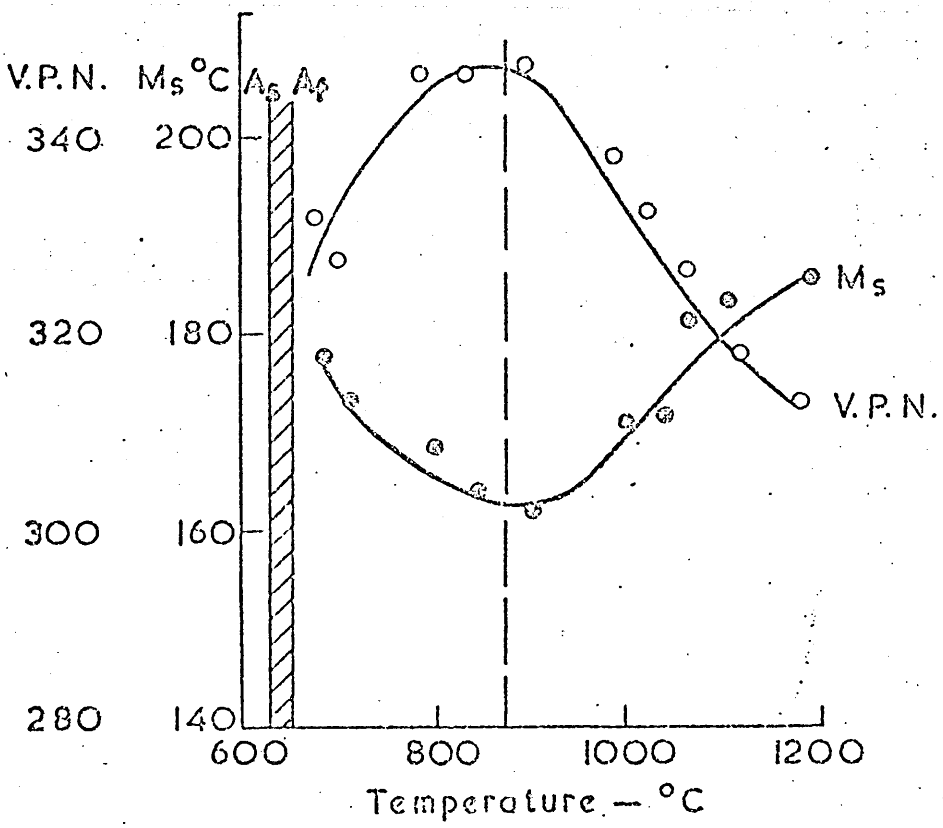
V.P.N.
Ms °C
As
Af
340
320
300
280
200
180
160
140
600
800
1000
1200
Temperature — °C
Ms
V. P. N.

FIG.51: The variation in microstructure of an iron - 10% manganese alloy after cycling through the $\alpha \rightarrow \gamma \rightarrow \alpha$ transformation.

Etched 2% Nital followed by Schummann's reagent.

FIG.51A: First cycle to 675°C held for one minute, cooled to room temperature and showing coarse distorted lath martensite.

x 400

FIG.51B: Second cycle to 725°C held for one minute, cooled to room temperature and showing very fine lath martensite structure.

x 400

FIG.51C: Third cycle to 830°C held for one minute, cooled to room temperature and showing coarsening of the prior austenite grain size.

x 400

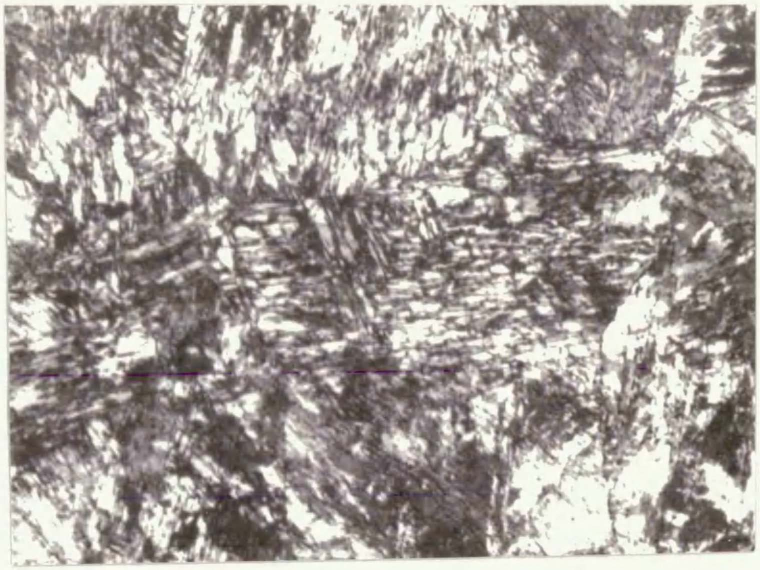

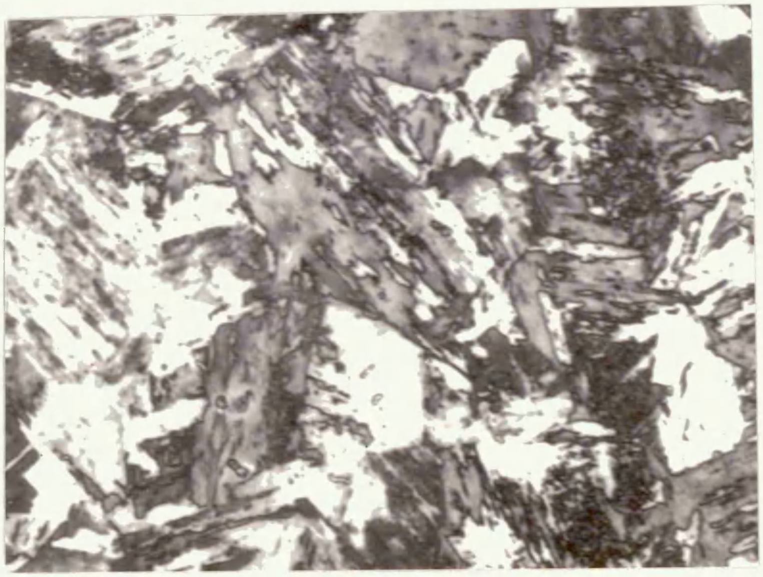

FIG.51D: Fourth cycle to 1100^{o}C held for one minute, cooled to room temperature, and showing fully recrystallized prior austenite grains.

x 400

FIG.52: The variation in hardness and M_s temperature produced in an iron - 10% manganese alloy by cycling through the $\alpha \rightarrow \gamma \rightarrow \alpha$ transformation. Each austenitizing temperature, i.e. cycle, was conducted with a separate specimen

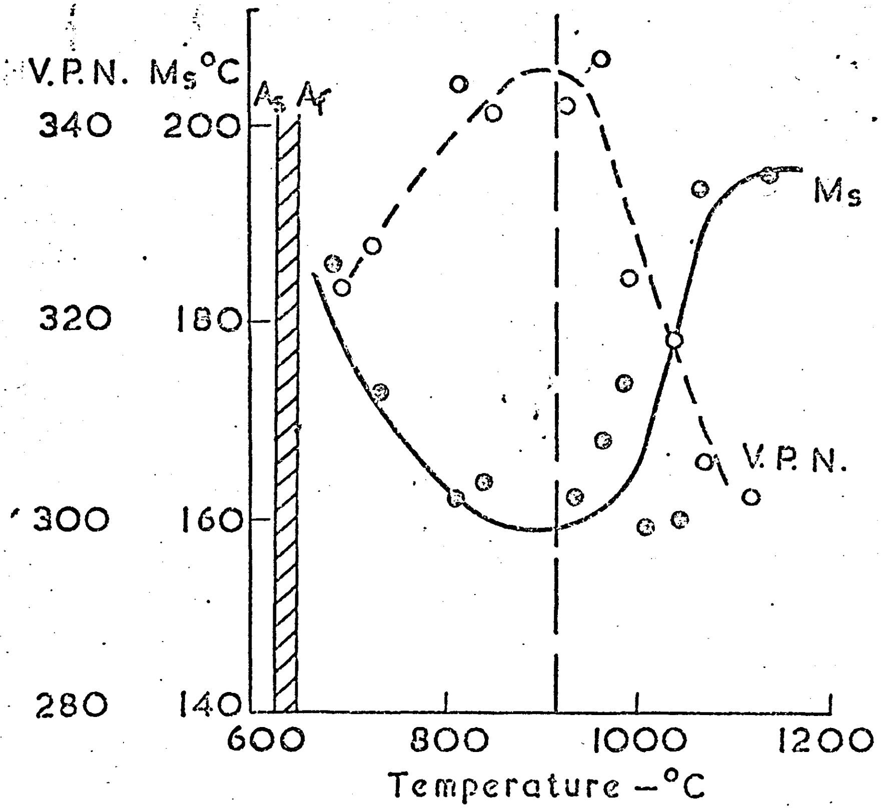
V.P.N.
Ms°C
As
Af
340
320
300
280
200
180
160
140
600
800
1000
1200
Temperature –°C
Ms
V.P.N.

FIG.53: The variation in hardness and M_s temperature for an iron - 10% manganese alloy after austenitizing for varying times at fixed austenitizing temperatures.

FIG.53A: Austenitizing temperature 700°C

FIG.53B: Austenitizing temperature 850°C

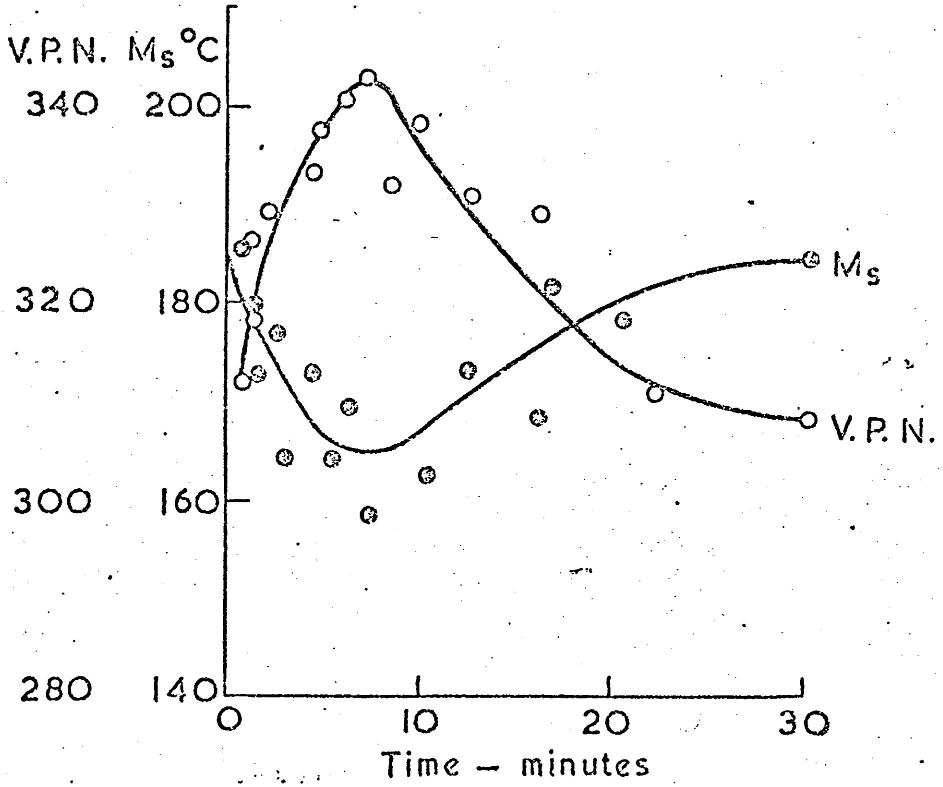
V.P.N.
Ms°C
340
200
320
180
300
160
280
140
0
10
20
30
Time – minutes
Ms
V.P.N.

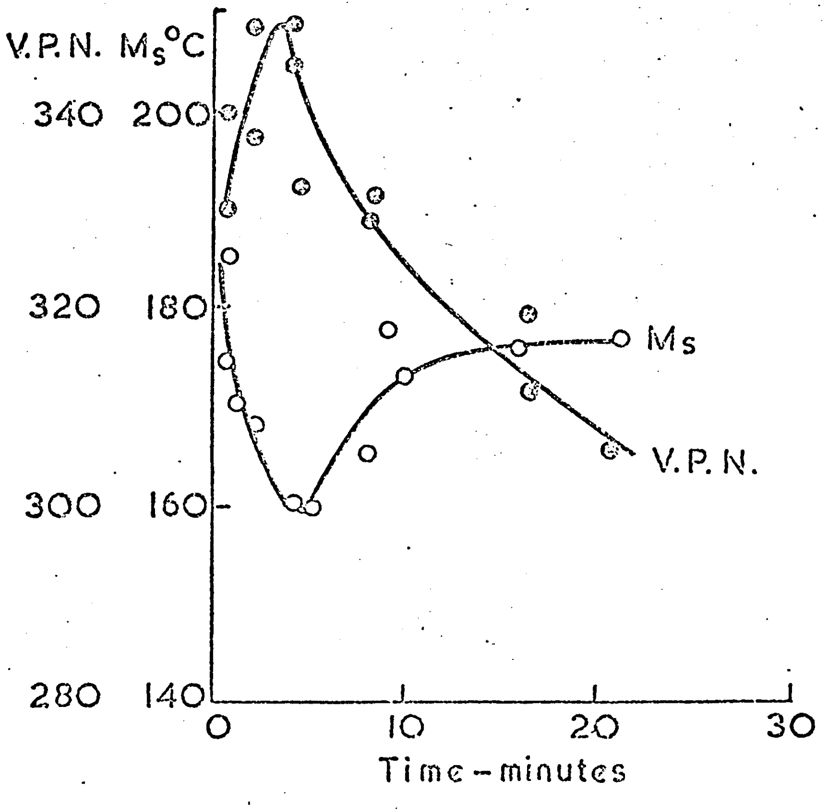
V.P.N.
Ms°C
340
200
320
180
300
160
280
140
0
10
20
30
Time – minutes
Ms
V.P.N.

FIG.53C: Austenitizing temperature 940°C

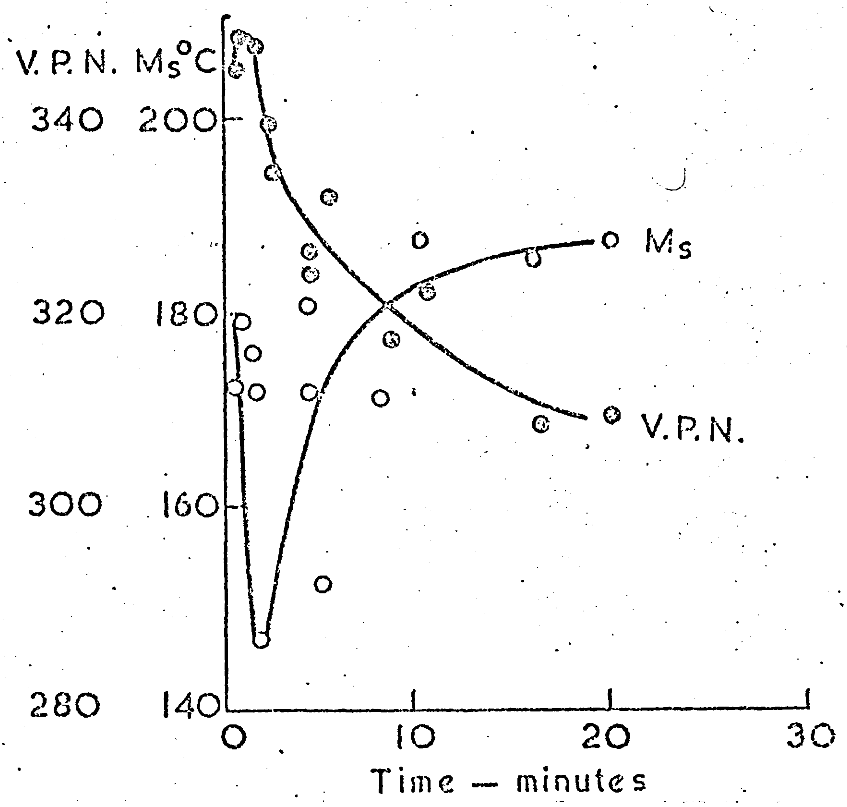
V. P. N.
M_s°C
340
320
300
280
200
180
160
140
0
10
20
30
Time — minutes
M_s
V. P. N.

FIG.54: The variation in hardness and M_s temperature after cycling an iron - 10% manganese alloy through successive $\alpha \rightarrow \gamma \rightarrow \alpha$ transformations using a constant austenitizing temperature of 700°C and a time of one minute.

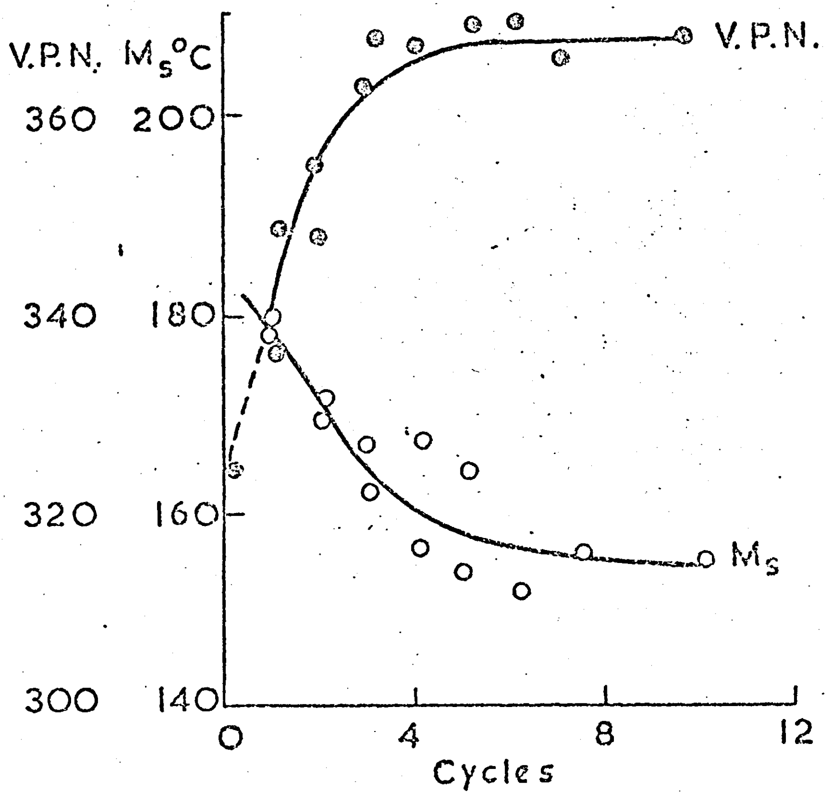
V.P.N.
M$_s$°C
360
200
340
180
320
160
300
140
0
4
8
12
Cycles
V.P.N.
M$_s$

FIG.55: Selected area diffraction pattern taken from a lath boundary such that both laths cause diffraction. The pattern is identical for both laths, i.e. $\langle 111 \rangle_{\alpha}$ zone, and indicates that there is little misorientation across the lath boundary.

FIG.56: Selected area diffraction pattern taken on a lath boundary, and showing a $\langle 100 \rangle_{\alpha}$ zone The same pattern is produced by both laths, and again indicates little misorientation between adjacent laths.

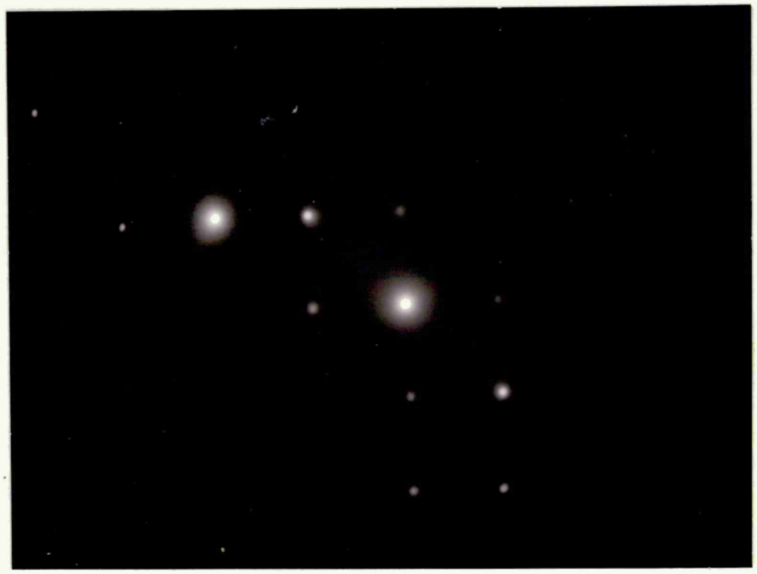

FIG.57: Standard cubic projection in which lath axis directions are shown to be close to $\{110\}_\alpha$ great circles.

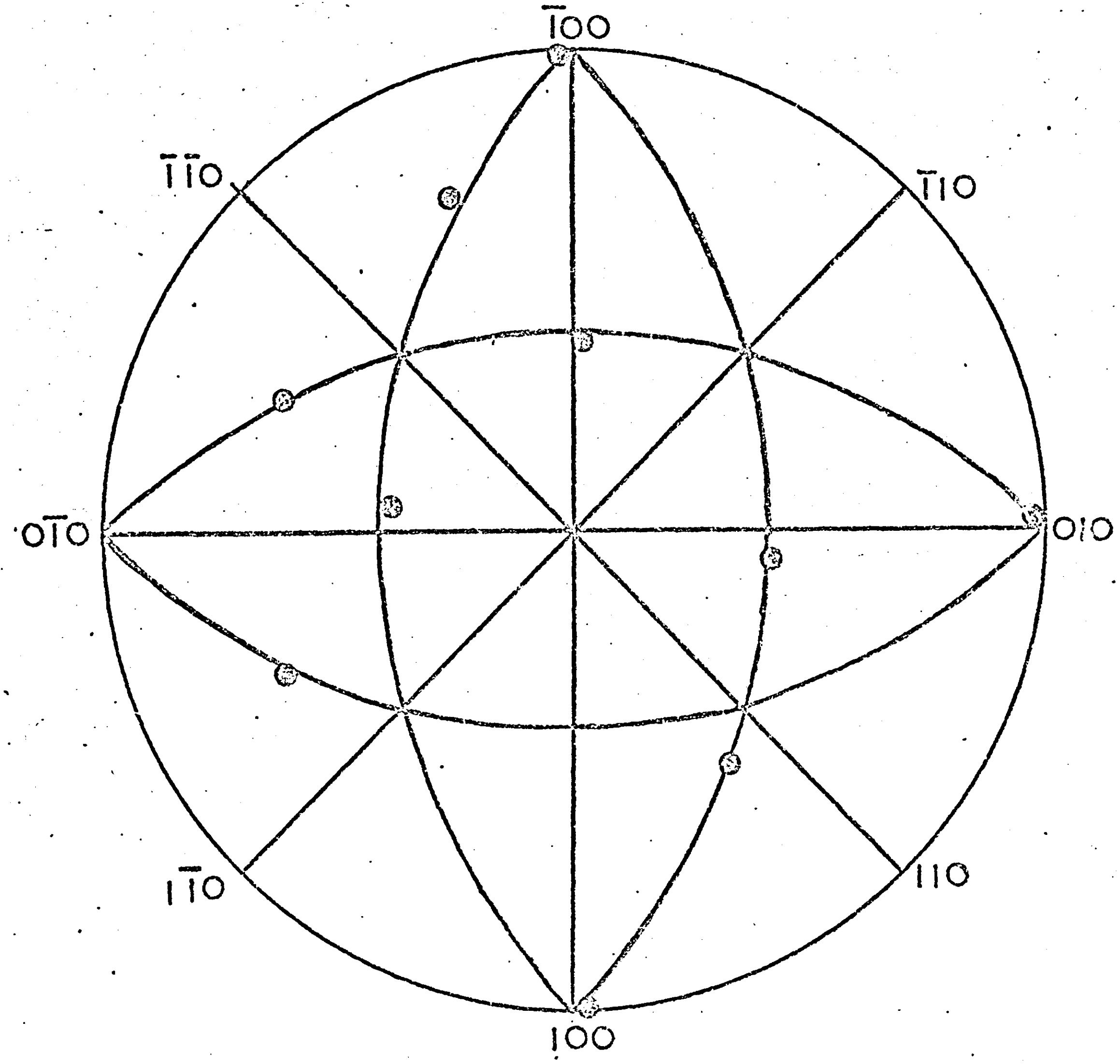
$\bar{1}00$
$\bar{1}\bar{1}0$
$\bar{1}10$
$0\bar{1}0$
010
$1\bar{1}0$
110
100

FIG.58: Thin foil electron micrograph of lath martensite in an iron - 6% manganese alloy with accompnying selected area diffraction pattern taken at the lath boundary and from which the lath boundary direction can be determined. The S.A.D.P. is for a $\langle 100 \rangle_{\alpha}$ zone

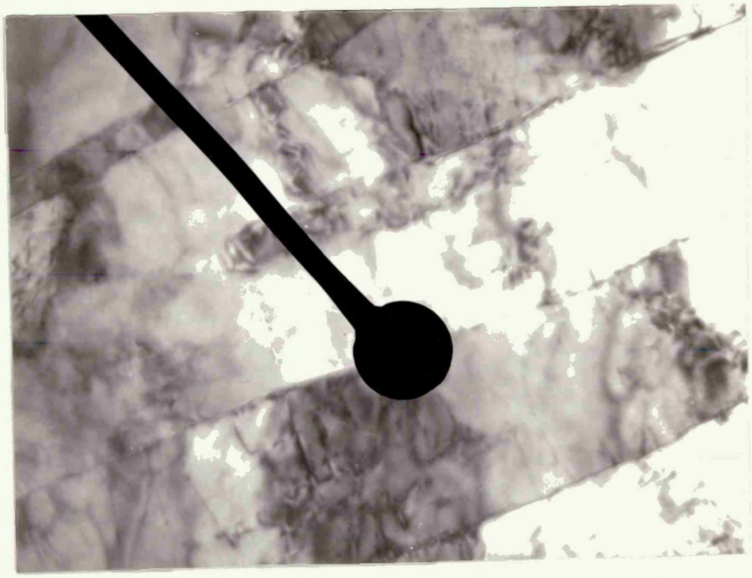

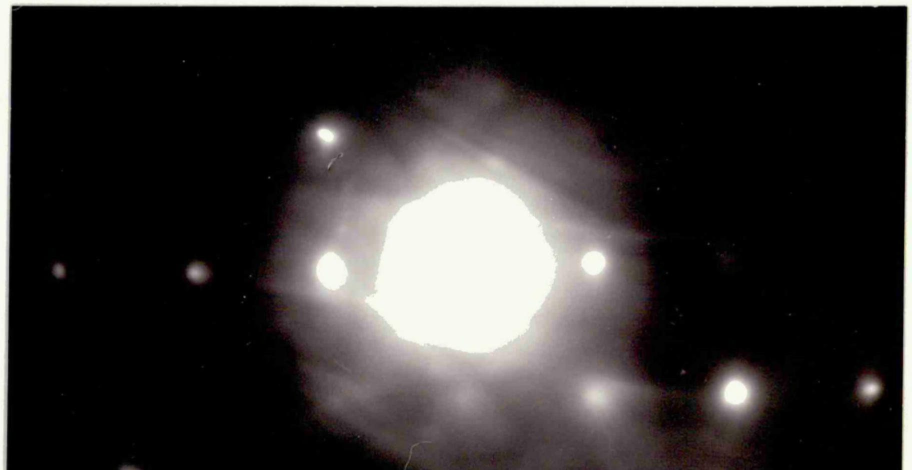

FIG.59: Lath martensite in an iron - 4% manganese alloy showing evidence of prior austenite annealing twins. Note that several martensite slabs lie parallel to the annealing twin boundary, and that slabs which cross the boundary are mirror images on either side of the boundary.

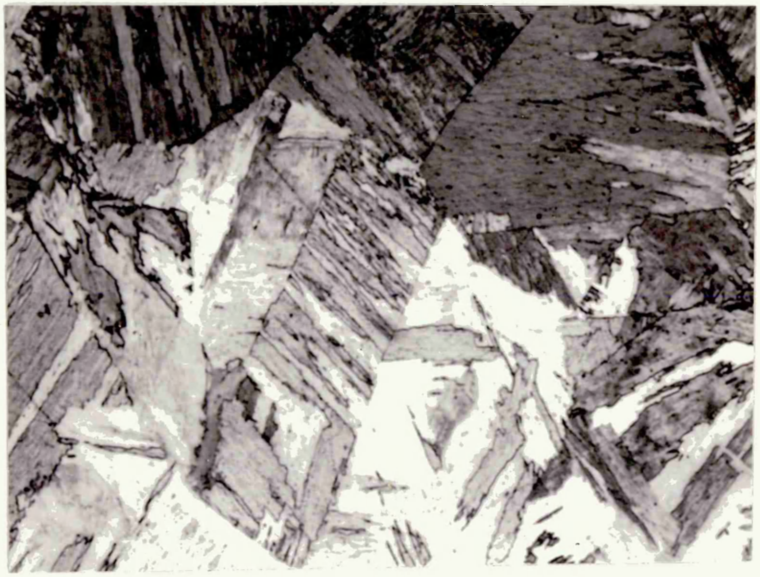

FIG.60: The variation in impact strength with both testing temperature and prior austenite grain size for lath martensites in a series of iron manganese alloys.

FIG.60A: 4% manganese brine quenched.

FIG.60B: 6% manganese brine quenched

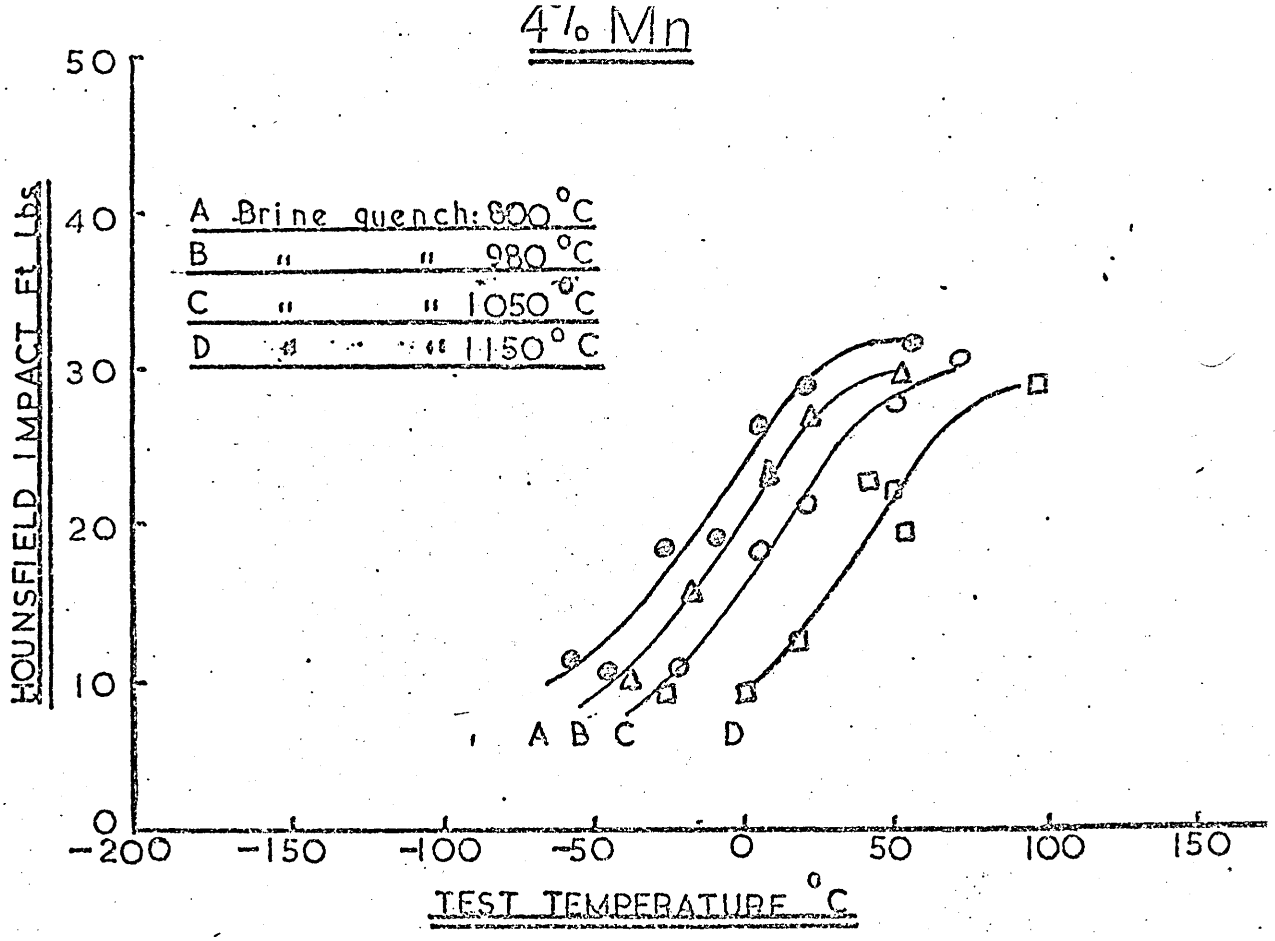
4% Mn
A Brine quench: 800 °C
B " " 980 °C
C " " 1050 °C
D " " 1150 °C
HOUNSFIELD IMPACT Ft Lbs
0
10
20
30
40
50
A B C D
−200 −150 −100 −50 0 50 100 150
TEST TEMPERATURE °C

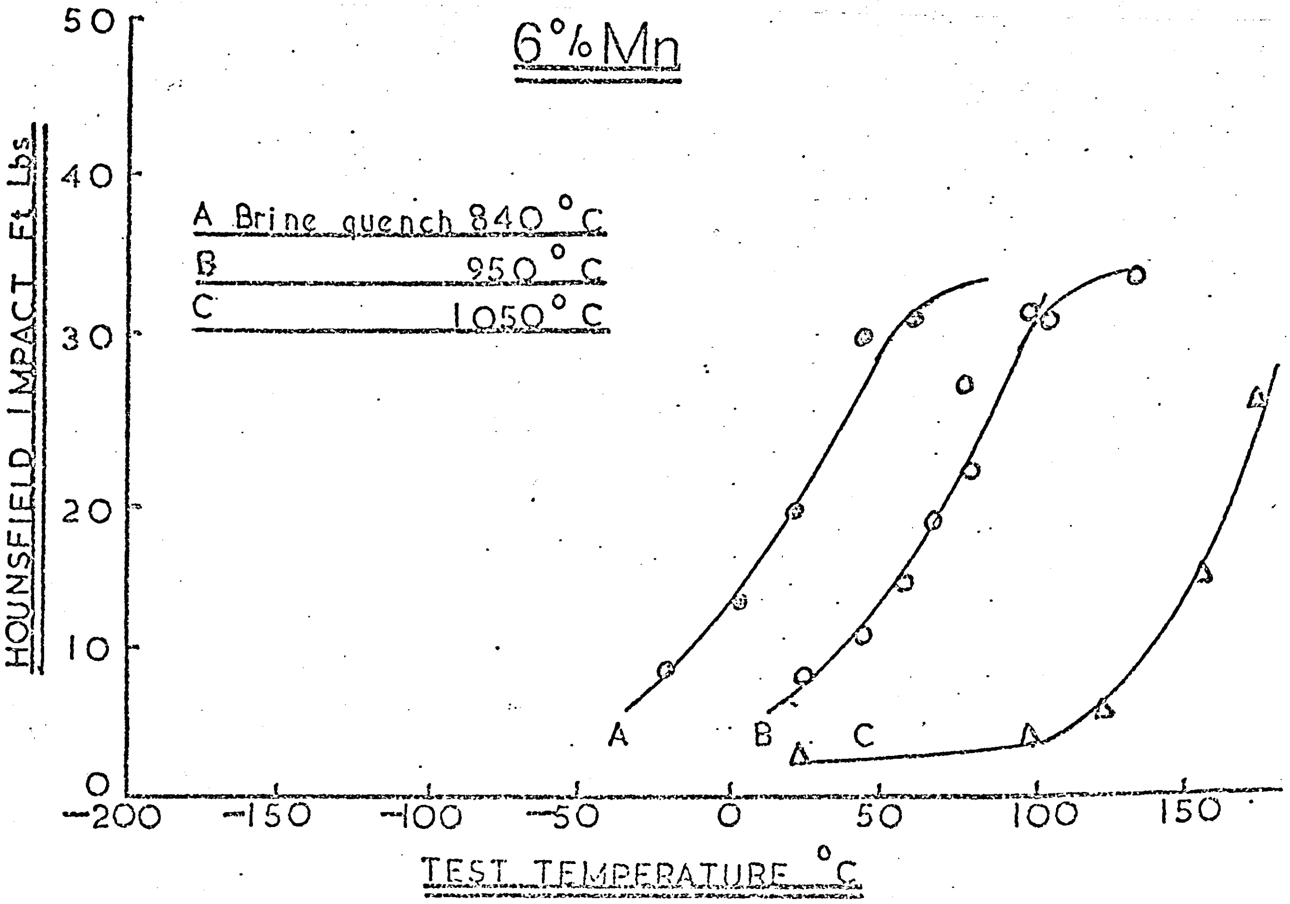
6% Mn
A Brine quench 840 °C
B 950 °C
C 1050 °C
HOUNSFIELD IMPACT Ft Lbs
0
10
20
30
40
50
A B C
−200 −150 −100 −50 0 50 100 150
TEST TEMPERATURE °C

FIG.60C: 8% manganese brine quenched.

FIG.60D: 10% manganese brine quenched

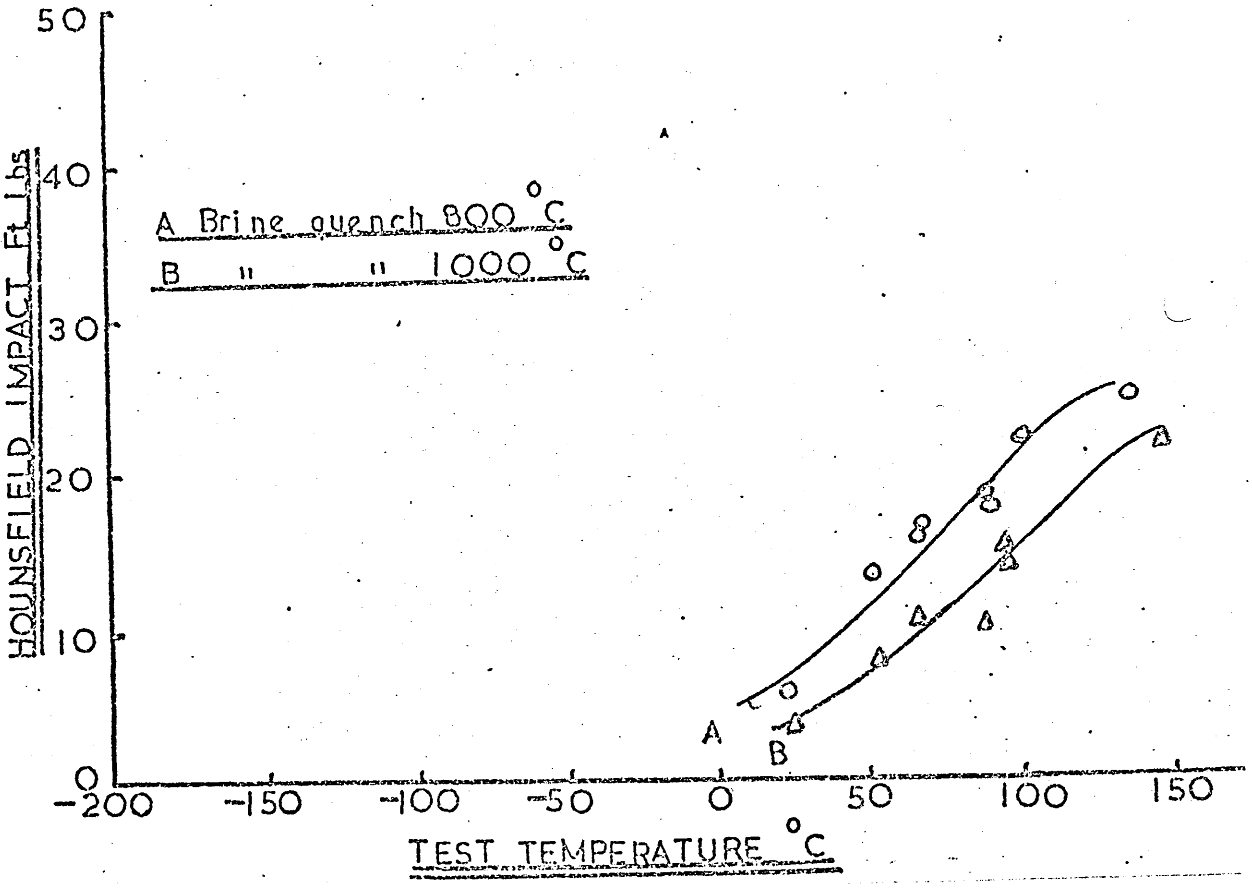

8% Mn

A Brine quench 800 °C
B " " 1000 °C
HOUNSFIELD IMPACT Ft. lbs
50
40
30
20
10
0
-200
-150
-100
-50
0
50
100
150
TEST TEMPERATURE °C
A
B

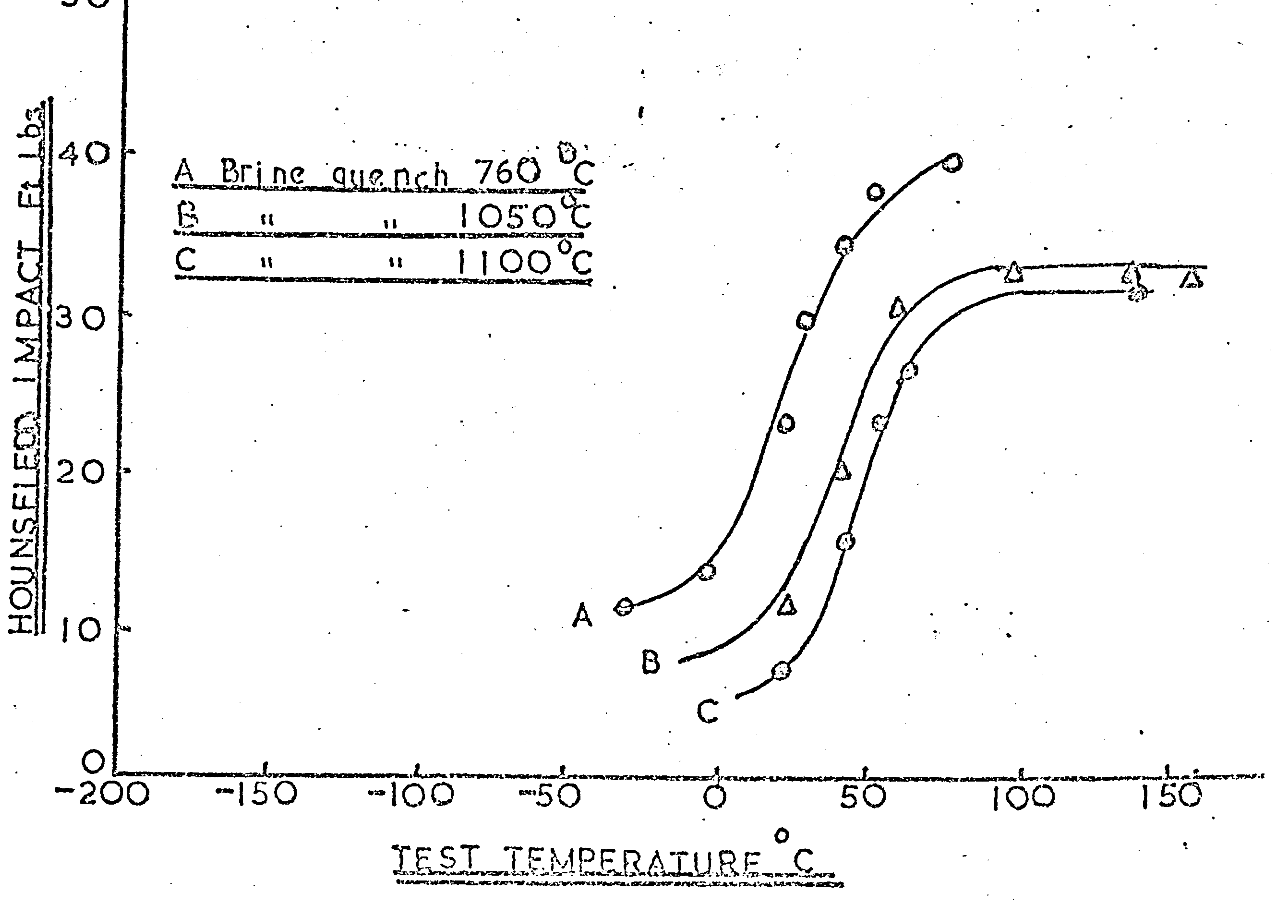

10% Mn

A Brine quench 760 °C
B " " 1050 °C
C " " 1100 °C
HOUNSFIELD IMPACT Ft. lbs
50
40
30
20
10
0
-200
-150
-100
-50
0
50
100
150
TEST TEMPERATURE °C
A
B
C

FIG.61: The variation in reciprocal impact transition temperature with prior austenite grain size for quenched lath martensite iron manganese alloys.

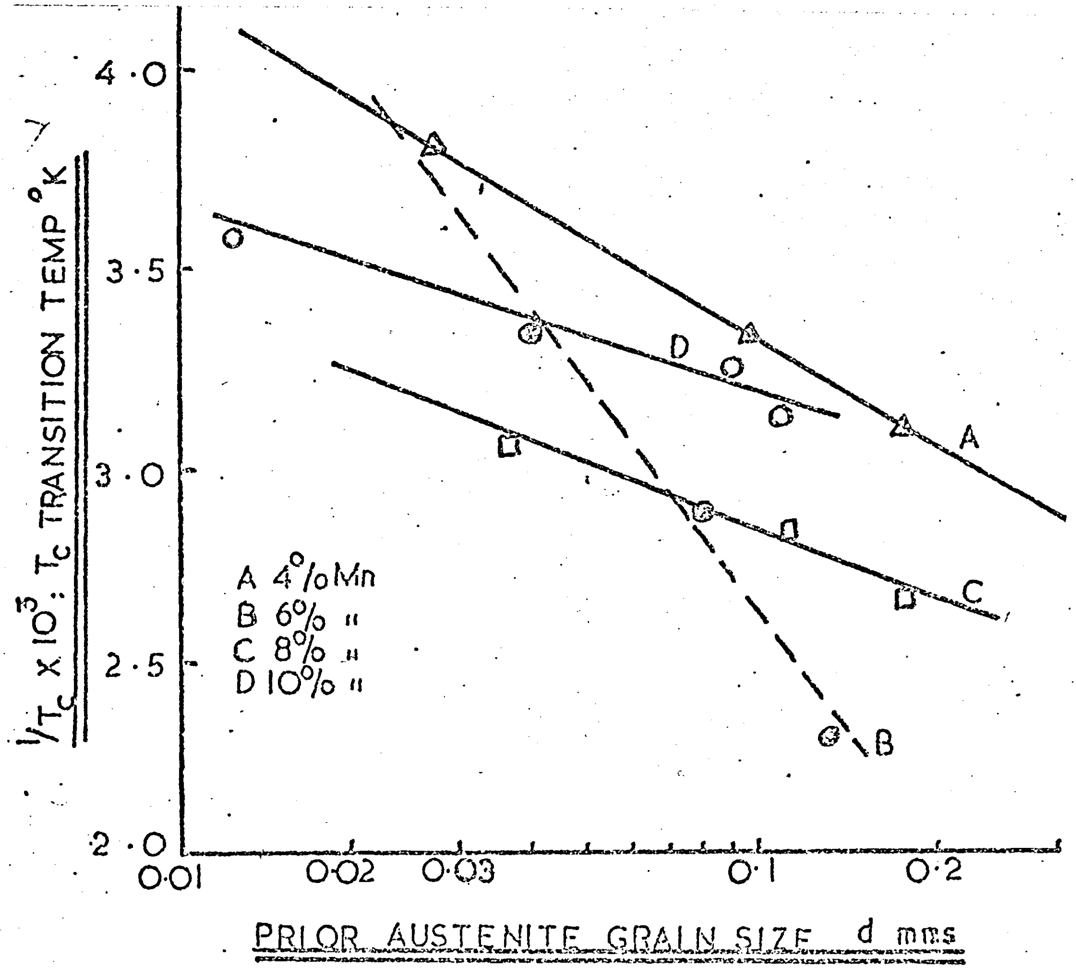

1/Tc x 10³; Tc TRANSITION TEMP °K
4·0
3·5
3·0
2·5
2·0
0·01
0·02
0·03
0·1
0·2
PRIOR AUSTENITE GRAIN SIZE d mms
A 4% Mn
B 6% "
C 8% "
D 10% "
A
B
C
D

FIG.62: Optical photomicrograph showing crack at a prior austenite grain boundary in a quenched iron - 6% manganese alloy.

Etched 2% Nital

x 800

FIG.63A: Scanning electron micrograph of the fracture surface of an iron - 10% manganese alloy impact test specimen tested below the ductile/brittle transition temperature. Fracture largely follows the prior austenite grain boundaries, but some small areas of cleavage also exist, i.e. note river markings.

x 200

FIG.63B: Enlargement of an area of cleavage failure shown in Fig. 63A.

x 1000

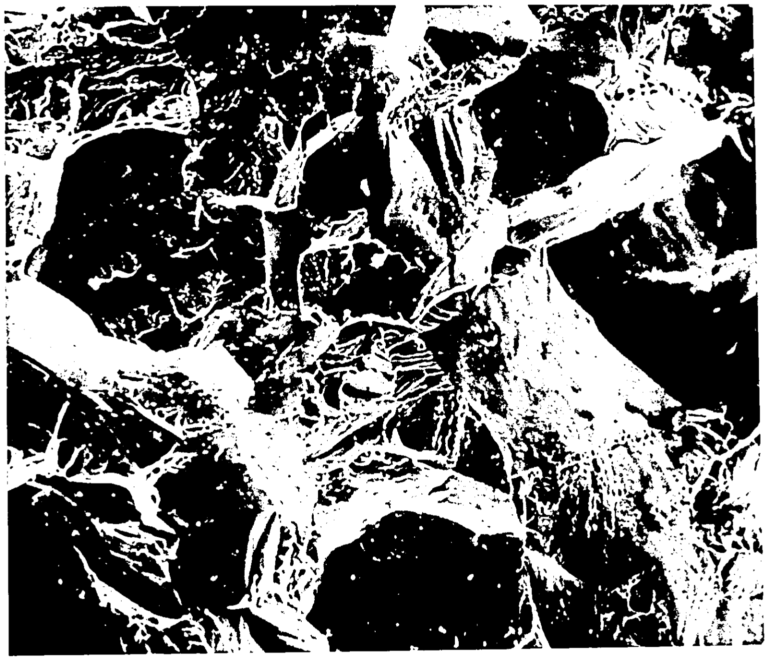

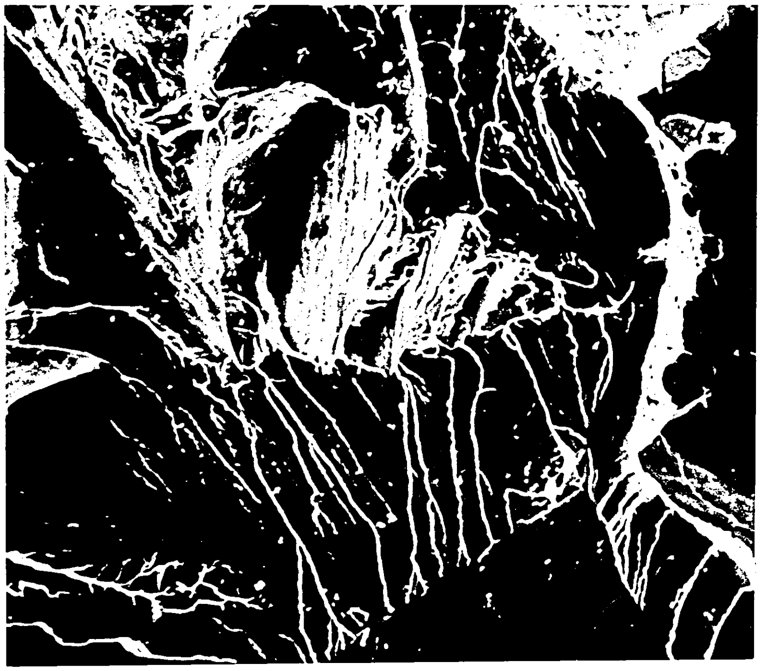

FIG.64: Scanning electron micrograph of the fracture surface of an as quenched iron - 4% manganese alloy showing both intergranular and brittle cleavage facets.

x 150

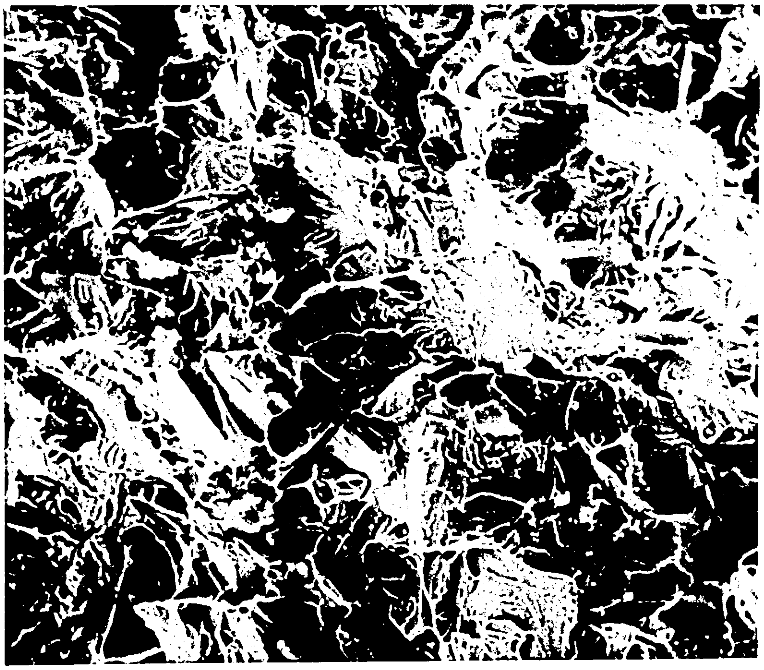

FIG.65: Carbon extraction replica of an iron - 6% manganese alloy quenched and tempered at 450°C and showing preferential etch pitting attack along a prior austenite grain boundary.

x 25,000

FIG.66: The variation in room temperature impact strength with tempering temperature for a series of iron manganese alloys.

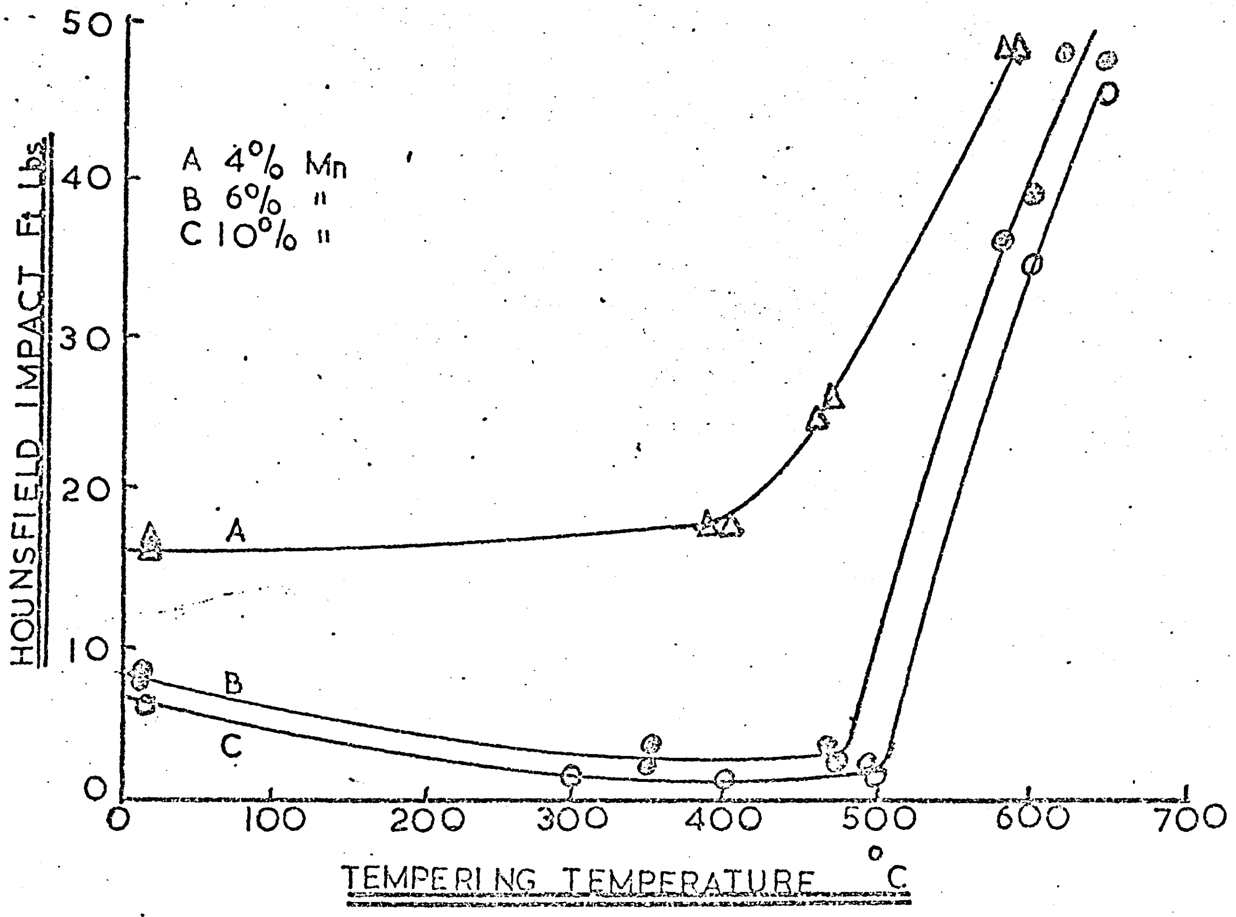

HOUNSFIELD IMPACT Ft Lbs
TEMPERING TEMPERATURE °C
A 4% Mn
B 6% "
C 10% "
A
B
C
0
10
20
30
40
50
0
100
200
300
400
500
600
700

FIG.67: The variation in impact strength with testing temperature for a series of iron manganese alloys after being given various tempering or slow cooling treatments.

FIG.67A Iron - 4% manganese.

FIG.67B Iron - 6% manganese.

4% Mn

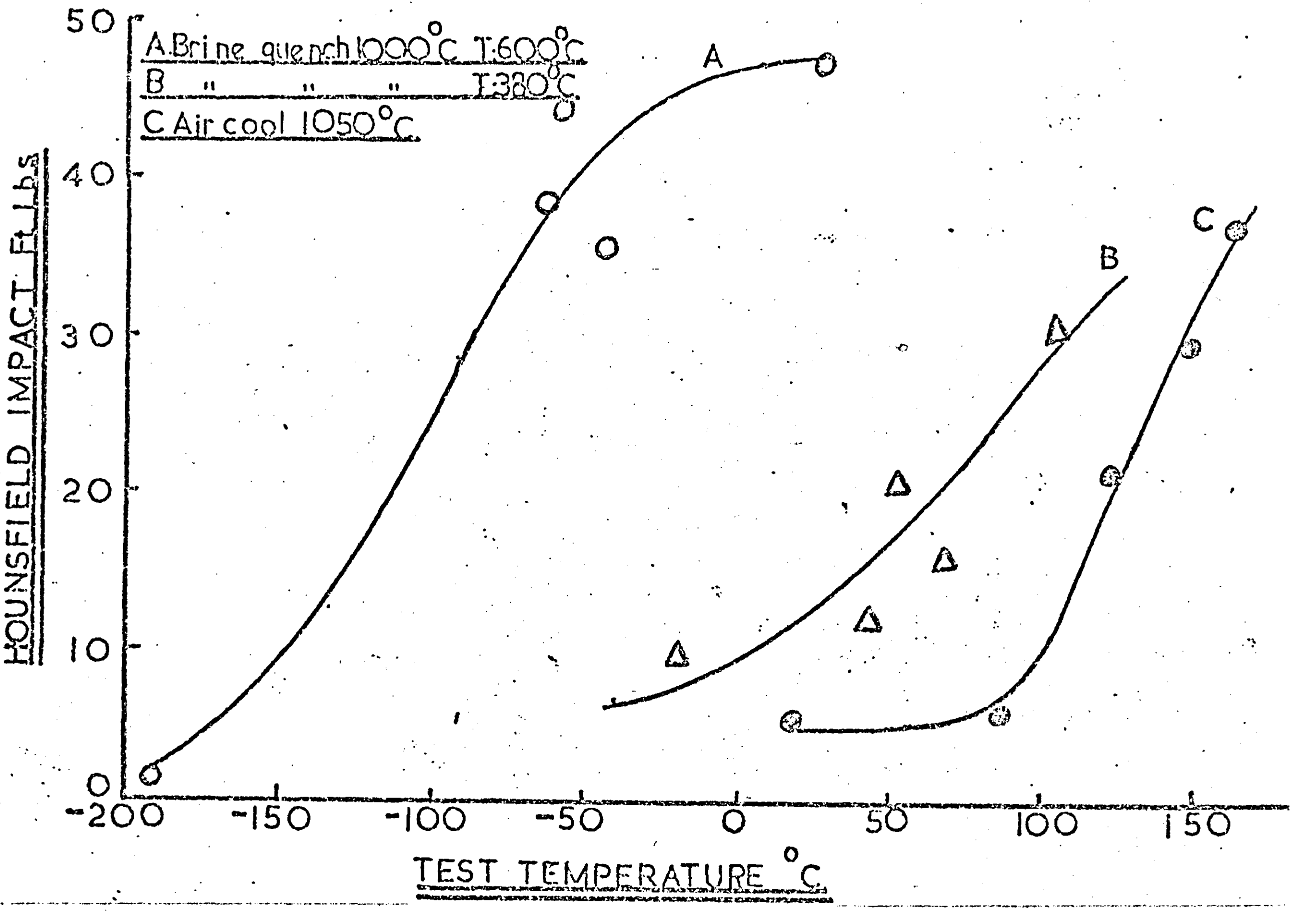
A Brine quench 1000°C T:600°C
B " " " T:380°C
C Air cool 1050°C
A
B
C
HOUNSFIELD IMPACT Ft.lbs
0
10
20
30
40
50
-200
-150
-100
-50
0
50
100
150
TEST TEMPERATURE °C

6%Mn

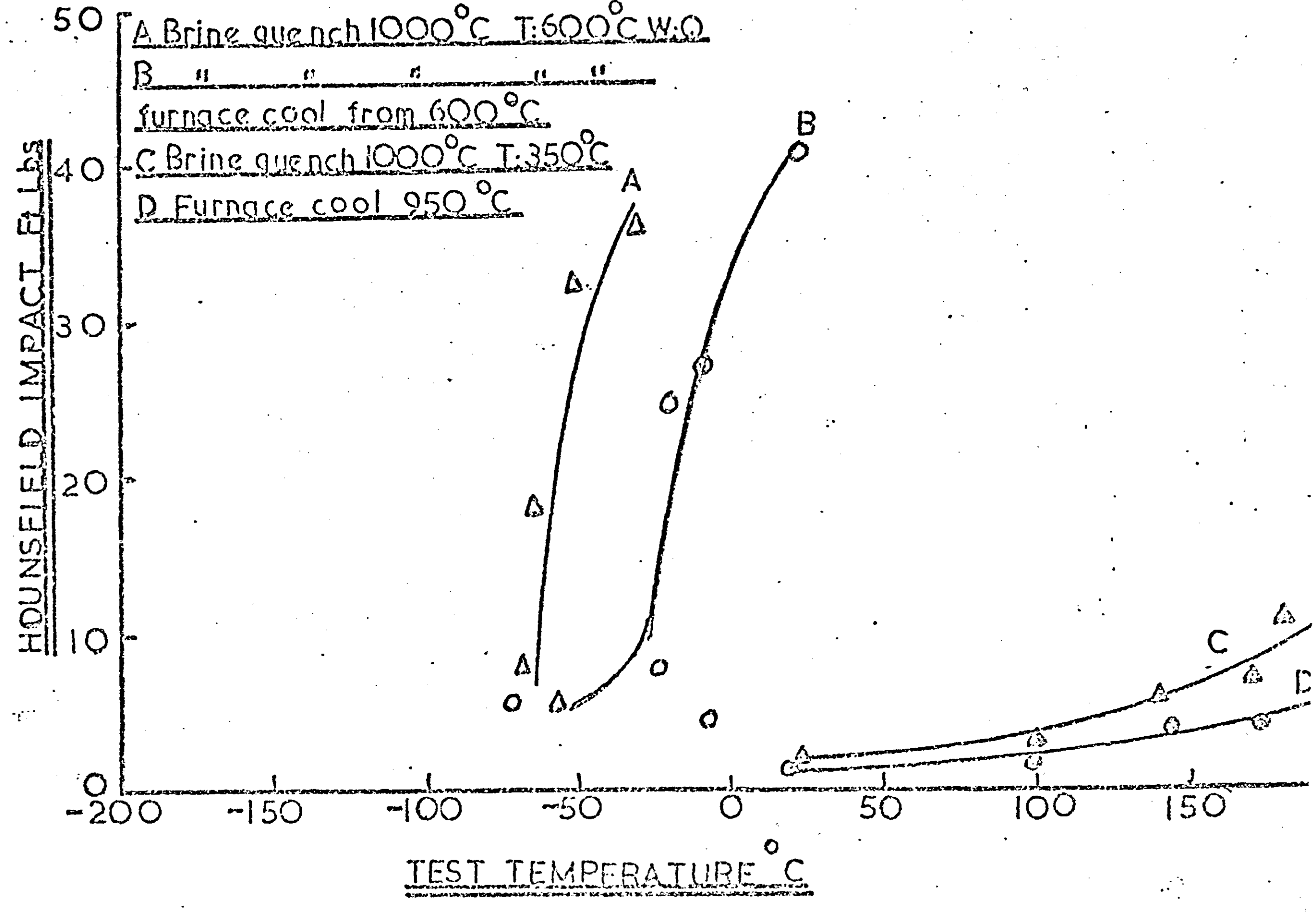
A Brine quench 1000°C T:600°C W.Q.
B " " " " "
furnace cool from 600°C
C Brine quench 1000°C T:350°C
D Furnace cool 950°C
A
B
C
D
HOUNSFIELD IMPACT Ft.lbs
0
10
20
30
40
50
-200
-150
-100
-50
0
50
100
150
TEST TEMPERATURE °C

FIG.67C: Iron - 10% manganese.

10% Mn

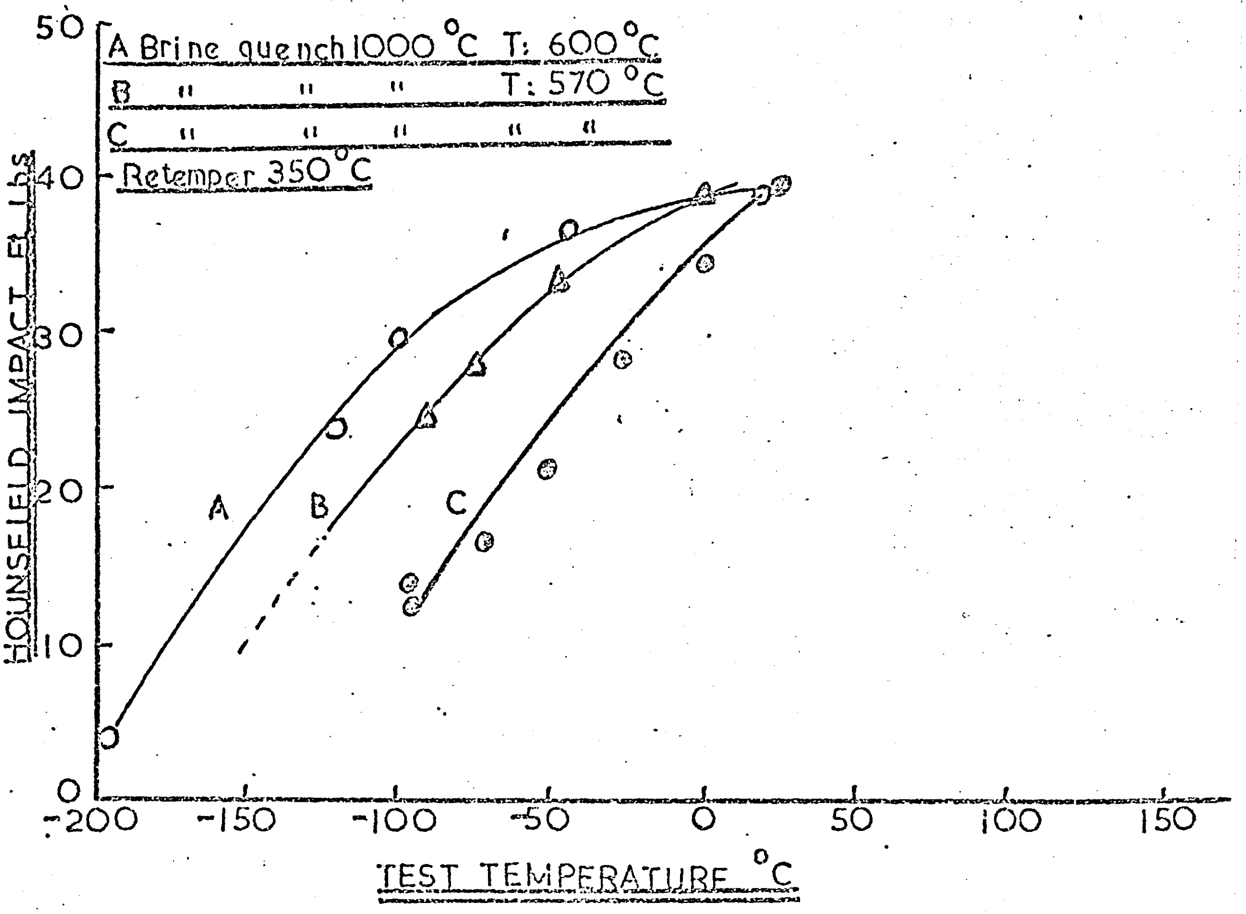
A Brine quench 1000 °C T: 600 °C
B " " " T: 570 °C
C " " " " "
Retemper 350 °C
HOUNSFIELD IMPACT Ft. lbs
0
10
20
30
40
50
A
B
C
-200
-150
-100
-50
0
50
100
150
TEST TEMPERATURE °C

FIG.68A: Scanning electron micrograph of the fracture surface of a quenched and tempered iron - 6% manganese alloy. The fracture occurred at -196°C in a completely brittle manner, and the tempering treatment consisted of one hour at 600°C followed by water quenching.

FIG.68B: Scanning electron micrograph of the fracture surface of a quenched and tempered iron - 6% manganese alloy, again showing brittle fracture but in a specimen which had been slowly cooled from its tempering temperature of 600°C. Note fracture at prior austenite grain boundaries.

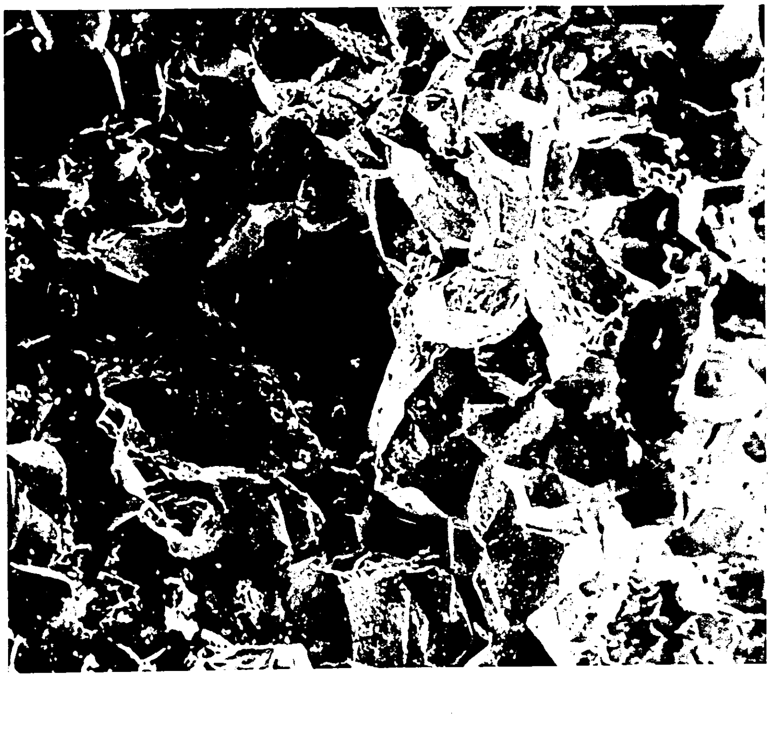

FIG.69: Scanning electron micrograph of the fracture surface of an iron - 4% manganese alloy which had been heat treated by air cooling from 1050°C. Brittle fracture was largely comprised of failure at the prior austenite grain boundaries.

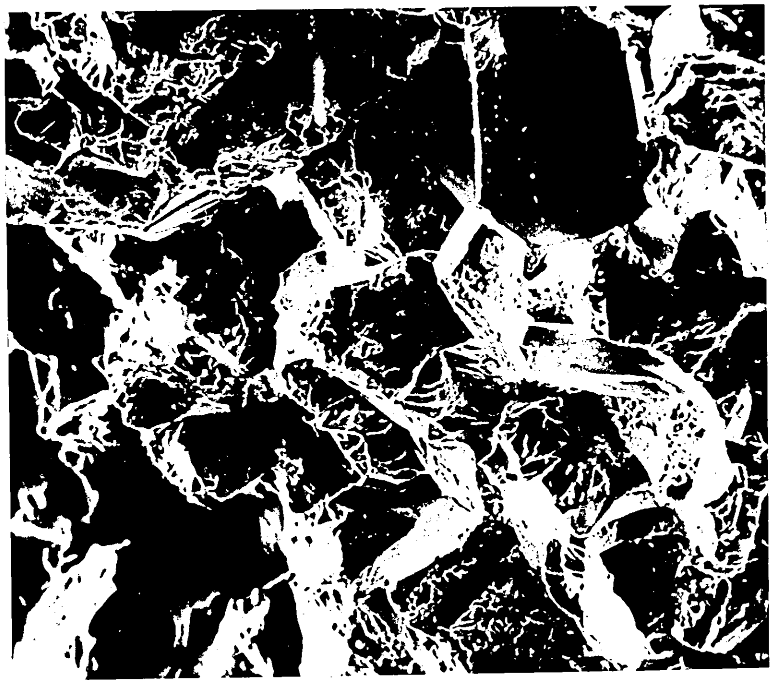

FIG. 70: Optical photomicrograph showing the breakup of a lath martensite structure in an iron - 6% manganese alloy due to tempering at 600°C

Etched 2% Nital followed by
Schummann's reagent.
x 800

FIG.71: The effects of tempering on the outline of an x-ray diffractometer trace of the $\{110\}_\alpha$ and $\{112\}_\alpha$ bcc relections.

FIG.71A: Iron - 10% manganese alloy, brine quenched.

FIG.71B: Iron - 10% manganese alloy, brine quenched and tempered at 600°C

10%Mn

BRINE QUENCHED 1000° C

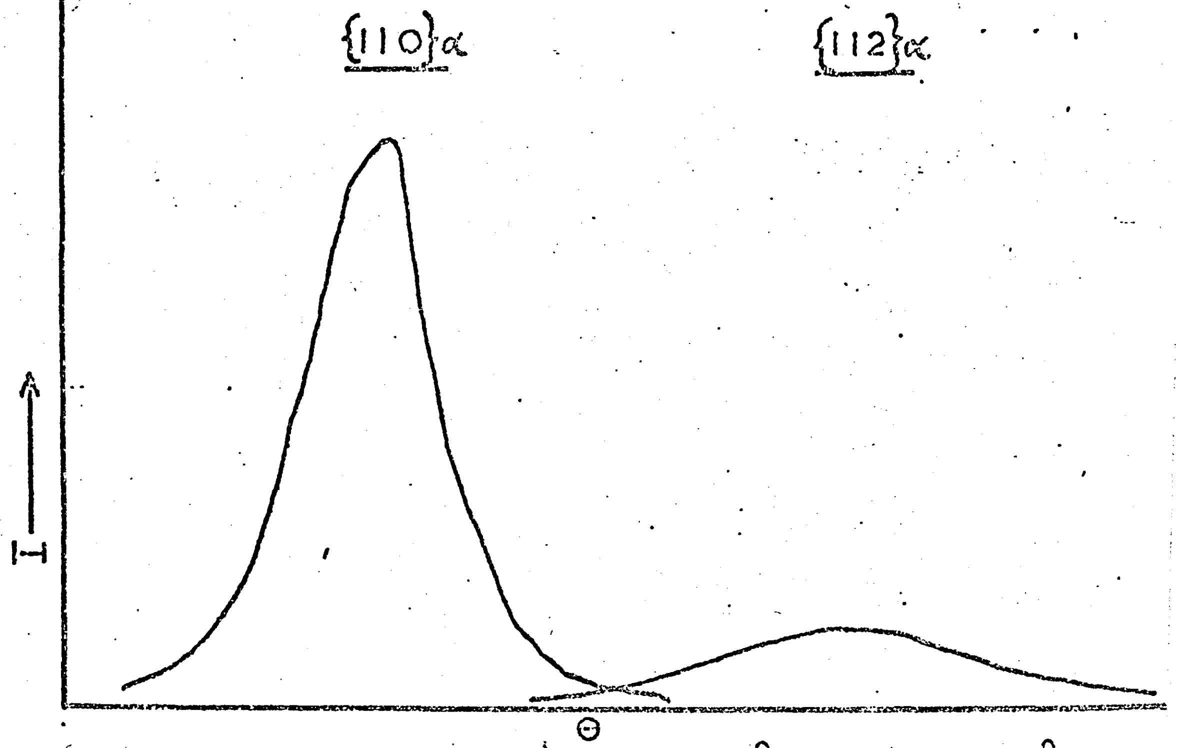

BRINE QUENCHED 1000° C; TEMPER 600° C

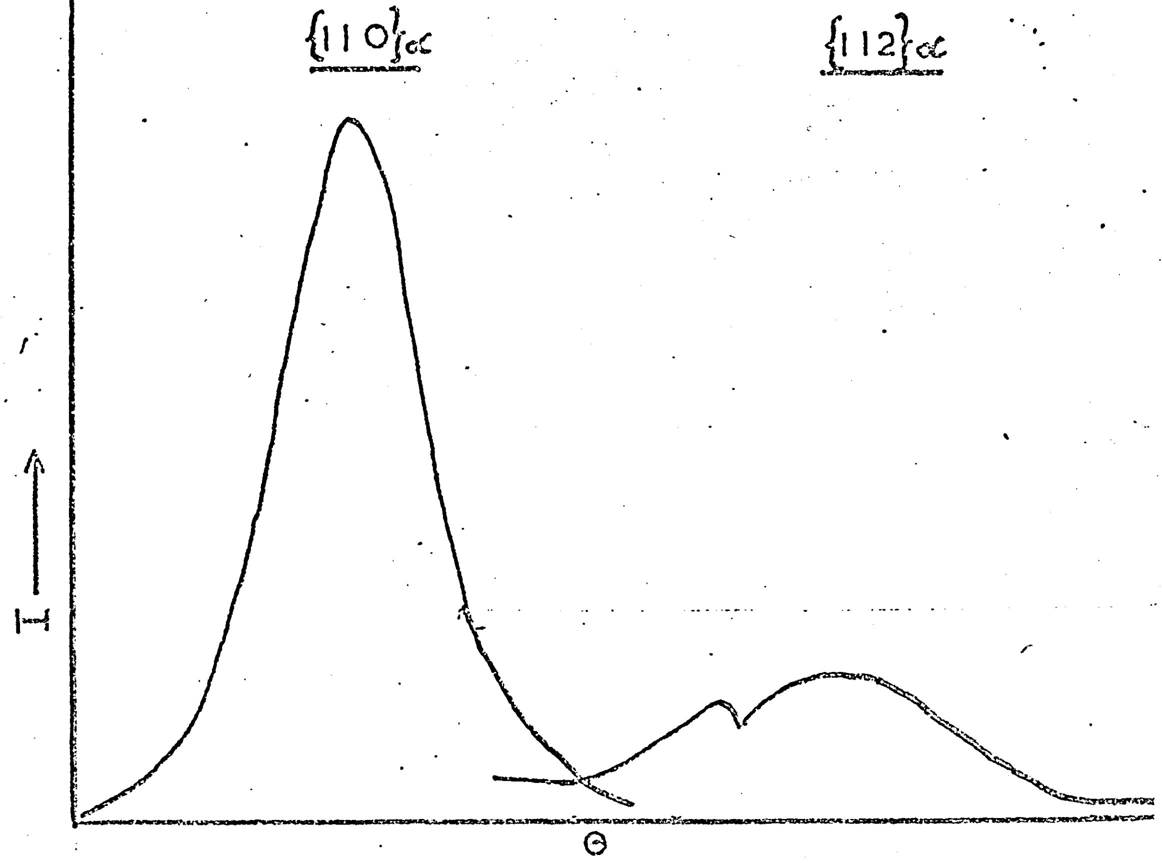

FIG.72: The variation in impact strength with testing temperature for a vacuum melted high purity iron - manganese; and iron - manganese molybdenum alloy, in both the quenched and tempered conditions.

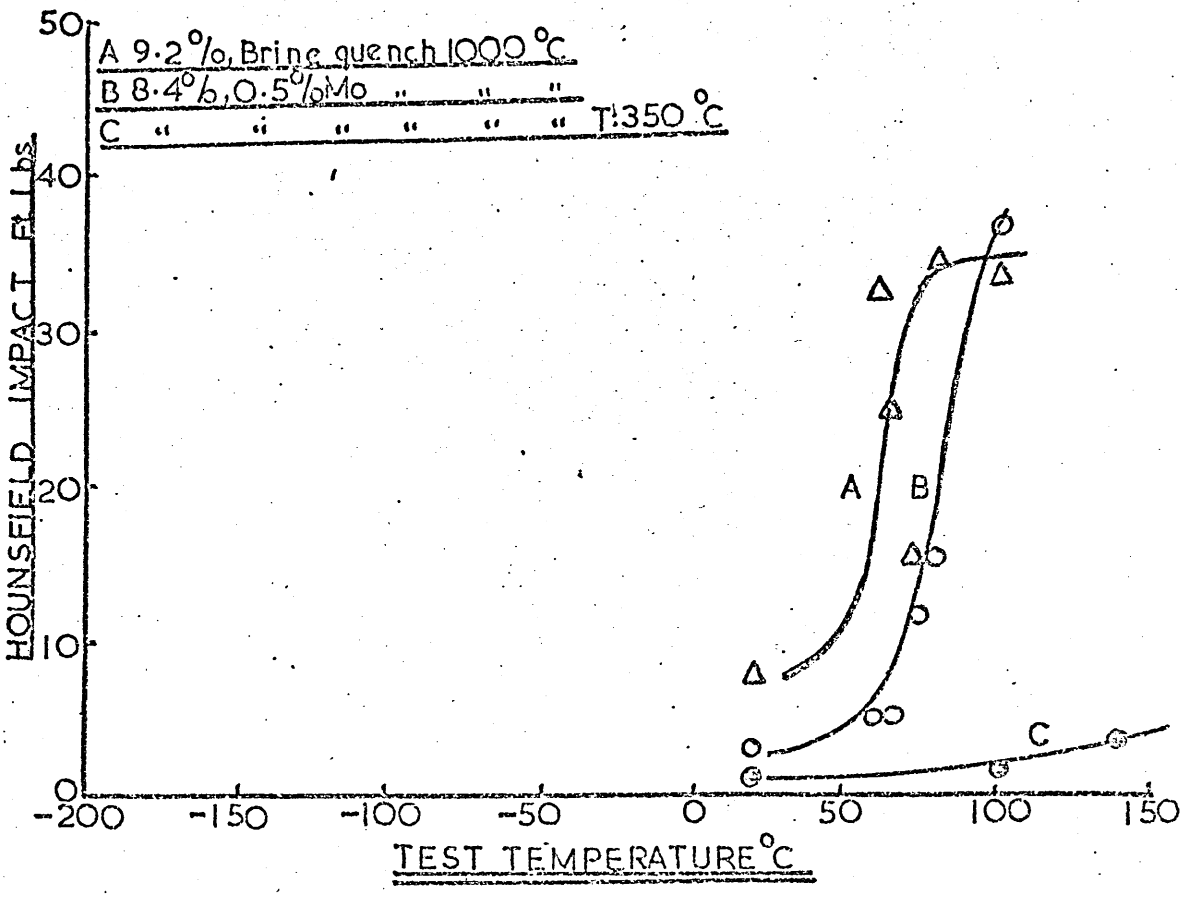
A 9·2%, Brine quench 1000 °C
B 8·4%, 0·5% Mo " " "
C " " " " " " T:350 °C
HOUNSFIELD IMPACT Ft Lbs
50
40
30
20
10
0
-200
-150
-100
-50
0
50
100
150
TEST TEMPERATURE °C
A
B
C

FIG.73: Typical load elongation curves obtained during the tensile testing of a series of brine quenched iron manganese alloys.

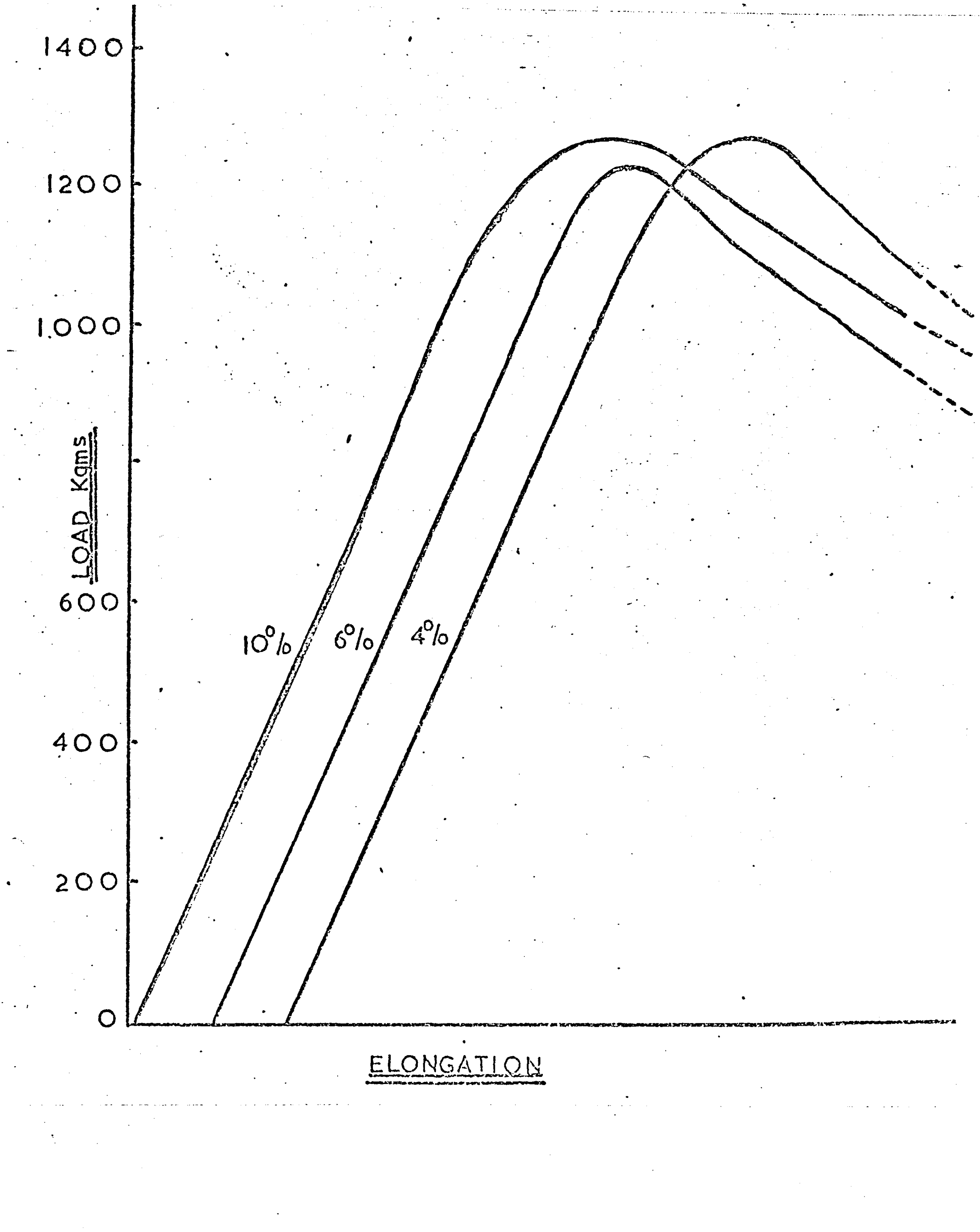

1400
1200
1.000
600
400
200
0
LOAD Kgms
10%
6%
4%
ELONGATION

FIG.74: Petch plots of flow stress versus the reciprocal square root of prior austenite grain size for a series of iron manganese alloys in the as quenched lath martensitic condition.

FIG.74A: Iron - 4% Manganese.

FIG.74B: Iron - 6% Manganese.

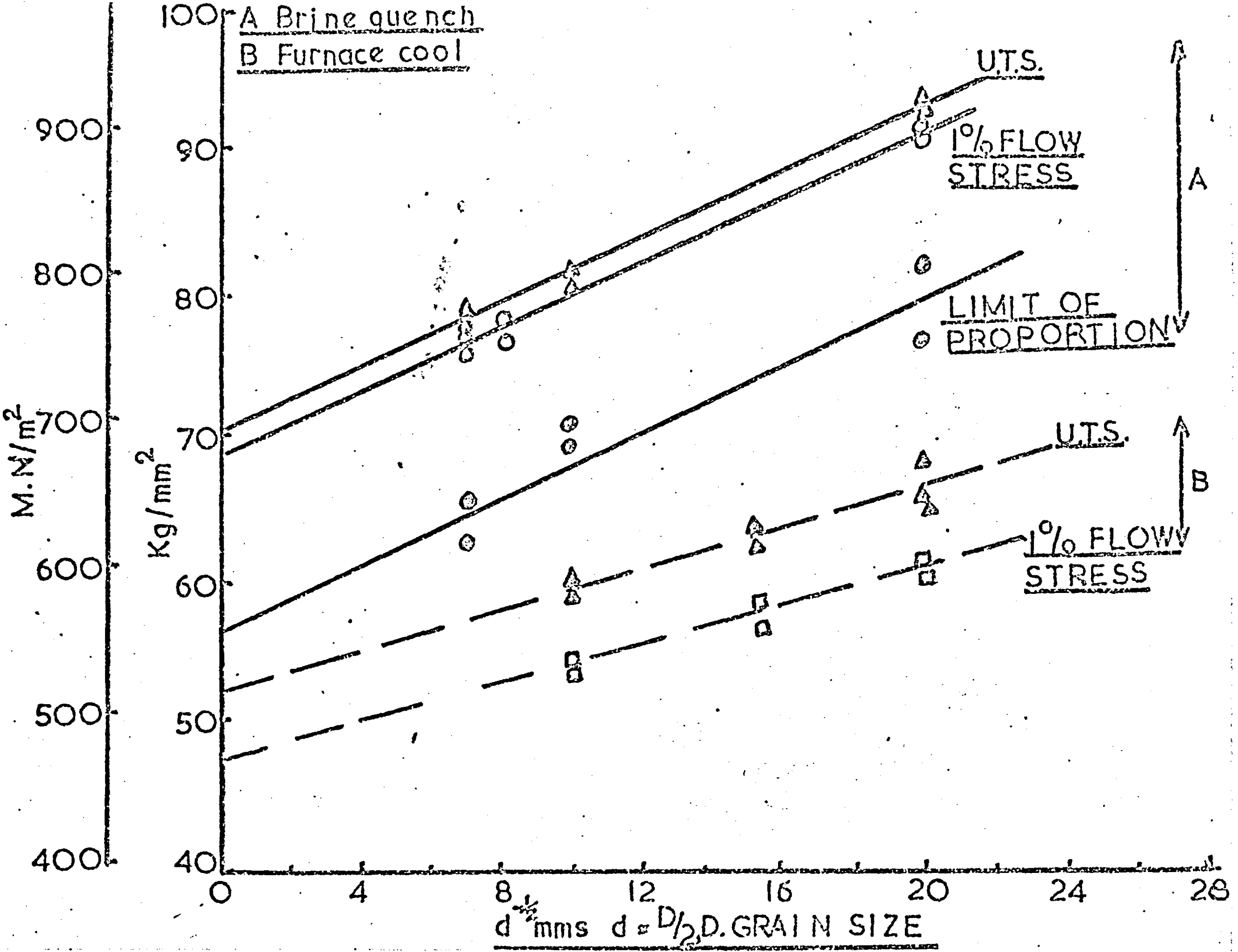
A Brine quench
B Furnace cool
U.T.S.
1% FLOW STRESS
LIMIT OF PROPORTION
A
U.T.S.
1% FLOW STRESS
B
M.N/m^2
400
500
600
700
800
900
Kg/mm^2
40
50
60
70
80
90
100
0
4
8
12
16
20
24
28
$d^{-1/2}$ mms d = D/2, D. GRAIN SIZE

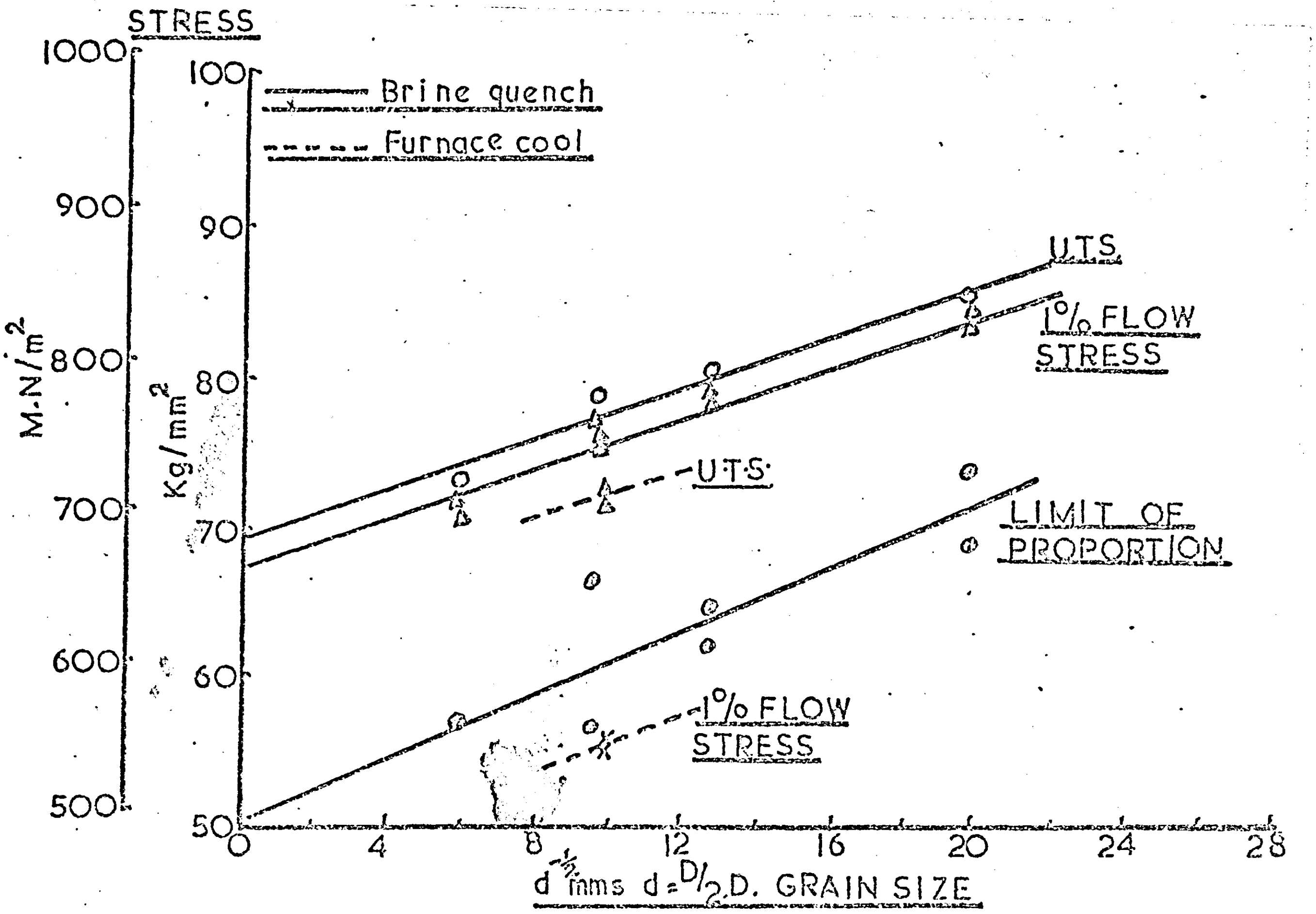
STRESS
Brine quench
Furnace cool
U.T.S.
1% FLOW STRESS
U.T.S.
LIMIT OF PROPORTION
1% FLOW STRESS
M.N/m^2
500
600
700
800
900
1000
Kg/mm^2
50
60
70
80
90
100
0
4
8
12
16
20
24
28
$d^{-1/2}$ mms d = D/2, D. GRAIN SIZE

FIG.74C: Iron - 8% Manganese.

FIG.74D: Iron - 10% Manganese.

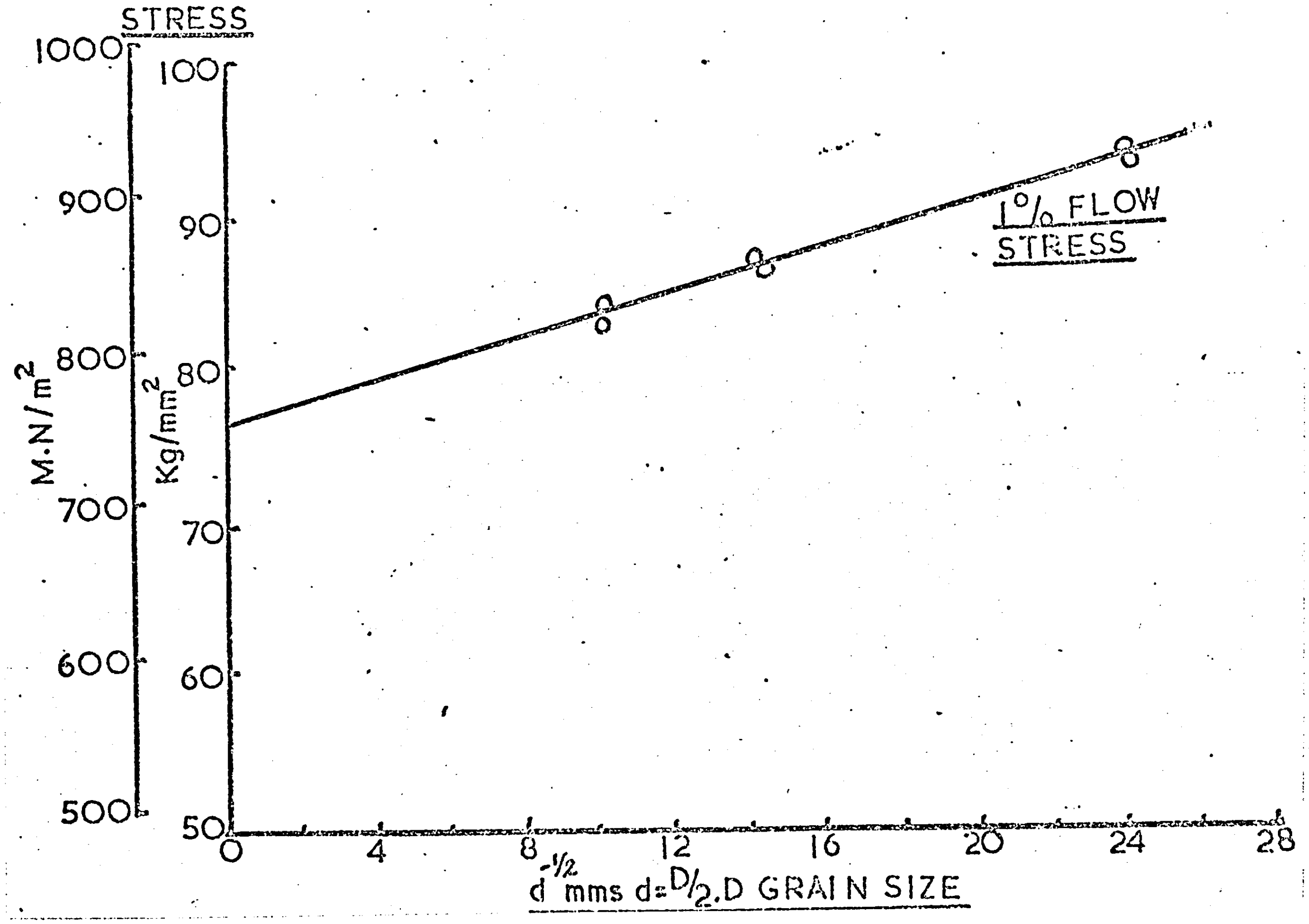
STRESS
M.N/m²
Kg/mm²
1000
900
800
700
600
500
100
90
80
70
60
50
0
4
8
12
16
20
24
28
d^-½ mms d=D/2.D GRAIN SIZE
1% FLOW STRESS

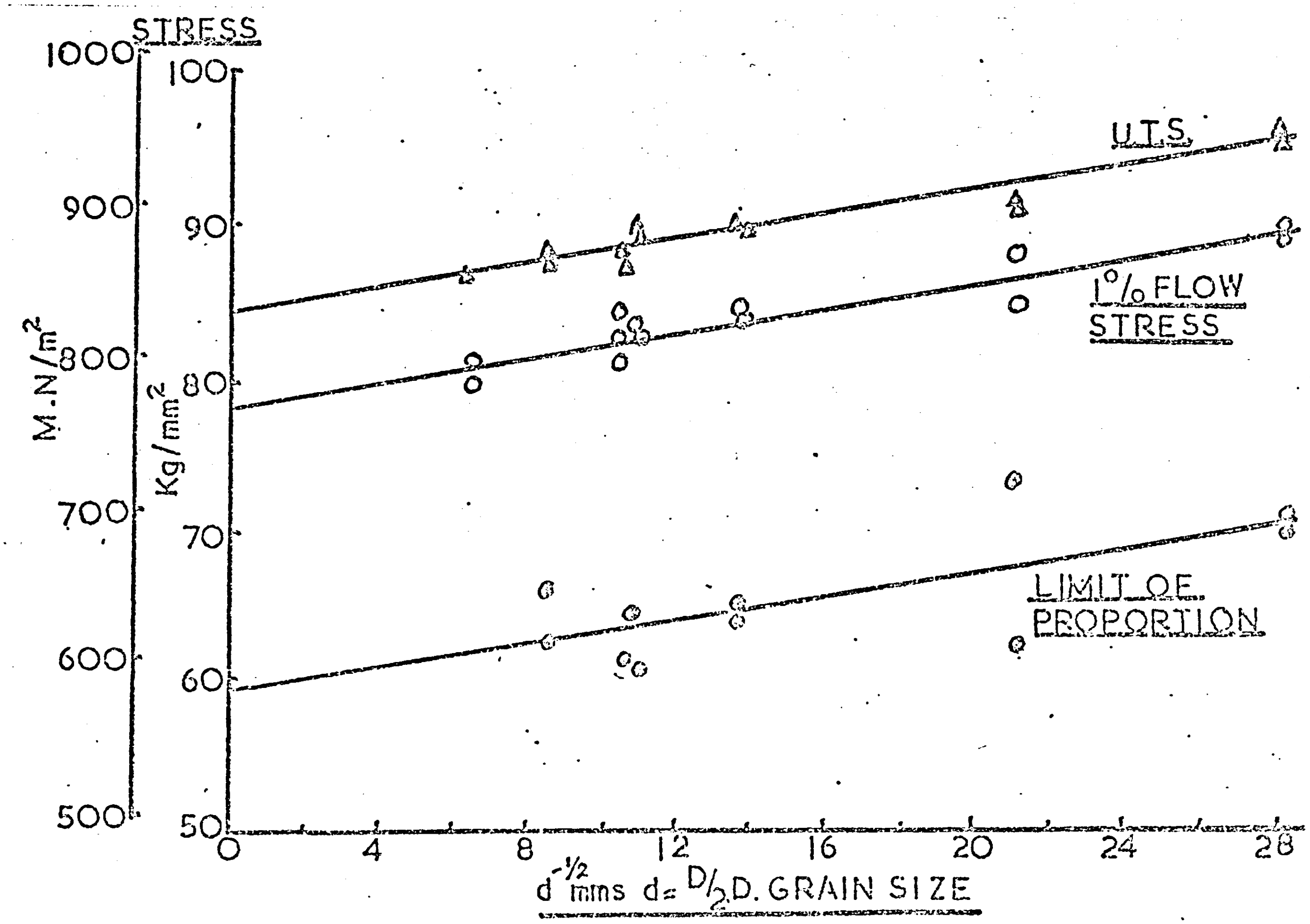
STRESS
M.N/m²
Kg/mm²
1000
900
800
700
600
500
100
90
80
70
60
50
0
4
8
12
16
20
24
28
d^-½ mms d=D/2.D. GRAIN SIZE
U.T.S.
1% FLOW STRESS
LIMIT OF PROPORTION

FIG. 75: The variation of K_y with manganese concentration

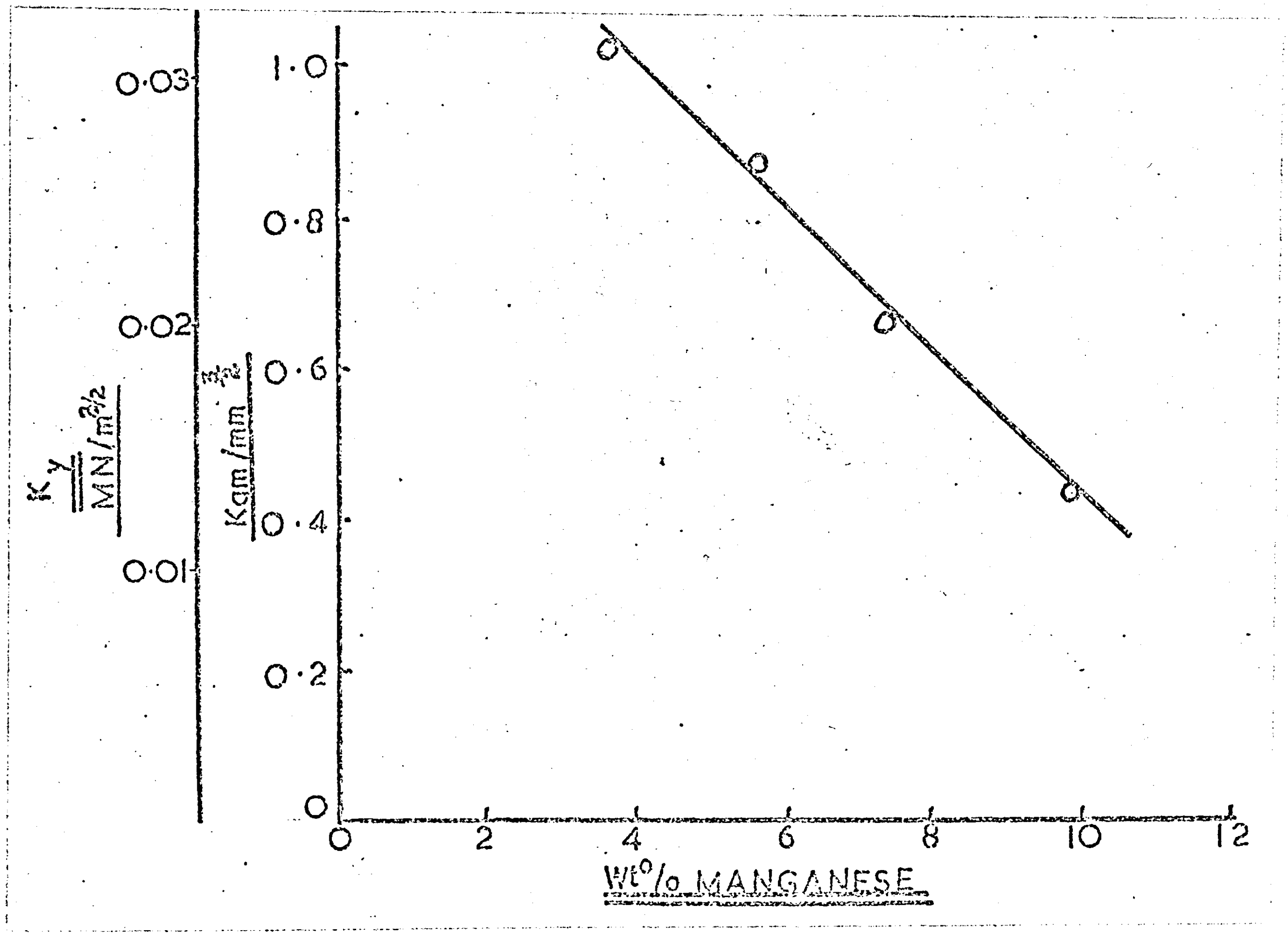

K_y
MN/m$^{3/2}$
0·03
0·02
0·01
Kgm/mm$^{3/2}$
1·0
0·8
0·6
0·4
0·2
0
0
2
4
6
8
10
12
Wt°/o MANGANESE

FIG.76: The variation in the flow stress $\sigma_i \simeq \sigma_o$ with manganese concentration.

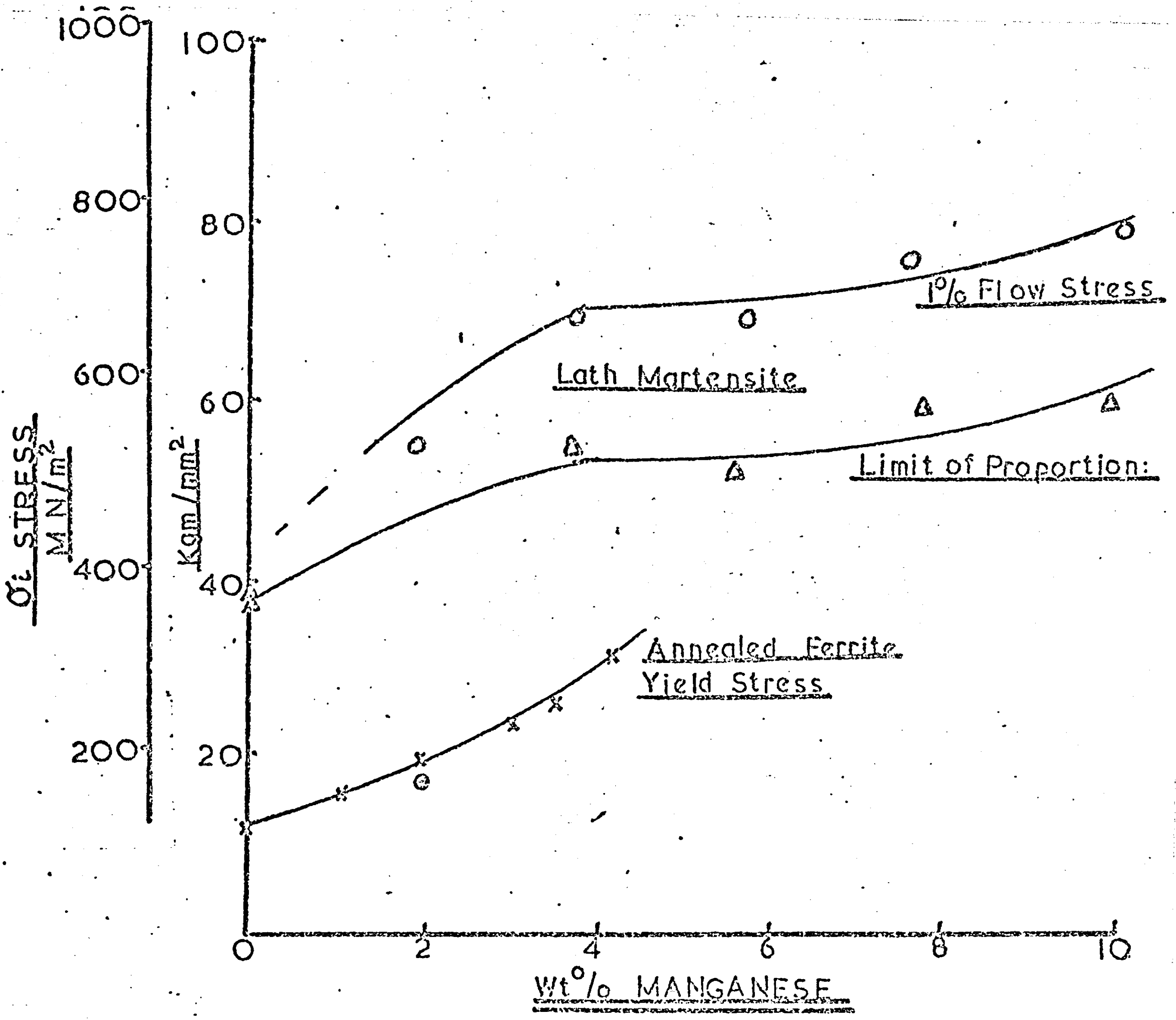
1000
800
600
400
200
σ_i STRESS
MN/m^2
100
80
60
40
20
Kgm/mm^2
0
2
4
6
8
10
Wt% MANGANESE
1% Flow Stress
Lath Martensite
Limit of Proportion:
Annealed Ferrite
Yield Stress

FIG.77: The variation in mean room temperature hardness with manganese concentration.

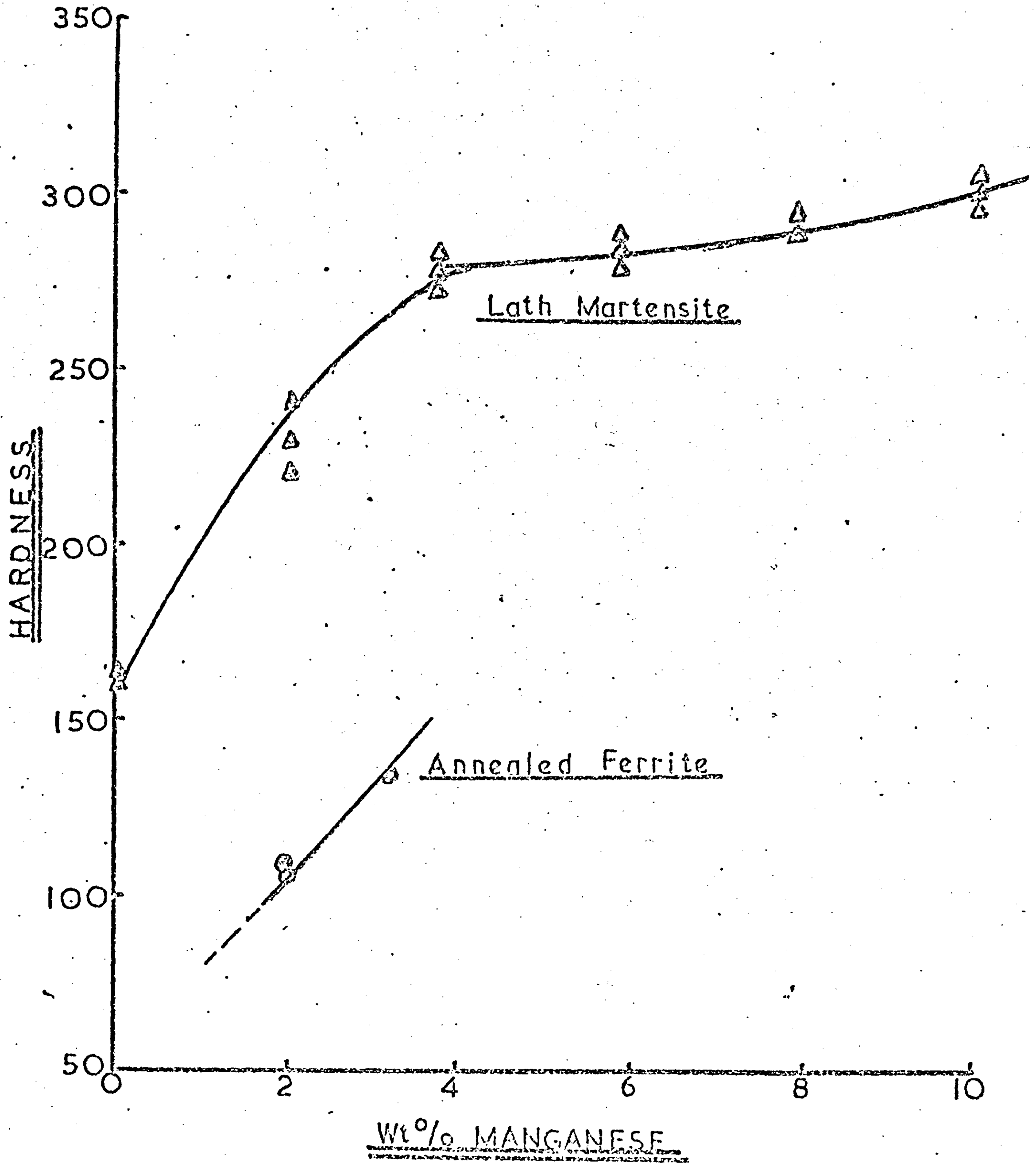
350
300
250
200
150
100
50
HARDNESS
Lath Martensite
Annealed Ferrite
0
2
4
6
8
10
Wt% MANGANESE

FIG.78: The variation in lattice parameter, a, with manganese concentration.

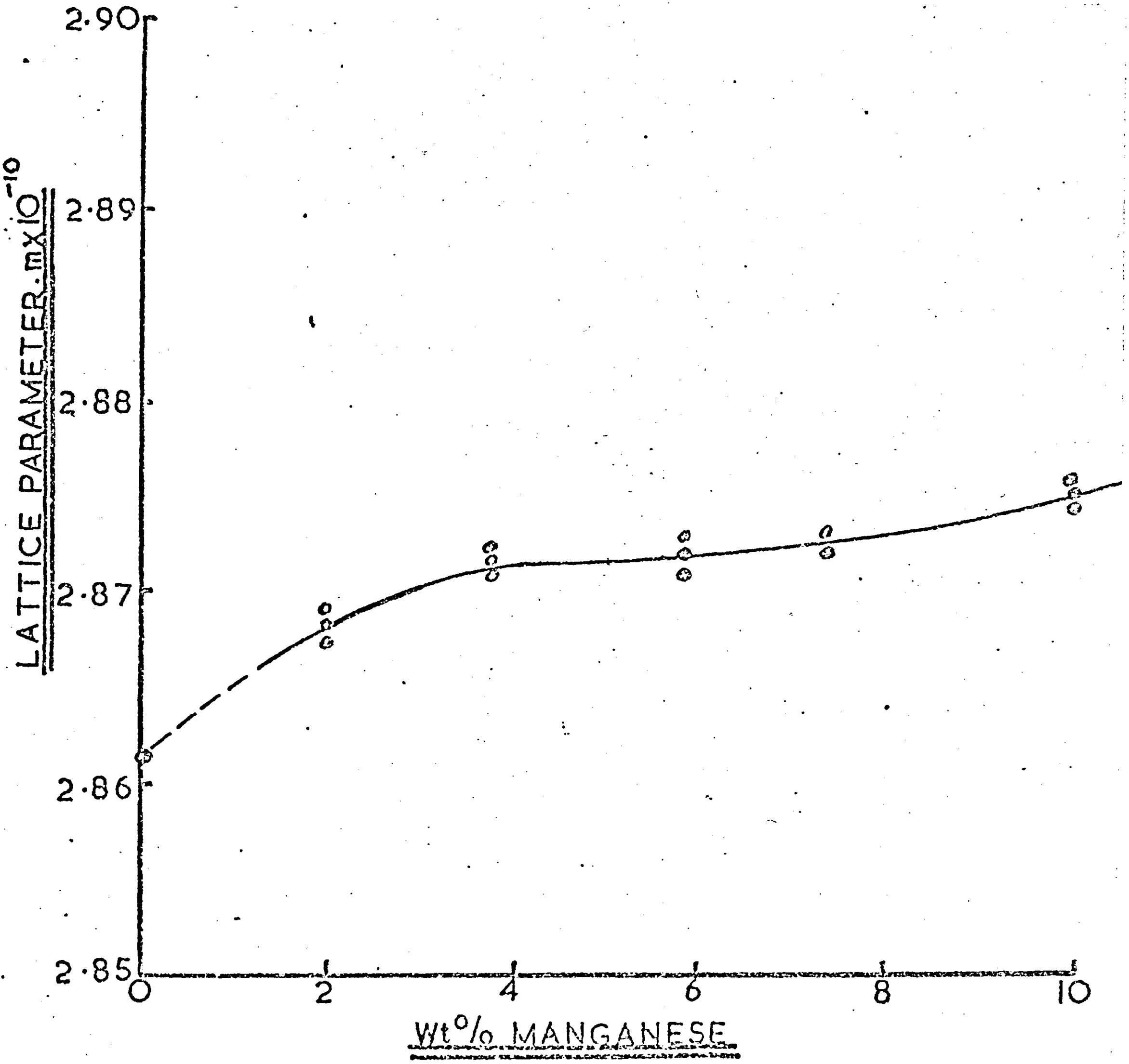

2·90
2·89
2·88
2·87
2·86
2·85
LATTICE PARAMETER. m X 10^{-10}
0
2
4
6
8
10
Wt% MANGANESE

FIG.79: Petch plot for fracture strength versus the reciprocal of the square root of grain size for iron manganese alloys within the range 4% - 10% manganese.

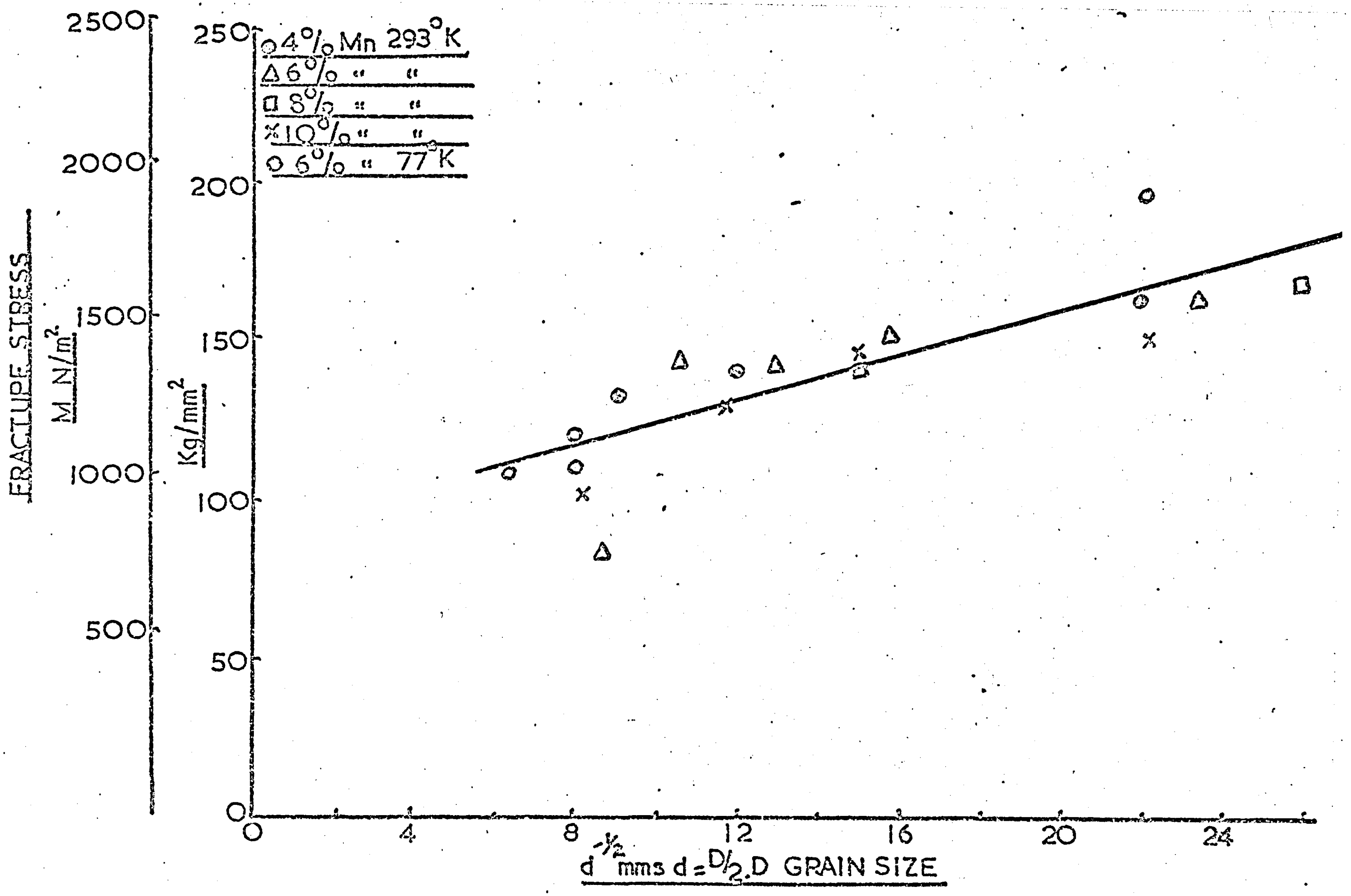
FRACTURE STRESS
M N/m²
Kg/mm²
2500
2000
1500
1000
500
250
200
150
100
50
0
0
4
8
12
16
20
24
$d^{-1/2}$ mms d = D/2, D GRAIN SIZE
○ 4% Mn 293°K
△ 6% " "
□ 8% " "
× 10% " "
○ 6% " 77°K

FIG.80: The variation in effective flow stress τ_* with testing temperature for iron - manganese alloys in the lath martensitic condition.

FIG.80A Shear strain rate $\dot{\gamma} = 0.604 \times 10^{-4}/s$

FIG.80B: Shear strain rate $\dot{\gamma} = 0.604 \times 10^{-3}/s$

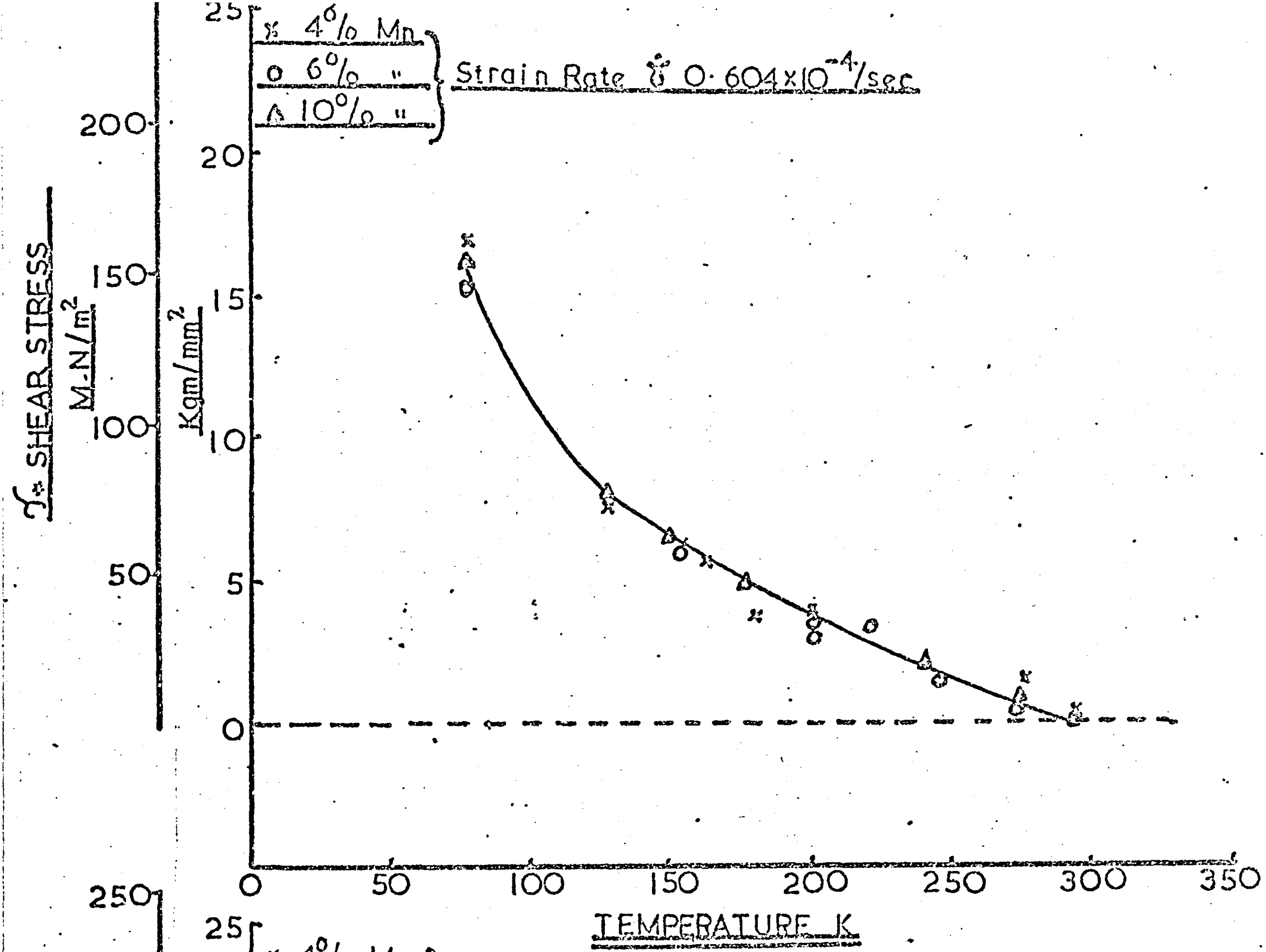
x 4% Mn
o 6% "
Δ 10% "
Strain Rate $\dot{\gamma}$ 0·604×10^{-4}/sec
τ_* SHEAR STRESS
M·N/m^2
Kgm/mm^2
0
50
100
150
200
0
5
10
15
20
25
0
50
100
150
200
250
300
350
TEMPERATURE K

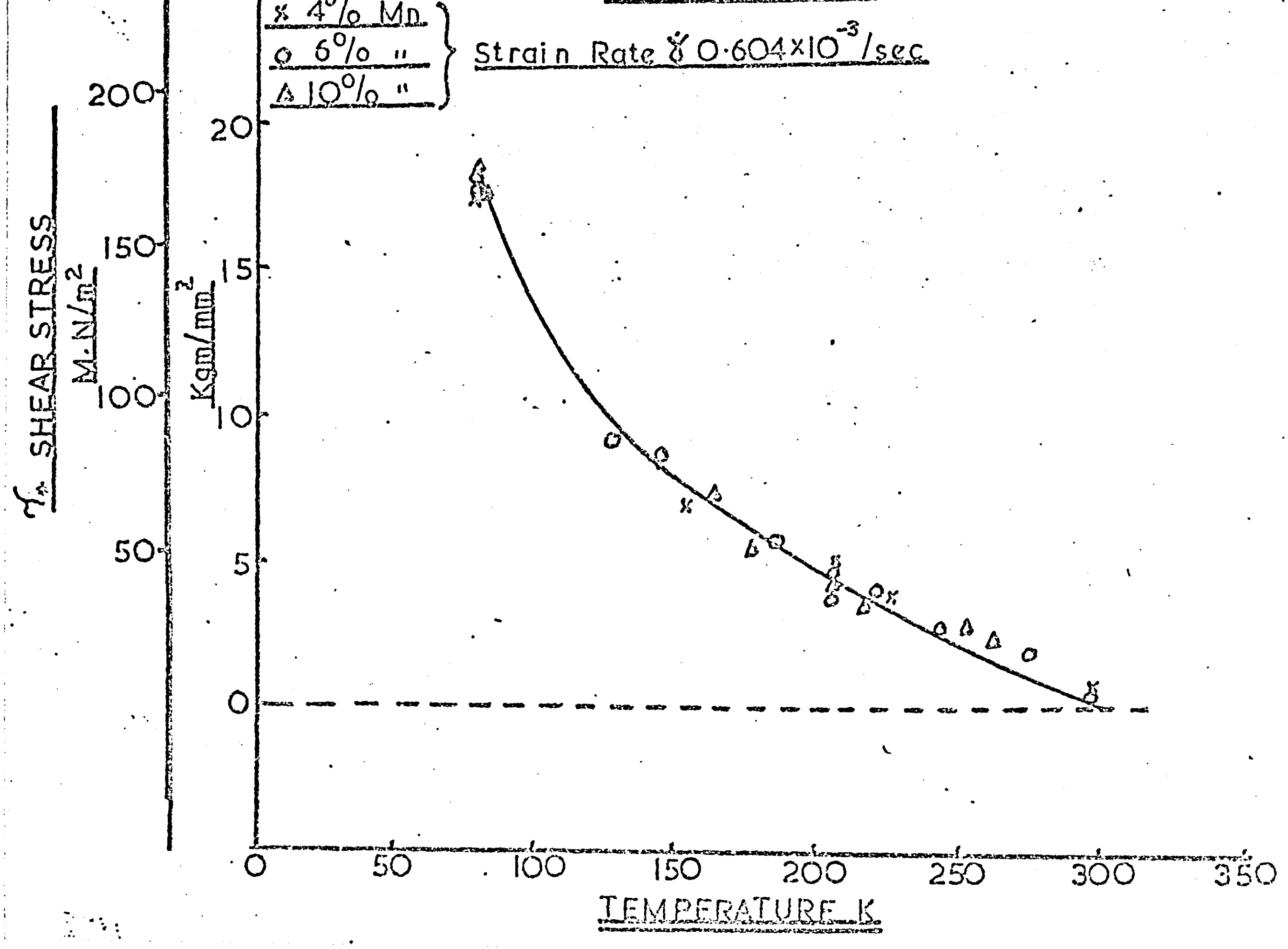
250
x 4% Mn
o 6% "
Δ 10% "
Strain Rate $\dot{\gamma}$ 0·604×10^{-3}/sec
τ_* SHEAR STRESS
M·N/m^2
Kgm/mm^2
0
50
100
150
200
0
5
10
15
20
25
0
50
100
150
200
250
300
350
TEMPERATURE K

FIG.80C: Shear strain rate = $0.604 \times 10^{-2}/s$

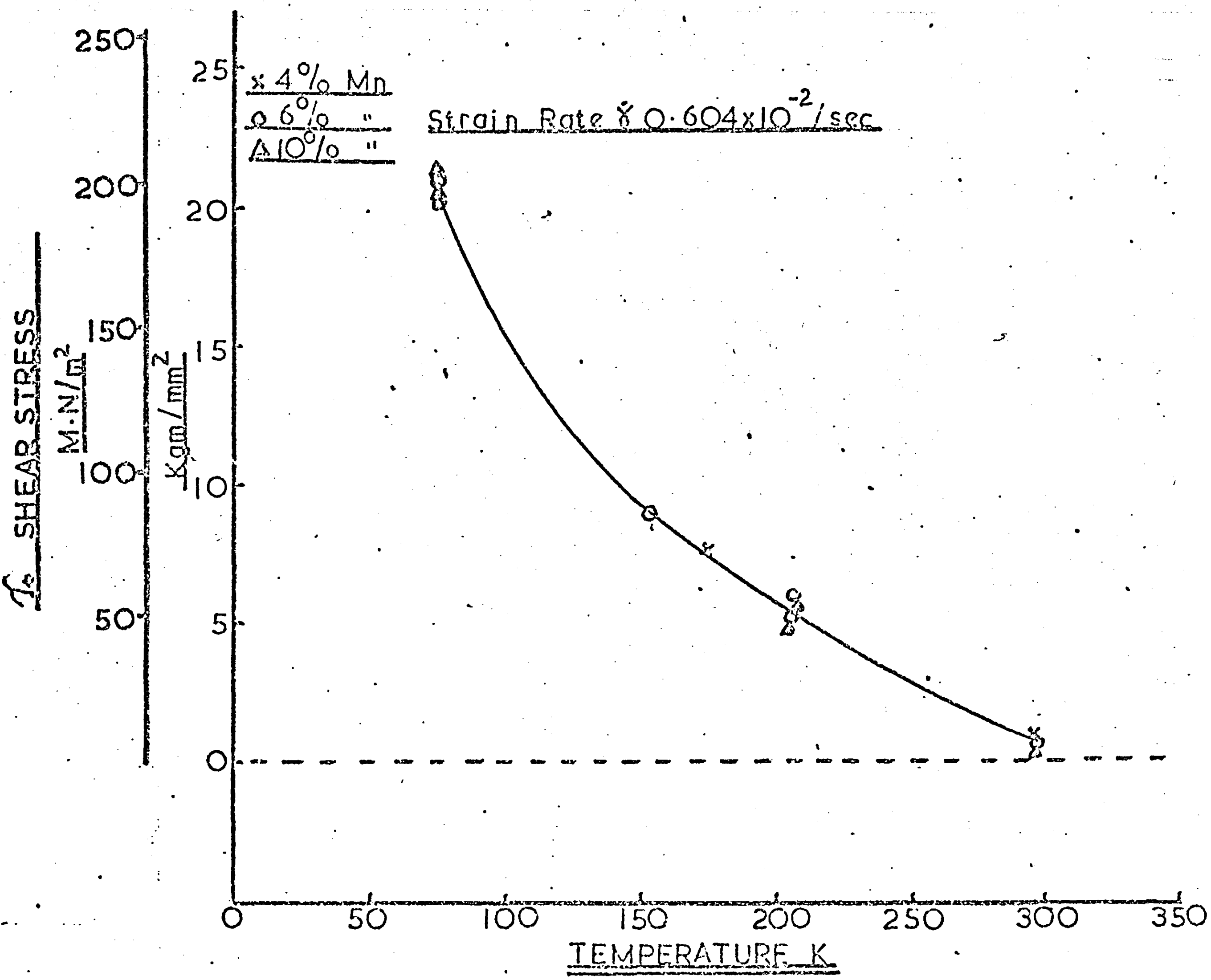x 4% Mn
o 6% "
Δ 10% "
Strain Rate γ̇ 0·604x10^-2/sec
τ SHEAR STRESS
M·N/m²
Kgm/mm²
250
200
150
100
50
25
20
15
10
5
0
0
50
100
150
200
250
300
350
TEMPERATURE K

FIG. 81: The variation in room temperature mechanical properties with tempering temperature.

FIG. 81A: Iron - 6% manganese tempered for one hour.

FIG. 81B: Iron - 10% manganese tempered for one hour.

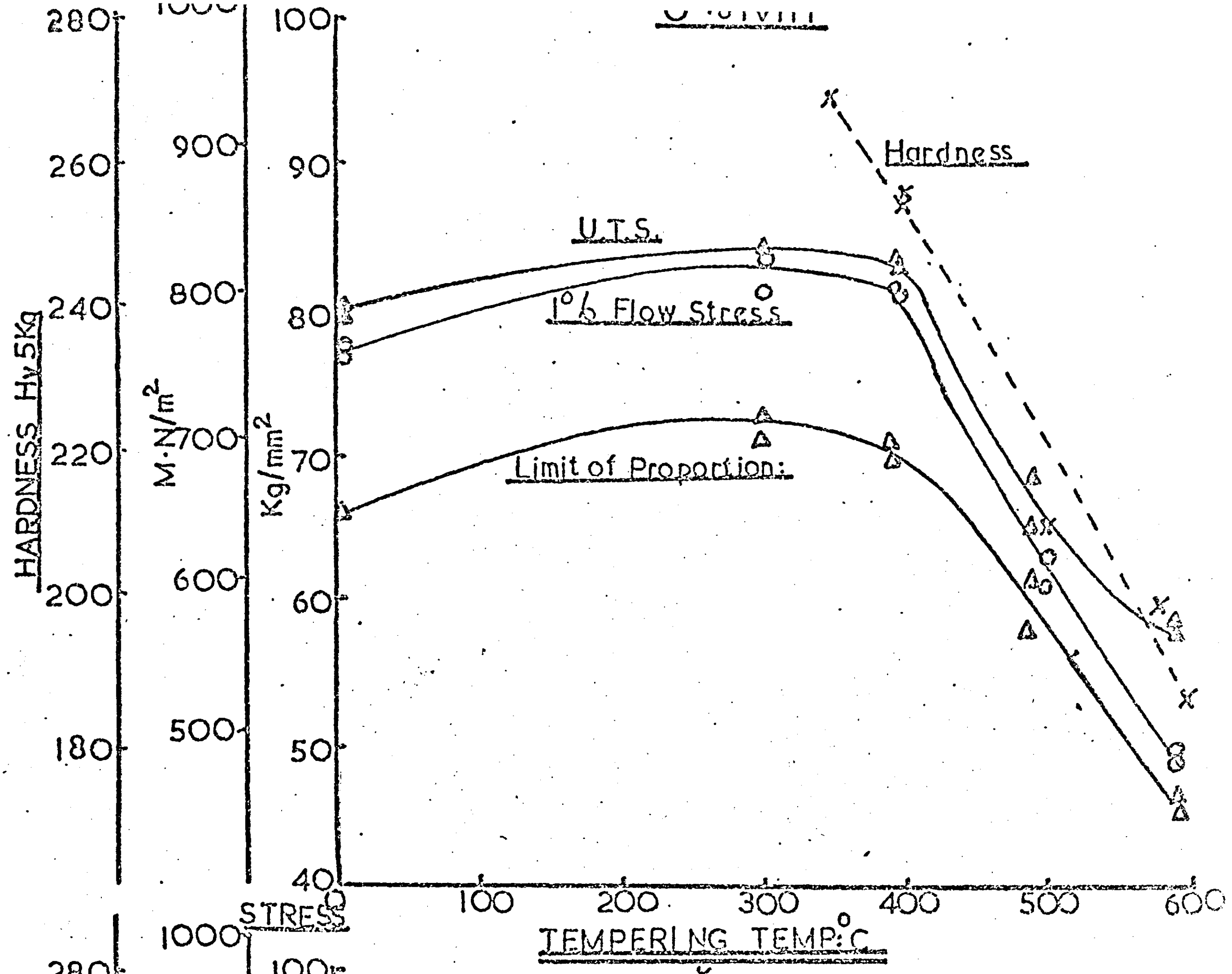HARDNESS Hv5Kg
280
260
240
220
200
180
M·N/m²
1000
900
800
700
600
500
Kg/mm²
100
90
80
70
60
50
40
Hardness
U.T.S.
1% Flow Stress
Limit of Proportion:
0
100
200
300
400
500
600
STRESS
TEMPERING TEMP °C

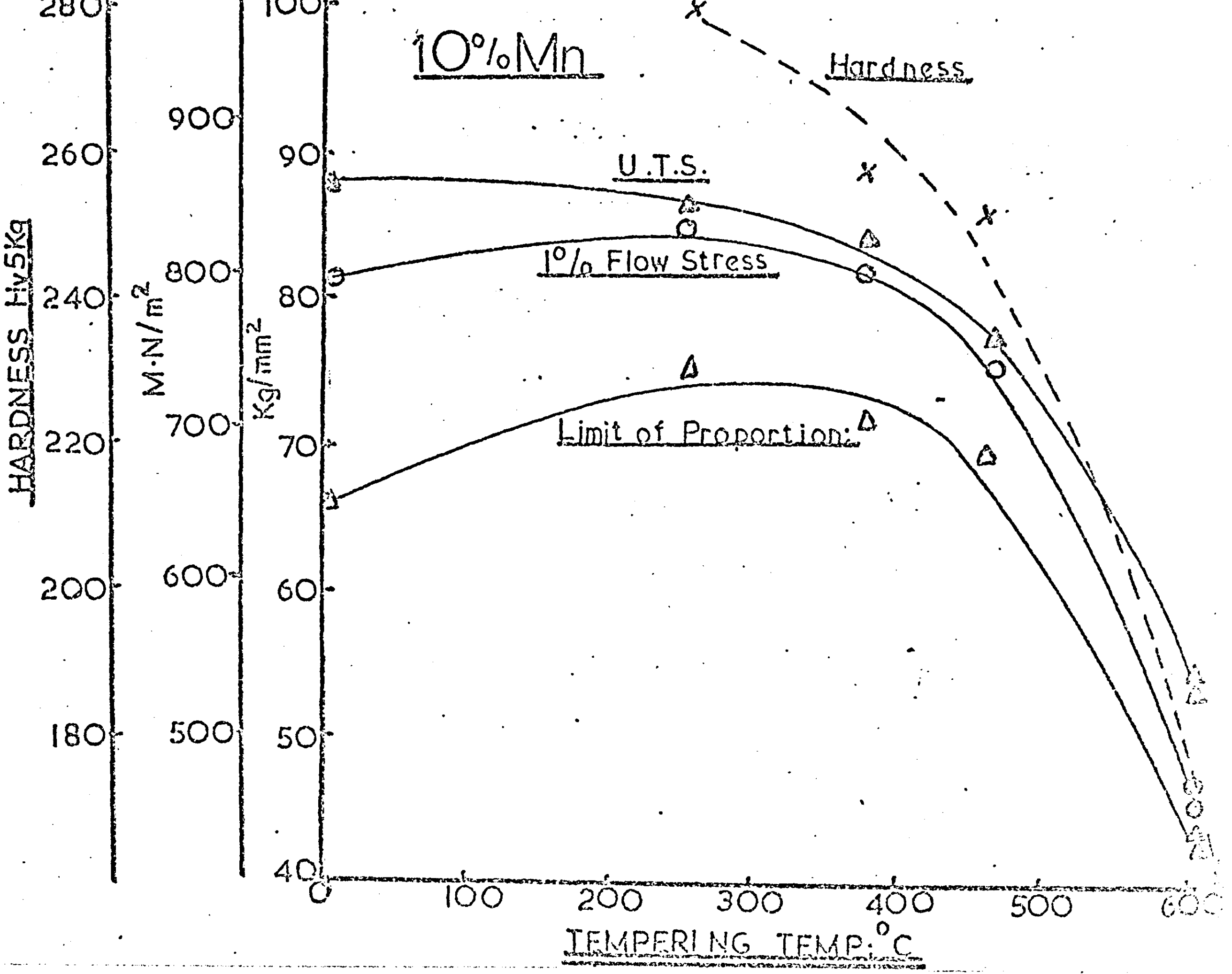10%Mn
HARDNESS Hv5Kg
280
260
240
220
200
180
M·N/m²
1000
900
800
700
600
500
Kg/mm²
100
90
80
70
60
50
40
Hardness
U.T.S.
1% Flow Stress
Limit of Proportion:
0
100
200
300
400
500
600
TEMPERING TEMP °C

FIG.82: The variation in the M_s, A_s and T_o temperature with manganese concentration

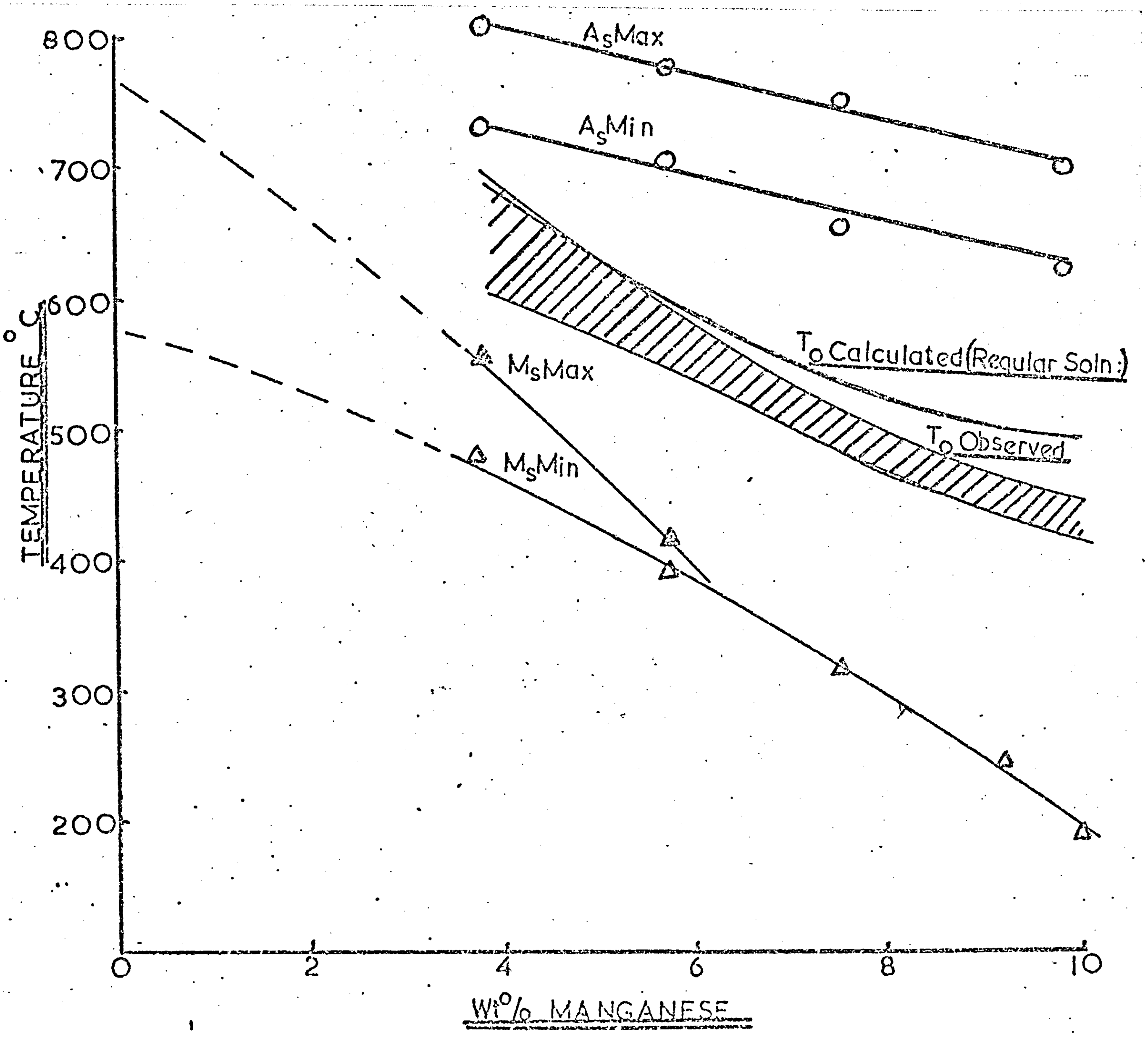

800
700
600
500
400
300
200
TEMPERATURE °C
0
2
4
6
8
10
Wt°/o MANGANESE
A_sMax
A_sMin
M_sMax
M_sMin
T_0 Calculated (Regular Soln.)
T_0 Observed

FIG.83A: Driving force for the $\gamma \rightarrow \alpha$ transformation according to an ideal solution model.

FIG.83B: Driving force for the $\gamma \rightarrow \alpha$ transformation according to a regular solution model

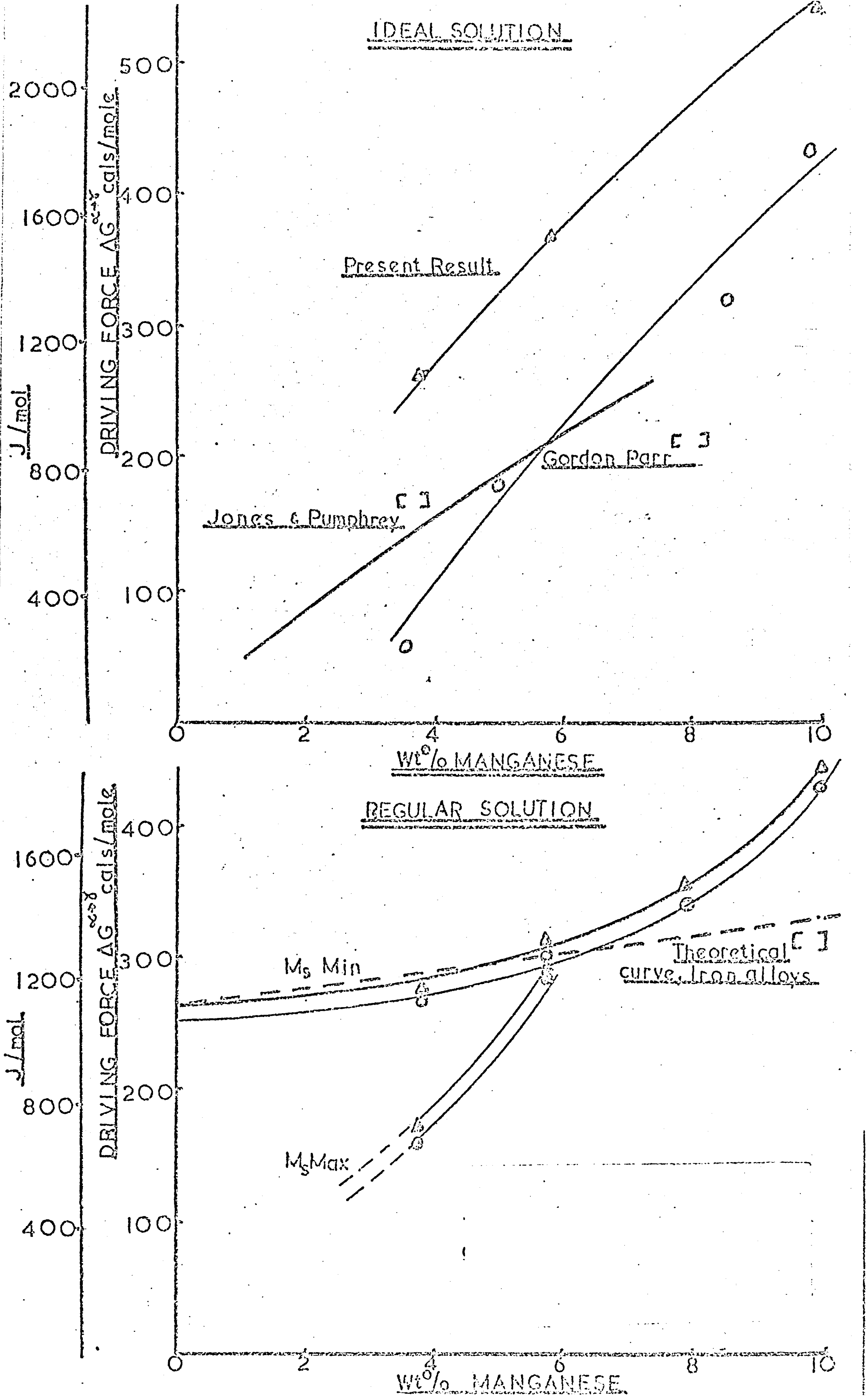
IDEAL SOLUTION
DRIVING FORCE ΔG^{α→γ} cals/mole
J/mol
2000
1600
1200
800
400
500
400
300
200
100
Present Result
Gordon Parr [ ]
Jones & Pumphrey [ ]
0
2
4
6
8
10
Wt% MANGANESE
REGULAR SOLUTION
DRIVING FORCE ΔG^{α→γ} cals/mole
J/mol
1600
1200
800
400
400
300
200
100
Ms Min
Theoretical [ ]
curve, Iron alloys
MsMax
0
2
4
6
8
10
Wt% MANGANESE

FIG.84: The variation in activation energy H for thermally activated flow, with the effective stress τ_* in iron manganese lath martensites.

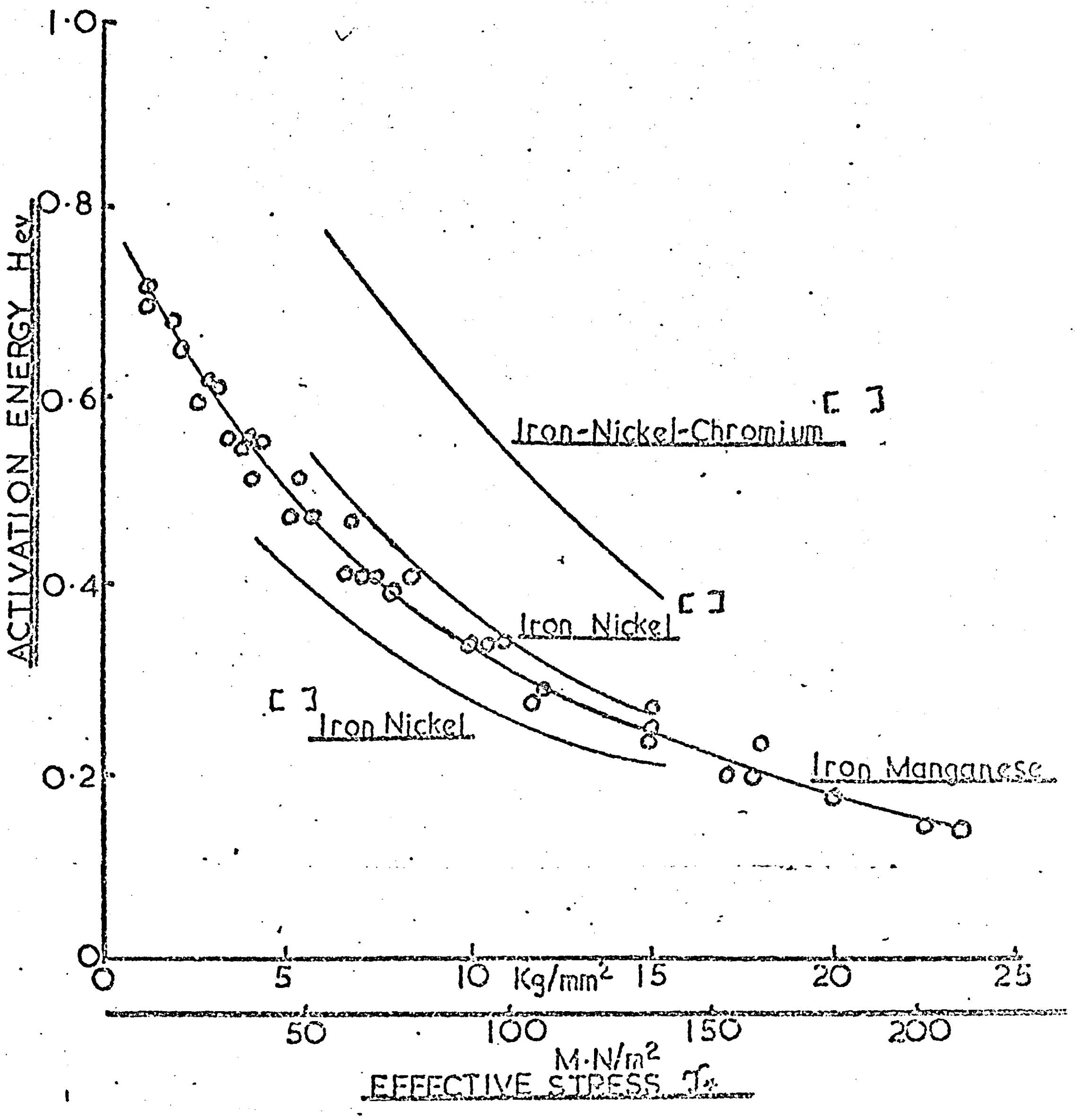
1·0
0·8
0·6
0·4
0·2
0
ACTIVATION ENERGY Hev
Iron-Nickel-Chromium [ ]
Iron Nickel [ ]
[ ] Iron Nickel
Iron Manganese
0
5
10 Kg/mm²
15
20
25
50
100
150
200
M·N/m²
EFFECTIVE STRESS τ*

FIG. 85: The variation in activation volume V_* with effective stress τ_* for iron manganese lath martensites.

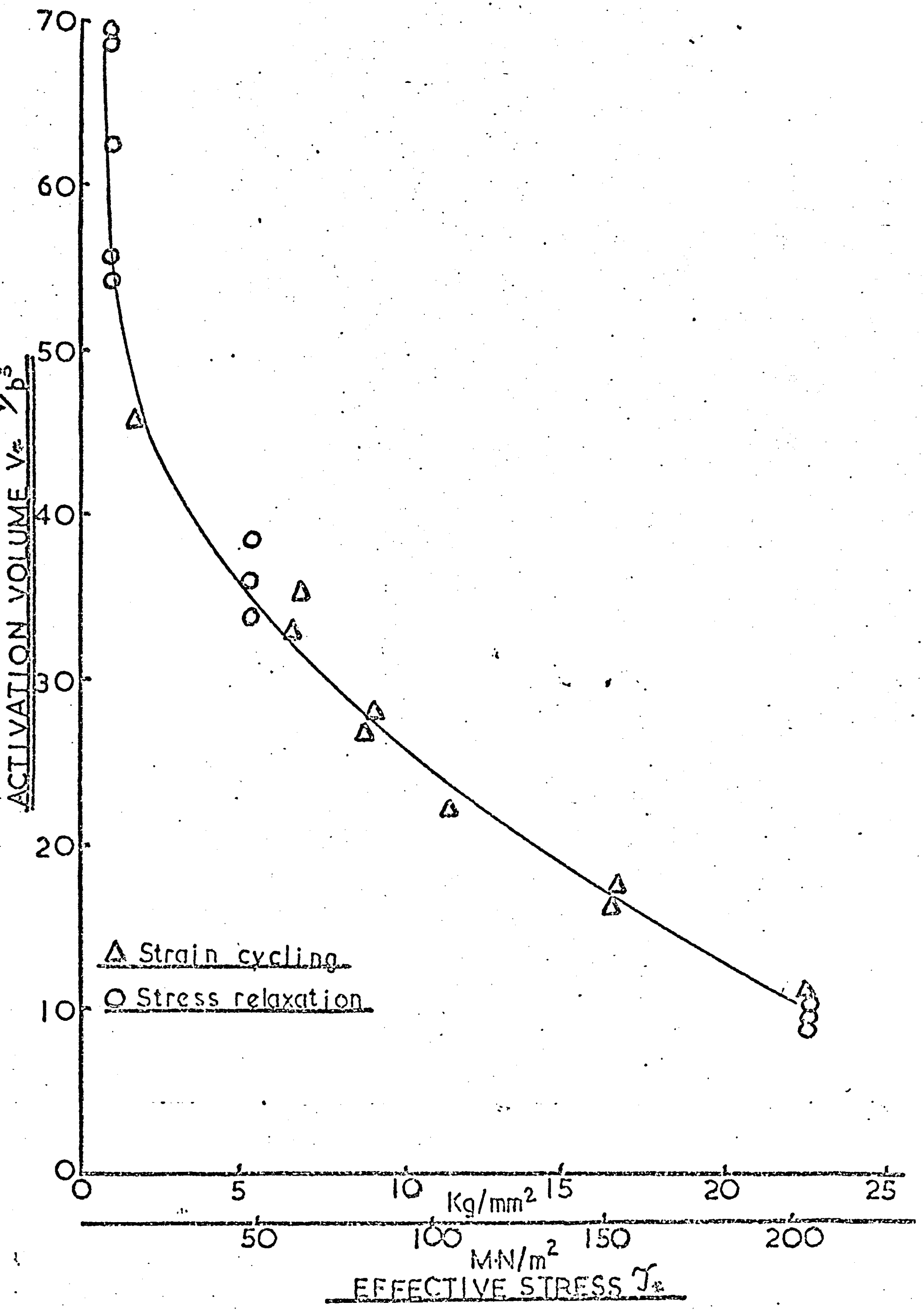
ACTIVATION VOLUME $V^* \; V^*/b^3$
0
10
20
30
40
50
60
70
△ Strain cycling
○ Stress relaxation
0
5
10
15
20
25
Kg/mm²
50
100
150
200
M·N/m²
EFFECTIVE STRESS τ^*

FIG.86: Typical log time versus stress relaxation curves for an iron - 4% manganese alloy at different testing temperatures.

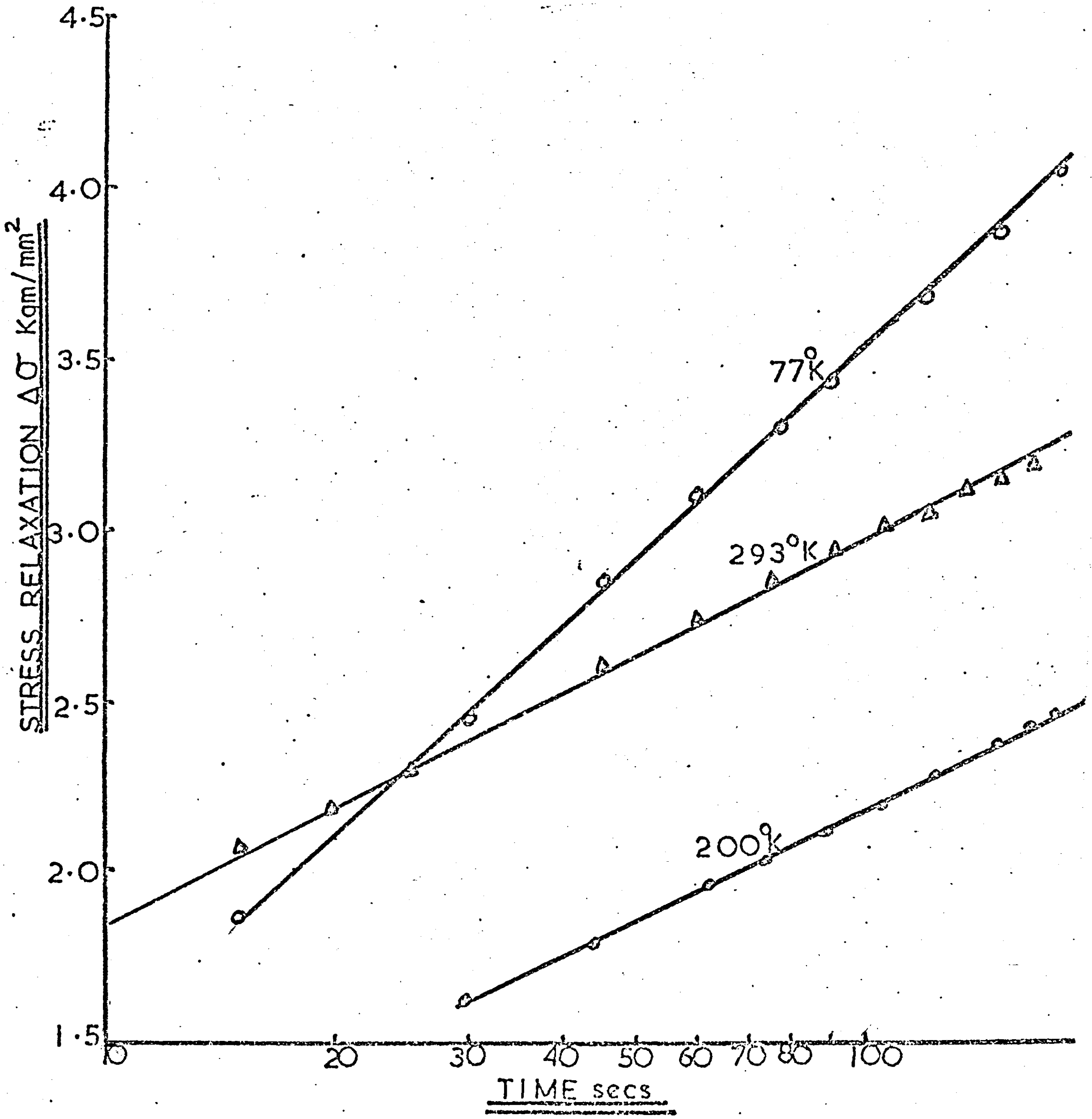

STRESS RELAXATION Δσ Kgm/mm²
4·5
4·0
3·5
3·0
2·5
2·0
1·5
10
20
30
40
50
60
70
80
100
TIME secs
77°K
293°K
200°K

FIG.87A: Plot of the theoretical relationship between $\frac{\tau_*}{\tau_p}$ and $\frac{T}{T_c}$ which fits the Dorn, Rajnak double kink mechanism for thermally activated flow. Also shown are the measured values of these parameters for iron manganese alloys.

FIG.87B: Plot of the theoretical relationship between $\frac{\tau_*}{\tau_p}$ and $\frac{H}{2H_k}$ which fits the Dorn, Rajnak double kink mechanism for thermally activated flow. Also shown are the measured values of these parameters for iron manganese alloys.

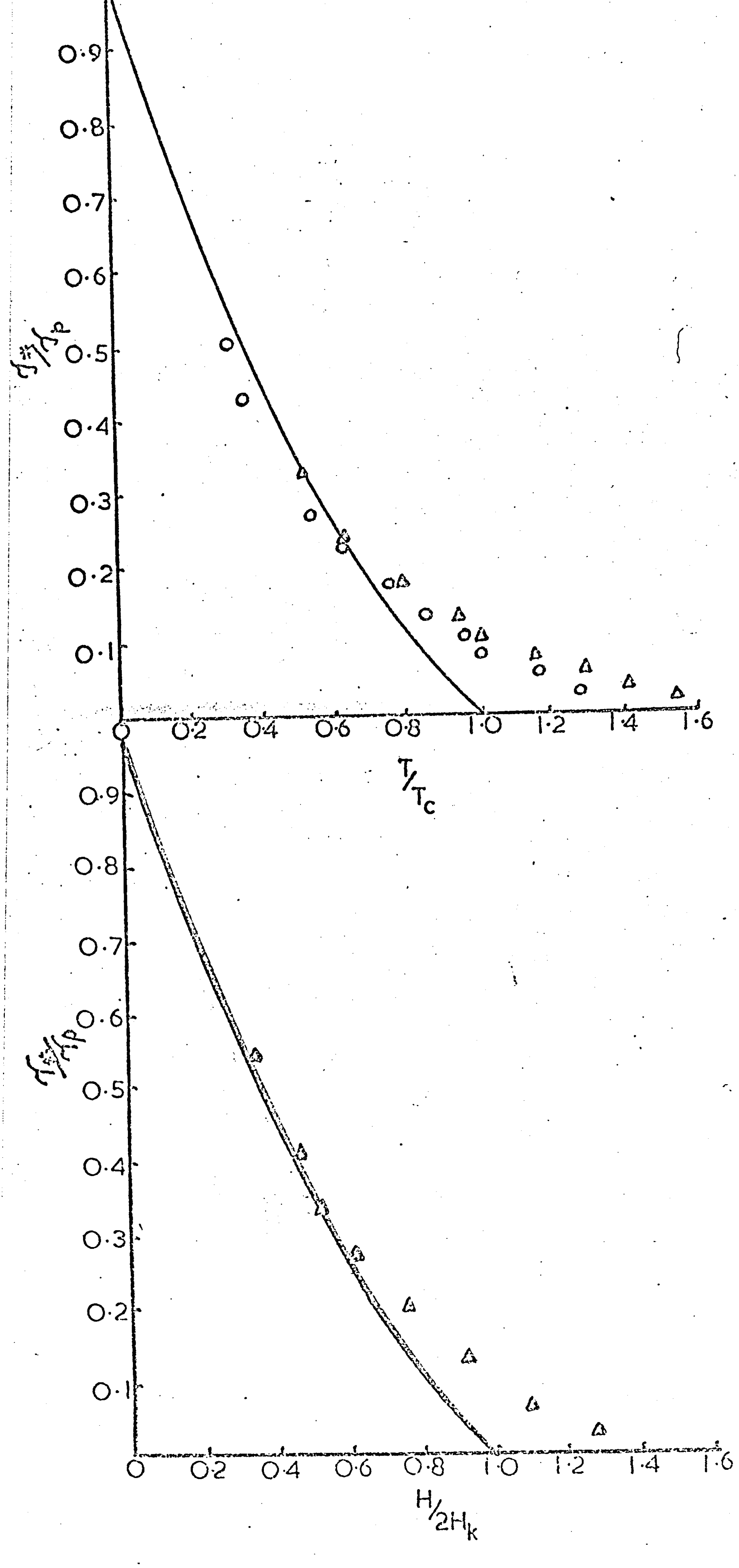
λ^*/λ_p
0·9
0·8
0·7
0·6
0·5
0·4
0·3
0·2
0·1
O
0·2
0·4
0·6
0·8
1·0
1·2
1·4
1·6
T/T_c
λ^*/λ_p
0·9
0·8
0·7
0·6
0·5
0·4
0·3
0·2
0·1
O
0·2
0·4
0·6
0·8
1·0
1·2
1·4
1·6
H/2H_k